KU LEUVEN

FACULTEIT WETENSCHAPPEN

Vrije Universiteit Brussel

Estimating the impact of earthquake-induced landslides on contemporary sediment yield

Towards a spatially distributed earthquake-induced landslide volume model

Jente BROECKX

Promotor: Dr. M. Vanmaercke

Co-promotor: Prof. Dr. J. Poesen

Proefschrift ingediend tot het behalen van de graad van Master of Science in de Geografie

Academiejaar 2013-2014

Preface

This master project was written in order to achieve the degree of Master of Science in Geography. The subject of this thesis was proposed by Dr. M. Vanmaercke and Prof. Dr. J. Poesen and fits in a broader framework of studies on the controlling factors of sediment yield. I would therefore like to thank both to make it possible to work on this interesting subject. Moreover, I am very grateful for the tremendous amount of time Dr. M. Vanmaercke invested in this whole research process and to be always ready to answer my deluge of questions. Further, I also wish to thank Dr. M. Vanmaercke and Prof. Dr. J. Poesen, for their ideas and additional input during the year and for their constructive comments on the writing of this dissertation. Finally, I wish to thank my parents for providing an ideal work atmosphere and M. Petrullo, for her mental support and aid on the lay-out of this dissertation.

Summary

Understanding catchment sediment yield is essential for several reasons: it plays a crucial role in landscape evolution as well as in several important biogeochemical cycles and affects human infrastructure. Sediment yield is assumed to be controlled by factors such as catchment area, climate, land use, topography and lithology. Recently however, several studies also revealed that seismic activity can strongly influence sediment yield, e.g. through earthquake-induced landsliding. Despite its suggested importance, this impact of earthquake-induced landslides on sediment yields is poorly understood and remains currently unquantified. Therefore, the aim of this thesis is to explore the impact of earthquake-induced landslides on catchment sediment yield.

On that account, a large global dataset (239 events) of earthquake events with information on associated landsliding was constructed. Compilation of this dataset was based on an extensive literature review. Subsets of these data were used to construct models that predict the total volume, number and likely spatial distribution of landslides associated with a given earthquake. The first two models were based on information of 77 earthquake events, while the latter was based on 25 earthquake-induced landslide inventories. Integration of these models allows simulating landslide volumes associated with a given earthquake in a spatially distributed way, based on the earthquake magnitude, earthquake epicenter and the local topography.

Despite large uncertainties on the originally reported landslide numbers and volumes and despite a lack of detailed data on potentially relevant variables such as main faults and lithology, these models allow for robust predictions. (1) Our total landslide volume model explained about 75% of the variation in reported volumes. (2) Deviations between the predicted and reported landslide volumes, which ranged over seven orders of magnitude,

were smaller than an order of magnitude for 64 of the 77 events. (3) For 24 out of 25 events our landslide distribution model performed better than a random prediction model (mean ROC value: 0.78). (4) Validation of the integrated model showed that errors on the spatial distribution of landslide versus non-landslide pixels can be mainly attributed to errors on the estimated total number of landslides.

The integrated model was applied to the Siret basin in Romania, which encompasses the seismic active Vrancea region. Simulated earthquake induced landslide masses (range of median values: 200-13000 t/km²/y) are mostly higher than the sediment yield (250-1800 t/km²/y) for catchments in the Vrancea region and are mostly lower (range of median values: 0-100 t/km²/y) than the sediment yield (55-400 t/km²/y) for catchments outside this region. The largest earthquake during the considered period (1977, M_w 7.4) contributed largely (20-50%) to the total generated landslide masses during this period in some of the catchments outside the Vrancea region, but little (0.4-10%) in most of the catchments in this region.

Referring to the aim of this thesis, the constructed models can be used as a global tool to investigate the impact of earthquake-induced landslides on the catchment sediment yield. To improve this model, further research should focus on a refinement of the volume estimates, rather than on the improvement of the allocation procedure.

Samenvatting

Inzicht in de sedimentexport in een rivierbekken is essentieel om verschillende redenen: het speelt een cruciale rol in zowel landschapsevolutie als verscheidene belangrijke biogeochemische cycli en het beïnvloedt menselijke infrastructuur. Het wordt verondersteld dat sedimentexport wordt gecontroleerd door factoren als bekken-oppervlakte, klimaat, landgebruik, topografie en lithologie. Recent echter, hebben verschillende studies aan het licht gebracht dat ook seismische activiteit de sedimentexport sterk kan beïnvloeden, bijvoorbeeld via grondverschuivingen veroorzaakt door deze aardbevingen. Ondanks het gesuggereerde belang, is de impact van deze grondverschuivingen op de sedimentexport slecht begrepen en is het tot nog toe niet gekwantificeerd. Daarom heeft deze thesis tot doel te onderzoeken wat de impact is van grondverschuivingen veroorzaakt door aardbevingen op de sedimentexport in een rivierbekken.

Om die reden werd een uitgebreide globale dataset samengesteld van 239 aardbevingen waarvan informatie omtrent veroorzaakte grondverschuivingen beschikbaar was. Deze dataset werd samengesteld op basis van een uitgebreid literatuuronderzoek. Subsets van deze gegevens werden vervolgens gebruikt om modellen op te stellen die het totale volume, het aantal en het ruimtelijk patroon van grondverschuivingen veroorzaakt door

een zekere aardbeving, voorspellen. De twee eerste modellen werden opgesteld op basis van 77 aardbevingen, terwijl het derde model gebasseerd is op 25 inventarissen van gronderverschuivingen veroorzaakt door één welbepaalde aardbeving. Het integreren van deze modellen laat dan toe om grondverschuivingsvolumes veroorzaakt door een zekere aardbeving te simuleren op een ruimtelijke manier. Vereiste parameters voor dit model zijn de moment magnitude, het aardbevings epicentrum en de lokale topografie in het getroffen gebied.

Deze modellen laten toe om robuuste voorspellingen te maken, ondanks de grote onzekerheden op de gerapporteerde grondverschuivingsaantallen en -volumes en ondanks het gebrek aan gedetailleerde gegevens omtrent potentieel relevante variabelen zoals de voornaamste breuklijnen en lithologie. (1) Het opgestelde grondverschuivings-volume model verklaarde ongeveer 75% van de variatie in de gerapporteerde volumes. (2) Afwijkingen tussen de voorspelde en gerapporteerde grondverschuivingsvolumes, die zeven grootteordes overspanden, zijn kleiner dan een factor tien voor 64 van de 77 aardbevingen. (3) Het grondverschuivings-distributie model scoort beter dan een willekeurig model voor 24 van de 25 aardbevingen (gemiddelde ROC-waarde: 0,78). (4) Validatie van het geïntegreerde model toonde aan dat de fouten op de voorspelde ruimtelijke verdeling van grondverschuivings- versus niet-grondverschuivingspixels voornamelijk konden worden toegeschreven aan fouten op de schatting van het aantal grondverschuivingen.

Het geïntegreerde model werd toegepast op het Siret bekken in Roemenië, dat de aardbevingsgevoelige Vrancea regio omvat. De gesimuleerde massa grondverschuivings-materiaal (spreiding mediane waardes: 200-13000 t/km²/j) is meestal groter dan de sedimentexport (250-1800 t/km²/j) voor bekkens in de Vrancea regio en is meestal kleiner (spreiding mediane waardes: 0-100 t/km²/j) dan de sedimentexport (55-400 t/km²/j) voor bekkens buiten deze regio. De grootste aardbeving tijdens de beschouwde periode (1977, M_w 7,4) droeg sterk (20-50%) bij aan het totale gegenereerde grondverschuivingsvolume tijdens deze periode in verscheidene bekkens buiten de Vrancea regio, maar droeg slechts weinig (0,4-10%) bij in bekkens binnen deze regio.

De opgestelde modellen kunnen dus worden gebruikt als een globaal instrument om de impact van grondverschuivingen veroorzaakt door een aardbeving op de sedimentexport na te gaan. Om het model te verbeteren, zou verder onderzoek zich moeten toeleggen op het verfijnen van de volume schattingen, eerder dan op een verbetering van de ruimtelijke toewijzingsprocedure.

Abbreviations

Al: individual landslide area (km²)

b_i: regression coefficient of variable I (-)

D: distance to epicenter (km)

D_{max}: maximum distance from the epicenter over which landslides are triggered or maximum landslide distance to the epicenter (km)

Dc: average catchment distance to the center of highest seismicity in the Vrancea region

DEM: digital elevation model (m)

DF: distance to main fault(s) (km)

DLV: integrated spatially distributed earthquake-induced landslide volume

DR: distance to river (km)

DS: standardized distance to the epicenter (-)

EEI: event efficiency index

EIL: earthquake-induced landslide

E-L: earthquake – landslide

EM: mean elevation (m.a.s.l.)

EP: exceedance probability (%)

EQ: earthquake

FD: focal depth (km)

GSHAP: Global Seismic Hazard Assessment Program

ID: identifier

K: kappa index of agreement (-)

K_l: kappa index of agreement for location (-)

$\hat{L}$: total likelihood (-)

LA: total landslide area (km²)

LAA: landslide-affected area (km²)

LAA_c: calculated landslide-affected area (km²)

LAA_r: reported landslide-affected area (km²)

LC-D: landslide concentration – distance to epicenter

LD: landslide distribution

LM: total landslide mass (t/km²/y)

LN: total landslide number

LN_m: modeled total landslide number

LN_s: simulated total landslide number

lr: likelihood ratio (-)

LR: local relief (m)

LR_{stdev}: standard deviation of the local relief (m)

LV: total landslide volume (10 E6 m³, km³)

LV_c: calculated total landslide volume (10 E6 m³, km³)

LV_{lc}: total landslide volume linearly corrected for the land fraction in the mask area (10 E6 m³, km³)
LV_m: modeled total landslide volume (10 E6 m³, km³)
LV_r: reported total landslide volume (10 E6 m³, km³)
LV_s: simulated total landslide volume (10 E6 m³, km³)
M: earthquake magnitude (-)
M-D: moment magnitude – maximum landslide distance to epicenter
M-V: moment magnitude – total landslide volume
M_b: body-wave magnitude (-)
M_l: local magnitude (-)
M_o: seismic moment (-)
M_s: surface-wave magnitude (-)
$M_{w:}$ moment magnitude (-)
MFI: modified Fournier index (-)
ML: maximum likelihood
MLR: mean local relief (m)
MMI: Modified Mercalli Intensity (-)
μ: mean
P: (mean annual) precipitation (mm/y)
p: probability (-)
p_{cum}: cumulative probability (-)
PGA: peak ground acceleration (m/s²)
PGV: peak ground velocity (m/s)
PS: total probability sum (-)
Q5: 5^{th} percentile
Q25: 25^{th} percentile
Q75: 75^{th} percentile
Q95: 95^{th} percentile
R: correlation coefficient (-)
R²: coefficient of determination (-)
R^2_{McF}: MCFadden's pseudo R² (-)
RMSE: root mean square error (-)
ROC: relative operation characteristic (-)
Ro: average annual runoff (mm/y)
SA: seismic activity
SD: sediment discharge (t/day, kg/s)
SE: sediment export (t/day, kg/s)
se: standard error (-)
SMA: maximum slope (%)
SME: mean slope (%)

SSP: subset selection procedure
SR: slope range (%)
SY: sediment yield (t/ha/y or t/km²/y)
σ: standard deviation (-)
T: (mean annual) air temperature (°C)
TC: tree cover (%)
USGS: United States Geological Survey
UTM: Universal Transverse Mercator
Vl: individual landslide volume (km³)
Vl_{max}: maximum individual landslide volume (10 E6 m³)
VIF: variance inflation factor (-)
W: Wald test statistic (-)
x_i: independent variable i
y: dependent variable

Table of contents

List of figures

List of tables

List of appendices

1 Introduction

1.1 Problem statement

Sediment discharge (SD) or sediment export (SE), i.e. the mass of solid material reaching the outlet of a catchment expressed in t/day or kg/s (Porterfield, 1972), and consequently also *sediment yield (SY)* in t/ha/y, are controlled by different factors, such as catchment area, climate, land use, topography and lithology (Vanmaercke et al., 2011b). Recently a number of studies revealed that also *seismic activity (SA)* is often important for explaining differences in sediment discharge of rivers (Chuang et al., 2009; Hovius et al., 2011; Korup, 2012; Vanmaercke, 2012; Vanmaercke et al., 2014a; Vanmaercke et al., 2014b). This relation is often explained by the fact that SA induces *landslides* that contribute to the SD (e.g. Burbank et al., 1996, Chuang et al., 2009; Hovius et al., 2011). Nevertheless, also other mechanisms may explain observed correlations between spatial patterns of seismic activity and sediment discharge, including *rock fracturing* (Scholz, 1968; Molnar et al., 2007) and *rock uplift* (Burbank et al., 1996; Hubbard & Shaw, 2009). Likewise, also Lavakas (i.e. large erosional gullies), were found to strongly correlate with SA in Madagascar, although the mechanisms explaining this correlation are currently poorly understood (Cox et al., 2010).

Earthquake-induced landslides (EIL) are defined as the movement of a mass of rock, earth or debris down a slope, under the influence of gravity and induced by an earthquake (EQ) (Cruden, 1991). EIL can be characterized by their volume and location. The location determines whether sediment is deposited directly into the river channel or at the hillslope, which will cause a different impact on the SD. Hovius et al. (2011) investigated the effect of the large Chi-Chi earthquake of 1999 in Taiwan by confronting detailed mapped landslides with the fluvial SD. They state that the observed, sudden pulse in SD (Figure 1) can be attributed to these EIL. However, other research questioned these findings (Huang & Montgomery, 2012). They argued that it is doubtful to attribute the landslides primarily to the effects of the Chi-Chi EQ, as it is also possible that the increased SD after 2000 resulted from climatic factors. Furthermore, the only studies that are currently available regarding the impact of earthquakes on temporal variations in SD, are case studies of highly tectonically active and steep catchments in Taiwan, which are strongly affected by typhoons (e.g. Hovius et al., 2011; Huang & Montgomery, 2012; Chuang et al., 2009).

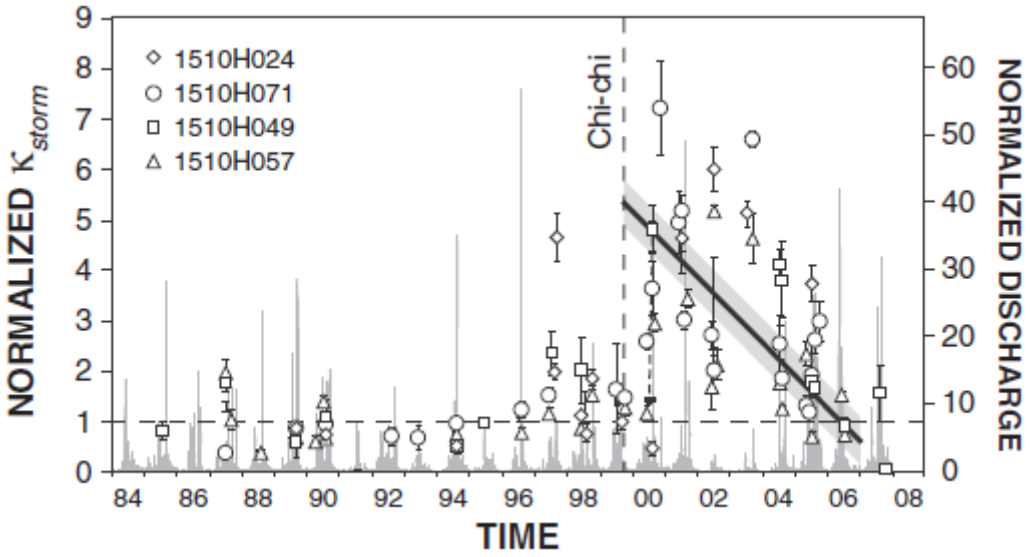

Figure 1: Evolution (1984-2008) of the unit sediment concentration in major storm floods (Kstorm) at four stations in the Choshui catchment (error bars show 1σ range). For direct comparison, values have been normalized to the mean of values prior to September 1999 at a station. The linear least squares best fit to the post-earthquake data (R^2=0.54) shows relaxation of the unit sediment concentrations from a peak after the earthquake in 6±0.8 y (1σ shown in grey). Water discharge, normalized to the average of 1984–2007 (~150 $m^3 s^{-1}$), is shown in the background (Hovius et al., 2011, p 3).

Despite the suggested importance of EIL (Burbank et al., 1996, Chuang et al., 2009; Hovius et al., 2011), their actual impact on SD and SY for catchments under different environmental and tectonic conditions remains poorly understood and unquantified. There is therefore a need for more studies in other regions, similar to Hovius et al. (2011) that compare detailed spatially distributed EIL inventories, with detailed SD data. However, detailed spatially distributed EIL inventories are scarce (Harp et al., 2011). This problem could be circumvented, if we succeed in correctly *simulating volumes and spatial distributions of EIL*, under different environmental and tectonic conditions. Recent advances concerning EIL (e.g. Malamud et al., 2004a, Parker, 2013) may make this possible. Therefore, the *correct simulation of earthquake-induced landslide volumes and their spatial distribution is the aim of this thesis*.

1.2 Background

1.2.1 Earthquake specific parameters

Earthquakes can be characterized by a number of different parameters. A first important parameter is the *epicenter*, which is defined as the point at the earth surface, vertically projected from the hypocenter, which is the point in the earth crust where a seismic rupture originates (USGS, 2012). The distance between the hypocenter in the earth crust and the epicenter at the earth surface is defined as the focal depth (FD). Another parameter is the *earthquake magnitude (M)*, a number indicating the size of an EQ or the energy released by an earthquake. Different scales have been developed, mostly used are: local magnitude (M_l) or Richter magnitude, surface-wave magnitude (M_s), body-wave magnitude

(M_b) and *moment magnitude (M_w)* (USGS, 2012). The first three scales are directly based on registered amplitudes of different waves (e.g. body waves travelling through the earth or surface waves travelling through the earth's upper layers) generated by an EQ and measured by a seismograph (Richter, 1935; Gutenberg & Richter, 2010). The fourth important scale (M_w) was introduced to cope with the problem of saturation at higher magnitudes and inadequate representation of greater (>100 km) rupture lengths (Kanamori, 1977; Campbell, 1997). Contrary to the other scales M_w is not based on the amplitude of the generated earthquake waves, but on the seismic moment (M_o), which is seen as one of the most precise measures of earthquake size. As explained before, M_w is more appropriate for large magnitudes compared to other measures, but approximates these measures for lower magnitudes (M_w < 7.5) (Kanamori, 1977; Keefer, 1994; Campbell, 1997). M_o and M_w are defined as follows (respectively: Kanamori, 1977; Hanks & Kanamori, 1979):

$$M_o = \mu \bar{D} s \quad (1)$$

$$M_w = \frac{2}{3} log_{10} M_o - 10.7 \quad (2)$$

With μ the rigidity, $\bar{D}$ the average fault slip and s the rupture area. The rigidity of a material (rock) is defined as the materials resistance to deformation and is expressed as the ratio between the normal stress and the strain (Baumgart, 2000). The fault slip is the relative displacement of two sides of a fault, ranging from centimeters for small earthquakes to tens of meters for large earthquakes (Ammon, 2014). The rupture area is the area at the earth surface that slipped (Ammon, 2014). Keefer (1994) states that a *M_w of 4 is required to induce landsliding*, with M_w smaller than 5 usually causing only a few landslides. Another frequently used type of parameters to characterize earthquakes is *intensity*. This measure indicates the severity of an EQ in terms of effects to human infrastructure and the earth's surface (USGS, 2012). The Modified Mercalli Intensity (MMI) scale is most commonly used and is associated with peak ground acceleration (PGA) and peak ground velocity (PGV) triggering damage at the earth surface (Keefer, 1984; USGS, 2013b). Unlike the characterization of an EQ by a single magnitude, MMI depends on the location in the earthquake region.

1.2.2 Landslide parameters linked to earthquake activity

The epicenter, magnitude and intensity can be used to assess the impact of an EQ in terms of landslides. Important characteristics of the earthquake-induced landslides are the *total landslide volume (LV)*, the total number of landslides (LN), the total landslide area (LA), the *landslide distribution (LD)*, the area affected by landslides (LAA) and the maximum distance from the epicenter over which landslides are triggered (D_{max}) LAA is defined as the area of a polygon enclosing all observed landslides. However, sometimes a rougher best fit polygon is applied, resulting in a larger reported LAA (LAA_r) (Jibson & Harp, 2012).

1.2.3 Predicting the total landslide volume

Current best estimates of *earthquake-induced landslide volumes (LV)* are based on the moment magnitude as an explanatory variable (e.g. Keefer, 1994; Malamud et al., 2004a). A first relation was constructed by Keefer (1994), based on fifteen historical earthquake events for which LV was determined from detailed field investigations and from interpretation of aerial photographs. All events occurred in areas with high historical seismicity, but would represent a wide variety of climatic and geologic conditions (Keefer, 1994). This empirical relationship was only slightly modified with the inclusion of the Northridge EQ (United States, 1994, M_w 6.7) by Malamud et al. (2004a). The proposed relation is presented in Figure 2 and shows a good power-law dependence of LV on M_w. However, the relation is based on relatively *few events* with a M_w ranging from 5.3 to 8.6 (Malamud et al., 2004a). This small amount of available data on LV is explained by the difficulty to produce comprehensive landslide inventories (Harp et al., 2011).

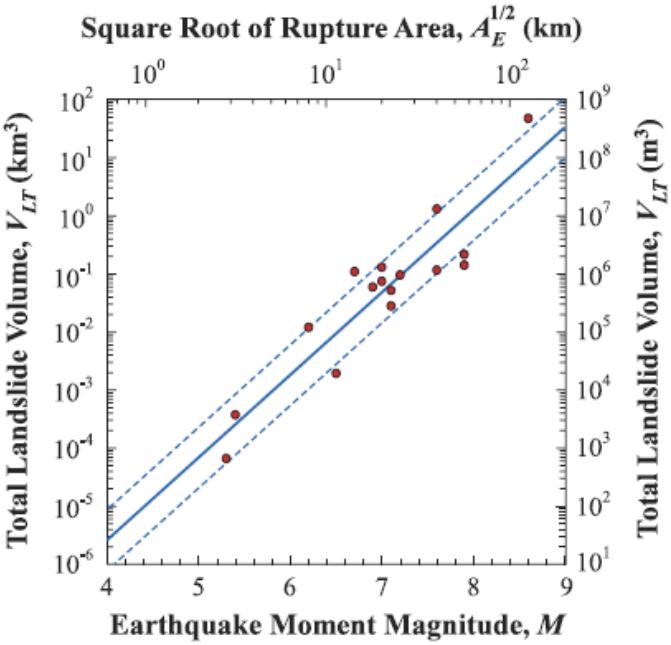

Figure 2: Total landslide volume generated by an earthquake (LV) as a function of the moment magnitude (Mw) (Malamud et al., 2004a, p 50).

Next to the relation between M_w and LV, Malamud et al. (2004a) proposed a *probability density distribution function* of landslide sizes for events triggering landslides (e.g. rainfall, snowmelt or earthquake). In Figure 3 it is shown that different events follow the same probability density distribution. The fitted function is the following (Malamud et al., 2004a):

$$p(A_l;\rho,a,s) = \frac{1}{a\Gamma(\rho)}\left(\frac{a}{A_l-s}\right)^{\rho+1} exp\left(-\frac{a}{A_l-s}\right) \quad (3)$$

With $\Gamma(\rho)$ the gamma function, ρ the parameter controlling the power-law decay for medium and large values of the three parameter inverse-gamma probability distribution, a the parameter controlling the location of maximum probability in the three parameter inverse-gamma probability distribution, s the parameter controlling the exponential rollover

for small values in the three-parameter inverse-gamma probability distribution and with Al the individual area of a landslide (Malamud et al., 2004b).

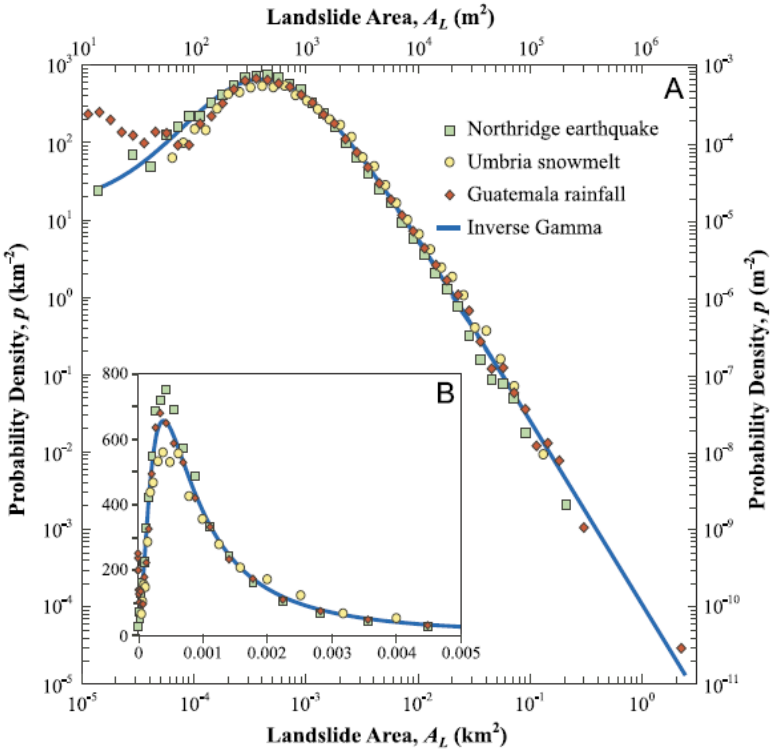

Figure 3: Dependence of the landslide probability densities (p) on the landslide area (A_L) for three landslide inventories (1) 11,111 landslides triggered by the 17 January 1994 Northridge earthquake in California; (2) 4233 landslides triggered by rapid snowmelt in the Umbria region of Italy in January 1997; (3) 9594 landslides triggered by heavy rainfall from Hurricane Mitch in Guatemala in late October and early November 1998 (Malamud et al., 2004a).

Based on this general distribution function, Malamud et al. (2004a) report a good agreement between LV and LN, regardless of the location or triggering mechanism of the landslide event. They derive the following equation (Malamud et al., 2004a):

$$\mathrm{LV} = 7.30 * 10^{-6} LN^{1.122} \tag{4}$$

Finally an empirical scaling relationship between the individual landslide area (Al, km²) and the individual landslide volume (Vl, km³), is proposed (Malamud et al., 2004a):

$$V_l = 0.05 * {A_l}^{1.50} \tag{5}$$

1.2.4 Predicting the spatial patterns of earthquake-induced landslides

Besides LV prediction, considerable work has been done on predicting the *location* where landslides are most likely to occur (e.g. Vanacker et al., 2003; Guzzetti et al., 2006; Van Den Eeckhaut et al., 2006; Miles & Keefer, 2009; Parker, 2013). However, most of these efforts were conducted in specific areas and require detailed input data that is unavailable on a global level (Miles & Keefer, 2009; Parker, 2013). Hence, these models are generally not appropriate for application in other regions. Parker (2013) made a first attempt towards

a general applicable EIL probability model. Different variables characterizing the local seismic forcing (e.g. fault plane distance and hillslope orientation with respect to seismic source) and the local stability of hillslopes (e.g. local hillslope gradient, solar radiation and precipitation) were tested. Based on his analyses, Parker (2013) constructed a model that predicts the susceptibility of landslides related to a given earthquake event based on M_w, the distance to the main fault (DF) and the local hillslope gradient. Still, this model was only based on landslide inventories from 5 relatively large earthquake events (M_w 6.7-7.9). Furthermore, this model requires spatially explicit information on the main faults.

Landslide distribution research concerning LAA, D_{max} and the landslide concentration with respect to distance to the epicenter (LC-D) can also give a better insight in the zones of landslide occurrence. Similar to LV, LAA and D_{max} are generally related to M_w (Keefer 1984; Keefer, 2002). The results presented in Figure 4, show increasing LAA and D_{max} with increasing M_w. Nonetheless, the scatter on these trends is large. Jibson & Harp (2012) suggest that part of this scatter might be explained by different tectonic settings, with smaller attenuation in non-plate-boundary settings explaining for greater LAA and D_{max}. It is also this *attenuation* of seismic waves that is put forward to explain for the observed decreasing landslide concentration away from the epicenter (Meunier et al., 2013). Indeed, different authors (e.g. Keefer, 2002; Guzzetti et al., 2009b; Gorum et al., 2011) find an exponentially decreasing LC in function of the distance to the epicenter. This is shown for the Wenchuan EQ (China, 2008, M_w 7.9) in Figure 5.

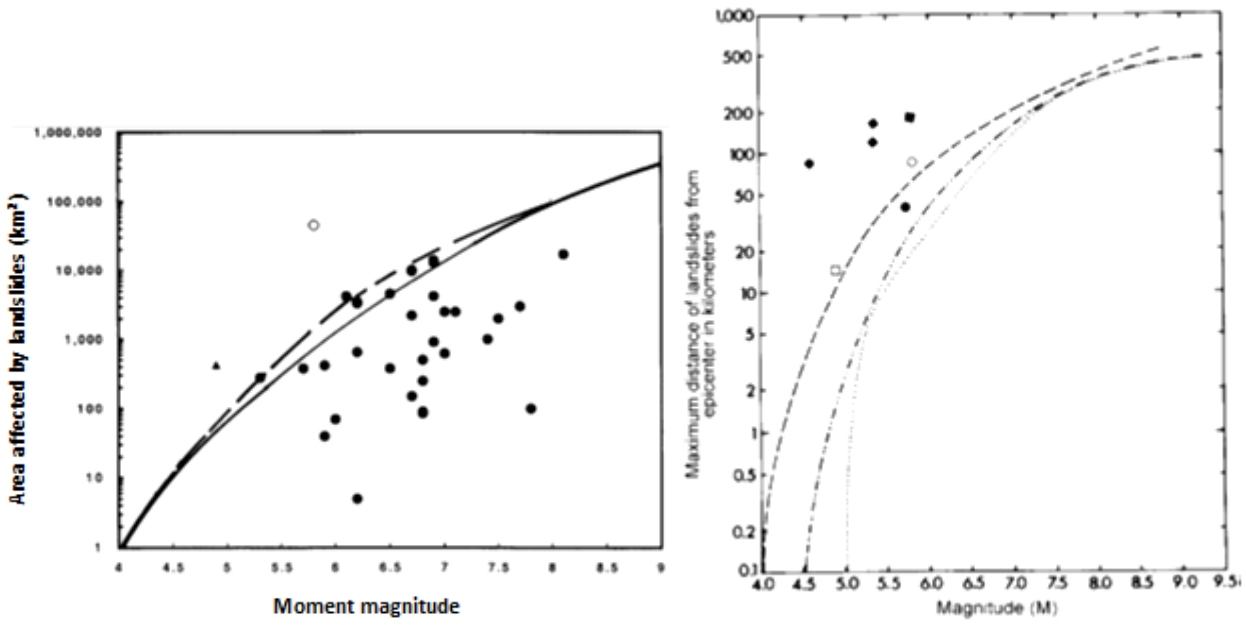

Figure 4: (left) Upper bounds for landslide-affected area (LAA) in function of moment magnitude (M_w). The solid line is an upper bound of Keefer (1984), the dashed line is an upper bound of Rodriguez et al. (1999). (right) Upper bounds for the maximum distance from the epicenter over which landslides are triggered (D_{max}) in function of the moment magnitude (M_w) in three major landslide categories (defined in Keefer, 1984) based on 40 historical earthquakes (Keefer, 2002, p 487).

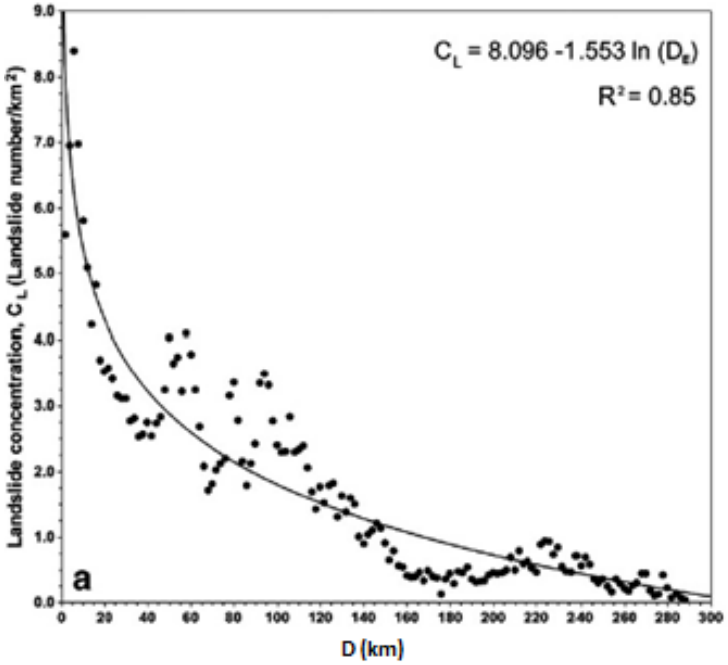

Figure 5: Landslide concentration (LC) in function of the distance to the epicenter (D, km) for the Wenchuan earthquake (China, 2008, M_w 7.9). D is displayed in x-axis in kilometer (Gorum et al., 2011, p 162).

1.2.5 Important factors for the occurrence of earthquake-induced landslides

The previous two sections already revealed the importance of magnitude, slope and distance to the seismic source. This section provides a general overview of factors that are stated to be important for the occurrence of EIL. These factors should be considered for both LD and LV prediction with the following difference. *LD prediction* requires the knowledge of predictor variables coupled to *individual locations* in order to investigate the locations susceptibility for EIL. For *LV prediction* on the other hand, the knowledge of certain predictor variables has to be *integrated over the potential LAA*, to assess the overall susceptibility of the affected area.

1.2.5.a Magnitude, distance to seismic source and focal depth

All current research finds log-linear positive relationships between M_w on the one hand and LV, LN and LAA on the other hand (e.g. Keefer, 1994; Rodriguze et al. 1999; Malamud et al., 2004a). Observed increasing *strength and duration of ground motions* can explain for the larger landslide concentration at a certain distance from the epicenter and the larger affected area with increasing M (e.g. Bommer & Martinez-Pereira, 1999; Jibson, 2007). Therefore, M provides a direct measure for the LV potential, whereas distance to the seismic source (D or DF) is useful to delineate areas of increased landsliding. In this context, Keefer (1994) states that the smallest earthquakes likely to trigger landslides have M_w of about 4 and that typically more than 95% of the EIL are concentrated in less than half of the LAA. Furthermore most of the generated landslide volume over time in a certain region is caused by a few large earthquakes (92% of volume by events with M_w>7)

(Keefer, 1994). For individual events the total volumes are dominated by a small number of large landslides (Guzzetti, 2008).

A parameter related with distance to the seismic source is *focal depth*. Similar to increasing distances from the epicenter, LN is stated to decrease with increasing FD (Parker, 2013).

1.2.5.b Seismic history and peak ground acceleration

Parker (2013) suggests that the *seismic history* might influence the amount of landslides triggered. He states that the same EQ could trigger a different LV depending on the accumulated damage by previous earthquakes. A detailed earthquake history preceding the event of interest, would then contribute to a better insight in the triggered landslide volume. *Peak ground acceleration* is another measure that could account for the seismicity of a region if it is used as an integrated measure. PGA represents how strong the ground accelerates (m/s^2). In this way a dataset of expected PGA, compiled based on historic earthquake events (Shedlock et al., 2000), is a good proxy for the seismicity of a region in general (Vanmaercke et al., 2014a).

Besides, PGA itself can be used to indicate the intensity of shaking at each location for a single earthquake event (Meunier et al., 2013). The United States Geological Survey (USGS, 2013b) uses PGA to compile so called 'Shakemaps'. These maps are a more detailed proxy for the attenuation of seismic waves, compared to the distance to the epicenter. For instance, Meunier et al. (2008) demonstrated that the amplification of PGA near ridge crests resulted in the occurrence of more landslides, which would not be accounted for by D. However, shakemaps are unavailable for many historical and smaller earthquakes.

1.2.5.c Topography

Landslide probability increases with increasing *slope gradient* (Keefer, 2000; Parker, 2013). Also many other topographic variables were used in previous landslide probability studies, for instance: slope aspect, catchment elevation, profile and plan curvature,… (e.g. Vanacker et al., 2003; Van Den Eeckhaut et al., 2006; Parker, 2013). However, most of these variables require high resolution input data, which is unavailable and computationally expensive on a global scale. Moreover, the results of their research indicate that the slope gradient is the most important factor. Apart from slope gradient, also local relief (LR) can be used to indicate the overall topography in a region. The advantage is that LR is still relevant when it is calculated based on coarser resolution data (e.g. GTOPO30). LR is defined as the maximum difference in elevation within a radius of five kilometer (Montgomery & Brandon, 2002; Vanmaercke et al., 2012). The work of Montgomery and Brandon (2002) suggests that next to LR, threshold variables focusing on

steep reliefs can be interesting to assess the overall susceptibility of a region for landsliding. They found a strong non-linear relation between mean local relief (MLR) and erosion rates, suggesting that certain thresholds in topography might explain for significant increases in erosion, for instance by landsliding.

1.2.5.d Lithology, land cover and climatic factors.

Different research demonstrates that landslide occurrence is influenced by the *substrate* underlying the landside area (e.g. Keefer, 2000; Alfaro et al., 2012; Meunier et al., 2013). Concerning *land cover*, Stokes et al. (2009) state that trees have more potential to prevent landsliding than other vegetation, by anchoring the ground. Also related to land cover is the fraction of water surfaces in the LAA. Keefer (1994) points out that earthquake epicenters might be located offshore, consequently severely limiting the potential areas of subaerial landsliding. Finally, also certain *climatic conditions* or weather events, such as extreme rainfall or rapid snowmelt can trigger landslides (e.g. Malamud, 2004a; TRIGS, 2009). As a consequence, it can be expected that reinforcing effects might occur when such events occur before, during or after an earthquake events (e.g. Hovius et al., 2011).

1.3 Relevance

This study will contribute to a better quantification of earthquake-induced landslides as a possible important factor in the *erosion budget* (Keefer, 1994). Consequently, it can also contribute to a better understanding of the observed seismic control on SY (Hovius et al., 2011; de Vente et al., 2013; Vanmaercke et al., 2014a). The results of this thesis will contribute to SY models that incorporate the role of EIL and may consequently yield predictions that are more spatially and temporally accurate. Furthermore, it might improve our knowledge about the effect of earthquakes on *long-term landscape evolution*, which is currently unconsidered (National Research Council, 2010). For instance, large amounts of earthquake-induced sediment reaching the river channel may influence the rate of bedrock incision for a long period after the EQ (Koi et al., 2008; National Research Council, 2010). Currently, earthquakes are mostly seen as a process modifying landforms by landsliding, but not directly as interfering in the process of landscape evolution, which is considered to be controlled by long term tectonic uplift and associated river incision (Schumm, 2005).

This master thesis also has practical relevance in the field of *catchment management and landslide hazard assessments*. More precise SY estimates lead to better assessment of the sustainability of human infrastructure (e.g. water reservoirs). Better insight in SD variability (e.g. sediment pulses) allows for the adaptation of this human infrastructure to accommodate for this variability and to enlarge their lifespan. This is important because many people are dependent on these reservoirs for hydroelectricity, water for agriculture or for other purposes. Besides, insight in landsliding and SY is also important for: an adequate land planning, predicting the impact of management interventions, assessing

flooding risk, export of sediment-fixed nutrients and sediment pollution, which underlines the ecological relevance of this study (Meybeck, 2003; Vanmaercke et al., 2011a; de Vente et al., 2013).

Apart from their significant contribution to the SD (Koi et al., 2008), landslides form an important *direct threat* to human lives and infrastructure. Therefore, this thesis may also contribute to a better understanding of natural hazard by EIL. This may facilitate or result in the creation of landslide susceptibility maps (e.g. Van Den Eeckhaut et al., 2006). Another severe risk is the occurrence of landslide dams in rivers triggered by earthquakes. These dams may cause a secondary hazard of subsequent flooding (e.g. Xu et al., 2009; Dong et al., 2009). Finally, this research may also contribute to a better prediction of *earthquake risk*. Better analysis of the sedimentary record, may contribute to better quantifications of EQ magnitudes on historical and geological timescales (Malamud et al., 2004b; Moernaut et al., 2007) In this context, one can also use the landslide distribution pattern, to supplement ground motion records, if accelerometers are lacking (Meunier et al., 2013).

1.4 Objectives

The overall objective is to get a better insight in the *total generated landslide volume and landslide distribution* as the result of an earthquake and to explore the link between earthquake-induced landslides (EIL) and sediment yield. More specific the objectives are:

1. To compile an *earthquake-landslide (E-L) dataset* with information on earthquakes and associated landslide properties (For the earthquake: name, country, date of occurrence, epicenter location, magnitude, intensity and focal depth. For the landslide properties: landslide-affected area, maximum distance from the epicenter over which landslides are triggered, total number of landslides, total landslide volume and volume of the largest individual landslide).
2. To construct a model that allows simulating the total earthquake-induced landslide volume *(LV model)* and distribution *(LD model)*. Both models will be constructed separately and will be integrated afterwards as a spatially distributed landslide volume model (*DLV model*).
3. To *apply* this integrated model to historical earthquake events and to confront it with measured SD data at the catchment scale. The application will be performed for the subcatchments of the Siret river in Romania, since daily sediment discharge data for a long measuring period is available and because a first analysis of this data is provided by Vanmaercke et al. (2014b).

1.5 Research question and hypotheses

The main research question of this thesis is:

'*Which factors determine the total generated landslide volume and landslide distribution caused by an earthquake?*'

The hypotheses underlying this study are:

1. Overall higher average sediment yields in seismically active regions can at least partly be attributed to an increase in sediment supply by earthquake-induced landslides (EIL) (section 1.1).
2. EIL will result in 'pulse' of sediment discharge after the earthquake, which will fade away over time (section 1.1).
3. The occurrence and magnitude of such pulses depend on catchment characteristics, the properties of an earthquake and the seismicity of the region.
4. The total earthquake-induced landslide volume (LV) can be estimated, based on properties of the earthquake (e.g. magnitude) and environmental characteristics (e.g. topography, lithology and climate) (section 1.2.5).
5. The spatial distribution of EIL can be estimated, based on properties of the earthquake (e.g. magnitude) and environmental characteristics (e.g. topography, lithology and climate) (section 1.2.5).
6. Both constructed models can be integrated to one model that can simulate spatially distributed landslide volumes.
7. Such an integrated model can be used to explore the impact of EIL on the sediment discharge.

2 Materials and Methods

2.1 Study area and time frame

Compilation of an E-L dataset and consequently the integrated spatially distributed landslide volume model are based on data that can be found in scientific literature. Still a time-space frame is useful to position the different parts of this thesis (Figure 6). The data collection is carried out on a global scale with data going as far back as the 16th century. Model application is carried out for the subcatchments of the Siret river in Romania, since daily SD data is available and because a first analysis of this data is provided by Vanmaercke et al. (2014b). SD is measured for several decades at 38 subcatchments (59-4092 km²) that were unaffected by reservoirs (Vanmaercke et al., 2014b). Considered EQ events in the region span a time period of several decades (1965-2014).

Regarding the considered processes in this study, individual EIL occur on the hillslope level, but the process can affect whole regions. Most EIL are very fast to relatively fast moving processes (Keefer, 1984). SD takes place at the catchment level and refers to the transport of solid material on the short term (t/day or kg/s) (section 1.1). Finally, seismic activity occurs on a regional to sub-continental scale. Single earthquakes are short lived, but the swarm of earthquakes with foreshocks and aftershocks included can last for several months (Guzzetti et al., 2009b).

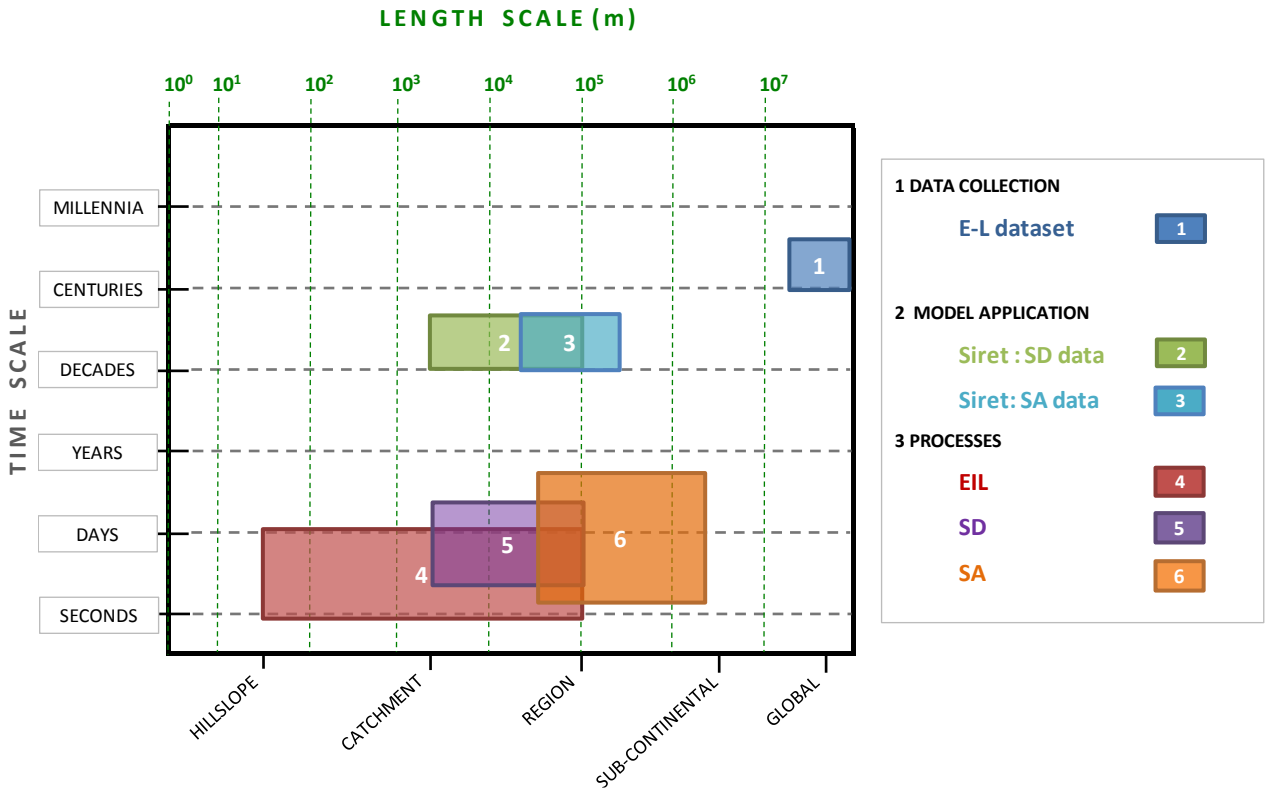

Figure 6: Time-space frame for the different parts and processes under consideration in this master thesis. With E-L: earthquake-landslide, EIL: earthquake-induced landslides, SD: sediment discharge and SA: seismic activity (own processing).

2.2 Compilation of an earthquake-landslide dataset

In order to construct our spatially distributed landslide volume model, an extensive literature review was conducted (section 1.4). The focus was on scientific publications containing information on landslides associated with specific and known earthquake events (e.g. USGS, 2013a). The *minimum requirement* to include an EQ event in the dataset is the availability of information on the earthquake data, epicenter location and magnitude, together with one of the following parameters: total landslide volume (LV), total landslide number (LN), total landslide area (LA), landslide-affected area (LAA) or maximum distance from the epicenter over which landslides are triggered (D_{max}). *Supplementary information* on the earthquake intensity, focal depth, volume of the largest individual landslide and remarks on landslide density, lithology and landslide type was added to the dataset as well. Earlier published review articles (e.g. Keefer, 1994; Rodriguez et al., 1999) were used to retrieve original sources. Next, also a thorough literature search was undertaken to retrieve more recent publications. Finally, to expand the coverage of the dataset, also specific literature published in other languages was searched for. Since it can be expected that certain, especially older, literature is not published in English (e.g. Spanish and Italian literature aiming for tectonically active regions in Southern Europe and Latin-America).

Some *additional remarks* on the compilation of this dataset have to be made. Compiling a large dataset from a variety of different sources is not easy and not entirely objective. For example, we noted quite often that different research on the same events reports different values for parameters such as epicenter location, M, LN, D_{max} and FD. Each time we tried to select the most recent or reliable data and, where possible, included a range of the reported values. Additionally also different measures are reported for the same parameter. For instance, M_s, M_l, M_b and M_w are used to define the magnitude, but it is not always mentioned, which specific magnitude is reported. However, for most events this is not a problem because the measures of magnitude approximate each other for lower magnitudes (section 1.2.1). Finally, in the case of imprecise epicenter locations (e.g. a location indicated on an undetailed map) or the total absence of reported epicenters, coordinates of the USGS (2013a) were used.

2.3 Predicting the total volume of earthquake-induced landslides associated with a specific earthquake event

2.3.1 Data selection and volume estimates

In order to develop a model that empirically predicts the total volume of landslides triggered by an earthquake, we *selected case-studies from our compiled database* (section 2.2), for which a total volume of the earthquake triggered landslides could be estimated. Some studies reported estimates of the total landslide volume (LV). Some studies reported

a range of LV. In these cases, the average of the range was used. Other studies do not report a total landslide volume but only (an estimate of) the total landslide number (LN). We only considered studies for which this LN was deemed to be complete (e.g. a clear counting of the number of landslides), or for which the range of estimated LN was limited to about one order of magnitude (e.g. 100 to 1000 landslides). In the latter case, we used the average of this range as the representative value. Reported landslide numbers were converted to a total landslide volume, using equation 4 (section 1.2.3). If possible, the LV estimates obtained with this equation were further refined with available information on the volume of the largest landslide. LN was then reduced by 1 and after converting to LV, the volume of this largest landslide was added.

In order to account for the uncertainty of the data with respect to the different LV acquisition methods, different *weights* were given to the earthquake events. The LV subset is given a weight of four, the LN subset is given a weight of two, and the LN range subset gets a weight of one. Even though this is an arbitrary choice, it is also a logic choice to rely more on better data.

2.3.2 Moment magnitude – maximum landslide distance to epicenter relation and mask file creation

In order to analyze which factors, other than earthquake magnitude (section 1.2.5.a), control the LV associated with a specific earthquake event, information on additional potentially relevant environmental characteristics was extracted for each earthquake event with a total LV estimate available (see previous section). To extract these characteristics, we required to know which area to consider (mask area). Therefore, a *magnitude-distance relationship* was developed, based on reported D_{max} values for specific events in our database. This relationship was used to determine the radius of a circle around the epicenter, which we considered as the zone in which environmental characteristics could have a relevant influence on the amount of earthquake-triggered landslides.

For several events, also the extent of the total landslide-affected area was reported. It could be argued that this presents a better measure to determine the area relevant for earthquake triggered landslides. However, there are two reasons why it is *better to use maximum distances*. First, it is easier to determine D_{max} more correctly, since it is just an Euclidean distance. The exact shape or delineation method of LAA on the other hand, was generally unknown, which entrained much uncertainty (section 1.2.2). Secondly, if no knowledge exists about the shape of the LAA, this area should be converted to a circular area, as the best approximation. As a consequence, it could result in calculating environmental characteristics for the wrong area. Using D_{max} as a basis for a circular mask area, at least guarantees that the whole LAA is taken into account, with the only drawback that partially non-affected marginal areas might be included in the mask. To cope with this

drawback, the analysis was repeated with circular areas determined by *half of the radius*. Previous research already indicated that most of the triggered landslides occur close to the epicenter (section 1.2.4). Consequently, it can be expected that the environmental characteristics in this central area are more important to explain for the total triggered landslide volume.

To create *mask areas*, epicenters were first located in Google^{TM} Earth (2013) for a manual check on the location. The actual mask area creation was then performed in ArcMap (Esri, 2013) with the BUFFER module. The resulting mask files were imported in IDRISI (Clarklabs, 2013).

2.3.3 Determination of environmental characteristics and earthquake event parameters

Table 1 lists the different variables we considered in our correlation and partial correlation (after correction for M_w) analyses with LV. These variables are further discussed in the subsections below.

Table 1: Overview of the considered variables for the correlation analyses, with indicated units and sources (own processing).

variable	unit	source
slope	%	CGIAR-CSI, 2004
local relief (LR)	m	USGS-EROS, 2013
peak ground acceleration (PGA)	m/s²	Giardini et al., 1999
mean annual temperature (T)	°C	New et al., 2002
mean annual precipitation (P)	mm/y	New et al., 2002
modified Fournier index (MFI)	-	New et al., 2002
tree cover	%	Defries et al., 2000
land fraction	%	CGIAR-CSI, 2004; USGS-EROS, 2013
lithology erodibility factor	-	Dürr et al., 2005
lithology classes	-	Dürr et al., 2005; Hartmann & Moosdorf, 2012
moment magnitude (M_w)	-	various sources (Appendix 1)
focal depth (FD)	km	various sources (Appendix 1)

By means of IDRISI (Clarklabs, 2013) the *environmental characteristics* for each mask file could be determined. The procedure of analysis was similar for the different environmental characteristics and is illustrated in Figure 7. This procedure was automatized my means of so called 'macro's' in the IDRISI software (Clarklabs, 2013). AVL-output files contained all required information for further processing in MATLAB (2013), in order to determine the average, minimum, maximum and standard deviation of the considered environmental characteristics in the mask area (e.g. mean slope and maximum slope). For the

earthquake specific parameters of M and FD no analysis was required, as data was directly available from scientific literature (section 2.2).

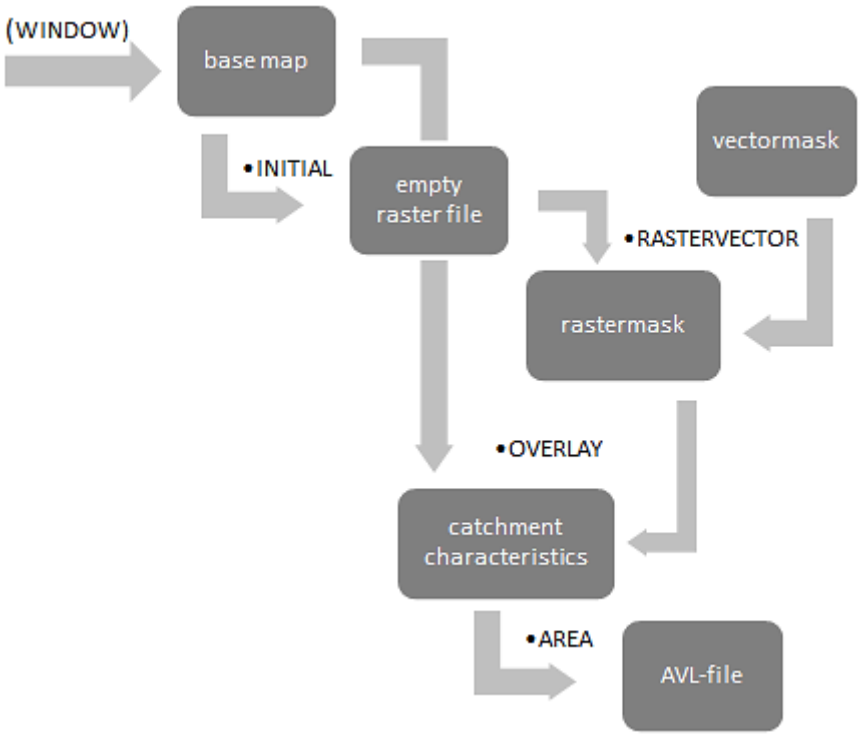

Figure 7: Schematic overview of the procedure to determine the environmental characteristics in IDRISI (Clarklabs, 2013) (own processing).

2.3.3.a Topography

Two topographic variables were considered: *slope and LR* (section 1.2.5.c). LR calculations were based on GTOPO30, a global digital elevation model (DEM) with a horizontal resolution of about 1000 meter (USGS-EROS, 2013). In a second phase also slope parameters were calculated, but based on higher resolution data: i.e. NASA's 'Shuttle Radar Topography Mission' (SRTM) data, with a resolution of about 90 meter (CGIAR-CSI, 2004). However, the coverage of this dataset extents only as far as 60° north, so that for the Denali earthquake in Alaska (United States, 2002, M_w 7.9), other data were required. For this event we used DEM data provided by de Ferranti & Hormann (2013) with the same resolution as SRTM.

Since our first analyses showed that slope and LR explained little of the variation in LV (see section 3.2.3.c) additional topographic variables were considered. For this purpose some slope-and LR derived threshold variables were added to provide robust measures that focus on the steep topography in the mask areas (section 1.2.5.c). The idea is that a measure as MLR might be too general for a large and diverse area, while a measure as maximum LR is less robust. The added variables were: (1) the fraction of land pixels in the mask area, surpassing a certain slope or LR threshold. With thresholds for LR set to 200, 500, 1000, 1500, and 2000 m and for slopes thresholds ranging from 10 to 100% with

increment of 10%. (2) Mean values of all pixels surpassing the 80th and 90th percentile for the slope and LR variable. Both type of measures are robust and focus on steep topography in the same time.

2.3.3.b Peak ground acceleration

As stated in section 1.2.5.b. The seismic history of the study area might influence the LV. However, this would require an individual earthquake history preceding each earthquake event. Reconstructing such histories was beyond the practical possibilities of this thesis. We therefore used a dataset of *expected PGA* (Shedlock et al. 2000) as a proxy for the general rate of seismic activity in the region around the epicenter. This map (Figure 8; resolution: 0.1°) indicates the expected PGA with a 10% exceedance probability (EP) in 50 years. It was based on a compilation of different studies taking into account historical earthquakes, active faulting and soil characteristics.

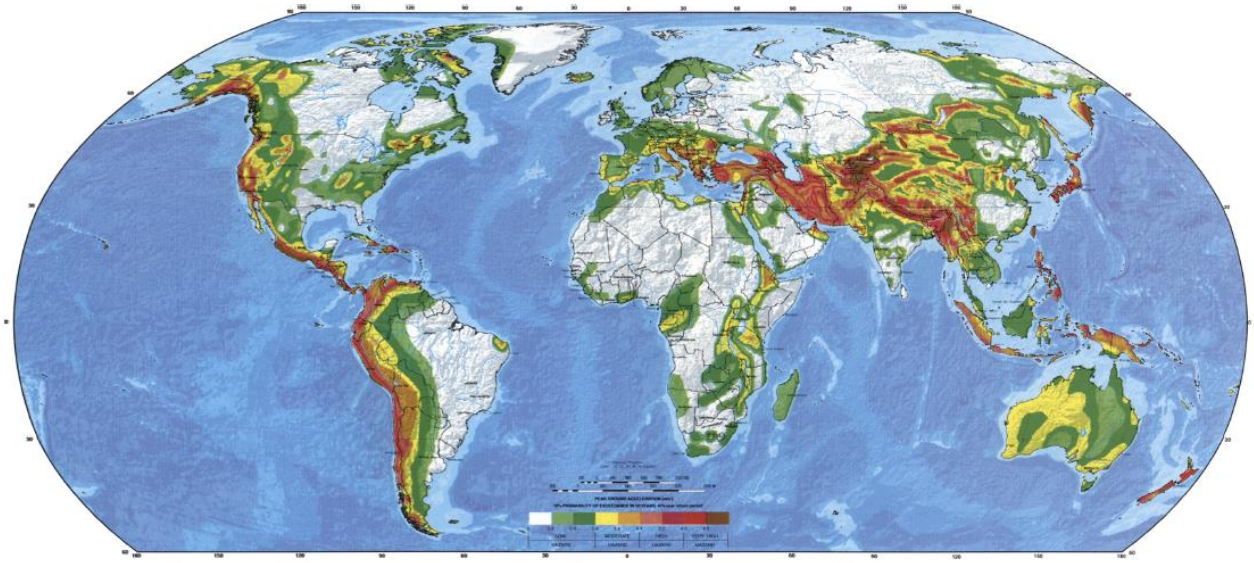

Figure 8: The Global Seismic Hazard Map. Peak ground acceleration (PGA) with a 10% chance of exceedance in 50 years is depicted in m/s². White and green correspond to low seismic hazard (0% - 8% g), yellow and orange correspond to moderate seismic hazard (8%-24%g), pink and dark pink correspond to high seismic hazard (24% - 40%g) and red and brown correspond to very high seismic hazard (>40%g) with g the acceleration of gravity (Shedlock et al., 2000, p 683).

2.3.3.c Mean annual air temperature, mean annual precipitation and modified Fournier index

To account for the potential role of climatic factors (section 1.2.5.d) several parameters were considered. Similar as for the seismic history it would be ideal to have detailed information on these weather conditions shortly before and after the earthquake events. These data were however not available. We therefore relied on long term climatic data. *Mean annual air temperature (T) and mean annual precipitation (T)* were derived from the "CRU-CL 2.0" climate dataset (New et al. 2002). These datasets contain average monthly rainfall and temperature data for the period 1961-1990. Not all earthquake events occur in the period whereupon this data is based, but it can be expected that the climate at a

certain location is a good proxy for earlier and later dates as well. Additionally, the *Modified Fournier Index (MFI)* was determined. This variable is expected to better represent intense rainfall events and rainfall variability throughout the year and consequently to better account for the importance of extreme weather conditions (section1.2.5.d). MFI is defined as (Arnoldus, 1980):

$$\mathrm{MFI} = \sum_{\mathrm{i}}^{12} \frac{\mathrm{Pi\hat{}2}}{\mathrm{Pjaar}} \tag{6}$$

2.3.3.d Tree cover and land fraction

Concerning land cover, especially tree cover and the fraction of land in the affected area might influence the LV (section 1.2.5.d). The *tree cover* data, with a resolution of about 1 km, is described in Defries et al. (2000), Hansen et al. (2000) and is based on data from the Advanced Very High Resolution Radiometer (AVHRR) from the years 1992-1993. Similar to the climate data, these data are not ideal for earthquake events occurring much earlier or later. However, opposed to slow changes in the climate (IPCC, 2014), tree cover changes can be very large over several decennia induced by human intervention (Vanacker et al., 2003). On the other hand, these induced changes might be rather local, limiting the impact over large areas represented by the mask areas.

Land fractions for each mask area are calculated based on SRTM and GTOPO30 data (CGIAR-CSI, 2004; USGS-EROS, 2013). SRTM data is preferable, because of the higher resolution and the consequent better representation of inland water bodies. However, for 4 events, the SRTM data was lacking for a part of the mask area. These 4 SRTM fractions could be calculated based on a regression function between GTOPO30 and SRTM land fractions of events for which both fractions are known. All reported landslide volumes were then linearly corrected by dividing them by their SRTM land fraction in the mask area (LV_{lc}).

2.3.3.e Lithology

To explore the role of *lithology*, three different datasets were used. Firstly, we used a global dataset compiled by Dürr et al. (2005), representing 15 different rock types as well as a class for water and for ice surfaces. The resolution of the map is 0.5°. A second dataset was a more recent lithology map, again available on a resolution of 0.5°, including 16 different classes (Hartmann & Moosdorf, 2012). As a third variable, the global dataset of Dürr et al. (2005) with nominal classes was reclassified based on the classification system of Syvitski & Milliman (2007). A score was assigned to each lithology, depending on the *erodibility*. This resulted in 6 new classes with values ranging from 0.5 for erosion resistant rock (e.g. metamorphic rocks) to 3 for very erodible lithologies (e.g. loess) (Syvitski & Milliman, 2007). Finally, based on the two nominal lithology datasets, a *binary variable* was created with weak lithologies on the one hand and stronger lithologies on the

other hand. A soil variable was not considered, because no good worldwide data was available for soil classes.

2.3.3.f Moment magnitude and focal depth

Finally, also two important EQ specific parameters: M_w and FD were considered (section 1.2.5.a). Both variables were retrieved from scientific publications (Appendix 1) and require no further processing. If multiple values for the FD were reported the average value of these was taken. For about 10% of the considered events no reported FD was available, but could be retrieved via the USGS (2013a).

2.4 Predicting the spatial distribution of earthquake-induced landslides

2.4.1 Obtaining earthquake-induced landslide inventories

In order to model the expected spatial distribution of the volumes associated with EIL, we compiled inventories of mapped landslides associated with specific earthquake events. These inventories were found in scientific literature, but were in most cases only available as a published map. Therefore, these maps were *first georeferenced*, before the landslides could be digitized. Since the quality of the georeferencing determines the accuracy of the eventually digitized landslides, this was done very carefully. Georeferencing was carried out with the module RESAMPLE in IDRISI (Clarklabs, 2013) with the number of selected ground control points ranging from 7 to 41. The module gives an indication of the overall accuracy of the georeferencing by means of a total root mean squared error (RMSE). This error should be minimized, but is not a very good indicator for the average location error of elements on the map, because georeferencing is often based on a grid, which can be more accurate than the map itself. Moreover, RMSE also strongly depends on the number of georeferenced points, i.e. it generally increases with the number of reference points. Both factors may result in an underestimation of the error on the mapped elements such as landslides. Therefore, the georeferenced image was converted to a KML-file to display in Google^{TM} Earth (2013). In this way, the error on the image could be estimated by selecting 5 points that were well distributed over the map and clearly recognizable on both the image and Google^{TM} Earth (2013). Based on these 5 points, an indication of the average absolute error (in meters) and the error range could be calculated. Also the dimensions of the image were measured in Google Earth to assess its resolution (i.e. for each image, only the number of rows and columns was known). Again this is an approximation, but the resolution error was estimated to be smaller than 1 m, which is more than sufficient.

After the image was georeferenced, the landslides were *digitized*. Mostly, landslides were digitized as separate points, but depending on the source map, also landslide areas were digitized. These areas were either digitized manually or, if possible, automatically using a

supervised classification method. The latter was done, using the RECLASS, MAKESIG and MAXLIKE modules in IDRISI (Clarklabs, 2013). Automatic digitization required additional corrections. For example, pixels representing a landslide area might by overlain by other map elements such as fault lines (e.g. for the 2008 Wenchuan earthquake; Parker, 2013), resulting in wrongly classified pixels. Also the epicenter, the study area (if provided, otherwise the original map boundaries were used) and (if available) major fault lines were digitized. Apart from georeferencing errors, the overall quality of the inventory was assessed, paying attention to the overall level of detail and original scale of the digitized map; the likely completeness of the landslide inventory; whether the mapped area was accurately indicated or not; the spatial extent of the investigated area in relation to the earthquake magnitude; and the quality of the digitization (e.g. are there zones where many indicated landslides overlap).

2.4.2 Determination of predictor variables

In order to model the likely distribution of landslides associated with specific earthquake events, data on *potentially relevant factors* were extracted (section 1.2.5) for every landslide and non-landslide pixel of the digitized landslide inventories (section 2.4.1). The area taken into account for each event is the study area as determined in the previous section. First, all inventories were rescaled to the same resolution of 500 meter in the Universal Transverse Mercator (UTM) projection. On the one hand this resolution is chosen in order to reduce the local errors of landslide locations (section 2.4.1). On the other hand, it is also a compromise between a sufficiently detailed and sufficiently robust and feasible model, taking into account the dimensions of some LAA.

Further processing of the data layers was carried out in IDRISI (Clarklabs, 2013) and Arcmap (Esri, 2013). For each event, all data layers were trimmed to the same window extent as the landslide inventory datasets (module: WINDOW) and converted to the appropriate UTM projection system (PROJECT). The projection to UTM was necessary to ensure that distances and topographic measures were uniformly calculated for all the globally distributed events. All layers were rescaled to a 500m resolution, except for the topographic variables. Those were retained on a 100m resolution, with a perfect correspondence between the pixels on the 500m resolution (IDRISI modules: PROJECT and CONTRACT). Analysis of the resulting data layers is carried out in MATLAB (2013) to compile a large total dataset, with each row representing a different landslide or non-landslide pixel and with the columns representing all predictor variables.

For each 500m x 500m pixel the following parameters were calculated:

- Distance to epicenter (D). This parameter was obtained using the DISTANCE module in IDRISI (Clarklabs, 2013).

- Standardized distance to epicenter (DS). This variable is included since the distance over which landslides are likely to occur depends on the earthquake magnitude (section 1.2.4). Standardization was based on D_{max}, which was calculated using the empirical relation indicated in Figure 16. This equation was obtained from our E-L dataset and will be further discussed in section 3.2.3.a.
- Topographic variables: mean slope (SME), maximum slope (SMA), slope range (SR) and mean elevation (EM) (based on SRTM data: section 2.3.3.a, CGIAR-CSI, 2004). Slope range is defined as the difference between the minimum and maximum slope in an area. EM is taken into account, as a rough proxy for the position on the hillslope (rather in valley or rather close to ridges) to account for potential PGA amplification effects towards the ridge crest (section1.2.5.b). All topographic variables were calculated on a rescaled SRTM resolution of 100 m in UTM projection. This implies that the variables were calculated based on 25 pixels in each 500 m resolution pixel.
- The fraction of tree cover (TC) (section 1.2.5.d)
- Earthquake moment magnitude (M_w) (various sources: Appendix 1)
- Focal depth (FD) (various sources: Appendix 1)
- Distance to river (DR) (based on SRTM HydroSHEDS data (USGS, 2010a) and processing in IDRISI (Clarklabs, 2013) with the DISTANCE module). Similar to the variable EM, distance to river might account for the position on the hillslope between the ridge crest and the river.

2.4.3 Theoretical background of logistic regression

Logistic regression techniques were applied to link the observed spatial patterns of EIL to the extracted parameters. Logistic regression is a widely used technique in landslide distribution/ susceptibility modeling (e.g. Dai & Lee et al., 2003; Vanacker et al., 2003; Ayalew & Yamagishi, 2005; Van Den Eeckhaut et al., 2006; Parker, 2013). The technique can be used to predict the outcome of a dichotomous dependent variable, in this case the occurrence or absence of landslides, based on one or more independent categorical and/or numerical predictor variables (Ayalew & Yamagishi, 2005; Parker, 2013). The general logistic function can be expressed as follows (Parker, 2013):

$$p(y = 1) = \frac{1}{1+e^{-(b_0+b_1x_1+b_2x_2\ldots+b_nx_n)}} \quad (7)$$

With p representing the probability, x_i the dependent variables, b_i the regression coefficients and y the known dependent variable (y = 1 or 0). The regression coefficients are estimated based on the maximum likelihood (ML) principle, much in accordance with the least square regression, which can however not be applied because of the dichotomous dependent variable. Moreover the ML principle can be used for nonlinear

models, since the logistic model is nonlinear; this is an appropriate technique (Kleinbaum & Klein, 2002). Figure 9 shows the logistic function (with 'z' representing the the exponent $b_0 + b_1x_1 + b_2x_2 \ldots + b_nx_n$ of equation 7). The function illustrates the advantage of the logistic modeling approach; i.e. the output value f(z) will always between 0 and 1, regardless of the range of predictor variables. Values between 0 and 1 can be interpreted as probabilities (Kleinbaum & Klein, 2002; Parker, 2013).

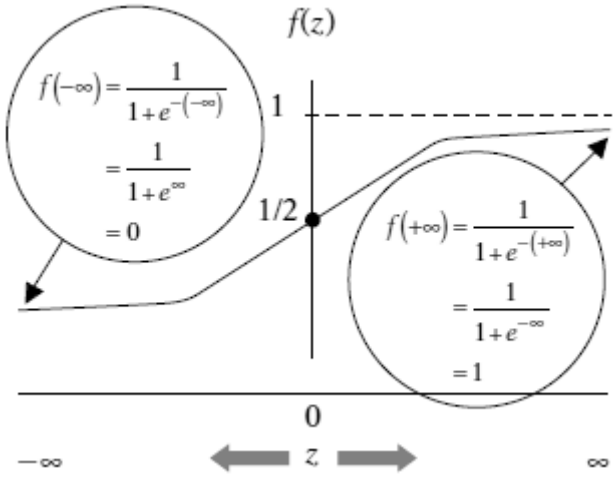

Figure 9: Schematic representation of the logistic model function with the term 'z' representing the exponent $b_0 + b_1x_1 + b_2x_2 \ldots + b_nx_n$ of equation 7 (Kleinbaum & Klein, 2002, p 19).

Another advantage of the logistic model for modeling landslide probabilities is the S-shape of the function. This means that for negative 'z' values the landslide probability remains low until a certain threshold value is reached. At that point the probability increases rapidly, until a second threshold is reached where increase flattens again. This threshold idea is conform to the idea of threshold values for slope stability (Kleinbaum & Klein, 2002; Parker, 2013). Logistic regression assumes the following conditions, after Chen et al. (2014):

1) The true conditional probabilities are a logistic function of the independent variables.
2) No important variables are omitted.
3) No extraneous variables are included.
4) The independent variables are measured without error.
5) The observations are independent.
6) The independent variables are not linear combinations of each other.

The *first assumption* can be best understood by considering the linear form of the model equation (equation 7) (Parker, 2013):

$$ln\left(\frac{p(y=1)}{1-p(y=1)}\right) = b_0 + b_1x_1 + b_2x_2 \ldots + b_nx_n \quad (8)$$

Where the left hand sight is defined as the log(odds) or logit(p), being a linear combination of the independent variables (Parker, 2013). With odds for a certain pixel defined as the probability of landsliding divided by the probability of no landsliding (Kleinbaum & Klein, 2002). The condition is met when the relationship between the logit of the outcome variable and the independent variables is linear. However, in practice this is often assumed since possible non-linearity is not a severe problem (Chen et al., 2014).

The *second condition* can be met by testing relevant predictor variables, but as discussed in the previous section some limitations arise because of data availability on a global scale.

The third condition will be validated with the likelihood ratio (lr) statistic (Kleinbaum & Klein, 2002) :

$$lr = -2\ln\hat{L}_0 - (-2\ln\hat{L}_1) = -2ln\left(\frac{\hat{L}_0}{\hat{L}_1}\right) \quad (9)$$

With $\hat{L}$ the total likelihood, which is analogue to the coefficient of determination (R^2) for linear regression. $-2\ln\hat{L}$ is defined as the log likelihood statistic. $\hat{L}$ is defined as the probability of occurrence of all observations. For testing the significance of individual predictor variables the log likelihood statistic of the full model (1: a model with one or more predictor variables) is subtracted from the log likelihood statistic of the null model (0: model without any predictor variables) (Kleinbaum & Klein, 2002). Interesting is that lr follows a χ^2 distribution, with the degrees of freedom determined by the difference of predictor variables taken into account in the models. Consequently, lr can be used to validate the null hypothesis 'there is no significant relationship between the predictor variable and the occurrence of landsliding'. Another test statistic can be used for the same purpose, i.e. the Wald test statistic (W) (Kleinbaum & Klein, 2002):

$$W = \left(\frac{b_i}{se_{b_i}}\right)^2 \quad (10)$$

With se_{b_i} the standard error of coefficient b_i. Similar to lr, W follows χ^2 distribution and both parameters give large and positive values for significant variables accordingly. It is shown that lr is preferable in situations with small data samples (how small has however never been documented: Kleinbaum and Klein, 2002). For large samples lr and W are similar. However, W is more convenient to use, since only the specification of the full model is required (Kleinbaum and Klein, 2002). For the sake of completeness and for preventing unreliable evaluations in the case of a small dataset, both measures were considered.

Condition 4 depends on the input data layers: i.e. the manually digitized landslide datasets, reporting of M_w and FD and the SRTM data. The accuracy of the landslide datasets is considered in section 3.3.1. Furthermore, the model resolution was determined so that the error of false positives and false negatives was reduced (section 2.4.2).

Condition 5 states that the data should be statistically independent, but auto-correlation between landslide and non-landslide pixels is common when landslide areas are taken into account (Van Den Eeckhaut et al., 2006). However, in the study by Van Den Eeckhaut et al. (2006) the problem arises because individual landslides cover many pixels of detailed DEMs. Since such a cluster of landslide pixels only represents one landslide, they resolved the problem, by selecting only one pixel for all mapped landslides. In our case this problem is avoided: mostly landslides in the datasets are digitized as point locations. Moreover, even if landslide areas are defined, they are generally resolved to a single pixel with a resolution of 500m. Of course, as a result, the accuracy of our data does not allow differentiating between landslide depletion and deposition zone, while it is preferable to focus on the depletion zones (Van Den Eeckhaut et al., 2006; Parker, 2013).

Condition 6, can be validated by measures testing for multicollinearity such as the variance inflation factor (VIF) (PennState, 2014):

$$VIF_i = \frac{1}{1-R_i^2} \tag{11}$$

With R_i^2 the coefficient of determination of the regression between the i^{th} variable as independent variable and the remaining variables as predictor variables (PennState, 2014).

2.4.4 Practical application of logistic regression for individual landslide inventories

Practically the following steps were undertaken to construct the logistic LD model, based on the compiled LD datasets. Analyses were carried out in MATLAB (2013) with the *'glmfit' function*. Required testing, as discussed in the previous paragraph, was based on own processing of the output and MATLAB code since MATLAB does not provide functions for basic statistics such as lr, W or VIF. Moreover, own MATLAB code was required to prevent underflow. Underflow means that very small values were rounded down to zero, since the total likelihood of a large amount of pixels can become very small and the number of bits used in MATLAB to store numbers is limited.

In order to get a first idea of the relative significance of the predictor variables under consideration (section 2.4.2), some *explorative logistic regression* was performed on all

inventories, considering all predictor variables. A technique of random sampling was repeatedly performed to also change the number of selected observations. Next, *univariate logistic regression* analysis of all independent variables for all datasets separately was carried out, with calculation of lr and W statistics to determine their significance. Additionally comparison plots were constructed representing the coefficients of the logistic model for each predictor variable for the different events. This allowed judging the physical plausibility and consistency of the predictor variables.

Based on the knowledge of the first two analysis steps, MCFadden's pseudo R² ($\mathrm{R}^2_{\mathrm{McF}}$) were iteratively calculated for the separate datasets, each time adding an additional predictor variable to the model to observe the predictive improvement of the extended model. A similar strategy was followed by Parker (2013), who stated that $\mathrm{R}^2_{\mathrm{McF}}$ was the preferred statistic to indicate the improvement offered by the full model over the null model (Allison, 2013; Parker, 2013):

$$R^2_{McF} = 1 - \frac{ln\hat{L}_1}{ln\hat{L}_0} \tag{12}$$

With $\hat{L}_1$ the probability of occurrence of all observations for the full model and $\hat{L}_0$ the probability of occurrence of all observations for the null model. The sequence of added variables was determined by the relative significance (lr, equation 9) of a variable for the considered event, each time adding the variable with highest lr based on the univariate logistic regression analyses. With each added variable, both lr and VIF were checked to assure the validity of the model.

2.4.5 Construction of a spatially distributed landslide model based on integrated landslide inventories.

The next step was the selection (based on previous analyses) and *testing of the appropriate combination of predictor variables for the integrated landslide inventories* (594546 pixels). In this way, also M_w, DS and FD can be taken into account. Three different 'subset selection procedures' (SSP) were used for randomly selecting sub datasets for model calibration and model validation. The following terms will be used to refer to these procedures: 'fixed', 'fraction', 'root'; respectively meaning that that for all events the same amount of pixels is taken, the same fraction of total pixels per event is taken or the square root of the total number of pixels per event is taken.

For all SSP the sub datasets were split in a *calibration subset* (2/3) and a *validation subset* (1/3). For the 'fixed' SSP, it was chosen to take the total amount of pixels from the smallest dataset (event 133: Japan, 2011, M_w 6.7: 826 pixels) for the four events with lowest assessed quality (ID's 11, 95, 133 and 240: see Table 5,) and double this amount (i.e.

1652 pixels) for all other events. This results in a calibration subset of 25300 pixels. For the ‘fraction’ SSP, 30% of each dataset was used, resulting in a calibration subset of 118909 pixels. The ‘root’ SSP takes the root of the total amount of pixels of each event, multiplied by 20. This factor was considered to be a compromise between a sufficiently large number of pixels and the smallest event dataset (826 < 20*sqrt(826)). This results in a calibration subset of 42609 pixels. This ‘root’ SSP is used to give a sufficiently large weight to large events (as they generate the largest volumes), but still do not neglect the smaller events.

Monte Carlo simulations with 50 or 100 iterations were carried out for every SSP, for all different variable combinations. Each iteration the R^2_{McF} was calculated. Additionally, the VIF was checked to test for multicollinearity. Next, to test for the influence of individual events on the total model outcome, separate Monte Carlo simulations were carried out for specific variable combinations with iteratively leaving out 1 of the earthquake-triggered landslide inventories. After this, a Monte Carlo simulation, with 101 iterations, was performed for the most appropriate SSP and variable combination, which results in 101 possible variable coefficient sets. Eventually, the median coefficient of the most significant variable was determined. It is this coefficient, together with the corresponding coefficients of the other predictor variables, which define the *LD model*.

2.4.6 Application and validation of the landslide distribution model

The final LD model was applied to the compiled LD datasets (2.4.1) by creating the right raster images on a 500 m resolution: a distance map, a slope map and a study area mask file. In this way, *probability maps* were generated. Additionally, for each event a relative operating characteristic (ROC) curve was constructed as a means of validation. ROC compares an observed landslide pattern with a predicted landslide pattern in the form of a probability map (Pontius & Schneider, 2001). To calculate this statistic, 100 random selections of the 101 coefficient sets were performed. The resulting 100 probability maps were summed. Secondly, the summed probability pixels were ordered towards descending probability. Next, 20 equal classes are determined; with for each class the determination of the fraction of false negatives and true positives. The fraction of true positives in each probability class is the number of observed landslide pixels in that class, divided by the total number of landslide pixels. The fraction of false negatives in each probability class is the number of observed non-landslide pixels in that class, divided by the total number of non-landslide pixels. These values are then cumulatively plotted with the false negatives on the x-axis and true positives on the y-axis, resulting in a graph starting at (0,0) and ending at (1,1). The ROC value is defined as the area under the curve, with values larger than 0.5 indicating that the models scores better than random (Van Dessel et al., 2008).

2.5 Construction of an integrated spatially distributed landslide volume model

2.5.1 Predicting landslide numbers based on the landslide distribution model

Previous sections described the steps towards the construction of a LV and a LD model. For the construction of a LV model (section 2.3), a large amount of variables were tested and some *'semi-subjective'* but well considered *choices* had to be made. For example, the considered area was arbitrarily defined as a circle, the reported LV was corrected for the fraction of water in the mask area and different weights were assigned to different events according to the way of LV acquisition. Even though, this gave a well constrained and useful model, it is worth to apply a different approach based on the LD model.

Since the LD model predicts the probability of landsliding at a certain location, the total probability sum (PS) for all pixels of an event could be used to correlate with reported total landslide volumes (LV_r) or with reported total landslide numbers (LN_r). The advantage is that no arbitrary area had to be delineated, since the LD model automatically sets the borders in the form of decreasing probabilities. These decreasing probabilities also mean that the model gives larger weight to pixels closer to the epicenter, which is a favorable characteristic, since landslide concentrations exponentially decrease with distance to the epicenter (section 1.2.4). Secondly, it also implied that no correction for the water fraction is required. Finally, it was also interesting to construct a model for predicting LN rather than LV, since more of the reported data is in the form of LN (section 2.3.1) and because the integrated model required LN as input, since LN needs to be converted to LV based on the inverse gamma distribution function for landslide size (section 1.2.3). Additionally, no weights had to be assigned to the different events according to the way of LV acquisition.

The first step to construct this model was the processing of the predictor variable data needed to construct landslide probability maps. This was similar to the method described in section 2.4.2. The subsequent probability map construction and probability sum calculation, was carried out in MATLAB (2013) for all events included in the LV model (section 2.3.1). To make this *computationally feasible*, it was made sure that at least all pixels with values larger than or equal to a probability of 0.01 were included in the image. Even though this is an arbitrary threshold, some arguments can be put forward for this choice. First of all, analyses of the LD model results (see section 603.3.4) showed that very few landslides occurred on pixels with probabilities lower than 0.01. Secondly, testing for the event with the largest M_w: i.e. the Valdivia earthquake (Chile, 1960) with an M_w of 9.5, showed that these probabilities reach as far as about 800 km, which surpasses D_{max} for such magnitude (section 1.2.4). Thirdly, correlation analysis between LN and PS for different thresholds (0.005, 0.02, 0.05) gave similar results.

2.5.2 The Monte Carlo simulation approach

At this point all required input for the construction of an *integrated spatially distributed earthquake-induced landslide volume (DLV)* model was available. This model can be applied to *any region in the world*, with the only prerequisite of a known earthquake epicenter and M_w. The model consists of four different simulation steps, which were integrated in a MATLAB (2013) script:

(1) landslide number determination;
(2) landslide probability map generation;
(3) landslide volume determination;
(4) landslide to pixel assignment.

For all four steps, the model uncertainties were taken into account by means of the Monte Carlo simulation approach. Such iterative simulation, by random number generation, gave a numerical estimate of the possible model outcomes, of which statistical parameters such as the average, median and range could be derived (Binder, 2005).

Step 1 required *LN* as input for the simulation; different models could be used here (see sections 2.3 and 2.5.1). For the integrated DLV, the LN model determined in the previous section was used, supported by the argumentation in that section. As a first step the model uncertainty was determined by means of model residues (observed LN/ predicted LN). The residues appeared to be best described by a logarithmic distribution, i.e. with no clear trend in the relative deviation of LN with increasing LN, but with an increase in the absolute deviation of LN with increasing LN. Consequently, the normal parameter estimates: mean (μ) and standard deviation (σ) of the 10^{th} logarithm of the residues could be determined. Random LN selection was then performed as follows (own processing):

$$LN = round\ (\ (2.57 * PS^{0.82}) * (10^{randn*0.65})) \tag{13}$$

The first factor on the right hand side of the equation represents the LN model (see Figure 35 in section 3.4.1) and the second factor generates a normally distributed pseudorandom number (MATLAB, 2013).

For assessing the uncertainty on the second step, one of the model *coefficient sets* (section 2.4.5) was randomly selected, for the calculation of a probability map. For a comparison with the landslide inventories (section 2.4.1), probability maps are delineated by the study areas. For the model application (see section 2.6) no boundary is set.

Step 3 made use of equation 3 (section 1.2.3). The individual landslide area (Al) range was discretized in 1000 classes, between 10^{-5} and 100 km², with a logarithmic increment. A logarithmic increment was preferred to a linear increment, since the Al range spans 7 orders of magnitude. The probability per Al class was then calculated by integrating the

probability densities over the different classes. Next, an empirical scaling relationship between Al and the individual landslide volume (Vl) (equation 5) determined Vl for each class. As a last part of this step volumes needed to be assigned to each landslide. Therefore, the cumulative probability (p_{cum}) for the different classes was calculated, based on equation 3 (Figure 10). For each landslide a random number between 0 and 0.9996 (the probability sum of all 1000 classes is slightly smaller than 1 because of the discretization and infinite tails) was assigned. The volume corresponding to the class with the closest, but larger p_{cum} value of this number was then selected for the landslide. This method implied that Vl with a higher probability of occurrence had a higher probability of being selected. It can be seen in Figure 10 that about 95% of p_{cum} falls within the Vl range of 1E-07 to 1E-04.

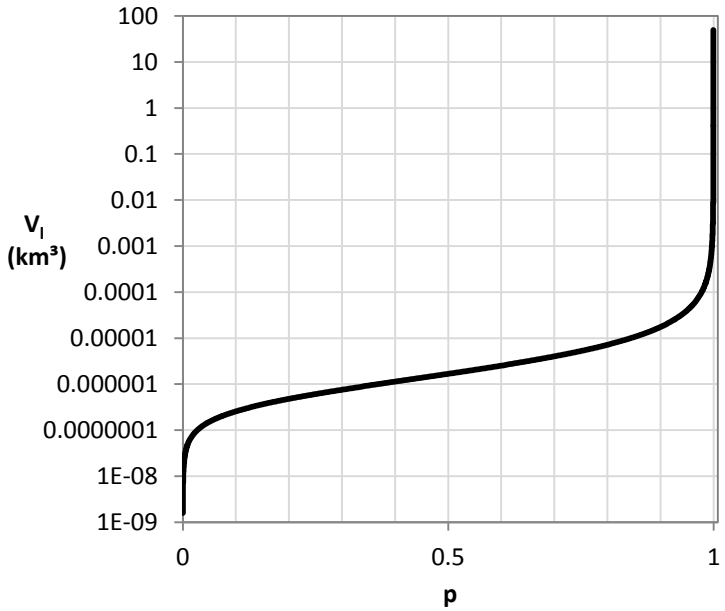

Figure 10: Cumulative probability (p) function for the different individual landslide volumes (Vl). The Vl range was discretized in 1000 classes with logarithmic increment (own processing).

Step 4 finally, is the most computationally intensive with the *allocation of the landslides* and corresponding volumes to pixels in the considered area. According to a procedure proposed by Van Rompaey et al. (2002), a random number between 0 and the maximum probability was generated. Secondly, a random pixel was selected. Both probability values were then compared, if the random number was smaller than the probability for the pixel, the landslide was assigned to that pixel, if not, the procedure was repeated and this until all landslides were spatially assigned. Pixels with assigned landslides were not excluded for subsequent landslide assignment, so that more than one landslide could be assigned to the same pixel. This method implied that pixels with higher probabilities for landslide occurrence had higher probability of landslide assignment (Van Rompaey et al., 2002). Also for this last step randomization was important, because this allowed for the generation of likely LV distribution patterns rather than one fixed pattern, which gives a false idea of model preciseness.

2.5.3 Validation of the integrated model

In the specific case of an earthquake event with mapped landslides the *Kappa index of agreement (K)* can be calculated (Pontius, 2000):

$$K = \frac{MP - chance\ agreement}{1 - chance\ agreement} \quad (14)$$

With MP the model performance: i.e. the number of correctly predicted pixels (landslide or no-landslide) divided by the total number of pixels. K is a measure for the pixel to pixel correctness of the landslide assignment, with values larger than 0 indicating that the model scores better than a random model and values of 1 indicating a perfect model (Pontius et al., 2004). Chance agreement is the agreement between an observed landslide pattern and a simulated pattern with no information on the location, but with information on the quantity. The chance agreement is calculated as follows (Pontius 2000):

$$chance\ agreement = S_{ls} * O_{ls} + S_{nols} * O_{nols} \quad (15)$$

With S_{ls} and O_{ls} the fraction of landslide pixels in respectively the simulated and observed landslide pattern and with S_{nols} and O_{nols} the fraction non-landslide pixels in respectively the simulated and observed pattern.

In the case of landslide modelling it is more interesting to use more specific parameters such as a Kappa index of agreement for location (K_l) (Pontius, 2000) and an error budget for a predicted landslide map (Pontius et al., 2004). K_l is a measure for the ability of the model to correctly predict the location of landslide/non-landslide pixels, regardless the error due to quantity (Pontius, 2000):

$$K_l = \frac{MP - chance\ agreement}{(\min(S_{ls}, O_{ls}) + \min(S_{nols}, O_{nols})) - chance\ agreement} \quad (16)$$

The error budget is complementary to K_l, as it indicates how much the simulation can be improved by a better quantification (disagreement due to quantity) and with a better allocation procedure (disagreement due to location), regardless the evaluation by K_l. For the error budget, the agreement due to chance, i.e. in this case with no information on quantity or location, for a two category model is 50%. Consequently, a model classifying more than 50% correct pixels scores better than a random model with no information. For a thorough explanation on the error budget methodology, see Pontius et al. (2004).

2.6 Model application and comparison with catchment sediment yields

2.6.1 Case study: the Siret basin

To apply the integrated spatially distributed landslide model, the *Siret basin* (45000 km²; Figure 11) in Romania was considered as a study area (section 2.1). The Siret river and its tributaries drain the central and eastern part of the Eastern Carpathians, Eastern Sub-Carpathians, Moldavian Plateau and the Siret Lower Plain (Vanmaercke et al., 2014b). The Carpathians resulted from convergent activity of several micro-plates with the Eurasian plate during the closure of the Tethys Ocean (Airinei, 1977). Currently, the subduction of the Black Sea micro-plate under the Carpathians is responsible for the tectonic activity in this region (Sandulescu, 1984), which makes it one of the most seismic active regions in Europe (see Figure 8). Several large earthquakes have taken place in the region during the past hundred years (Table 2, Vanmaercke et al., 2014b). In general earthquake epicenters are confined to a relatively small region of 40x80 km in the Vrancea region (Figure 11).

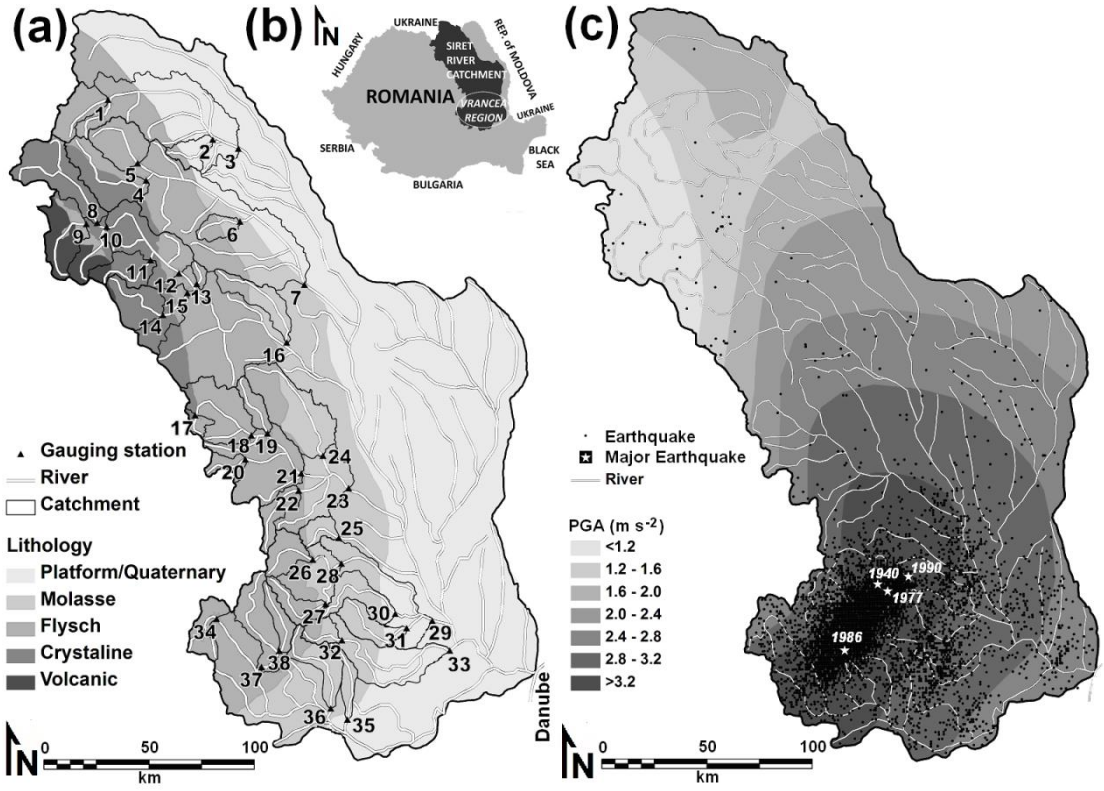

Figure 11: Map of the Siret basin. (a) Subcatchments of the Siret basin (n = 38) of which sediment yield observations were retrieved. Numbers correspond to those of Table 3 and grey shadings indicate major lithological units. (b) Location of the Siret basin within Romania. (c) Seismic activity in the Siret basin. Grey shadings indicate the expected peak ground acceleration (PGA) with a recurrence interval of 100 years (Lungu et al., 2004). Superimposed are all earthquakes with a magnitude (M) of 0.5 or higher, registered between 1900 and 2010. Stars and their corresponding years indicate the epicenters of major earthquakes indicated in Table 2 (Vanmaercke et al., 2014b).

Table 2: Major earthquakes in the Vrancea Region during the past 100 years (see Figure 11 for epicenter locations, Vanmaercke et al., 2014b).

Date	Magnitude (Mw)	Epicenter depth (km)	Geographical coordinates	
			Latitude (°)	Longitude (°)
10.11.1940	7.6	150	45.7994	26.6975
04.03.1977	7.4	94	45.7692	26.7575
30.08.1986	7.1	132	45.5189	26.4881
30.05.1990	6.9	91	45.8297	26.8883

2.6.2 Model application and confrontation with sediment yield

Two model simulations were carried out with the integrated spatially distributed landslide model as explained in section 2.5.2. The first simulation considered *the 1977 earthquake* (Table 2). This earthquake was chosen because it is the largest earthquake that occurred during the measuring period of sediment yield in the subcatchments (Table 3). The second simulation considered *all earthquakes* with magnitude larger than or equal to four that affected the Siret basin in the *period 1965 till April 2014* (n = 292). These events were retrieved from the USGS (2013a) and NCEDC (2013). Systematic earthquake registration for this region was available from 1965 onwards, which corresponds quite well to the start of SY measurements (Table 3).

For both analyses *50 Monte Carlo simulations* were carried out. Landslide probability maps were generated for a wide area as the earthquake impact might extend beyond the basins borders. Restriction of the simulations to the Siret subcatchments would result in an overestimation of the assigned landslide numbers and volumes. However, to make computations feasible, a probability threshold of 0.0001 was set for the landslide to pixel assignment (section 2.5.2). This means that only pixels with a probability larger than 0.0001 can get a landslide assigned. For the 1977 earthquake (M_w 7.4) such a threshold corresponds to a distance limit of about 240 km, which is in agreement with the upper bound limit of landslide occurrence (Figure 4, section 1.2.4). In order to determine LN and LV for each subcatchment, mask files were created based on data received from Vanmaercke et al. (2014b). By integrating all pixels over each subcatchment, catchment specific LN and LV could be obtained. In this way, simulated catchment LN and LV could be compared with other catchment characteristics (Table 4).

Table 3: Measured average annual runoff (Ro) and sediment yield (SY) for the 38 considered subcatchments in the Siret river basin. 'Nr.' indicates the gauging station number, corresponding with Figure 11 (Vanmaercke et al., 2014b).

Nr.	River	Gauging station	Location Gauging Station		Measuring Period	Ro (mm y^{-1})	SY (t $km^{-2}y^{-1}$)
			Latitude (°)	Longitude (°)			
1	SUCEAVA	BRODINA	47.8867	25.4219	1971-2010	371	284.5
2	SOLONEȚ	PĂRHĂUȚI	47.7119	26.0861	1973-2010	192	464.1
3	SUCEAVA	IȚCANI	47.6719	26.2472	1957-2010	228	208.2
4	MOLDOVA	PRISACA DORNEI	47.5400	25.6611	1958-2010	426	152.1
5	MOLDOVIȚA	DRAGOȘA	47.6147	25.6081	1971-2010	345	204.5
6	RÂȘCA	BOGDĂNEȘTI	47.3606	26.2503	1965-2010	260	174.4
7	MOLDOVA	TUPILAȚI	47.0847	26.6483	1959-2010	262	298.9
8	BISTRIȚA	DORNA GIUMALĂU	47.3608	25.3497	1956-2010	499	87.4
9	DORNA	DORNA CANDRENI	47.3556	25.2817	1959-2010	421	55.9
10	BISTRIȚA	DORNA ARINI	47.3433	25.4089	1960-2010	469	76.6
11	NEAGRA	BROȘTENI	47.1992	25.6833	1965-2010	411	58.4
12	BISTRȚA	FRUMOSU	47.1422	25.8622	1967-2010	421	101.6
13	BOLĂTĂU	POIANA LARGULUI	47.0950	25.9731	1978-2010	257	214.0
14	BISTRICIOARA	TULGHEȘ	46.9647	25.7581	1965-2010	240	59.6
15	BISTRICIOARA	BISTRICIOARA	47.0572	25.9128	1974-2010	259	112.9
16	CRACĂU	SLOBOZIA	46.8393	26.5298	1956-2010	128	163.1
17	TROTUȘ	LUNCA DE SUS	46.5347	25.9553	1976-2010	285	100.4
18	TROTUȘ	GOIOASA	46.4447	26.2997	1980-2010	264	194.0
19	ASĂU	ASĂU	46.4508	26.4008	1977-2010	315	324.9
20	UZ	VALEA UZULUI	46.3428	26.2608	1969-2010	350	84.2
21	TROTUȘ	TÂRGU OCNA	46.2769	26.6047	1957-2010	262	270.1
22	OITUZ	FERĂSTRĂU	46.2042	26.5867	1973-2010	367	248.2
23	TROTUȘ	VRÂNCENI	46.2097	26.8950	1966-2010	267	342.4
24	TAZLĂU	HELEGIU	46.3514	26.7417	1971-2010	213	401.6
25	SUȘIȚA	CIURUC	45.9984	26.8305	1961-2010	234	836.8
26	PUTNA	TULNICI	45.9078	26.6647	1959-2010	208	363.0
27	ZĂBALA	NEREJU	45.7169	26.7369	1974-2010	210	1163.9
28	PUTNA	COLACU	45.8883	26.8403	1974-2010	164	1141.0
29	PUTNA	BOTÂRLĂU	45.6331	27.3864	1956-2010	117	1137.4
30	MILCOV	GOLEȘTI	45.6672	27.1622	1957-2010	55	1710.0
31	RÂMNA	JILIȘTE	45.6037	27.2405	1971-2010	42.6	1784.0
32	RĂMNICU SĂRAT	TULBUREA	45.5603	26.8317	1964-2010	268	1603.2
33	RĂMNICU SĂRAT	TĂTARU	45.5036	27.4889	1956-2010	76.2	816.0
34	BUZAU	SITA BUZAU	45.6608	26.0686	1950-2010	509	318.2
35	CALNAU	POTARNICHESTI	45.2200	26.8542	1965-2010	63.8	1345.3
36	SLANIC	CERNATESTI	45.2692	26.7550	1968-2010	103	1151.6
37	BASCA	BASCA ROZILEI	45.4525	26.3383	1960-2010	494	376.0
38	BASCA MICA	VARLAAM II	45.5200	26.4489	1963-2010	466	533.4

Table 4: Properties of the 38 considered subcatchments of the Siret basin. 'Nr.' refers to the numbers indicated in Figure 11. A = catchment area; ED = earthquake density; CMD = cumulative magnitude density; PGA = expected peak ground acceleration with a recurrence interval of 100 years; L = lithology score; R = total catchment relief. Slope = average catchment slope; MLR = mean local relief; Forest = percentage forest cover in 1990; AL = percentage of arable land in 1990; P = average annual rainfall depth; Ro = average measured runoff depth (Vanmaercke et al., 2014b).

Nr.	Gauging station (River)	A (km²)	ED (km^{-2})	CMD ($Mw\ km^{-2}$)	PGA ($m\ s^{-2}$)	Dominant Lithology *	L	R (m)	Slope (°)	MLR (m)	Forest (%)	P ($mm\ y^{-1}$)	Ro ($mm\ y^{-1}$)
1	BRODINA (SUCEAVA)	366	0.000	0.000	0.90	F	1.0	952	14.8	561	33.2	784	371
2	PĂRHĂUȚI (SOLONEȚ)	204	0.000	0.000	1.18	P & Q	1.4	643	6.8	294	33.5	627	192
3	IȚCANI (SUCEAVA)	2334	0.000	0.000	1.34	P & Q	1.3	1265	8.2	350	32.9	680	228
4	PRISACA DORNEI (MOLDOVA)	664	0.002	0.006	0.86	C	0.7	1272	14.9	644	55.8	772	426
5	DRAGOȘA (MOLDOVIȚA)	463	0.002	0.010	1.08	F	1.0	888	13.7	531	80.2	747	345
6	BOGDĂNEȘTI (RÂȘCA)	181	0.006	0.014	1.57	F	1.4	821	11.5	489	89.3	634	260
7	TUPILAȚI (MOLDOVA)	3928	0.003	0.010	1.55	F	1.2	1611	10.6	469	55.8	670	262
8	DORNA GIUMALĂU (BISTRIȚA)	758	0.001	0.003	0.78	C	0.5	1445	17.1	680	75.5	831	499
9	DORNA CANDRENI (DORNA)	565	0.014	0.038	0.78	V	0.6	1158	12.0	603	74.4	801	421
10	DORNA ARINI (BISTRIȚA)	1690	0.006	0.016	0.78	C	0.6	1458	14.7	669	59.5	818	469
11	BROȘTENI (NEAGRA)	292	0.014	0.046	0.84	C	0.5	1264	18.1	749	84.7	791	411
12	FRUMOSU (BISTRȚA)	2858	0.005	0.015	1.06	C	0.6	1698	16.5	737	69.8	798	421
13	POIANA LARGULUI (BOLĂTĂU)	59	0.000	0.000	1.57	F	1.0	799	14.8	647	66.3	677	257
14	TULGHEȘ (BISTRICIOARA)	408	0.000	0.000	0.92	C	0.5	1010	16.3	690	61.9	768	240
15	BISTRICIOARA (BISTRICIOARA)	760	0.003	0.006	1.27	C	0.6	1145	17.3	740	66.5	751	259
16	SLOBOZIA (CRACĂU)	445	0.002	0.007	1.97	M	1.7	945	7.5	340	33.4	605	128
17	LUNCA DE SUS (TROTUȘ)	88	0.000	0.000	1.57	F	0.8	568	14.7	458	13.4	742	285
18	GOIOASA (TROTUȘ)	781	0.003	0.007	1.85	F	1.0	1167	16.2	711	45.7	745	264
19	ASĂU (ASĂU)	204	0.000	0.000	2.23	F	1.0	980	17.1	671	90.9	703	315
20	VALEA UZULUI (UZ)	150	0.007	0.015	1.96	F	1.0	906	15.7	605	77.1	743	350
21	TÂRGU OCNA (TROTUȘ)	2091	0.009	0.022	2.42	F	1.0	1406	15.2	685	56.2	711	262
22	FERĂSTRĂU (OITUZ)	267	0.015	0.032	2.52	F	1.0	1206	15.0	684	65.8	709	367
23	VRÂNCENI (TROTUȘ)	4092	0.010	0.022	2.82	F	1.6	1495	12.9	586	54.8	665	267
24	HELEGIU (TAZLĂU)	998	0.004	0.009	2.64	M	1.6	1221	10.4	435	48.8	605	213
25	CIURUC (SUȘIȚA)	178	0.163	0.379	3.01	M	1.8	985	10.6	499	62.6	645	234
26	TULNICI (PUTNA)	313	0.236	0.623	2.53	F	1.0	1280	16.8	753	88.5	759	208
27	NEREJU (ZĂBALA)	263	6.091	20.430	2.83	F	1.1	1253	14.8	714	84.3	781	210
28	COLACU (PUTNA)	1087	2.435	7.749	2.87	F	1.3	1508	14.9	719	71.0	735	164
29	BOTÂRLĂU (PUTNA)	2450	1.511	4.608	3.00	P & Q	1.5	1755	10.3	506	51.3	642	117
30	GOLEȘTI (MILCOV)	406	1.426	4.180	3.14	M	1.9	1219	10.3	472	55.8	595	55
31	JILIȘTE (RÂMNA)	398	0.611	1.482	3.14	P & Q	1.9	860	7.5	325	36.9	570	42.6
32	TULBUREA (RĂMNICU SĂRAT)	187	1.610	4.652	3.14	M	1.6	1033	14.5	650	65.1	709	268
33	TĂTARU (RĂMNICU SĂRAT)	1048	0.659	1.727	2.95	P & Q	1.9	1375	5.1	242	26.1	569	76.2
34	SITA BUZAU (BUZAU)	360	0.144	0.329	2.19	F	1.0	1250	12.0	550	39.9	788	509
35	POTARNICHESTI (CALNAU)	194	0.423	1.036	3.14	M	1.9	627	7.7	313	17.6	585	63.8
36	CERNATESTI (SLANIC)	422	1.225	3.474	3.13	M	1.8	1210	12.0	521	35.6	661	103
37	BASCA ROZILEI (BASCA)	783	2.126	6.561	2.62	F	1.0	1360	14.4	660	82.4	803	494
38	VARLAAM II (BASCA MICA)	239	3.339	10.435	2.72	F	1.0	1211	14.6	701	84.1	824	466

* Dominant Lithology: F = Flysch, P & Q = Platform and Quaternary sedimens, C = Crystalline, V = Volcanic, M = Molasse

3 Results

3.1 The earthquake-landslide dataset

Appendix 1 summarizes the E-L dataset and reports the country, year, magnitude and consulted sources for each event. The table also indicates which events were used for the LV model, LD model and M-D relation. In total, 239 events with at least information on one of the landslide parameters: LV, LN, LA, LAA or D_{max} are included in this dataset. These 239 events are likely to represent the largest part of earthquakes with available information on associated landslides being reported in scientific literature. The epicenter locations, with indication of their magnitude are shown in Figure 10 (for 3 events, the epicenter could not be located). Earthquake prone regions such as the ring of fire and the southern margin of the Eurasian plate are clearly represented in the dataset. Figure 13 indicates for what purposes each event was used.

Additional descriptive statistics are presented in Figure 14. The left pane presents a bar chart, indicating the amount of EQ events that contain information on the indicated landslide variables. LAA, D_{max} and LN (including ranges and minimum or maximum estimates) were often reported, whereas information on LV (including ranges and minimum or maximum estimates), Vl_{max} and a published landslide distribution inventory is rather scarce. The right pane presents the exceedance probability (EP) of the magnitude and year of occurrence of earthquake events in the dataset (Appendix 1). All retrieved EQ events have magnitudes larger than four. Only about 20% of the events have a magnitude smaller than 6 and just about 5% has a magnitude larger than 8. It is clear that most of the events in the dataset are from more recent years, more than 50% of the investigated events occurred after 1975.

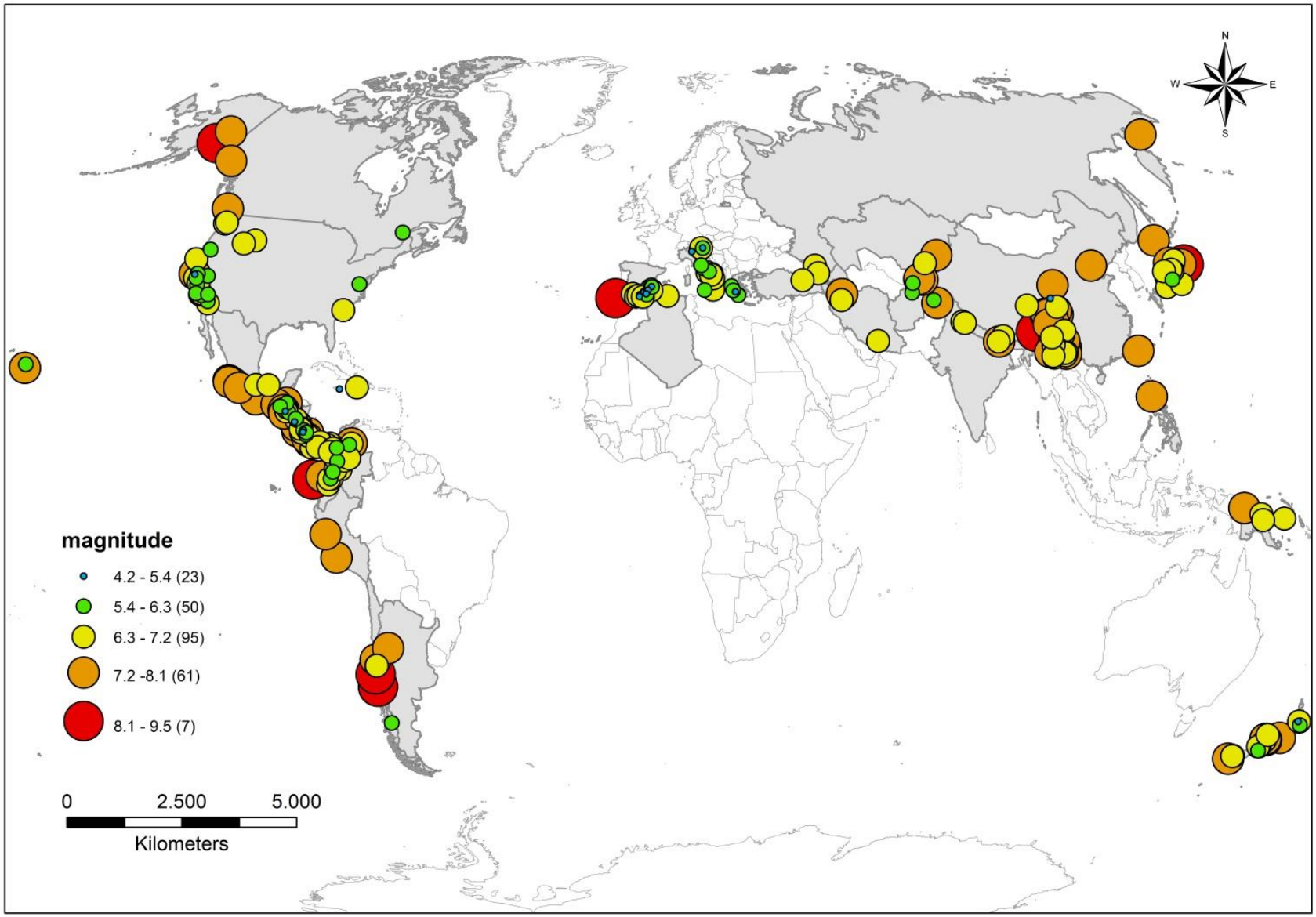

Figure 12: Epicenters of earthquakes in the earthquake-landslide dataset with indication of magnitude. 236 of 239 earthquake events in the dataset are displayed on the map. For the other three, the epicenter location was unknown. Countries where epicenters are located are marked in gray (Appendix 1, own processing).

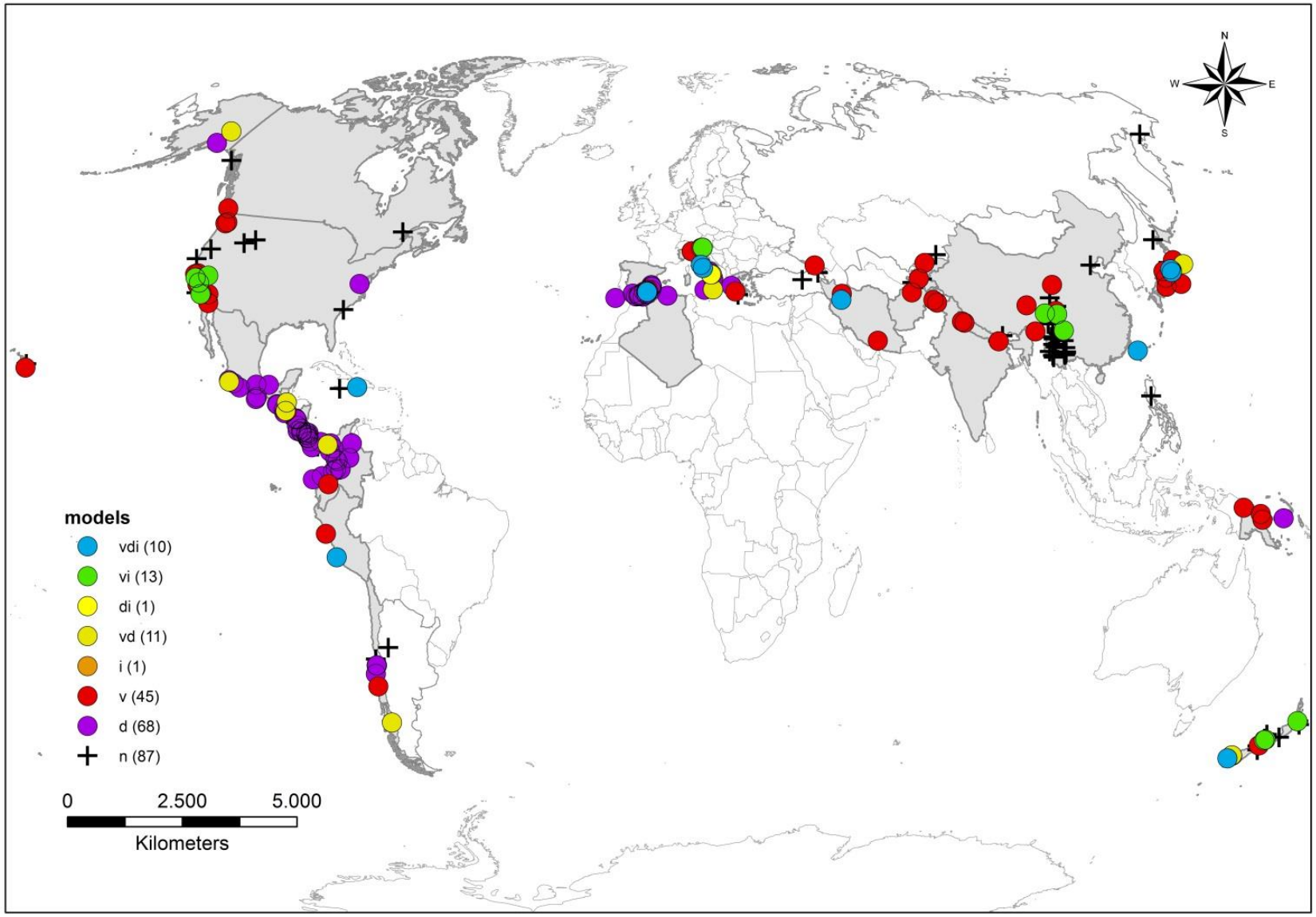

Figure 13: Epicenters of earthquakes in the earthquake-landslide dataset with indication of the models wherein the events are used. Countries where epicenters are located, which are used in one of the models are marked in gray. Model codes are: n: not used, d: used in moment magnitude – maximum landslide distance to epicenter relation, v: used for the total landslide volume model and i: used for the landslide distribution model as an inventory dataset (Appendix 1, own processing).

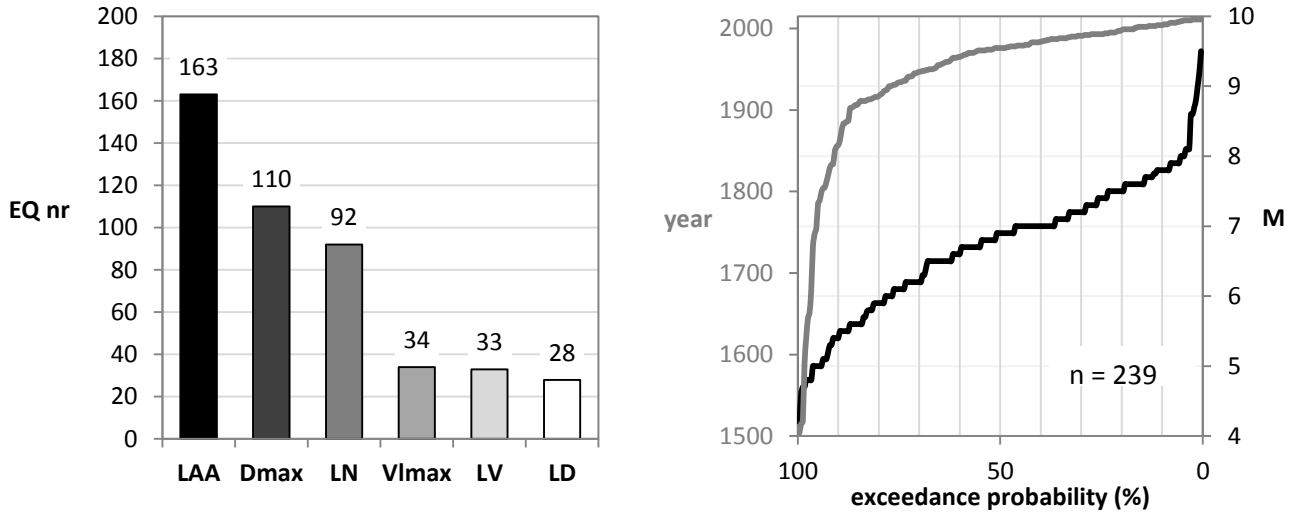

Figure 14: (left) Number of earthquakes (EQ nr) in the dataset containing information on: landslide-affected area (LAA), maximum distance from the epicenter over which landslides are triggered (D_{max}), landslide number (LN), total landslide volume (LV), maximum individual landslide volume (Vl_{max}) and the published landslide distribution inventory (LD). The sum of events with information on the different parameters exceeds 239, as for one event more parameters can be reported. (right) Exceedance probability (EP) of the magnitude (black) and year of occurrence (grey) of earthquake events from the dataset (Appendix 1, own processing).

3.2 Predicting the total earthquake-induced landslide volume

3.2.1 Data selection and preparation

77 earthquake events were retained from the earthquake-landslide dataset (indicated in Appendix 1 and Figure 13) to construct a landslide volume model: 25 with a reported LV (of which two with a LV range), 30 with a reported landslide number and 22 with a reported landslide number range. Figure 15 shows a comparison between reported LV (LV_r) and calculated LV (LV_c) (section 2.3.1) for events with both known LV and LN. This provides an assessment of the goodness of the LN-to-LV conversion with equation 4 and the additional refinement with the largest individual landslide (Vl_{max}) (section 2.3.1). Especially the extra refinement of the LV with Vl_{max} (diamonds) proves useful, resulting in deviations usually smaller than a factor three. Still, some deviations are slightly higher than a factor ten and one deviation even amounts to a factor 100. This last case concerns the Coalinga earthquake (United States, 1983, M_w 6.7).

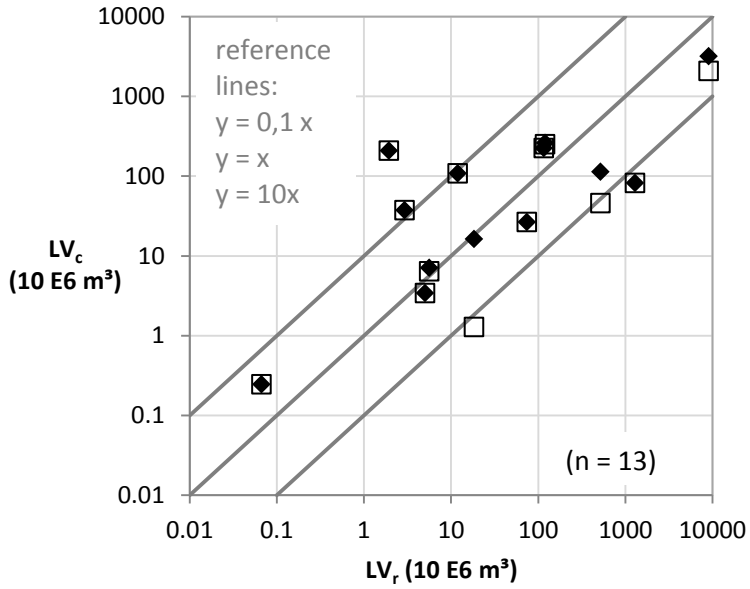

Figure 15: Comparison between reported total landslide volumes (LV_r) generated by an earthquake and calculated total landslide volumes (LV_c), given the total number of landslides (LN) (section 2.3.1). Open squares represent LV_c based on equation 4, while filled diamonds also take refinements of the maximum individual landslide volume into account (Appendix 1, own processing).

3.2.2 Delineation of the landslide-affected area

The EQ events used to construct the *moment magnitude – maximum landslide distance to epicenter (M-D) relation* are indicated in Appendix 1 and Figure 13. 91 events containing information on D_{max} could be used for this purpose, resulting in the relation presented in Figure 16. This relationship was used to delineate mask areas as a proxy of the LAA in which environmental characteristics were considered (section 2.3.2).

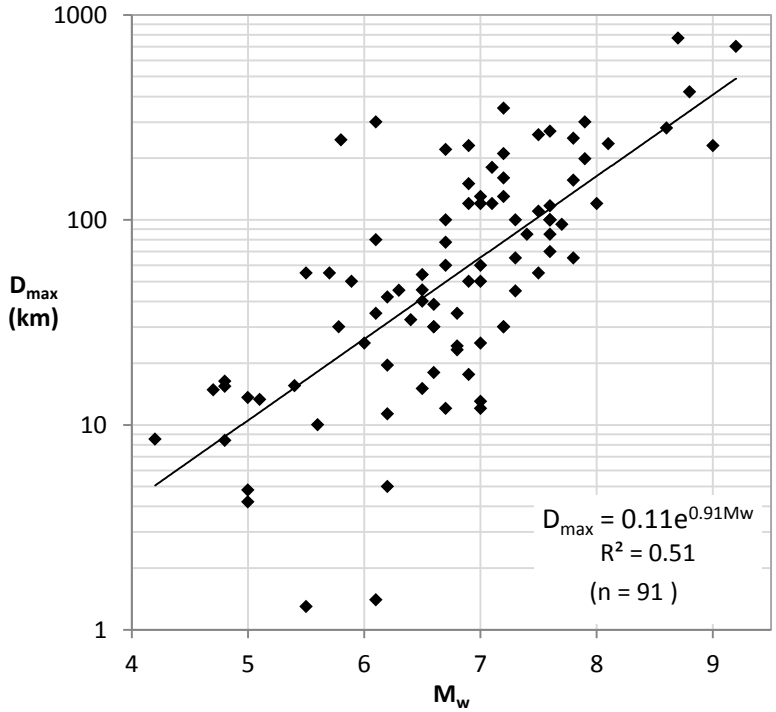

Figure 16: Relation between moment magnitude (M_w) and maximum distance from the epicenter over which landslides are triggered (D_{max}). The events used to construct this relation are indicated in Appendix 1 (own processing).

Also a relatively good relationship between moment magnitude *and total landslide-affected area (LAA)* could be established based on 132 earthquake events (Figure 17). Figure 18 compares the calculated landslide-affected areas based on D_{max} (LAA_c) (section 2.3.2) with the reported LAA (LAA_r). Even though a strong correlation exists, it is clear that LAA_c generally overestimates the LAA_r.

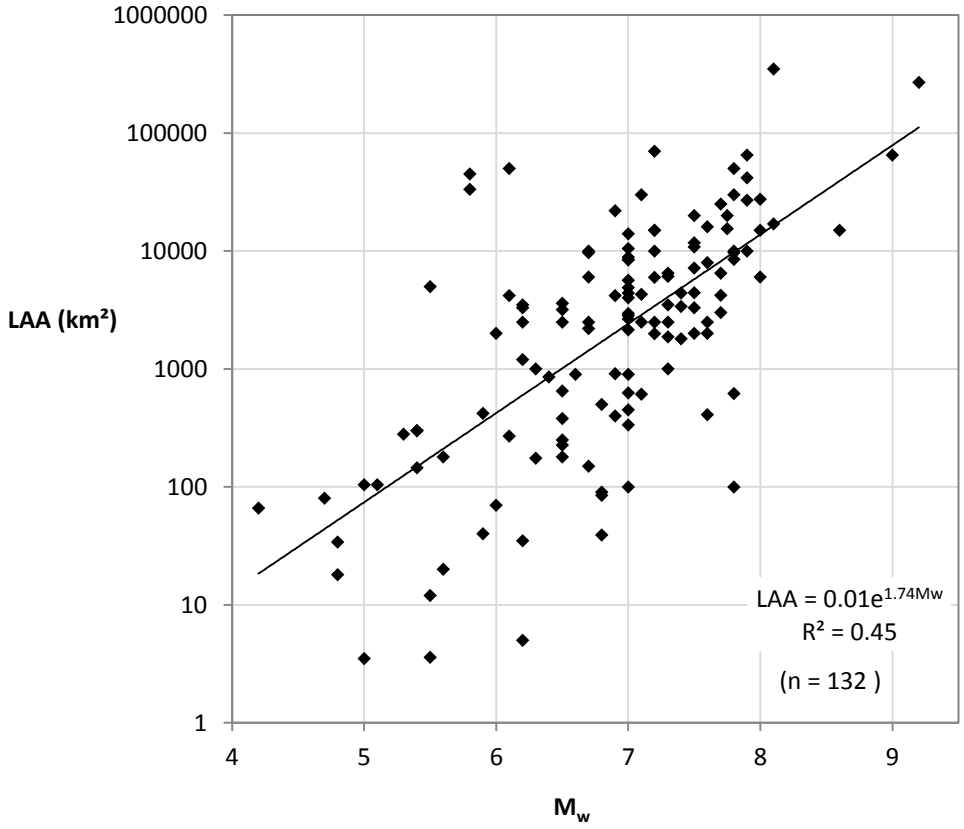

Figure 17: Relation between moment magnitude (M_w) and total landslide-affected area (LAA) (Appendix 1, own processing).

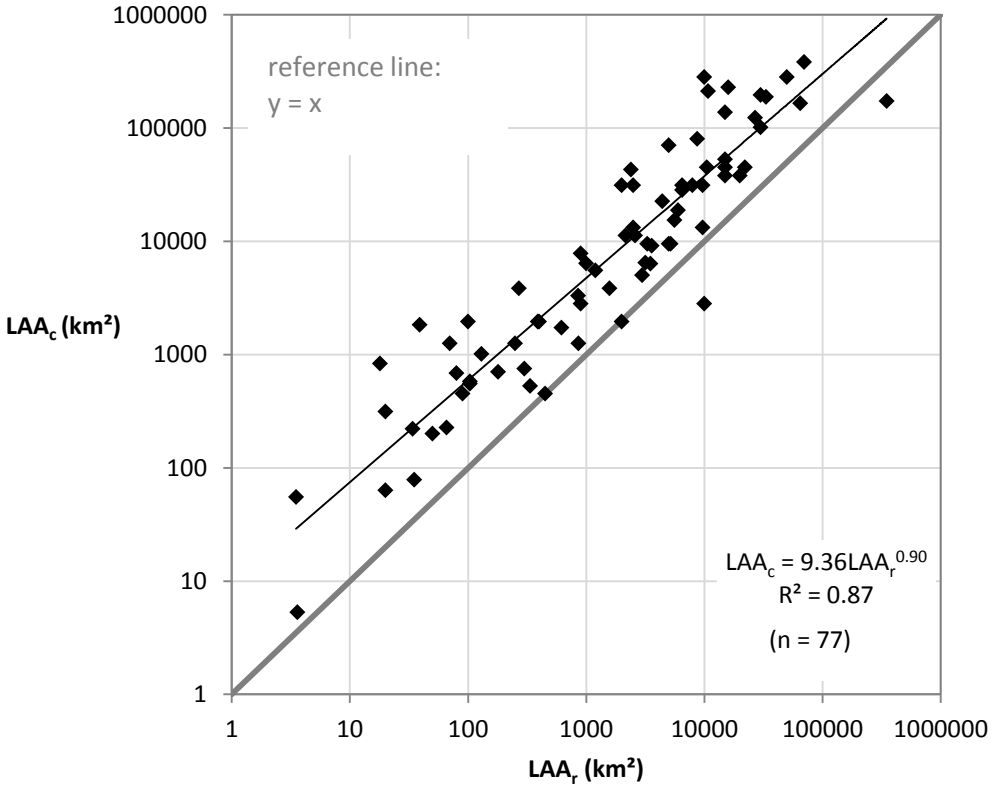

Figure 18: Relationship between reported landslide-affected area (LAA_r) of earthquake events and calculated affected areas (LAA_c) based on the maximum distance from the epicenter over which landslides are triggered (D_{max}) of that event (Appendix 1, own processing).

Figure 19 presents the mask areas of events taken into account for the LV model. Both circular masks with radii directly derived from the relation presented in Figure 16 and masks with half of these radii are shown (section 2.3.2). The mask areas give a good indication of the large difference in landslide affected area between the events, with some very large events in Japan, China and South America, but with mask areas that are hardly discernable on this scale in Italy and Spain. The inset maps illustrate the longitudinal extension of the circular mask areas towards the poles.

Figure 19: Overview map of all 77 mask areas for events used in the analyses with both full and half radius (determined by the relation in Figure 16) masks displayed, the inset maps indicate the flattening of mask areas towards the poles. The countries where epicenters are located are marked in green (Appendix 1, own processing).

3.2.3 Factors controlling earthquake-induced landslide volumes

3.2.3.a Moment magnitude

Similar to previous research (section 1.2.3) a *moment magnitude – total landslide volume (M-V)* relationship is presented in Figure 20. A strong positive relationship exists between both variables, where M_w can explain about 59% of the variation in LV.

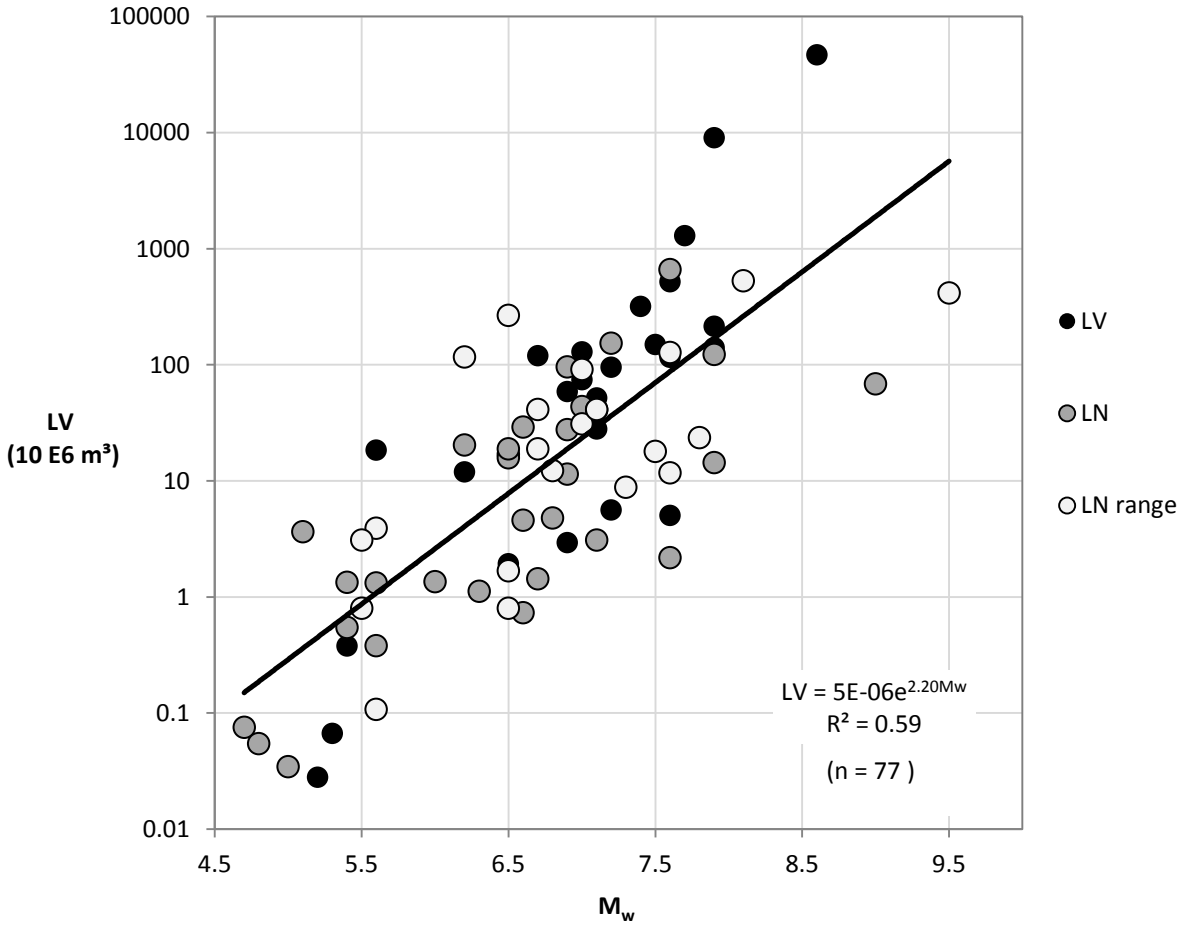

Figure 20: Relation between earthquake moment magnitude (M_w) and total generated landslide volume (LV). A distinction is made based on the type of LV acquisition. LV: reported total volume, LN: reported total landslide number, LN range: reported total landslide number range (Appendix 1, own processing).

3.2.3.b Land fraction

Before carrying out correlation analyses, the LV was *linearly corrected for the land fraction* in each mask area (LV_{lc}) (section 2.4.2). Figure 21 presents the relation between LV_{lc} and M_w. For comparative purposes the original volumes are shown as well. After this correction M_w explains about 63% of the variation in LV_{lc}. It is these corrected volumes that were used for the further correlation analyses.

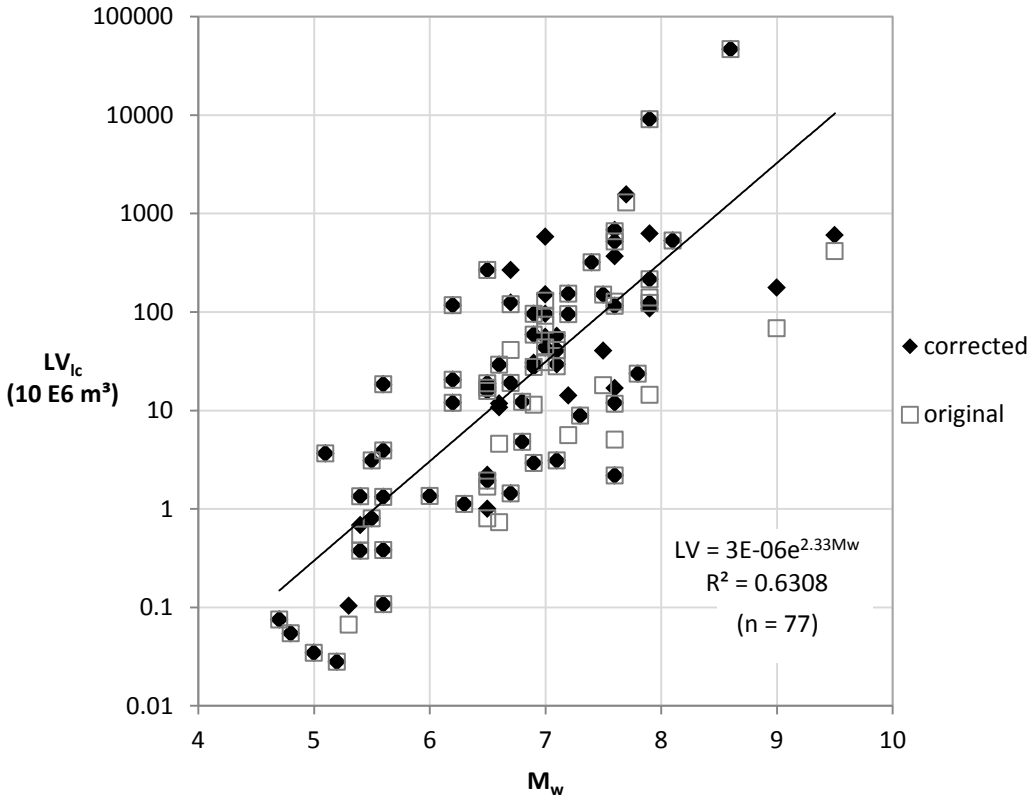

Figure 21: Relation between earthquake moment magnitude (M_w) and total generated landslide volume linearly corrected for the land fraction in the mask area (LV_{lc}). The original (uncorrected) volumes are indicated by open squares (Appendix 1, own processing).

3.2.3.c Correlation and partial correlation analysis: testing other predictor variables

After correction for the land fraction, a general correlation analysis and a partial correlation analysis were carried out for both mask areas with full radius and with half this radius (section 2.3.2). The correlation matrices showed slightly *better results for the smaller mask areas*. Therefore and because of earlier considerations (section 2.3.2), it was decided to work with these data to construct the LV model. Additionally, we tested whether variables show stronger correlations on a linear basis, a log-linear basis or a logarithmic basis. A *log-linear relation* (in agreement with the relation presented in Figure 20) shows the strongest correlation for most variables. This means that linear predictor variables explain for the logarithmic variation in volume.

The correlation analysis shows that M_w, mean precipitation, mean MFI and mean slope, with respectively a correlation coefficient (R) of 0.81, 0.25, 0.29 and 0.24, are significant on the 0.05 significance level to explain for LV_{lc}. Except for the correlation with M_w, these *correlations are very weak*, as shown in Figure 22 for mean P and mean slope. For many of the considered variables, the minimum, maximum and standard deviations showed significant correlation with LV_{lc}. However, these values are strongly determined by the size of the different mask areas and consequently also strongly autocorrelated with M_w.

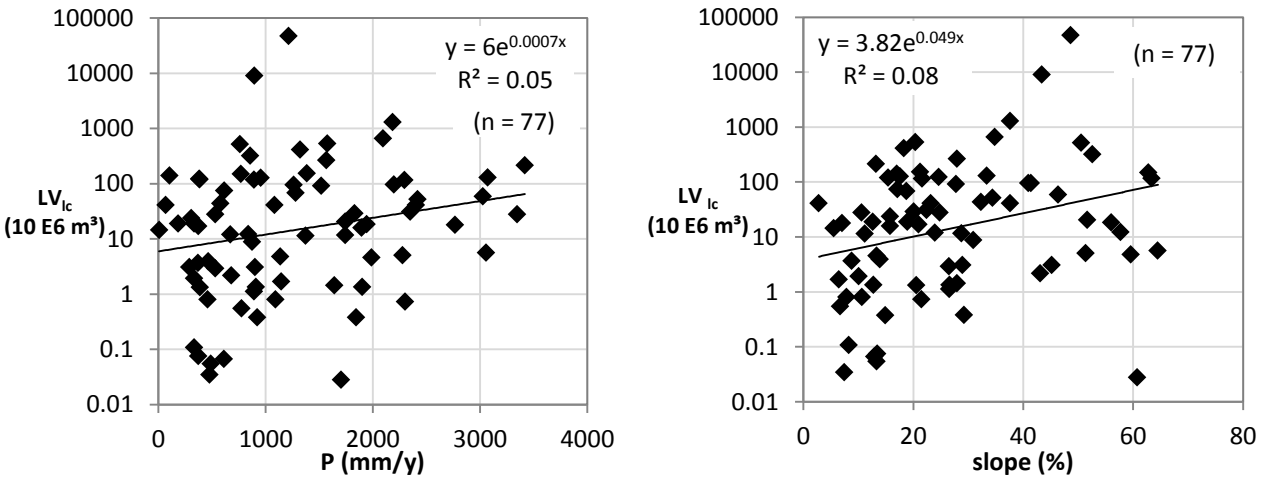

Figure 22: (left) Correlation between precipitation and total landslide volume, linearly corrected for the land fraction in the mask area (LV_{lc}) and (right) between slope and LV_{lc} (Appendix 1, own processing).

Because M_w is by far the most significant variable explaining the observed variability of LV_{lc}, a *partial correlation analysis* was carried out with correction for M_w. In this case only three variables remain significant on the 0.01 significance level: standard deviation of LR (LR_{stdev}), maximum temperature and the lithology class 'acid plutonic rocks' (Hartmann & Moosdorf, 2012), with respective partial-R values of 0.39, 0.29 and 0.30. The fact that all previously significant variables describing the minimum, maximum and standard deviations of a considered factor within the mask area, are no longer significant, confirms their dependence on M_w through the mask size.

Further analysis of the residue plots after correction for M_w (Figure 23) shows a robust positive relation between LR_{stdev} and LV_{lc}. Also a robust, but weak relation exists between the maximum temperature and LV_{lc}. The lithology factor (acid plutonic rocks) however is not robust, depending only on a few events. Furthermore, other factors related to lithology (e.g. the fraction of hard rocks in each affected area) showed no significant (partial) correlation with LV_{lc}. Therefore, this factor was not taken further into account.

Based on these results, we conducted another partial correlation analysis, correcting for both M_w and LR_{stdev}. In this case also the maximum temperature turns insignificant on the 0.05 significance level. *Consequently only M_w and LR_{stdev} could be identified as significant variables* for explaining the variability in LV_{lc}.

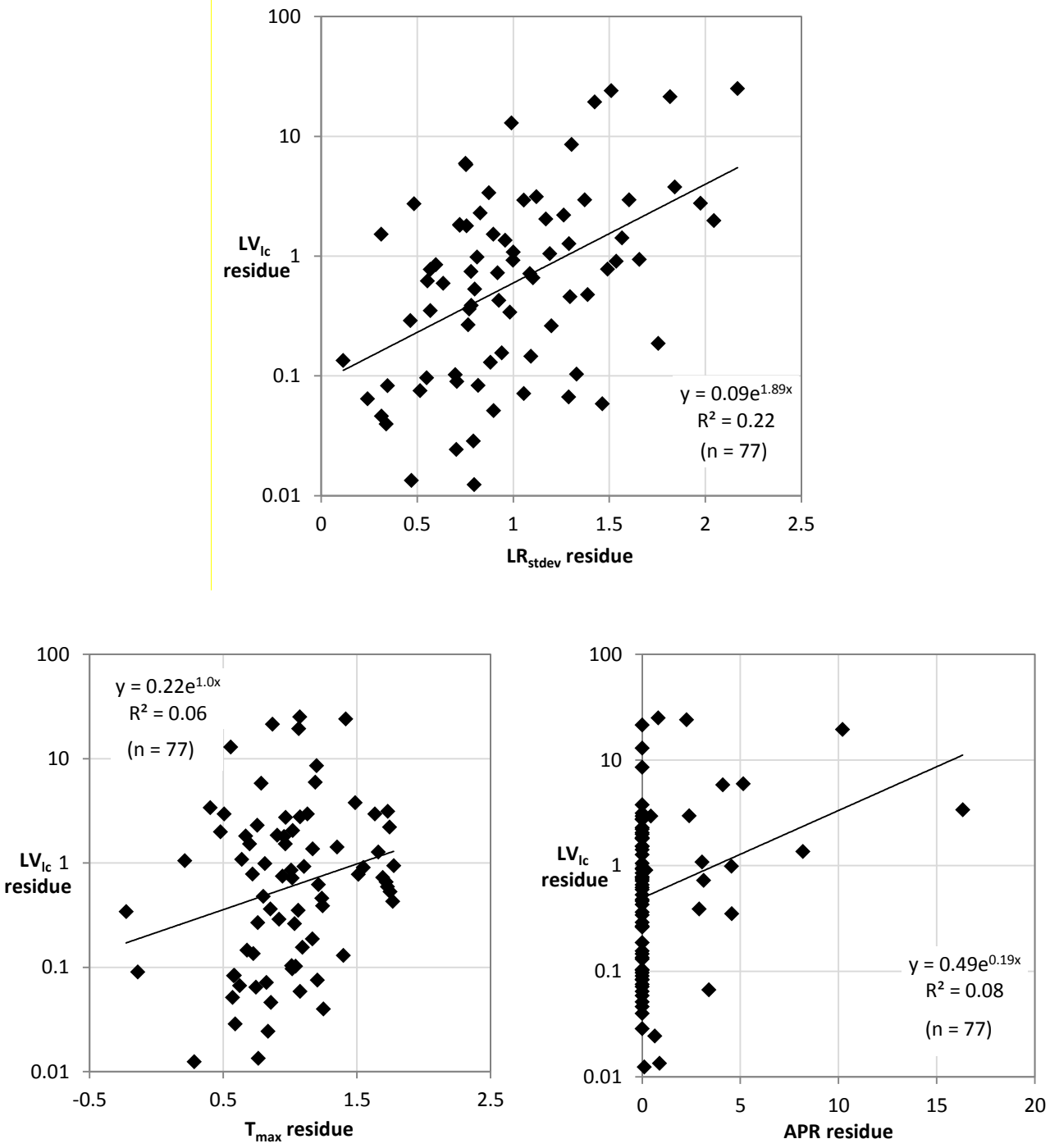

Figure 23: Scatter plots of predictor variable residues after correction for the moment magnitude (M_w) with relations between the standard deviation of the local relief (LR_{stdev}) and the landslide volume linearly corrected for the land fraction in the mask area (LV_{lc}), between the maximum annual air temperature (T_{max}) and LV and between the lithology class acid plutonic rocks (APR) and LV (Appendix 1, own processing).

3.2.4 Landslide volume model

Based on the analyses explained in the previous sections, a model could be established between the independent variable (LV_{lc}) and the other significant predictor variables (the moment magnitude and the standard deviation of the local relief). As explained in section 2.3.1, a weighted calibration was applied during model calibration, with weights depending on the expected accuracy of the LV estimates.

Figure 24 presents the eventual *relationship* between the modeled landslide volume (LV_m) on the on hand and the reported landslide volumes (after linearly correcting for the fraction of land in the affected area) on the other hand. Symbols in this figure are shaded according to the way of LV acquisition (reported LV, reported LN or reported LN range). A vast increase in R^2 from 0.59 to 0.75 compared to the M-V relation (Figure 20) is observed. Deviations are in general smaller than an order of magnitude and also smaller compared to the M-V relation; about 80% of the predictions falls within an order of magnitude, and 97.5% falls more or less within an order of magnitude, with only two strongly deviating data points. Furthermore the predictions show no bias for large or small LV_{lc}, with a trend closely to the 1:1 reference line. The additional factors taken into account compared to the M-V relation, i.e. a linear correction for the land fraction in the mask area, LR_{stdev} and weighting the model, respectively explain an additional 4.5%, 7.5% and 4% of the variation in LV. The resulting model equation is the following (own processing):

$$\boldsymbol{LV_{lc} = 10^{0.94 * M_w + 0.0023 * LR_{stdev} - 5.68}} \quad (17)$$

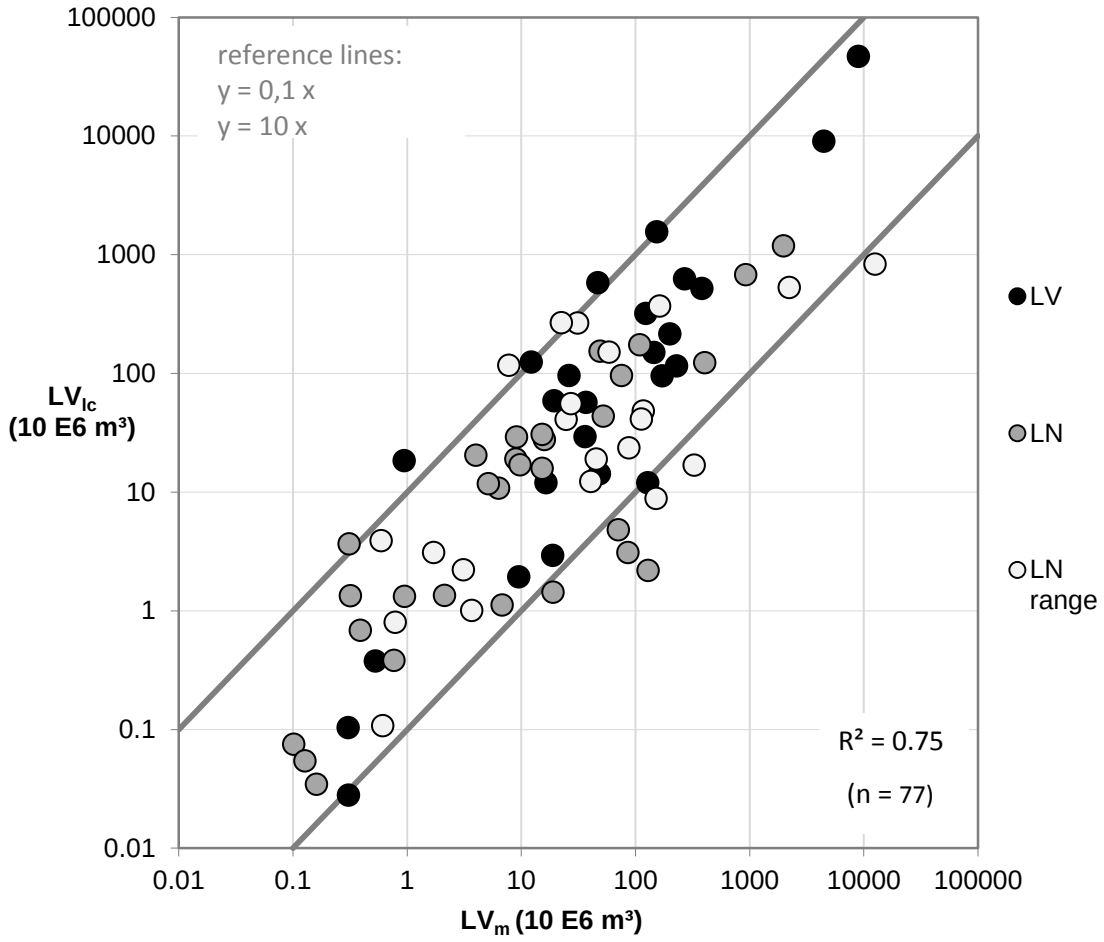

Figure 24: Relation between the modeled landslide volume (LV_m) and the reported or derived landslide volume linearly corrected for the fraction of land in the mask area (LV_{lc}) (equation 17). Model variables are the moment magnitude (M_w) and the standard deviation of the local relief (LR_{stdev}). The regression is weighted according to the quality of the three different input datasets. The trendline of the combined data is not plotted as it does not take into account these different weights. The displayed R^2 referes to the model fit of equation 17 (Appendix 1, own processing).

3.3 Predicting the spatial distribution of earthquake-induced landslides

3.3.1 Overview of the earthquake-induced landslide inventories

The effort of georeferencing and digitizing LD maps resulted initially in *28 datasets* that could be used to construct the LD model. Table 5 gives an overview of these events and Table 6 provides an indication of the quality of the data for the most important assessed parameters. According to this table, the quality of the different datasets appears quite variable for the different parameters. Based on this assessment it was found that events with ID's: 51, 87 and 139 did not meet the quality requirements. Event 51 lacks a major part of the LAA, event 87 depicts large landslide areas, which are too large to deduce meaningful environmental characterization of landslide versus non-landslide pixels and event 139 could not be digitized with sufficient accuracy for analyses on a 500m resolution. The final selection of *25 events* resulted in a dataset of *594546 pixels* that were categorically classified as either a 'landslide'-or 'no-landslide' pixel. The contribution of each of the 25 subsets to this total dataset is shown in Figure 25. The overall contribution is largest for event 123, whereas event 91 contributes mostly when only landslide pixels are considered.

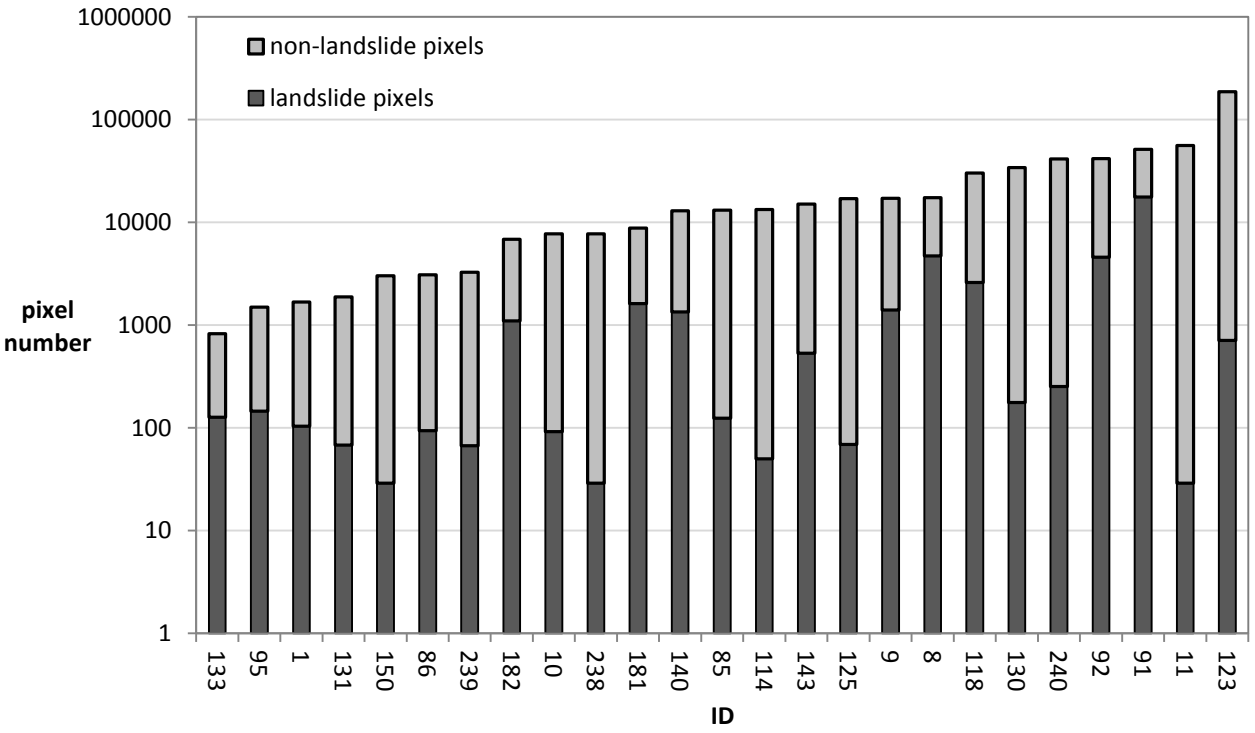

Figure 25: Amount of landslide and non-landslide pixels for each landslide inventory. Events (ID) are sorted by increasing total pixel number (Table 5, own processing).

Table 5: Overview table of digitized landslide inventories (n = 28), with indicated identifier (ID) referring to Appendix 1, event name or location, country, year, moment magnitude (M_w), an overal quality assessment and source of the dataset. The quality assesment is an overall score based on indivdual quality parameters, whereof the most important parameters are displayed in Table 6, the classes are: excellent, very good, good, sufficient and insufficient. Events not used for constructing the landslide distribution (LD) model are displayed in italic (own processing).

ID	name/location	country	year	M_w	overal quality	source
1	Lorca	Spain	2011	5.1	excellent	Alfaro et al., 2012
8	Buller	New Zealand	1929	7.7	excellent	Parker, 2013
9	Inangahua	New Zealand	1968	7.1	excellent	Parker, 2013
118	Northridge	United States	1994	6.7	excellent	Harp & Jibson, 1995
140	Haiti	Haiti	2010	7.0	excellent	Gorum et al., 2013
181	Mammoth Lakes	United States	1980	6.2	excellent	Harp et al., 1984
182	Coalinga	United States	1983	6.7	excellent	Rymer & Ellsworht, 1990
239	Lake Rotoehu	New Zealand	2004	5.4	excellent	Hancox et al., 2004
10	Umbria-Marche (Sept.)	Italy	1997	5.8	very good	Guzzetti et al., 2009
86	Zhaotong	China	1974	7.1	very good	Chen et al., 2012
92	Chi-Chi	Taiwan	1999	7.6	very good	Parker, 2013
125	L'aquila	Italy	2009	6.3	very good	Guzzetti et al., 2009
130	Dusky Sound	New Zealand	2009	7.6	very good	Fry et al., 2010
131	Krn Mountains	Slovenia	1998	5.6	very good	Gosar, 2012
143	Loma Prieta	United States	1989	7.0	very good	Keefer, 1998
150	Krn Mountains	Slovenia	2004	5.2	very good	Mikos et al., 2006
238	Umbria-Marche (Oct.)	Italy	1997	5.7	very good	Guzzetti et al., 2009
51	*Guatemala*	*Guatemala*	*1976*	*7.6*	*good*	*Harp et al.,1981*
85	Luhuo	China	1973	7.6	good	Chen et al., 2012
87	*Longling*	*China*	*1976*	*7.4*	*good*	*Chen et al., 2012*
91	Wenchuan	China	2008	7.9	good	Parker, 2013
114	Avaj	Iran	2002	6.5	good	Mahdavifar et al., 2006
123	Pisco	Peru	2007	8.0	good	Lacroix et al., 2013
11	Irpinia	Italy	1930	6.7	sufficient	Esposito et al., 2009
95	Niigata Chuetsu-Oki	Japan	2007	6.6	sufficient	Collins et al., 2012
133	Northern Nagone Prefecture	Japan	2011	6.7	sufficient	Has et al., 2013
240	Fiorland	New Zealand	2003	7.2	sufficient	Trigs, 2009; Fry et al., 2010
139	*Ancash*	*Peru*	*1970*	*7.9*	insufficient	*Plafker et al., 1971*

Table 6: Quality overview table of digitized landslide inventories indicated in Table 5. With the identifier (ID) referring to Appendix 1. The determination of landslide numbers (LN) with 'field' refering to mapping in the field, 'aerial' referring to aerial photography and 'satellite' referring to satellite imagery. The completeness of the reported landslide inventory, an assessment of the completeness of the landslide-affected area (LAA), the goodness of digitization (i.e. the ability to digitize all indicated landslides on the map), the map resolution and the average error of the map. Errors are determined based on a comparison between 5 locations on the map and 5 locations in google earth (section 2.4.1). Asterix: * in column 7, indicates inventories where no 5 exact locations for comparison could be found, but for which the indicated topograpy on the maps allowed estimating the average error (own processing).

ID	determination of LN	completeness of reported LN	completeness of LAA	goodness of digitization	resolution of input map (m)	average error (m)
1	very detailed in field	complete	complete	very good	20	26
8	field + aerial	probably quite complete	probably quite complete	perfect	76	69
9	field + aerial	probably quite complete	probably complete	perfect	76	69
118	very detailed field + aerial	not entirely complete	probably complete	perfect	-	0
140	extremely detailed aerial	probably complete	complete	perfect	61	79
181	detailed field + aerial	probably complete	probably complete	perfect	7	<100*
182	-	probably complete	probably complete	perfect	11	<100*
239	aerial	only main landslides	probably complete	perfect	23	49
10	field, aerial	probably quite complete	probably complete	very good	42	<100*
86	detailed field	probably quite complete	probably complete	very good	29	-
92	very detailed aerial	landslides larger than 625m²	complete	very good	151	-
125	field, aerial, satellite	probably quite complete	probably complete	very good	65	±100*
130	aerial	probably quite complete	probably complete	perfect	175	140
131	very detailed field + aerial	complete	probably complete	very good	19	92
143	very detailed field	probably complete	probably complete	good	17	138
150	very detailed field	probably complete	probably complete	very good	43	67
238	field, aerial	probably quite complete	probably complete	perfect	42	<100*
51	very detailed field + aerial	not entirely complete	incomplete	very good	4	91
85	detailed field	unlikely to be complete	probably complete	very good	65	249
87	detailed field	probably quite complete	probably complete	perfect	94	-
91	field + aerial	incomplete	incomplete	perfect	159	-
114	detailed field	probably complete	probably complete	perfect	63	234
123	field + aerial	landslides larger than 100m² for aerial	probably complete	very good	283	285
11	-	unlikely to be complete	probably complete	perfect	223	336
95	field + aerial	incomplete: no small roadcut failures	probably quite complete	good	35-60	270
133	aerial	maybe some missing, selective area	maybe not entirely complete	good	60	100-200*
240	-	not entirely complete	probably complete	good	613	333
139	field + aerial	maybe some missing	incomplete	very good	107	1318

3.3.2 Evaluation of the potential predictor variables, based on individual landslide inventories

Figure 26 and Figure 27 display comparison plots of the likelihood ratio, the Wald test statistic and the logistic model coefficients (respectively equations 9, 10 and 7 in section 2.4.3) of the *univariate logistic regression analysis* for all 25 datasets. For a good comparison, lr and W statistics of the same variable are plotted next to each other. Many of the lr and W values surpass the display limit of 30, but this limit is set for visualization purposes of smaller values. Moreover, higher values are of no importance, since the interest goes to the significance level of 0.01 which is reached at the value of 6.635 for a χ^2 distributed parameter with one degree of freedom (Beirlant et al., 2005).

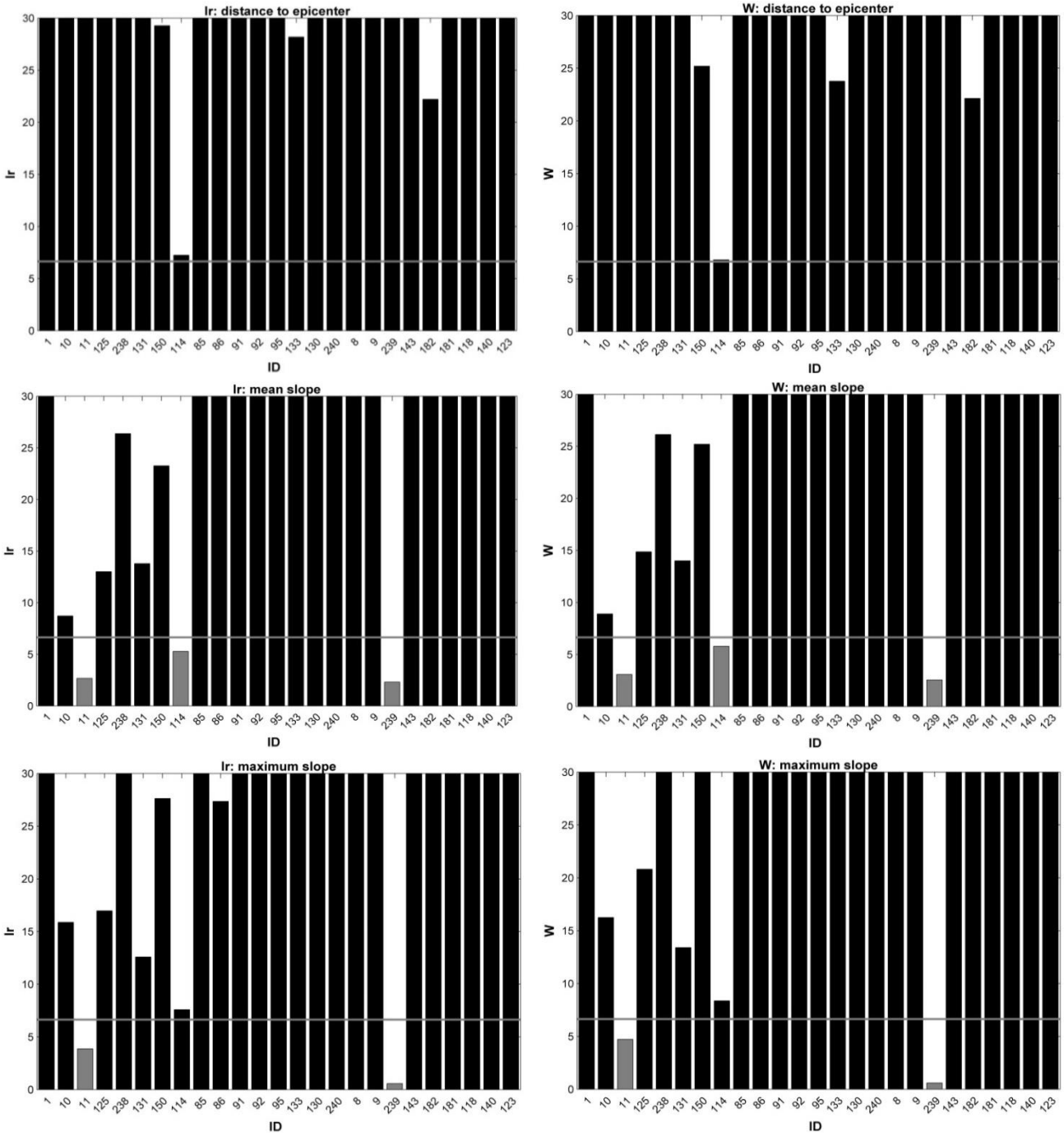

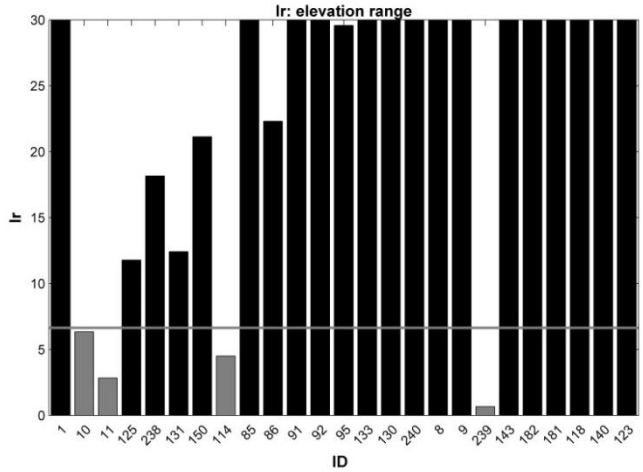
Ir: elevation range
Ir
ID
1 10 11 125 238 131 150 114 85 86 91 92 95 133 130 240 8 9 239 143 182 181 118 140 123

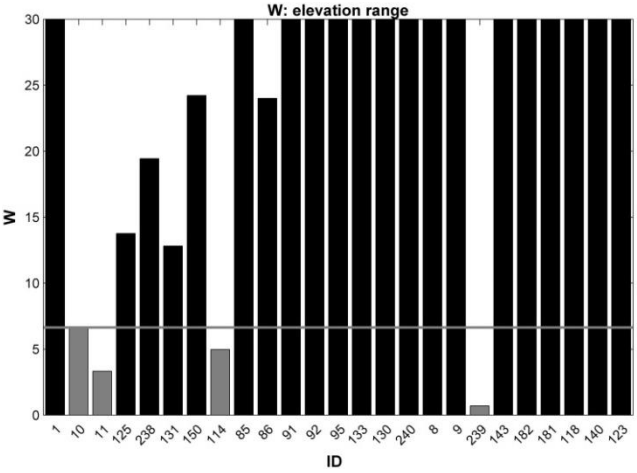
W: elevation range
W
ID
1 10 11 125 238 131 150 114 85 86 91 92 95 133 130 240 8 9 239 143 182 181 118 140 123

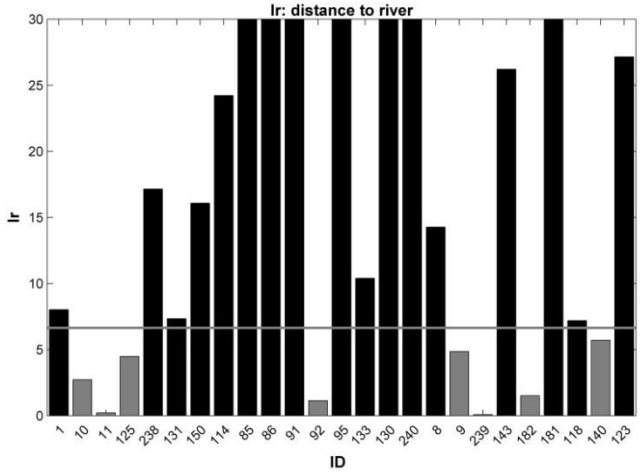
Ir: distance to river
Ir
ID
1 10 11 125 238 131 150 114 85 86 91 92 95 133 130 240 8 9 239 143 182 181 118 140 123

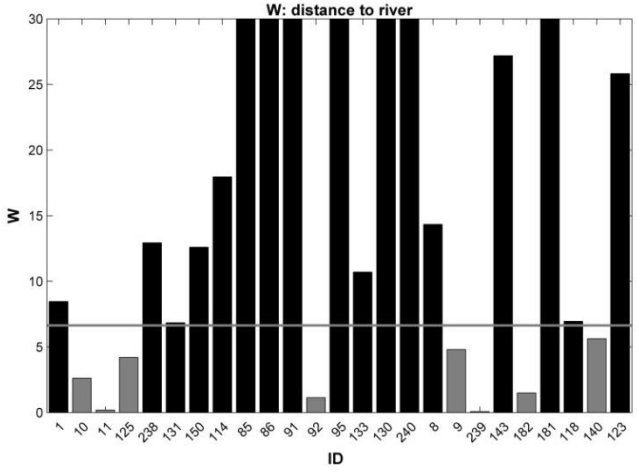
W: distance to river
W
ID
1 10 11 125 238 131 150 114 85 86 91 92 95 133 130 240 8 9 239 143 182 181 118 140 123

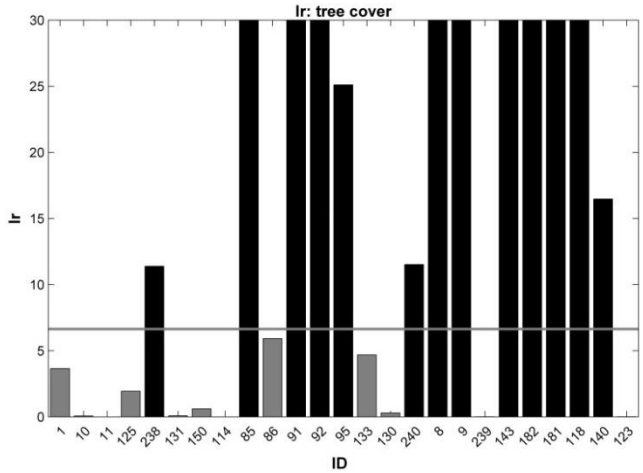
Ir: tree cover
Ir
ID
1 10 11 125 238 131 150 114 85 86 91 92 95 133 130 240 8 9 239 143 182 181 118 140 123

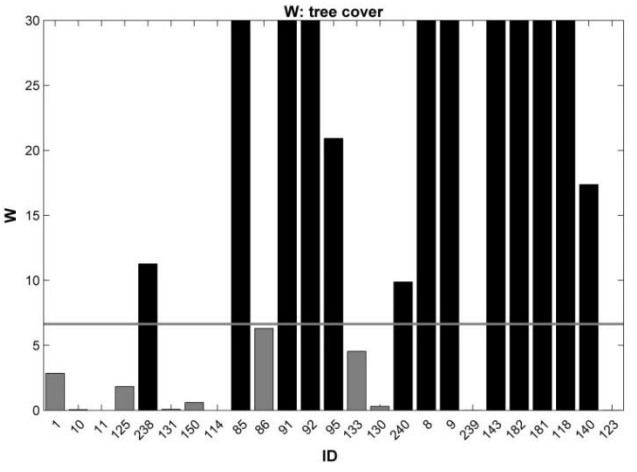
W: tree cover
W
ID
1 10 11 125 238 131 150 114 85 86 91 92 95 133 130 240 8 9 239 143 182 181 118 140 123

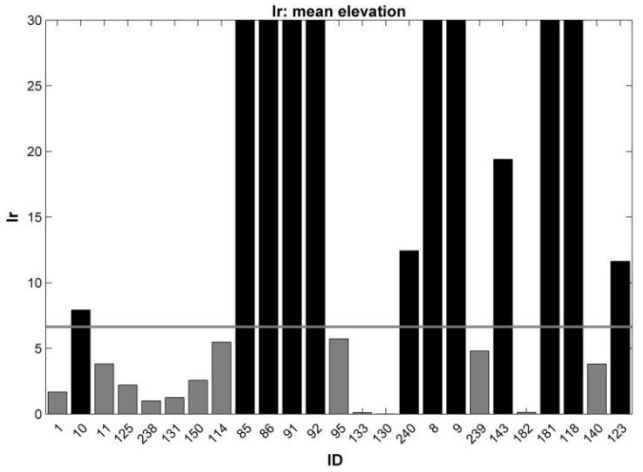
Ir: mean elevation
Ir
ID
1 10 11 125 238 131 150 114 85 86 91 92 95 133 130 240 8 9 239 143 182 181 118 140 123

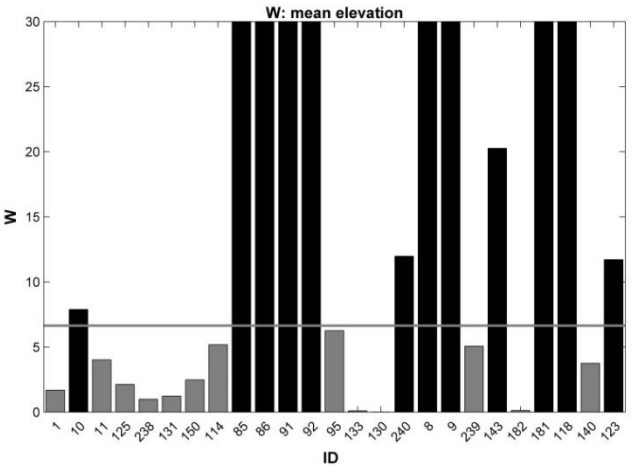
W: mean elevation
W
ID
1 10 11 125 238 131 150 114 85 86 91 92 95 133 130 240 8 9 239 143 182 181 118 140 123

Figure 26: Comparison plots of likelihood ratio's (lr, left column) and Wald statistics (W, right column) for all 25 events (for ID's see Table 5) for 7 different predictor variables. The y-axis limit is set to 30 to allow for a better comparison between the smaller values. The 0.01 significance level of 6.635 is indicated by the grey line. Values not reaching this limit are displayed in grey, values surpassing this limit are displayed in black. (Table 5, own processing).

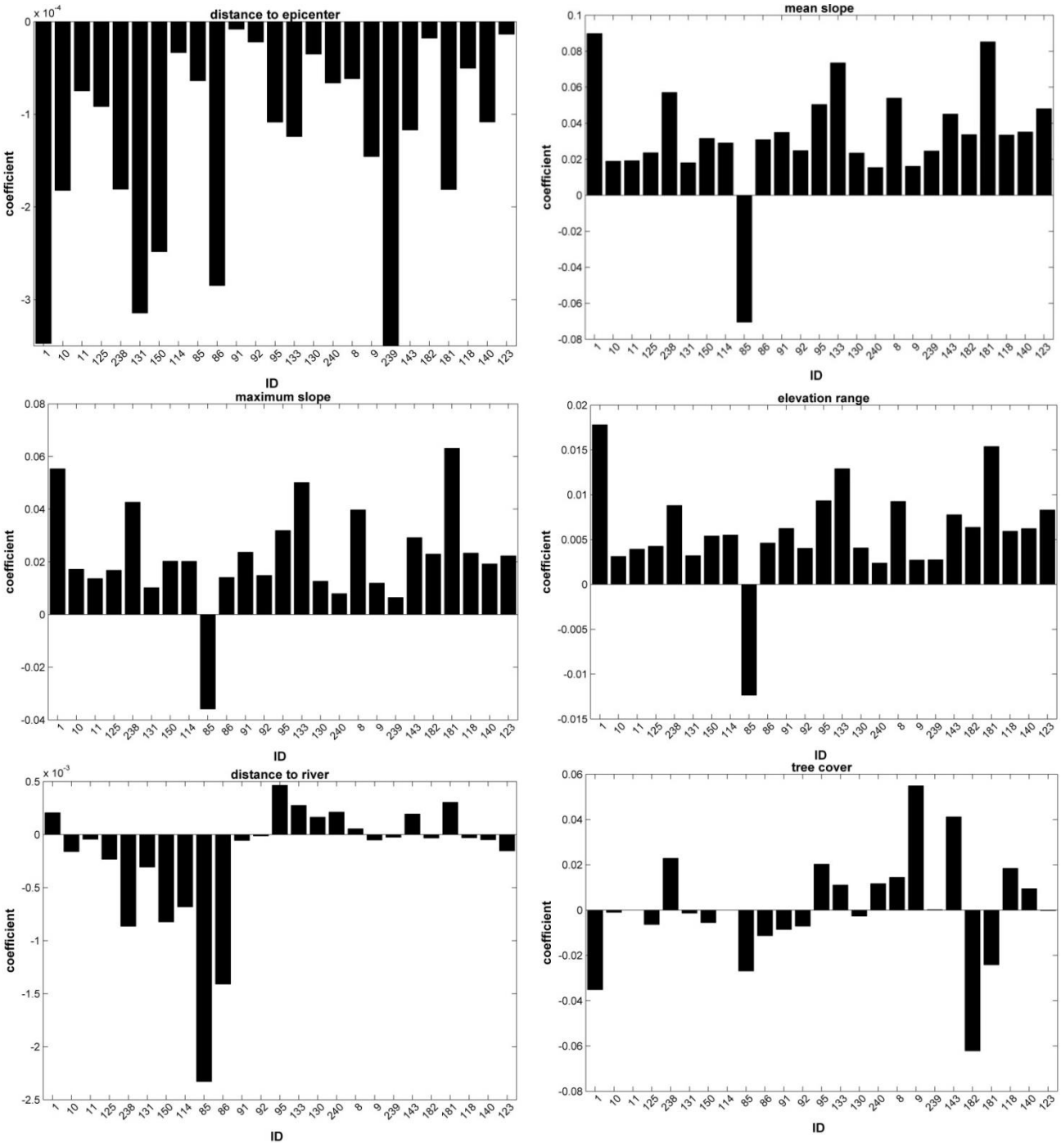

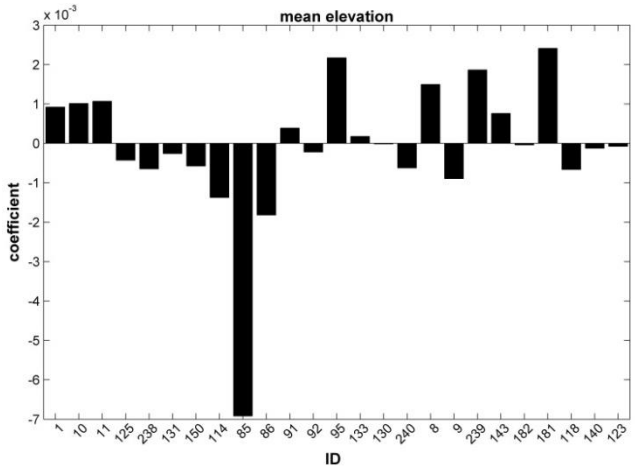

Figure 27: Comparison plots of the logistic model coefficients for all 25 events (for ID's see Table 5), obtained after separately testing each single variable for each event (see section 2.4.4) (Table 5, own processing).

Figure 26 clearly shows that W and lr approach each other. For all seven variables and all 25 events they are in agreement on whether or not the variable is significant on a significance level of 0.01. The variable 'tree cover' for events 11 and 114 (respectively Irpinia earthquake: Italy, 1930, M_w 6.7 and Avaj earthquake: Iran, 2002, M_w 6.5), is not appropriate for logistic regression analysis. The reason is that for these events the landslide pixels all have the same value of 5% treecover. In this way no variation in treecover values exists so that the predictor variable is not useful to differentiate between landslide and non-landslide pixels.

Figure 26 and Figure 27 also show that for the same variable, the lr, W and coefficients strongly vary between different events. However, a *consistent picture* is apparent: D, SME, SMA, and ER, are for most events significant on the 0.01 significance level and have consistently positive or negative coefficients for the different events. Only event 85 (Luhuo earthquake: China, 1973, M_w 7.6) behaves as an exception for the coefficients of the topographic variables (Figure 27) and event 239 (Lake Rotoehu earthquake: New Zealand, 2004, M_w 5.4) has a very low lr and W for these topographic variables. The other three variables (DR, TC and EM), on the other hand, are often insignificant on the 0.01 significance level and are, depending on the event, either negative or positive.

Figure 28 presents *the model improvement by* adding the indicated predictor variables for the *full model* compared to the null model (section 2.4.3 and 2.4.4) for four of the 25 events. The 25 obtained models are interesting results in itself, but the aim is to combine the different events in one model. Therefore, these individual results are not discussed in detail. The events presented in Figure 28 were chosen for comparison with results of Parker (2013) and in the light of the discussion of the two previous analysis steps. In general (for all 25 events), the full model is significantly better than the null model, with R^2_{McF} ranging from about 0.1 to about 0.5. Overall, it was found that especially D and the

relief variables SMA, SME and ER mostly contribute to the improvement of the full model. Event 85 forms an exception with a large improvement provided by EM.

Finally a comparison between the R^2_{McF} of models taking into account the variables distance to epicenter, the distance to the main fault lines and both, is shown in Figure 29. For this figure, the analysis was carried out for earthquake events with mapped main faults on the published landslide inventory maps. The results for D appear very variable, whereas *DF* appears more *robust* and also scores better than D for six of the nine events. The combination of both shows no large improvement compared to DF.

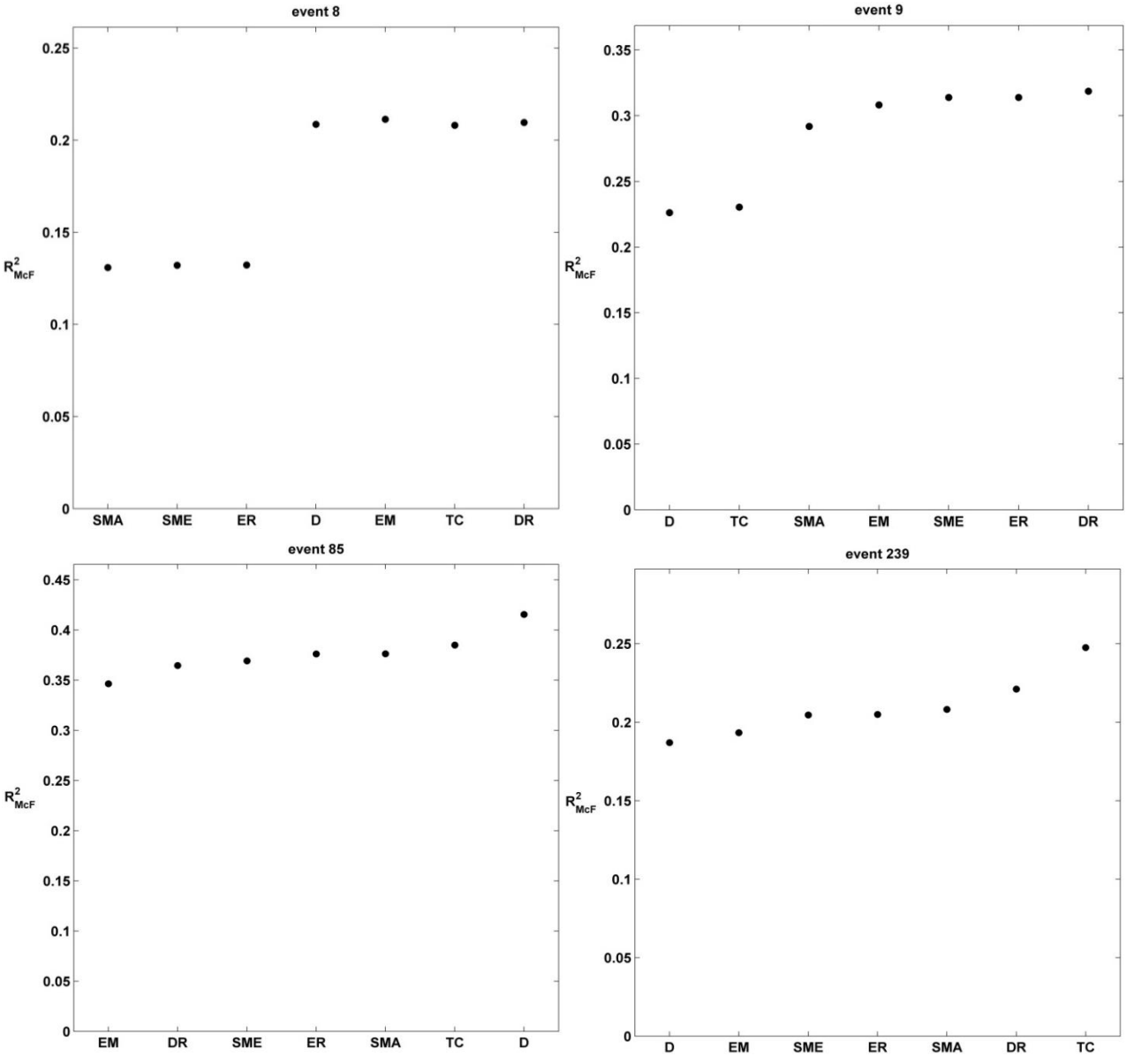

Figure 28: Plots showing the contribution (expressed as Mc Fadden's Pseudo R² (R^2_{McF}, section 2.4.4) of different predictor variables for predicting landslide occurrence of the full model compared to the null model, for a selection of events. Variables indicated on the x-axis have to be read from left to right, indicating which variable is added to the model taking into account all previous variables as well. The sequence was determined by the likelihood ratio (lr), each time adding the variable with the highest lr based on the univariate logistic regression analysis of each event individually. For event ID's see Table 5 (own processing).

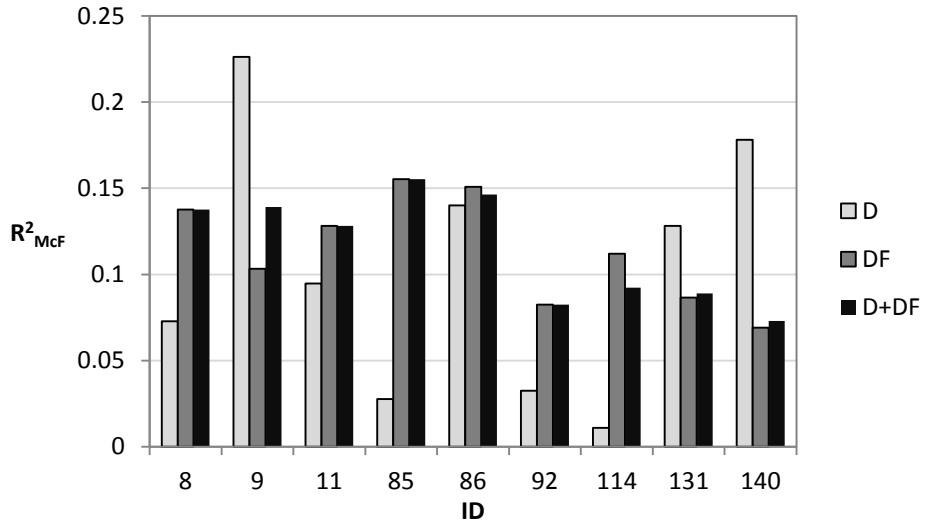

Figure 29: Comparison of Mc Fadden's Pseudo R² (R^2_{McF} , section 2.4.4) between models taking into account distance to the epicenter (D), distance to faults (DF) or their combination. The analysis is performed for events with mapped main faults on the published landslide inventory maps (Table 5, own processing).

3.3.3 Construction of a spatially distributed landslide model based on integrated landslide inventories

Previous analyses demonstrated that *D, SME and SMA* are the most important predictor variables (section 3.3.2). Together with the additional variables (M_w, FD, DS), which only become relevant when different earthquake events are considered, this results in 12 variable combinations that should be tested. Figure 30 shows the calibration and validation results of the Monte Carlo simulations for the three different subset selection procedures (SSP) 'fixed', 'fraction' and 'root' (explained in section 2.4.5) for these 12 different variable combinations.

A first general finding is that, validation performance is very similar to the calibration performance. Overall, highest $\mathrm{R}^2_{\mathrm{McF}}$ are found for the 'fraction' SSP, with lower values for the 'root' SSP and lowest values for the 'fixed amount' approach. Regarding the parameter combinations, models with the standardized distance (i.e. DS instead of D), score markedly better. Likewise, models with Mw score better than models where the earthquake magnitude is not explicitly included. Depending on the subset selection procedure used, models with focal depth (FD) give better or worse results than models without. Furthermore, maximum slope (SMA) generally leads to somewhat better model performances than mean slope (SME).

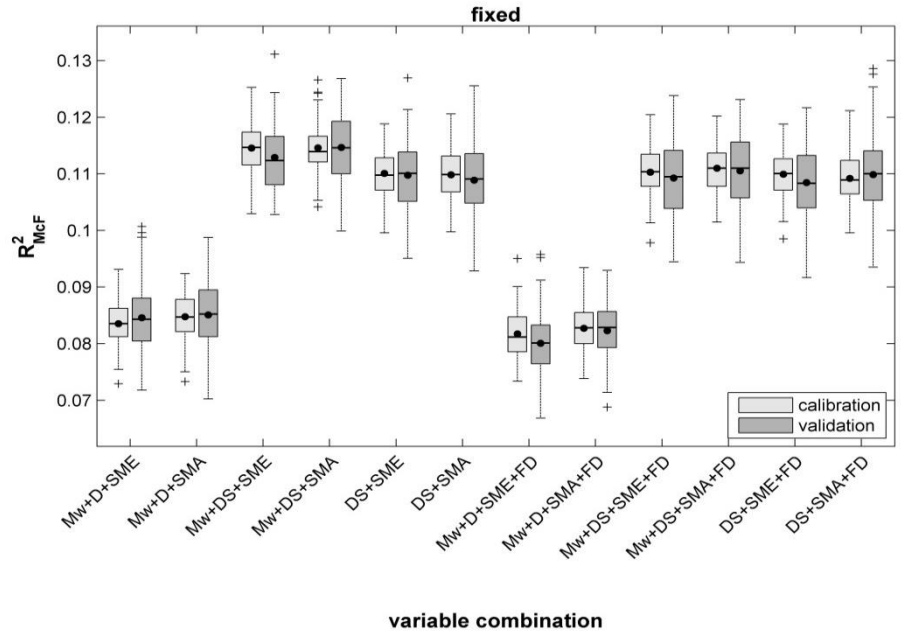
fixed
R^2_{McF}
0.13
0.12
0.11
0.1
0.09
0.08
0.07
calibration
validation
Mw+D+SME
Mw+D+SMA
Mw+DS+SME
Mw+DS+SMA
DS+SME
DS+SMA
Mw+D+SME+FD
Mw+D+SMA+FD
Mw+DS+SME+FD
Mw+DS+SMA+FD
DS+SME+FD
DS+SMA+FD
variable combination

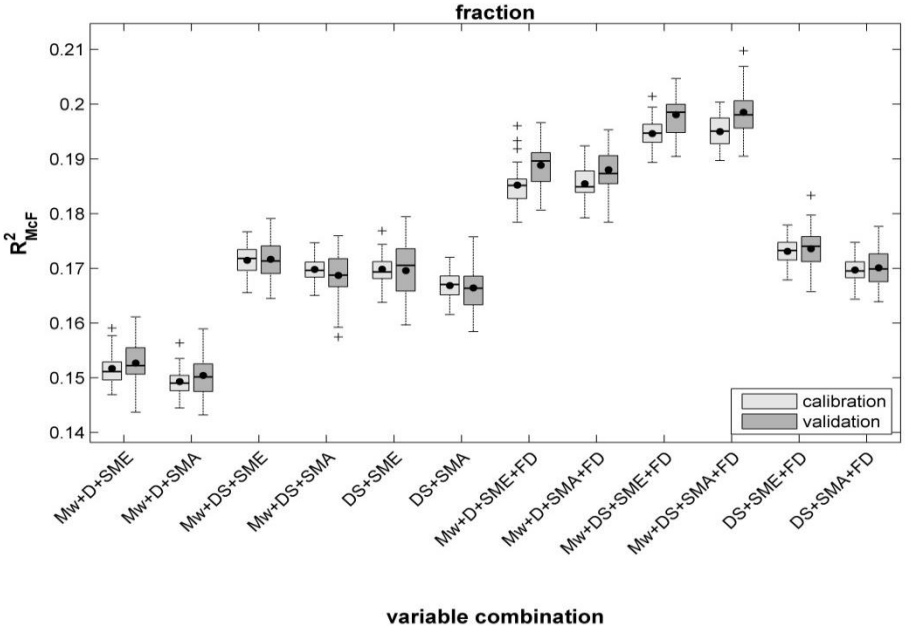
fraction
R^2_{McF}
0.21
0.2
0.19
0.18
0.17
0.16
0.15
0.14
calibration
validation
Mw+D+SME
Mw+D+SMA
Mw+DS+SME
Mw+DS+SMA
DS+SME
DS+SMA
Mw+D+SME+FD
Mw+D+SMA+FD
Mw+DS+SME+FD
Mw+DS+SMA+FD
DS+SME+FD
DS+SMA+FD
variable combination

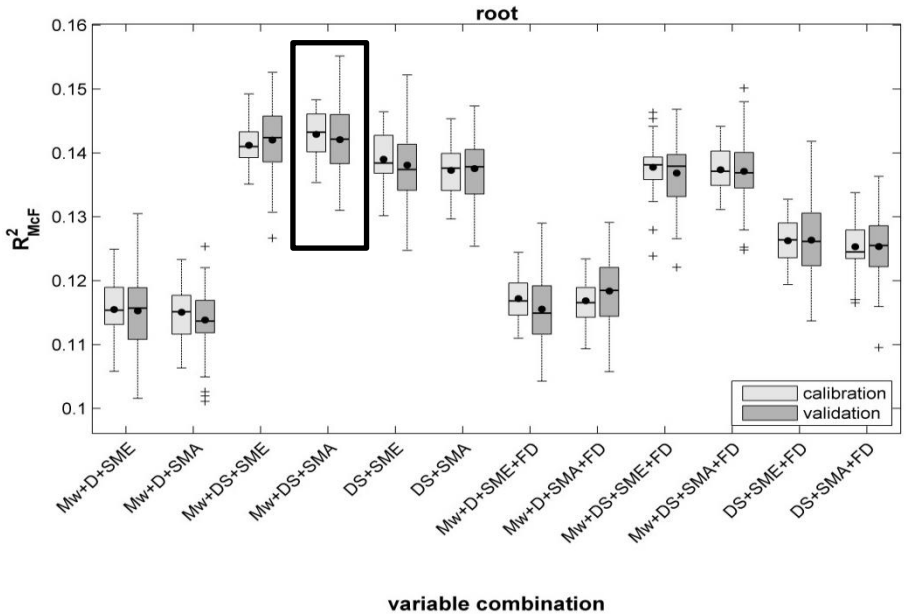
root
R^2_{McF}
0.16
0.15
0.14
0.13
0.12
0.11
0.1
calibration
validation
Mw+D+SME
Mw+D+SMA
Mw+DS+SME
Mw+DS+SMA
DS+SME
DS+SMA
Mw+D+SME+FD
Mw+D+SMA+FD
Mw+DS+SME+FD
Mw+DS+SMA+FD
DS+SME+FD
DS+SMA+FD
variable combination

Figure 30: Boxplot charts displaying the contribution (expressed as Mc Fadden's Pseudo R²: R^2_{McF}, section 2.4.4) of the full model relative to the null model of different predictor variable combinations. Boxplots are based on 100 iterations for the 'fixed amount' subset selection procedure (SSP) and on 50 iterations for the 'fraction' and 'root' SSP (see section 2.4.5). The different predictor variables are the following: moment magnitude (M_w), distance to the epicenter (D), standardized distance to the epicenter (DS), mean slope (SME), maximum slope (SMA) and focal depth (FD). Dots inside the boxplots indicate the mean. The black rectangle indicates the eventual selected model setup (Table 5, own processing).

Based on the results shown in Figure 30, the *eventual model set up* was selected: i.e. the *'root' procedure with variable combination: M_w, DS and SMA* (indicated in Figure 30 by the rectangle). To obtain a representative set of final model coefficients, additional Monte Carlo simulations with 101 iterations were carried out. This resulted in 101 coefficient sets that give an idea of the coefficient range for each predictor variable. Boxplots of these coefficients are shown in Figure 31.

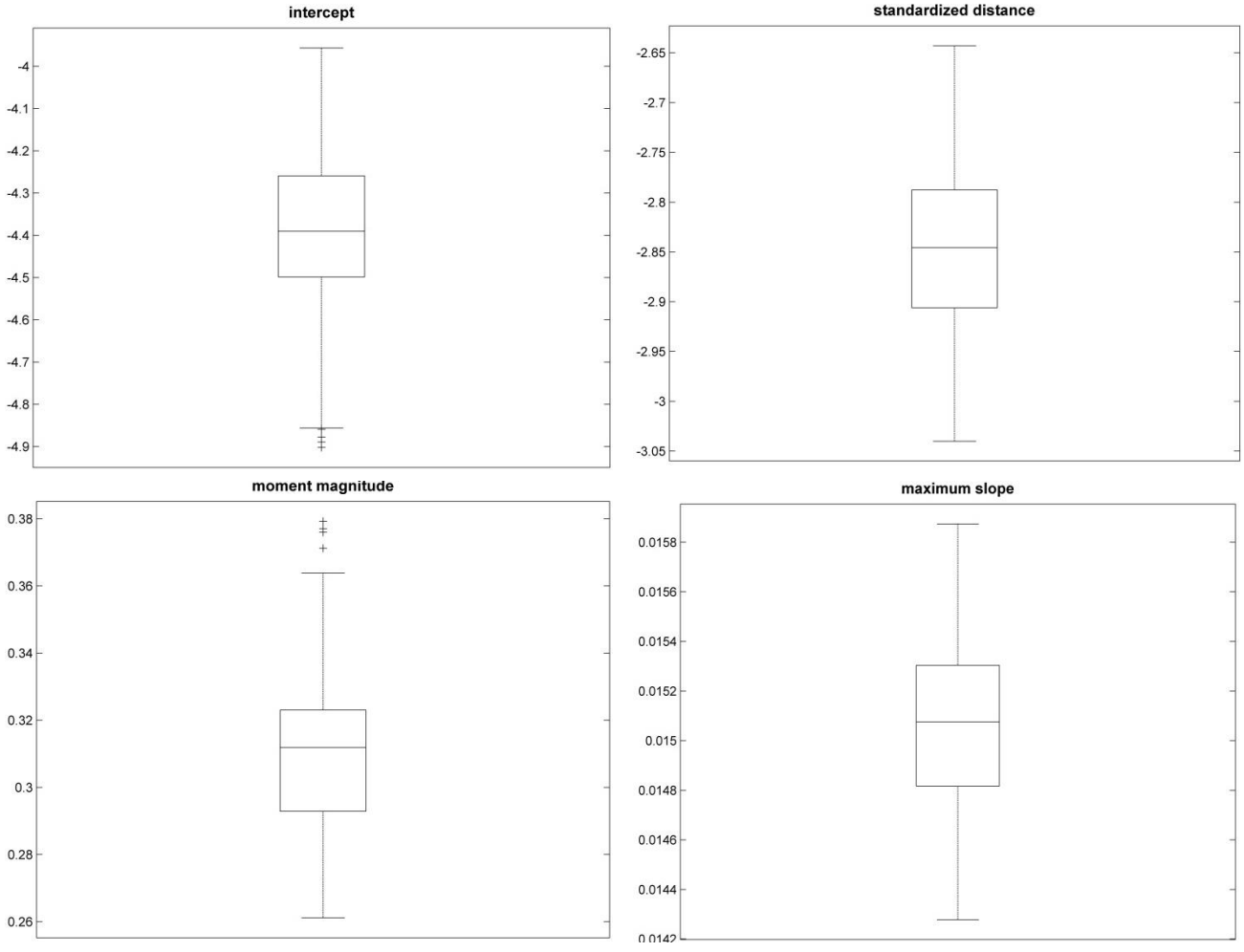

Figure 31: Boxplots displaying the range in coefficients (n = 101) for the variables taken into account in the landslide distribution model (equation 18) (Table 5, own processing).

To determine the most important predictor variable, univariate Monte Carlo simulations were carried out for the model variables M_w, DS and SMA. The calculated R^2_{McF} indicate that DS is the most important predictor variable for the model. It is the median coefficient of this variable together with the corresponding coefficients for the other variables that is used as the central coefficient set for the LD model. The resulting logistic regression equation is the following (own processing):

$$p(y=1) = \frac{1}{1+e^{-(-4.23-2.85*DS+0.28*M_W+0.0156*\mathrm{SMA})}} \quad (18)$$

Figure 32 shows two boxplot charts, where the variable combination M_w, DS and SMA are tested for the *impact* of excluding each time one of the 25 landslide inventories from the calibration, for respectively the 'fraction' and 'root' SSP. Overall the deviations from the average R^2_{McF} are small, with some larger deviations (especially for the 'fraction' SSP) for events 8, 11, 85, 91 and 130.

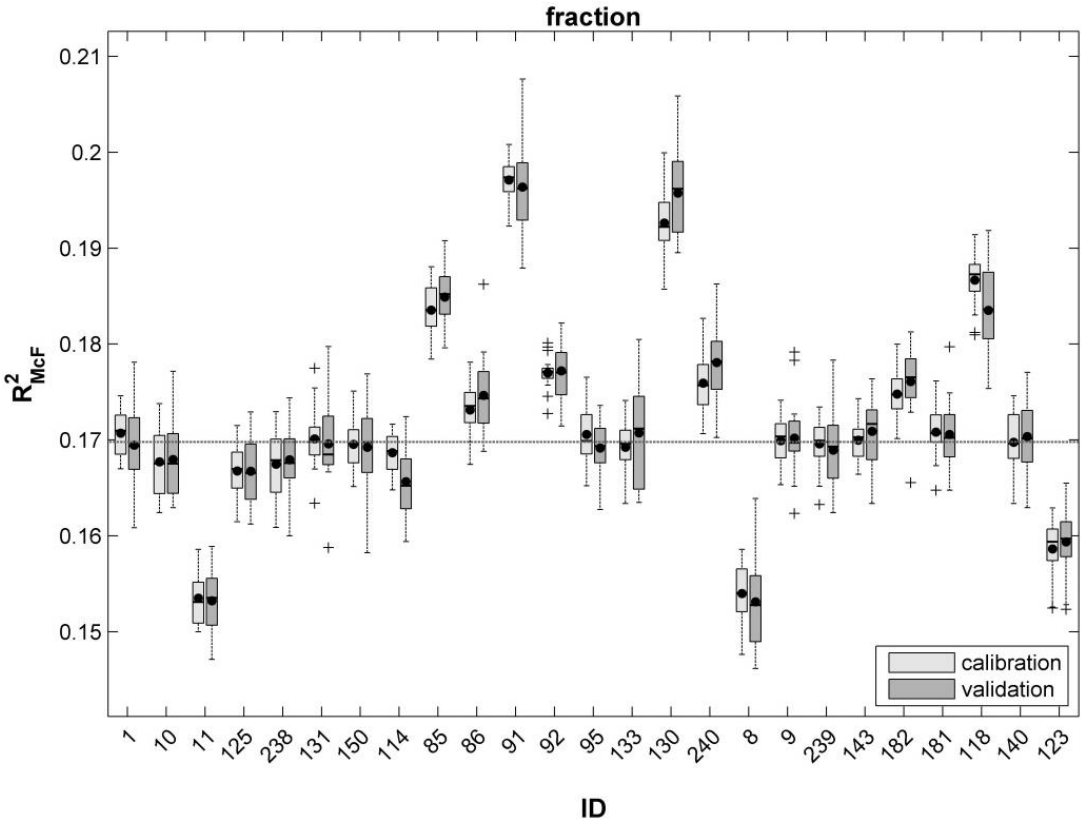

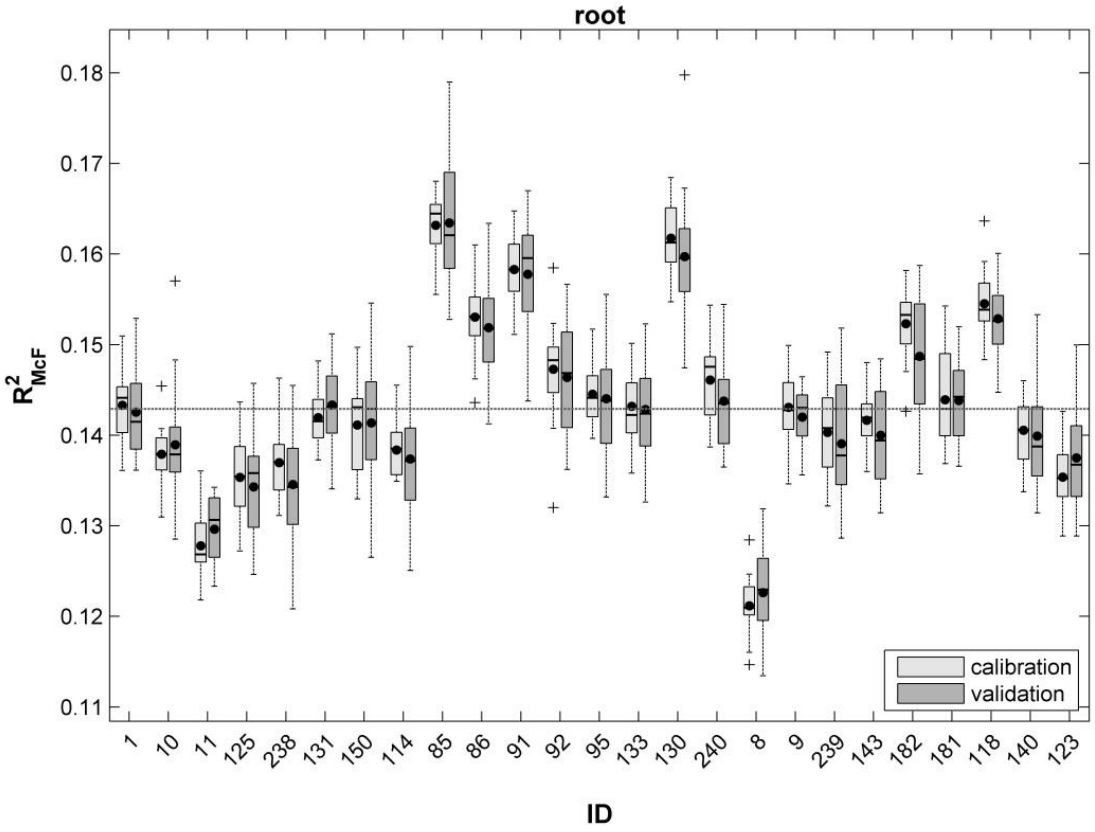

Figure 32: Boxplot charts to test for the impact of specific events, by iteratively leaving out 1 of the 25 landslide inventories. Two different subset selection procedures (SSP): 'fraction' and 'root' (section 2.4.5) are displayed for both calibration and validation datasets. On the x-axis the ID's of the event not taken into account are displayed (Table 5). The variable combination for this simulation is the combination of moment magnitude (M_w) with standardized distance to the epicenter (DS) and with maximum slope (SMA). Each boxplot is based on 20 iterations for both SSP, with dots in the boxplots indicating the mean. The reference line indicates the mean R^2_{McF} of the corresponding procedures and variable combination in Figure 30, with respectively values of 0.1698 and 0.1429 for the 'fraction' and 'root' SSP (Table 5, own processing).

3.3.4 Application and validation of the landslide distribution model

Figure 33 shows two of the resulting probability maps for two selected events (event 85: Luhuo: China, 1973, M_w 7.6 and event 181: Mammoth Lakes: United States, 1980, M_w 6.2). For comparison also the originally mapped landslide distribution is indicated. These two figures illustrate two clearly contrasting examples of the performance of our model (equation 18): spatial patterns are generally badly predicted for event 85, while the model performs well for event 181. The remaining 23 probability maps are shown in appendix.

Visual interpretation of all maps shows that the model scores well to very well for most events. Only for events 91, 92 and 114 poorer results are obtained and for event 85 the model scores badly. Figure 34 shows ROC curves for events 85 and 181. It is again clear that the model scores bad (ROC value < 0.5) for event 85 and very good (ROC value > 0.9) for event 181. The ROC values for all other events are also displayed, only for event 85, a value smaller than 0.5 is obtained.

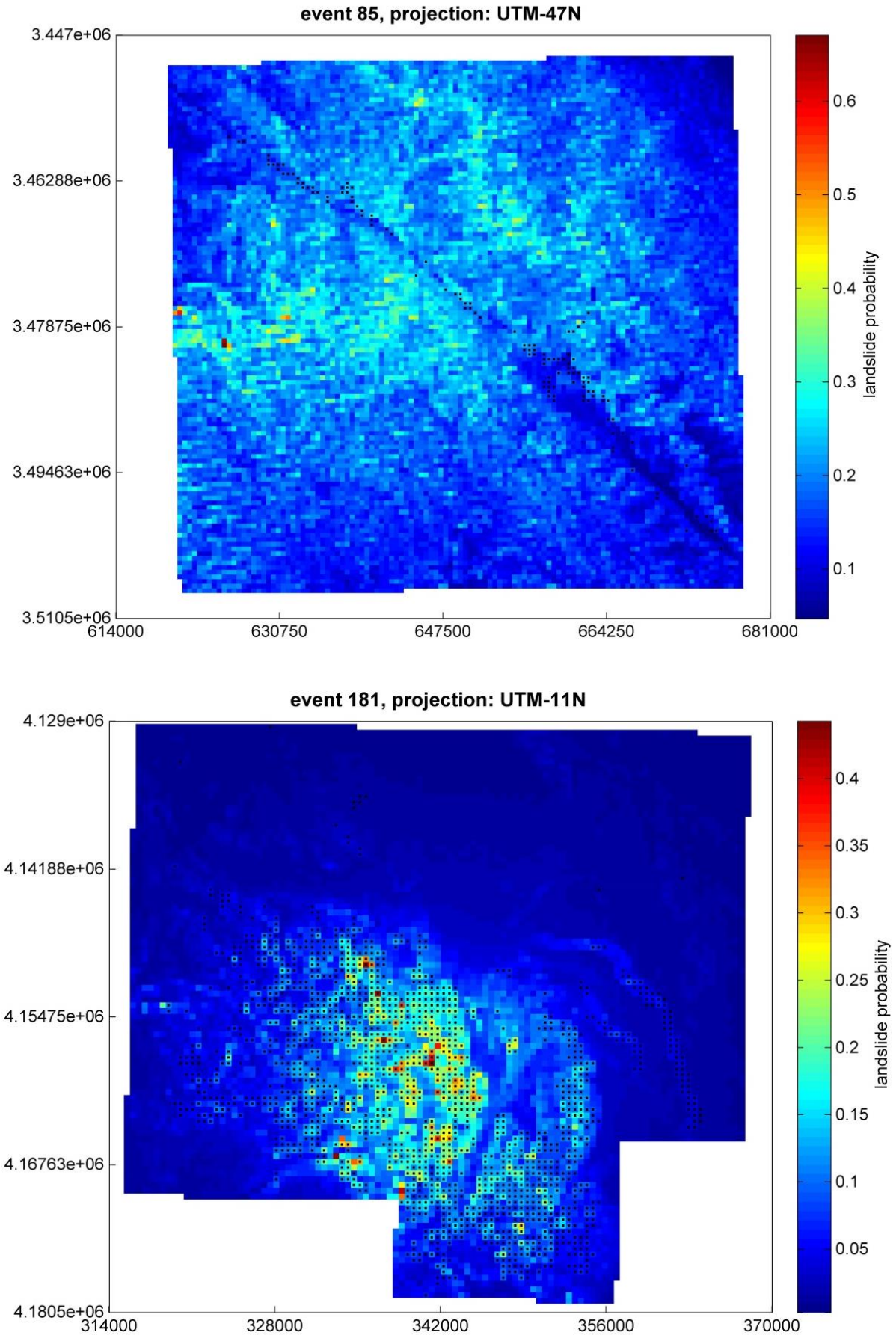

Figure 33: Landslide probability maps for event 85 and 181 (for ID's see Table 5). Mapped landslides are indicated by black dots, coordinates are in the UTM projection (Table 5, own processing).

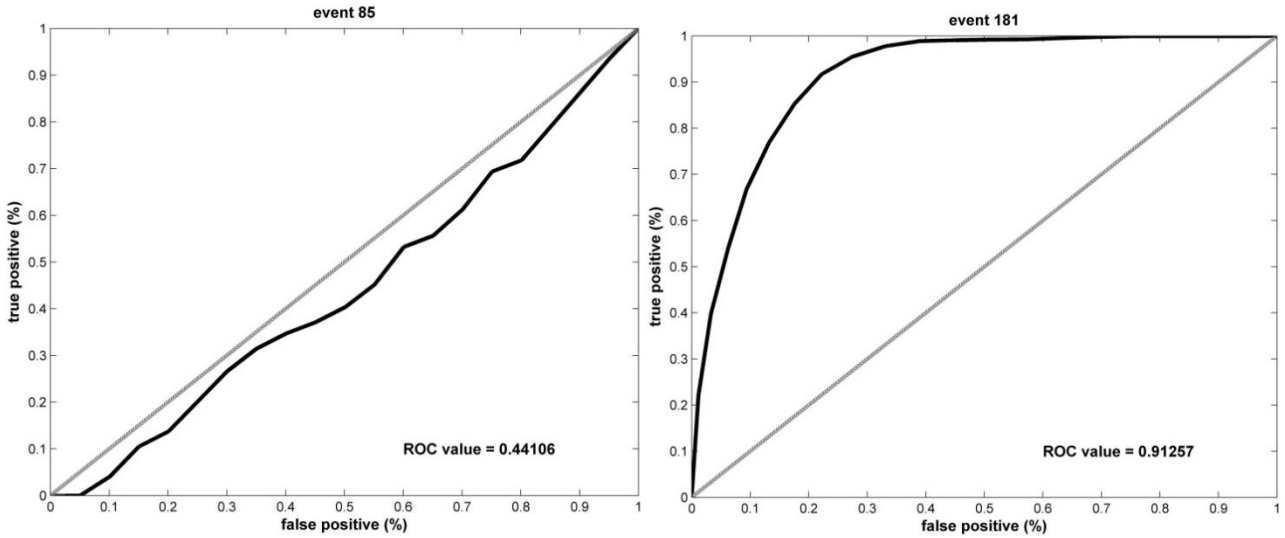

ID	1	8	9	10	11	85	86	91	92	95	114	118	123
ROC	0.86	0.80	0.86	0.83	0.82	0.44	0.76	0.74	0.71	0.75	0.65	0.79	0.80
ID	125	130	131	133	140	143	150	181	182	238	239	240	
ROC	0.80	0.78	0.75	0.73	0.83	0.82	0.83	0.91	0.62	0.86	0.83	0.82	

Figure 34: Relative operating characteristic (ROC) curves for event 85 and 181 (for ID's see Table 5), based on summed probabilities of 100 iterations with each time randomly selecting 1 of the 101 coefficient sets and with the 1:1 reference line indicated in grey corresponding with a ROC value of 0.5. ROC values for all events are shown in the table (Table 5, own processing).

3.4 The integrated spatially distributed landslide volume model

3.4.1 Predicting landslide numbers based on the distribution model

As explained in section 2.5.1, the LD model can be used to *predict landslide numbers (LN)* based on the simulated total probability sum (PS). Figure 35 shows the resulting relation between the modeled total landslide number (LN_m) and the reported or derived LN. The model equation is the following:

$$\boldsymbol{LN = 2.57 * PS^{0.82}} \qquad \text{(Appendix 1, own processing)} \qquad (19)$$

The model can explain about 59% of the variation in LN and seems robust with no deviating trend towards low or high landslide numbers. Only 9 LN_m deviate more than an order of magnitude from LN, with the largest deviation for event 85.

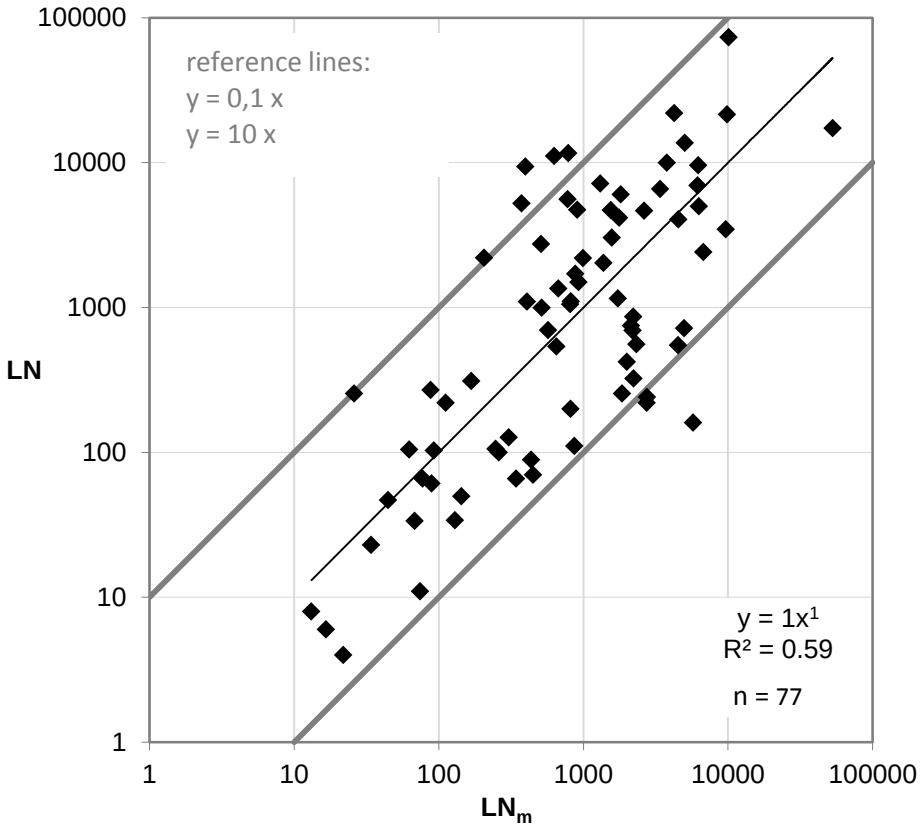

Figure 35: Relation between the modeled total landslide number (LN_m) and the reported or derived total landslide number (LN) (equation 19). PS is the total probability sum, calculated via the LD model (equation 19) (Appendix 1, own processing).

3.4.2 Model application and comparison with available inventories

The integrated model was applied to the 23 events that are both included in the LN model (Appendix 1) and the LD model (Table 5). These are all events from the LD model except for event 11 and event 240, for which no reliable LN was found. Simulations for each event were based on 100 iterations and the assigned LN and LV were summed for each pixel over these 100 iterations.

As a means of validation for the correctness of the simulated LN and LV, a comparison of the model landslide number (LN_m) (equation 19) and model landslide volume (LV_m) (the model equation for predicting LV based on PS is not used in the integrated model and is therefore not further discussed in this thesis, but is analogue to the procedure for the LN model described in section 2.5.1) is made with the simulated LV (LV_s) and the simulated LN (LN_s) (Figure 4). Such a validation is required to check whether no systematic bias in the LN_s or LV_s exists, after adding a random factor to account for the model uncertainty (section 2.5.2). Both mean and median values of the 100 simulations for each event are plotted. It can be observed that mean values are systematically higher compared to the median values of the simulations. Besides, median LN_s and LV_s are consistent with LN_m and LV_m. Finally, it can also be observed that the deviation between mean LV_s and LV_m is relatively larger than the deviation between mean LN_s and LN_m.

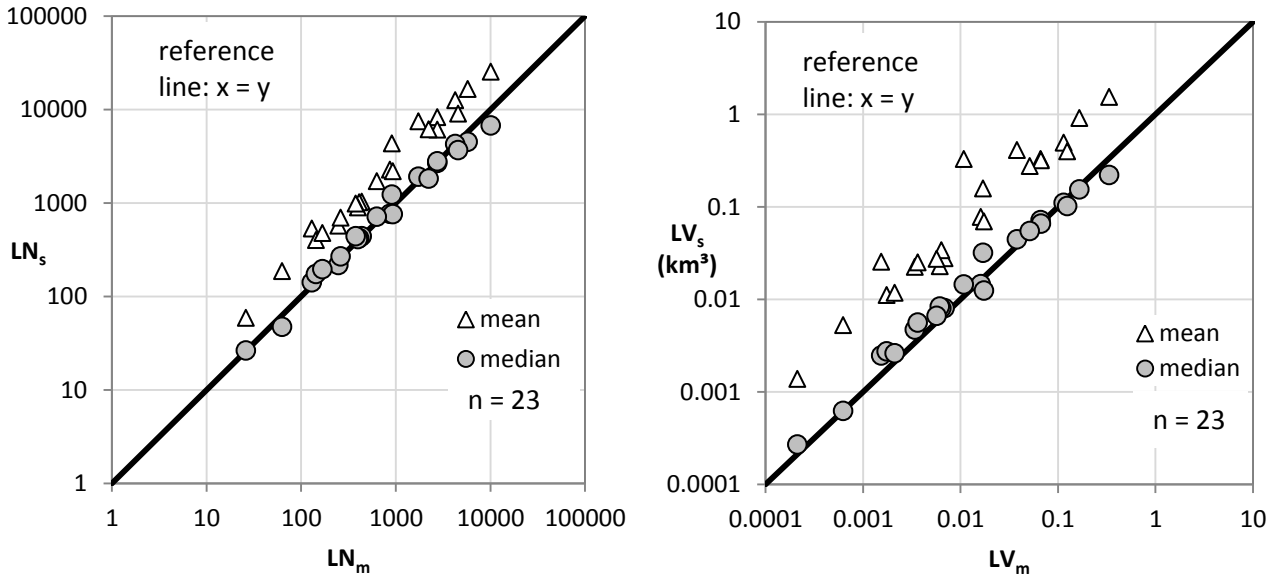

Figure 36: (left) Comparison of the total landslide number predicted by the LN model (equation 19, LN_m) with the mean and median values of the simulated LN (LN_s). (right) Comparison of the total landslide volume predicted by a LV model based on the probability sum (PS) (the model equation for predicting this LV based on PS is not used in the integrated model and is therefore not discussed in this thesis, but is analogue to the procedure for the LN model described in section 2.5.1) with the mean and median values of the simulated LV (LV_s). Mean and median values are based on 100 iterations of the integrated model for each event (Table 5 and Appendix 1, own processing).

To allow for a comparison with event 181 in Figure 33, the simulation results for this event are shown in Figure 37. Presenting as well the maps with cumulatively added LN_s and LV_s for 100 iterations as a possible landslide and volume induced pattern for one iteration. For the cumulative maps a clear pattern corresponding to the probability map in Figure 33 arises, with especially for the LN_s a clear correspondence. Obviously the pattern contains more scatter for a single iteration, but still higher concentration of LN_s and larger LV_s can be observed in the high probability zones. The simulation statistics in the table confirm the larger mean values than median values, show the very large range between minimum and maximum values and also indicate the more moderate range for 50% of the simulations between the 25th percentile (Q25) and 75th percentile (Q75).

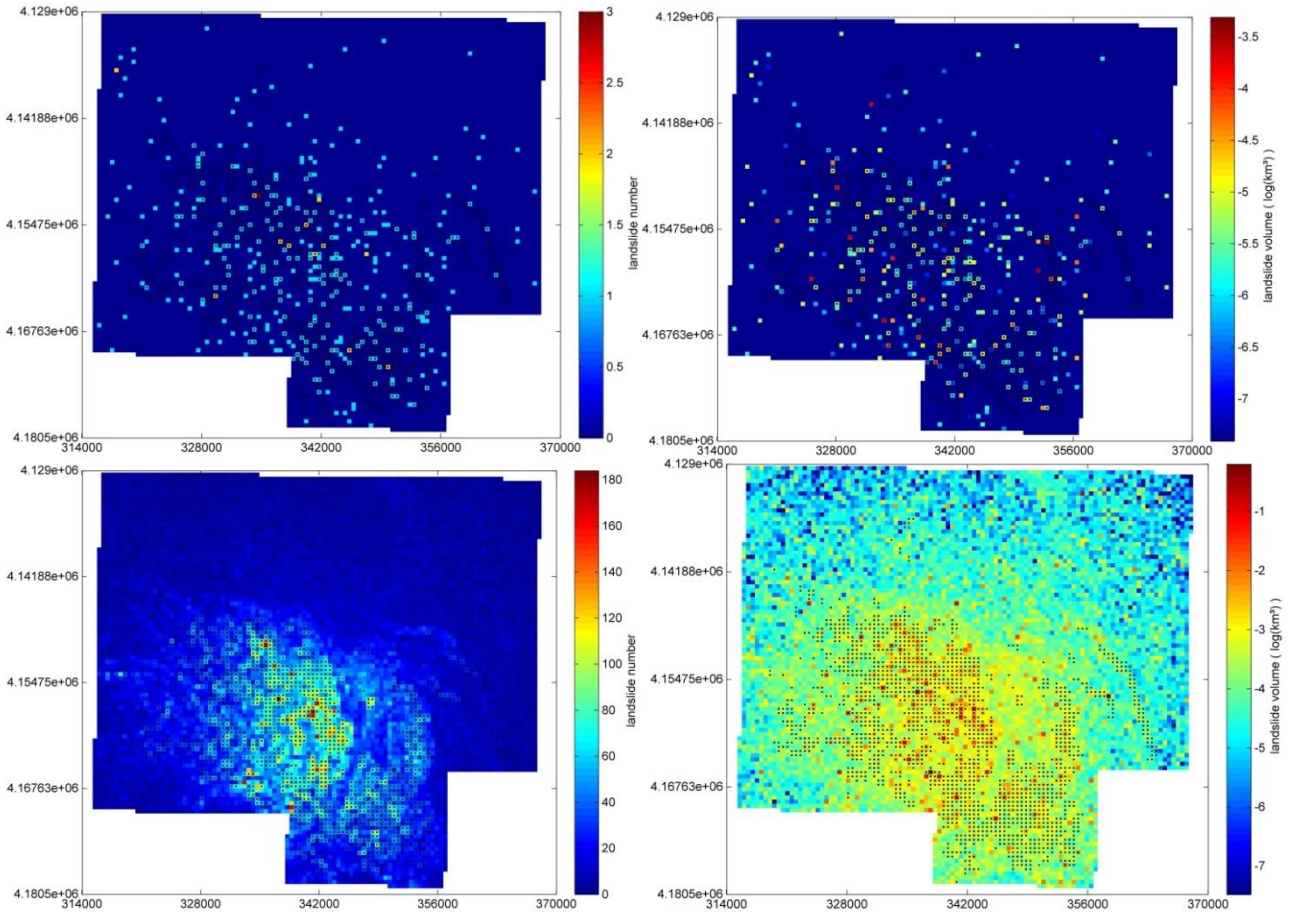

	reported	mean	median	minimum	maximum	Q25	Q75
LN	5253	1.74E+03	349	9	72186	114	892
LV (km³)	0.012	0.0689	0.0075	4.97E-05	3.7736	0.002	0.0229

Figure 37: Model simulations for event 181, with cumulative number (left) and volume (right) maps for 1 iteration on top and 100 iterations in the bottom maps. The selected iteration is the iteration with LN_s closest to the median LN_s of the 100 iterations. Mapped landslides are indicated by the black dots and axes values specify the UTM-11N coordinates. Statistical properties of the simulation are shown in the bottom of the figure, with Q25 the 25th percentile and Q75 the 75th percentile (Table 5, own processing).

A general evaluation of the model is provided by means of the Kappa index of agreement for location (K_l) in Figure 38 and by an error budget in Figure 39. All events, except for event 85, have positive median and mean K_l values. For all events, larger mean than median values can be observed. Figure 39 shows that most events have more than 50% of the pixels correctly classified, although large differences between individual events can be observed. For most events disagreement due to quantity is larger than disagreement due to location. This means that a wrong classification of individual pixels is mostly caused by errors in the landslide quantity assessment rather than due to a wrong spatial allocation of these landslides.

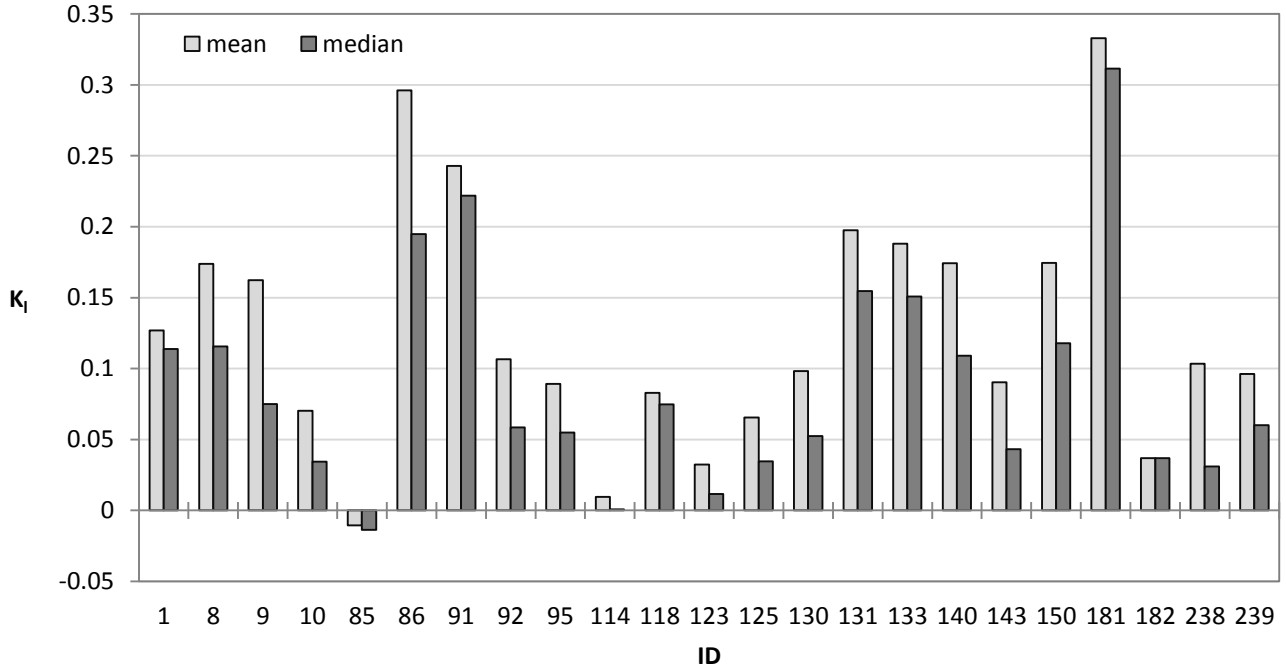

Figure 38: Mean and median values of the kappa index of agreement for location (K_I, equation 16). Mean and median values are calculated from 100 simulations carried out for each event (Table 5, own processing).

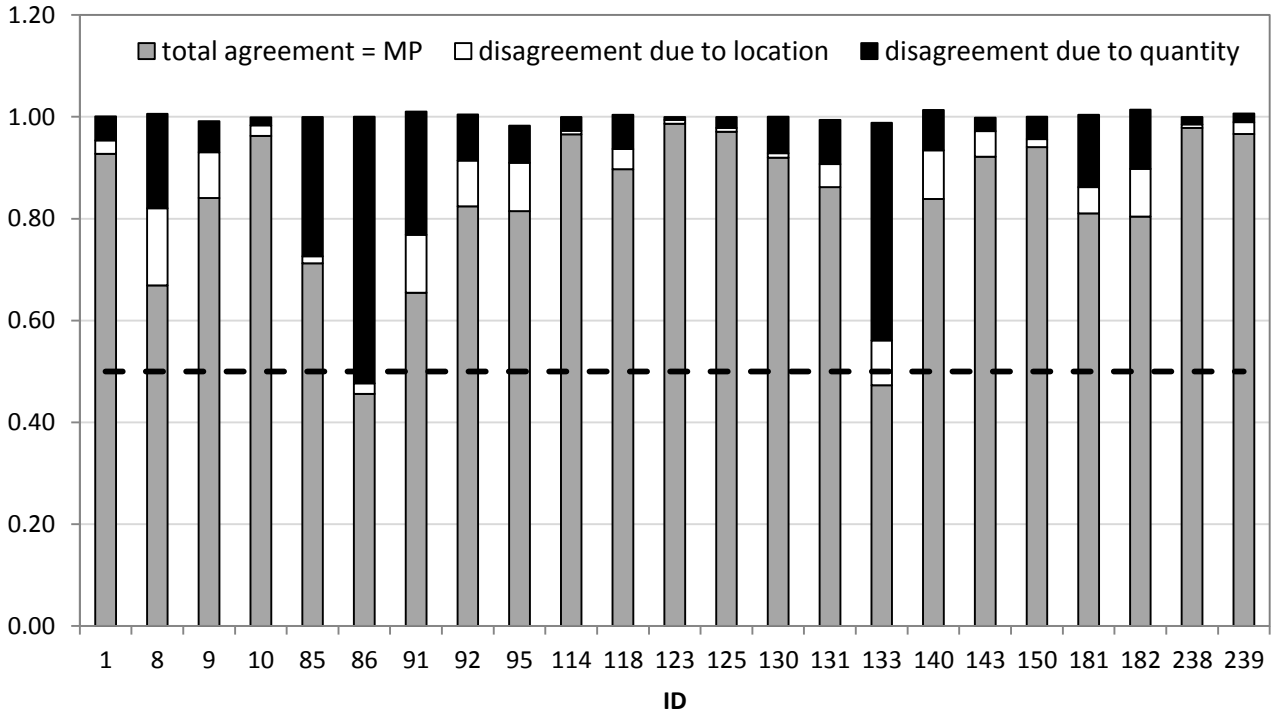

Figure 39: Error budget of the simulated earthquake-induced landslide maps based on 100 simulations for each event. Plotted agreement and disagreement values are the median values of all simulations. The total agreement or model performance (MP) is the fraction of correctly simulated pixels, compared to the mapped pattern. Disagreement due to location is the disagreement that can be attributed to wrong landslide allocation, and disagreement due to quantity can be attributed to a wrong landslide number prediction. The dashed line indicates the 0.5 threshold as a reference for a random model with no information on quantity and location (Table 5, own processing).

3.5 Model application and comparison with sediment yield

Simulation results for the Siret catchment are displayed in Figure 40. On the left, *annual average landslide volumes* of all earthquakes (with magnitude larger than or equal to four) of the considered period (section 2.6.2) are displayed. On the right, *average landslide volumes* for the 1977 earthquake (M_w 7.4) are shown. A clear pattern is observed with highest annual average volumes in the region with largest seismic activity (Figure 11), and much smaller volumes outside this region. For the 1977 earthquake this pattern is less pronounced. A comparison between both maps learns that the 1977 event generated larger volumes than the annual average for parts of the area outside the region of highest seismicity.

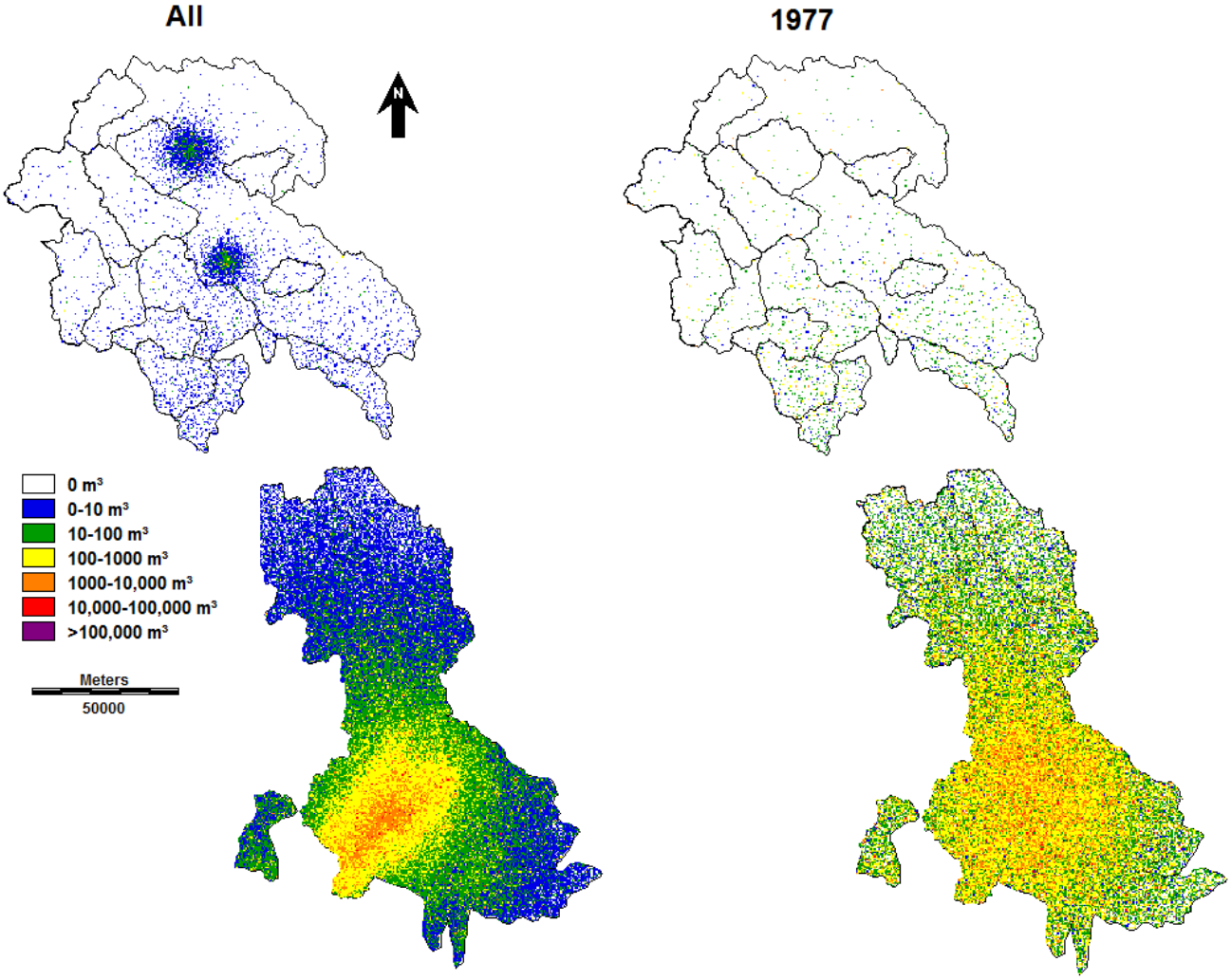

Figure 40: Simulated landslide volumes in the Siret basin for 292 earthquakes in the period 1965 till April 2014 (left) and for the 1977 earthquake (right). Volumes for all events are yearly averages based on 50 simulations of all 292 events, the volumes for the 1977 event are the average of 50 simulations for this event (own processing).

The simulated landslide volumes were converted to annual catchment weighted landslide masses (LM, t/km²/y) for all events and to catchment weighted landslide masses (LM, t/km²) for the 1977 event, to allow for a better comparison with the SY. A dry bulk density of 1.8 g/cm³ was assumed. Figure 41 presents resulting correlations with the average

annual SY (Table 3), expected PGA (Table 4), average slope (Table 4) and average catchment distance to the center of highest seismicity in the Vrancea region (Dc). The center of highest seismicity was arbitrarily determined as the most central earthquake epicenter (45.658°N, 26.527°E) in this region. However, to illustrate that LM decreases with increasing Dc, it is not important if the real center would slightly deviate from this location.

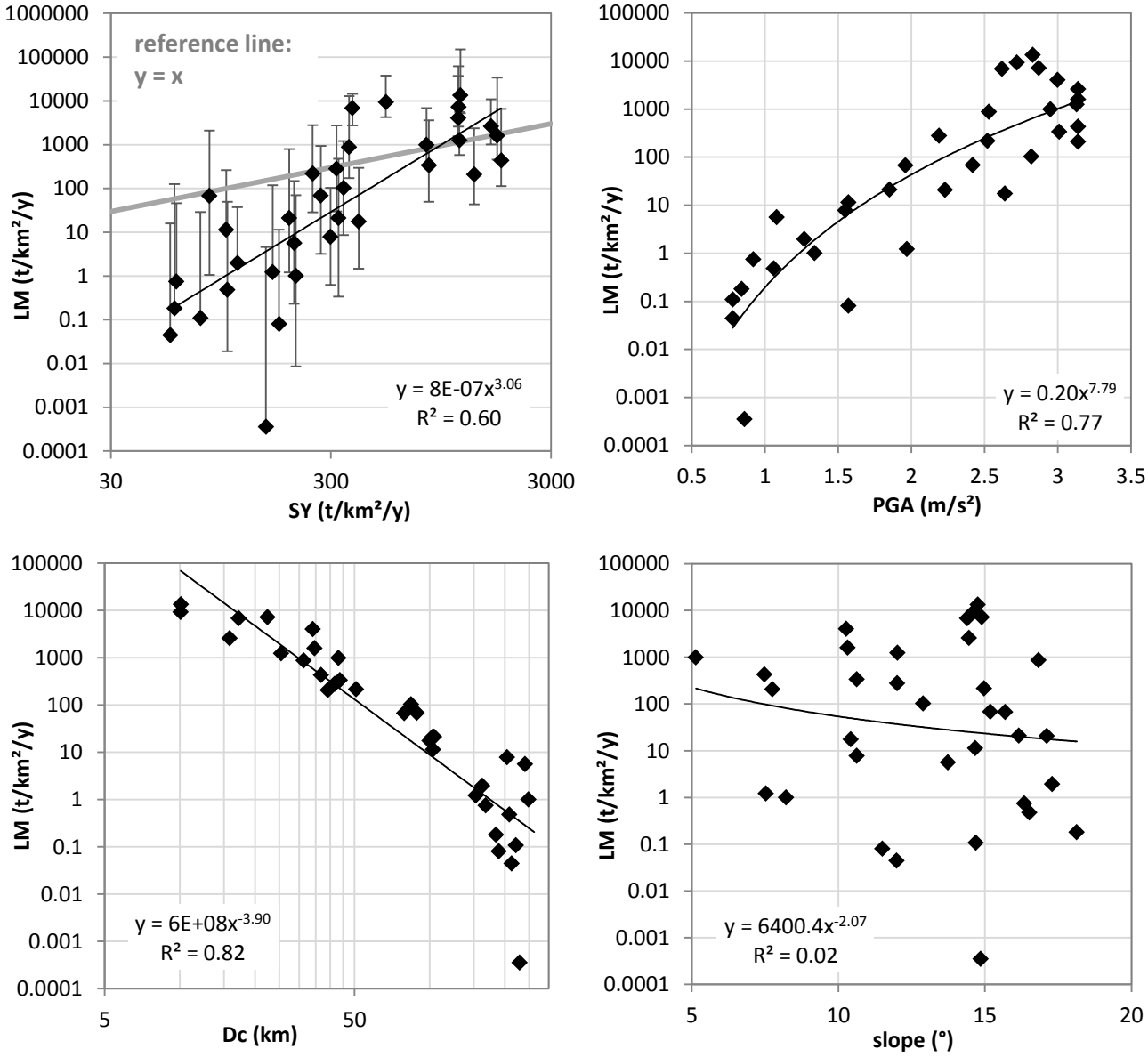

Figure 41: Scatter plots of simulated median (50 iterations) annual landslide masses (LM) per catchment in the Siret basin (n = 34) for 292 earthquakes in the period 1965 till April 2014 (section 2.6.2) and other catchment characteristics. (upper left) average annual sediment yield (SY), (upper right) expected peak ground acceleration with a recurrence interval of 100 years (PGA), (lower left) average catchment distance to the center of highest seismicity in the Vrancea region (Dc, Figure 11)) and (lower right) average slope (S). Error bars indicate the 5th-95th percentile (Q5-Q95) interval of the simulations. Four catchments with median landslide volumes being zero were discarded from the analysis (Nr.: 1, 2, 8, 13: see Table 3) because these cannot be displayed on a log scale. For the same reason Q5 could not always be displayed. (Table 3 and Table 4, own processing).

All but the correlation with the average slope are significant on the 0.01 significance level. SY and PGA show strong positive correlations with LM and Dc shows a strong negative correlation. Although a clear positive relationship between LM and SY is observed, the reference line shows that LM is lower than SY for small LM and larger than or equal to SY for high LM. A comparison with Figure 42 learns that the landslide mass generated by the 1977 earthquake is for more of these catchments larger than the average annual SY. This confirms the observations in Figure 40. However, error bars also show that the uncertainty on the landslide masses for the 1977 event is larger than the uncertainty on annual average LM for all events, especially for larger LM.

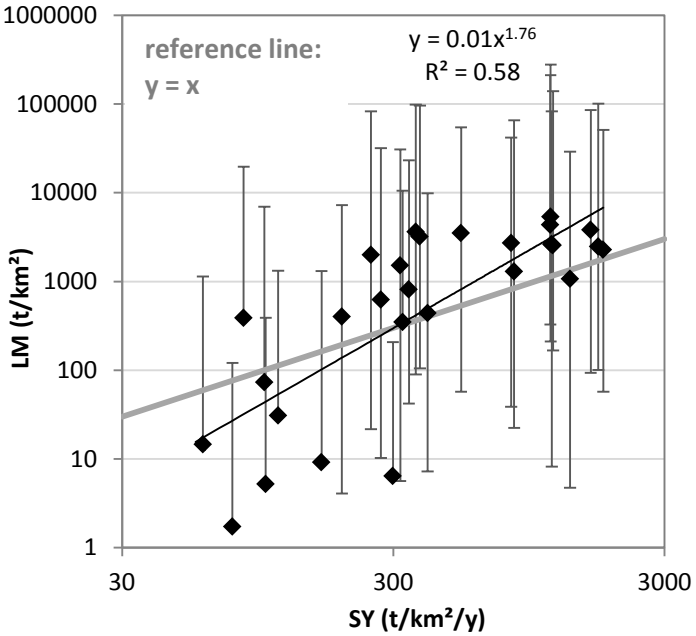

Figure 42: Scatter plot of the simulated median (50 iterations) landslide masses (LM) per catchment in the Siret basin (n = 28) for the 1977 earthquake and the average annual sediment yield (SY). Error bars indicate the 5th-95th percentile (Q5-Q95) interval of the simulations. 10 catchments with median landslide volumes being zero were discarded from the analysis because these cannot be displayed on a log scale. For the same reason Q5 could not always be displayed (Table 3, own processing).

Figure 43 displays the median landslide mass per catchment for both the 1977 earthquake and all considered earthquakes in the region. Additionally the fraction of the generated LM by the 1977 event as a part of the LM generated by all earthquakes is shown. It can be observed that in absolute terms LM decreases with increasing Dc for both the 1977 event and all events together. On the other hand the fraction of the 1977 event as part of the LM of all events increases with increasing Dc. In this way the 1977 event contributes only little to the total LM of all events in catchments in the central area, whereas for catchments further from this center it often contributes largely. The median fraction for all catchments together is 2.1% with a Q5-Q95 range of: 0.1-40.2%. Finally, it was calculated that median simulated landslide masses (dry bulk density 1.8 g/cm³) amount to 1.44E+09 ton (Q5 - Q95: 6.48E+08 – 6E+09) and 6.41E+07 ton (Q5 – Q95: 5.58E+06 – 1.73E+09) for

respectively all events and for the 1977 event (for this purpose also simulated landslides outside the Siret basin were considered).

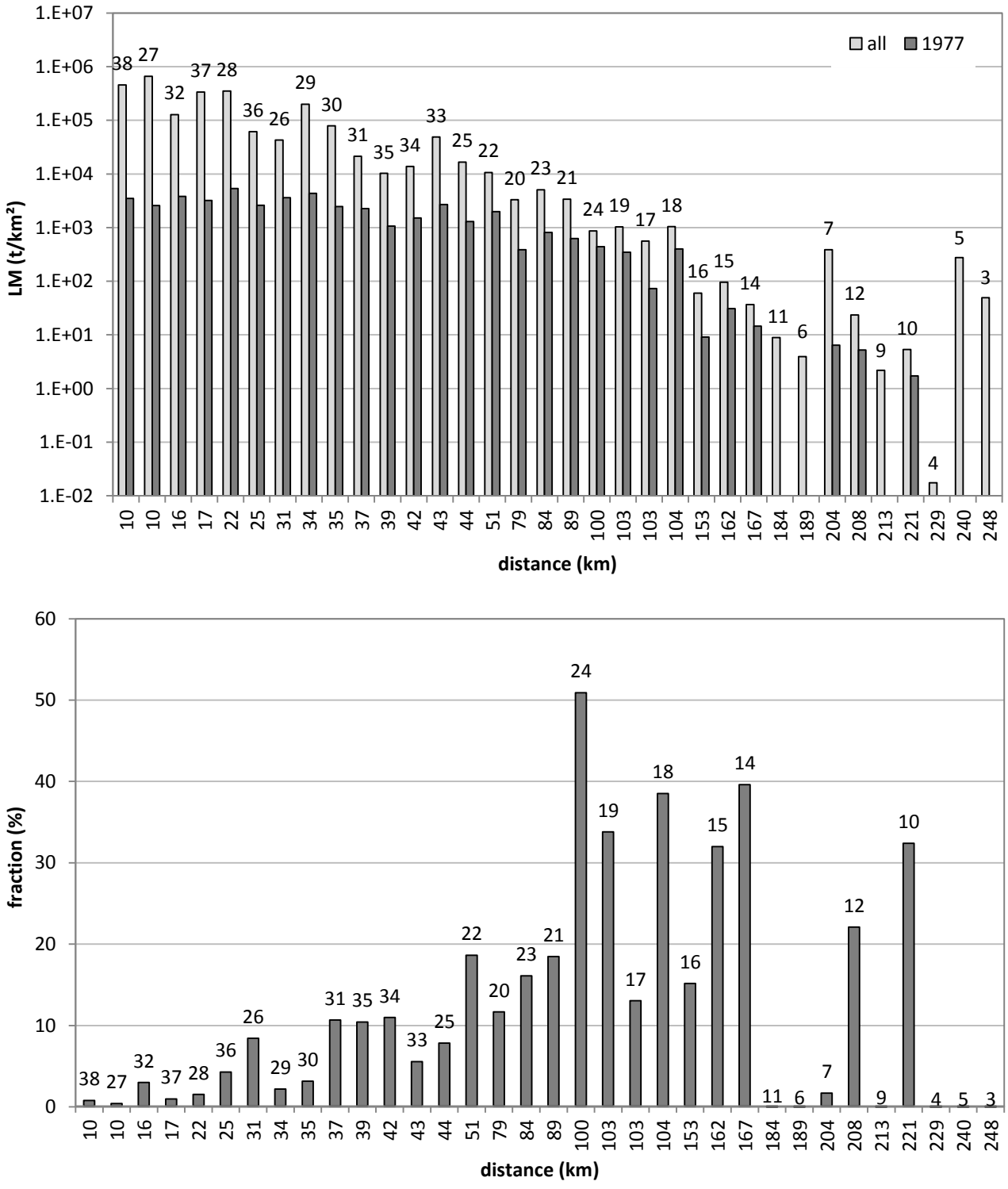

Figure 43: (top) Simulated median (50 iterations) landslide masses per catchment (LM) (n = 34) for all considered earthquakes together (All, section 2.6.2), and for the 1977 earthquake separately (1977). (bottom) Fraction of LM generated by all earthquakes, induced by the 1977 earthquake. Catchments are ordered according to distance to the center of highest seismicity in the Vrancea region (Dc, Figure 11) and catchment numbers are indicated on top of each bar (own processing).

4 Discussion

4.1 The earthquake-landslide dataset: Reliability and representativeness

A compilation of a dataset from many different sources always entrains *uncertainty* (section 2.2). Comparing different sources, selecting the most reliable data (e.g. recent or well-explained) and omitting unreliable or incomplete data resulted in a useful dataset for data extraction concerning earthquake-induced landslides.

One of the most important factors for the reliability is the *completeness of the investigated area*. The literature study revealed that many studies focused on specific areas or landslides rather than the total impact of EQ events in terms of landsliding (e.g. Barnard et al., 2001; Pan et al., 2004; Lee & Evangelista, 2006; Miyagi et al., 2011). These are often very detailed studies, but could not be used since they represent just a fraction of the landslide-affected area. On the other hand, many studies just report some information on the landslides (e.g. LN or LAA), without further explanation on how the data was acquired or an indication of the uncertainties on these values. Nonetheless, it is highly likely that most inventories are incomplete to a certain extent (Keefer, 2002). This incompleteness can be caused by technical limitations related to detecting the smallest landslides (e.g. Pisco earthquake: Peru, 2007, M_w 8.0: Lacroix et al., 2013), because of incomplete coverage of high resolution satellite imagery (Harp et al., 2011; e.g. Wenchuan earthquake: China, 2008, M_w 7.9) or because some landslides resulting from older earthquake events could no longer be detected (e.g. Irpinia earthquake, Italy, 1930, M_w 6.7). These limitations are only occasionally reported and may give a false idea of completeness. Reports concerning the Northridge earthquake (United States, 1994, M_w 6.7: Harp & Jibson, 1995; Harp & Jibson, 1996) and the Pisco earthquake (Lacroix et al., 2013) on the other hand give an assessment of these limitations. Both datasets were assessed to be very reliable. Nevertheless, they give the idea that smaller landslides might be missing by reporting detection limits of respectively 1-10m across and 100m².

The previous examples illustrate that a careful consideration of the data quality is required and that one may not be misled by the absence of information on data limitations, since the most reliable investigations are often those, reporting these limitations. Besides it also indicates that reported landslide numbers and consequently also reported landslide volumes are likely to give an *underestimation* of the total landslide volume triggered by an earthquake. On the other hand, it is suggested that directly estimated landslide volumes, are overestimations of the actual triggered volumes (Vanmaercke, pers. comm.). These estimates are often based on empirical relationships between LA and LV (e.g. equation 5). However, disentangling different landslides based on aerial photography is often difficult. In this way many smaller landslides might be taken together as one large landslide,

resulting in an overestimation of the landslide depth and a consequent overestimation of the landslide volume (Vanmaercke, pers. comm.).

Figure 12 and Figure 14 give an indication of the *representativeness* of the compiled E-L dataset. A comparison with the expected PGA map (Figure 8) indicates that the most seismic active regions in the world are well represented on the map. Additionally, it shows that these events span a wide range of magnitudes (M 4.2 – 9.5).

Important is the *exceedance probability* (EP) of the events in the dataset with respect to magnitude. It is stated that the smallest magnitude for earthquakes triggering landslides is four (section 1.2.5.a). This threshold corresponds very well to the smallest events in our dataset shown in Figure 14. Even though the range in magnitude in our dataset spans the entire range of magnitudes likely to trigger landslides, we want to test if our dataset is representative for all registered earthquake events in this magnitude range. In order to do so all registered earthquakes with M larger than or equal to four were retrieved for the period 1950-2013 (NCEDC, 2013). The EP for these data is shown in Figure 44 in comparison to the EP of our dataset.

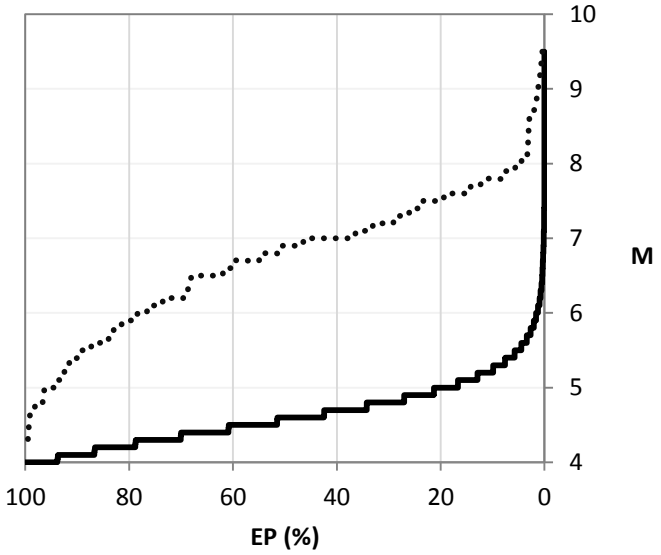

Figure 44: Exceedance probability (EP) of the magnitude for all earthquake events with magnitude larger than or equal to four for the period 1950-2013 as derived from the NCEDC database (solid line, n = 373106) and for all earthquake events in the dataset compiled in the framework of this thesis (dotted line, n = 239) (NCEDC, 2013: own processing).

There is clearly a bias towards an *overrepresentation of large events* between earthquakes in our dataset and earthquakes in general. For instance EQ events with a magnitude of seven have an EP of about 40% in our dataset, while only about 0.1% of all earthquakes with magnitude larger than four exceeds magnitude seven. This may indicate several things.

First, it indicates that previous research especially focused on large events with a vast impact. Secondly, it might also suggest that earthquakes with a certain magnitude not always trigger landslides. For instance, Jibson et al. (2006) state that the Denali earthquake (United States, 2002, M_w 7.9) triggered an exceptionally small amount of landslides. Related to this, it might also point to a bias in the location (with respect to topography) of earthquake events in our dataset. This was tested by comparing the local relief (LR) for all NCEDC earthquake epicenters (with location on land) with the local relief of the data we used in the LV model (Figure 45). The boxplots indicate that our data indeed shows a bias towards larger topographic relief. A Wilcoxon rank sum test was performed under the null hypothesis that both datasets are continuous distributions with equal medians (Beirlant et al., 2005). This null hypothesis was rejected on the 0.01 significance level. Such a bias could explain why the topographic variables (besides LR_{stdev}: section 4.2.3.d) are not significant to explain for LV after correction for the magnitude: i.e. the variation in relief for all 77 events is too small.

Thirdly, the bias in magnitudes can also point to the fact that many earthquakes that trigger landslides were not investigated. The truth will possibly be in between these explanations. On the one hand, it can be expected that some earthquakes trigger less or no landslides (e.g. Denali) and that research focusses on locations where more landslides were triggered. On the other hand, it is almost certain that EQ events in deserted places, older EQ events or rather small earthquakes may have triggered a substantial amount of landslides, which remains unstudied. As observed for the Siret basin, also these small earthquakes may significantly contribute to the total triggered landslide volume, exactly because they are so many (section 3.5). Additionally most recent inventory studies are based on satellite imagery, tracing distortions in the vegetation (e.g. Lacroix et al., 2013). This as well leads to a bias in studies, since for arid to semi-arid regions such as Turkey or Iran, it is more difficult to apply such techniques. Finally, one should also keep in mind that, a vast fraction of the earthquakes occurs offshore, limiting their impact for landsliding.

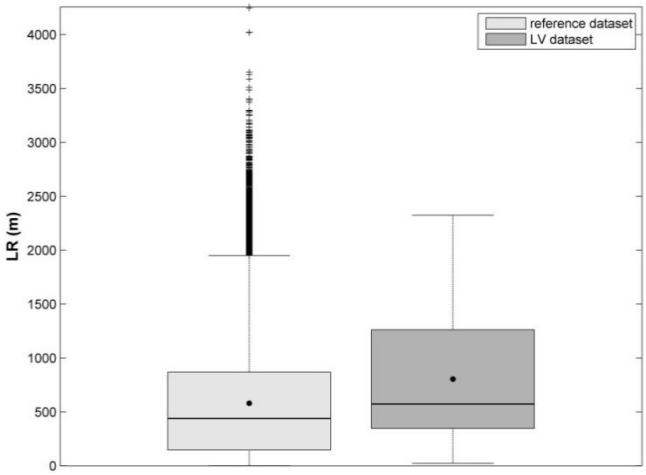

Figure 45: Comparison between local relief (LR) for all earthquake events with magnitude larger than or equal to four for the period 1950-2013 as derived from the NCEDC database (n = 115473) and LR for all earthquake events in the dataset compiled in the framework of this thesis (n = 66). Only epicenter locations on land are considered.

4.2 Predicting the total earthquake-induced landslide volume

4.2.1 Data selection and uncertainties

Because of the *scarcity of events* with directly reported landslide volumes, a LN-to-LV conversion was used to expand the dataset (section2.3.1 and 3.2.1). Testing of this conversion in Figure 15 shows one outlier, the Coalinga earthquake (United States, 1983, M_w 6.7). An explanation for the large deviation between the reported and calculated LV might be the very detailed mapping of landslides in the field and on aerial photographs, also including the smallest ones. On the other hand also the very large amount of small landslides or the absence of larger landslides (Harp & Keefer, 1990) might play a role. The first reason would indicate that the proposed relationship by Malamud et al. (2004a) is based on events lacking a detailed inventory of the smallest landslides, which is not the case. The second reason indicates that significant variability in the landslide size-frequency distribution might exist between different events with the same magnitude. Therefore, a conversion between LN-to-LV should always be applied with care. Nevertheless, the error is acceptable, taking into account that also uncertainties on the direct measurements of LV exist, which are often unknown. Nonetheless, for individual landslides the uncertainties on the volume estimate can be in the same order of magnitude as the estimated volume itself (Brunetti et al., 2009; Guzzetti et al., 2009a). Moreover, the applied relation is the only practical applicable conversion method that is currently available.

Still, a LN-to-LV conversion as used in this thesis (section 2.3.1) is more prone to the in general underestimation of the LV for a specific EQ event (section 4.1), which is explained as follows. Imagine an earthquake triggering landslides, of which the 20% smallest is not detected (200 landslides out of 1000). A direct assessment of the volume of the largest 80% of the landslides, will account for almost 100% of the total landslide volume, since this total volume heavily depends on a few large landslides (section 1.2.5.d). For the LN-to-LV conversion on the other hand, the size of the landslide does not play a role in the total count. In this case the LN-to-LV conversion with equation 4 would give an underestimation of the triggered volume of about 22%. Therefore, LN-to-LV conversion is likely to give an underestimation of the volume for incomplete datasets. On the other hand, the bias in scientific research towards events with a significant impact (section 4.1) may counter this underestimation in the total dataset of 77 EQ events. All in all it can be concluded that *potential biases exist on the constructed relation* (equation 17), induced by probable underestimations of the total landslide volume for events were only a number of landslides was reported, and by overrepresentation of earthquake events having a disproportionally large impact in terms of landsliding. However, these potential biases may to some extent counteract each other.

4.2.2 Delineation of the landslide-affected area

To determine the radius of the *mask areas* around each epicenter, the least square fit of the relation between M_w and D_{max} (Figure 16) was used. Some events show significantly larger maximum distances, much in accordance with the relations shown in Figure 4. Nevertheless, an upper bound function was not used since it is not necessarily better to consider a larger area for some marginal landslides (section 1.2.4). Furthermore, the calculated LAA in Figure 18 was based on this least square fit and still shows a systematic overestimation of the area. Therefore, the use of half of the radius, as suggested in section 2.3.2, is justified. This approach focusses better on the area of interest, i.e. closer to the epicenter since this is generally where the majority of landslides occurs (section 1.2.4). One step further would be that distance weighted environmental characteristics are taken into account, but this requires a better insight in the landslide distribution. In this way different weights could be given to locations according to a relation between landslide concentration and distance to the epicenter, calibrated for many earthquake inventories. Therefore in a second phase, a similar approach was applied to construct a LN model based on the knowledge of the LD (section 2.5.1).

4.2.3 Factors controlling earthquake-induced landslide volumes

4.2.3.a Moment magnitude

The distribution of delineated areas in Figure 19 and Figure 12 indicates a *good representation* of the seismic active regions in the world (Figure 8) by the events used for the LV model. Main data gaps only exist for the East African graben region and the Indonesian archipelago. Earlier proposed M-V models were determined without including any data for a seismic active region such as Japan and with only one event for the whole Eurasian continent (section 1.2.3). As a result, the better representation together with the vast increase of the number of events (16 compared to 77) is a clear improvement for the *robustness* of the relationship between M_w and LV. Nevertheless, our M-V relation scores not better than these previous M-V models. On the one hand, this can be attributed to the uncertainties on the data (section 4.2.1). On the other hand, this can also be attributed to the fact that more events are taken into account, expanding the range of variability in other factors (e.g. topography, lithology, land cover, climatic conditions, earthquake mechanics, etc.).

The different *subsets* indicating how LV was estimated (LV, LN and LN range: section 2.3.1), show no large bias for LV as a function of M_w. Still, a slightly steeper trend appears for the LV sub dataset. The question is whether this deviation is (1) inherent to the applied relationship of Malamud (2004a and 2004b: equation 3), (2) because of the variation in the earthquake events, i.e. different environmental conditions and/or (3) because of the limited amount of events in each class and the uncertainty on all the estimates. It was explained in section 4.2.1, that an underestimation can be expected when calculating LV based on

LN. However, if this would explain the deviation, the LN based volume estimates should be systematically below the directly obtained volumes and this is not observed. Still, it could be that equation 3 systematically overestimates LV for small landslide numbers, and underestimates LV for large landslide numbers. For this purpose it would be interesting to further validate this function with other very good landslide inventories, which is also encouraged by the authors themselves (Malamud et al., 2004b). The second and third argument are in the same line and it can be expected that the deviations will be reduced by taking into account other environmental characteristics. Furthermore, weighting of the subsets also partially accounted for these potential biases (section 2.3.1).

4.2.3.b Land fraction

A first additional variable to take into account is the *land fraction*, shown in Figure 21. It was chosen to directly correct the reported landslide volumes with the land fraction in each mask area to avoid over fitting of the model (LV_{lc}), when this factor would be taken into account as an additional predictor variable. Correcting for the land fraction clearly improves the relation between M_w and LV with a 4.5% increase of R^2. Especially two events, at the high end of the magnitude scale (Tohoku: Japan, 2011, M_w 9.0; Valdivia: Chile, 1960, M_w 9.5), contribute to the increased R^2, because they have a relatively large fraction of the mask area in the sea and because they are the only data points for these large magnitudes.

4.2.3.c Correlation and partial correlation analysis: the importance of other predictor variables

Correlation and partial correlation analysis with correction for M_w gave better results for the smaller mask areas. This confirms the *importance of the areas closer to the epicenter* as discussed in section 4.2.2.

An interesting result is the fact that *none of the considered variables, besides M_w* shows a strong correlation with the total landslide volume, linearly corrected for the fraction of land in the mask area (LV_{lc}), despite their stated importance by earlier research (section 1.2.5). This clearly underlines the importance of the magnitude to explain for the variability in LV at a global scale. The absence of other important variables might be surprising, taking into account the large variability in LV for a specific magnitude (sections 4.1 and 4.2.1). However, *three main reasons* might explain this. First, the *uncertainty on the input LV data*, should not be underestimated. There is clearly room for improvement on the LV data (section 4.1 and 4.2.1), which would be likely to result in a better correspondence with factors such as mean slope and lithology for a certain LAA. On the other hand, also the *input data of the predictor variables* is not always ideal (section 2.3.3.c and section 2.3.3.d). In the case of PGA, climate and tree cover data, for example, an important limitation is the time frame of these data which is not adapted to the occurrence of each

earthquake event. Especially in the case of heavy precipitation events, which were found to be important (section 1.2.5.d), it is clear that such a stochastic process can hardly be captured by a measure such as mean annual precipitation or even by the modified Fournier index. Additionally, these factors do not accurately focus on their potential different state or role before and after the earthquake. A second way in which the predictor data is not ideal is the resolution of the data. This was a strong limitation in the case of lithology maps with data on a resolution of about 50 km, which is for many events even larger than the LAA. A third reason is the fact that different environmental factors interfere and might counteract each other. For example, weaker lithologies might result in more moderate topography.

4.2.3.d Possible role of the 'standard deviation of local relief' as a predictor variable.

Even though no very strong correlating factors were found, still some additional variation in LV_{lc} could be explained by the *topography* after correction for M_w. It was not one of the more obvious topographic variables, such as maximum, or mean slope, but the standard deviation of local relief (LR_{stdev}) which showed to be a significant, but also robust predictor variable (Figure 23).

It should be asked why the standard deviation of local relief is a significant variable, as one needs a *physical ground*, and not just a statistical principle of correlation, to proof this factor can play a role. LR_{stdev} indicates how much the LR varies within the considered mask area, which means that both areas with a low and high local relief should be present in the area to get a high LR_{stdev}. It is especially surprising that LR_{stdev} performed better than variables describing the average or maximum local relief in the considered mask area. Even though it is generally known that landslide probability increases with increasing topography (e.g. slope gradient; see section 1.2.5.c), this does not explain why the LR_{stdev} performs better than variables describing the average rate of topographic differences.

The reason for its better correlation with LV_{lc} than measures as MLR or maximum LR, might be that it combines the best of both of these measures. On the one hand MLR is a more robust measure of relief, but it might be averaged out too much by contrasting landscapes in the mask area. The maximum LR on the other hand better represents the importance of large LR, which is more relevant for landsliding, but it is not so robust as it gives only the maximum value in the mask area. However, in this case also the other topographic measures that were introduced to quantify the proportion of very steep topography in the mask area (section 2.3.3.a), should score at least as good. These variables indeed score better than MLR and maximum LR, but score significantly worse than LR_{stdev}. This is an interesting observation: *LR_{stdev} is a significant factor, but (at least partially) not because it focusses on steep topography*.

In order to find an explanation, it might be interesting to consider which *real world situations* result in high LR_{stdev}. For this purpose we focused on the 5 earthquake events with highest and the 5 events with lowest LR_{stdev} of our LV model. It is found that the five events with highest LR_{stdev}, respectively: 91, 15, 92, 188, 175 (Table 5), are located at highly active subduction zones: Himalayan, Taiwanese and Andean orogeny (Chai, 1972; Kao & Chen, 2000). The five events with the lowest LR_{stdev} on the other hand, respectively: 192, 239, 196, 179, 3 (see Table 5), are located along transform boundaries (San Andreas Fault in United States, Alpine Fault in New Zealand) or at the margin of a convergent boundary, with also mainly strike-slip faulting (Betic Cordillera in Spain) (Weijermars, 1991; Zoback, 1992; Norris & Cooper, 2000). These observations suggest that high landslide volumes for a given earthquake magnitude are inherent to a specific geographical setting, which is reflected by LR_{stdev}. Indeed active subduction zones typically consist of a relatively flat foreland basin, bordering very steep mountain ranges. Figure 30 shows the example of the Wenchuan earthquake (China, 2008, M_w 7.9) and the Assam earthquake (Tibet, 1950, M_w 8.6) with respectively the highest and second highest LR_{stdev}. The first one is located along a fold-and-thrust belt, representing the eastern margin of the Himalayan orogeny (Hubbard & Shaw, 2009), the second one at the eastern margin of the collision zone between the Indian and Eurasian plate (Ben-Menahem et al., 1974). The relief maps created with Earth Explorer 6.1 (2009) clearly show their location at the mountain margin and an associated positive skewness for the LR histograms. The large amount of small LR values might be attributed to the the relatively flat foreland basins in the area.

Of course these observations *need more rigorous* testing, but some ideas can be put forward to explain this observation. The main *hypothesis* could be that after correcting for the magnitude of an earthquake event, earthquakes with epicenters located closer to active margins of converging plates (i.e. at the interface between the foreland basin and mountain range) generate larger LV. Physically this could be explained by specific conditions that might be structurally different from conditions further away from the active margins, for instance: different lithologies, different geological structure or a systematic difference in the distance of the steepest slopes from the epicenter. Another hypothesis is that a specific mechanism such as ‘hillslope memory’ might play an important role (Parker, 2013). This means that areas close to the subduction zone are also more often struck by smaller earthquakes, compared to more distant areas. This frequent occurrence of smaller earthquakes can weaken the substrate (Molnar et al., 2007). Consequently, with a subsequent large earthquake, the subduction area can be expected to generate more landslides. Moreover, Molnar et al. (2007) state that the amount of fracturing in the hanging wall of a fault system depends on the amount of time this lithological layer spends in the so called ‘bend’ (Figure 47, between the two red lines). Since this bend zone becomes larger with increasing depth and since deeper layers are exposed at the surface

closer to the main fault, this implies that the exposed rock closer to the main fault (in the area of high LR_{stdev}) is more fractured and hence more prone to landsliding.

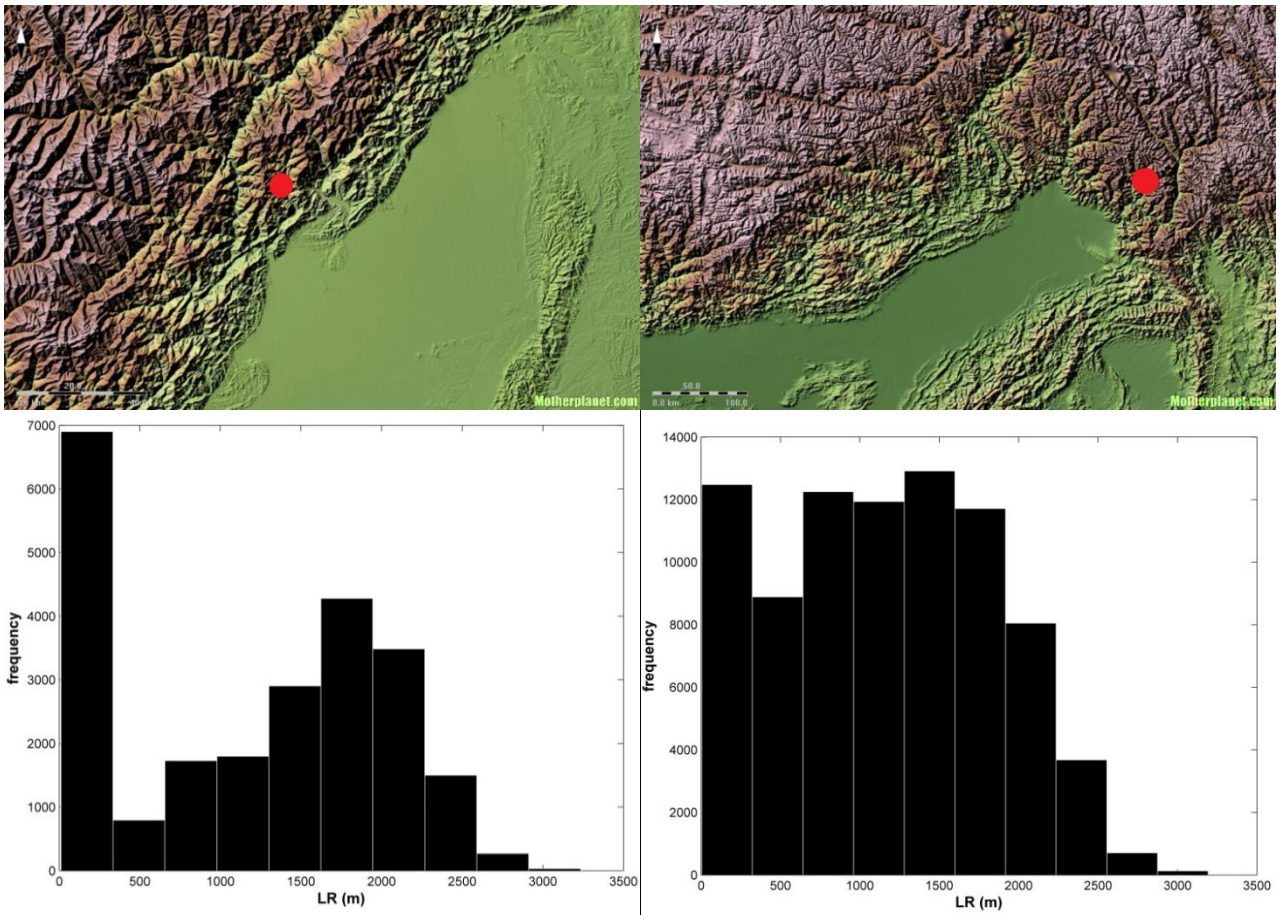

Figure 46: Relief maps for the Wenchuan (left) and Assam (right) earthquakes, respectively in China in 2008 (LR_{stdev}: 848m) and in Tibet in 1950 (LR_{stdev}: 689m) (Earth Explorer 6.1, 2009). Red dots indicate the earthquake epicenters. Below the associated histograms of the local relief (LR) are displayed, indicating the number of pixels sorted into 10 equally spaced LR classes (Appendix 1, own processing).

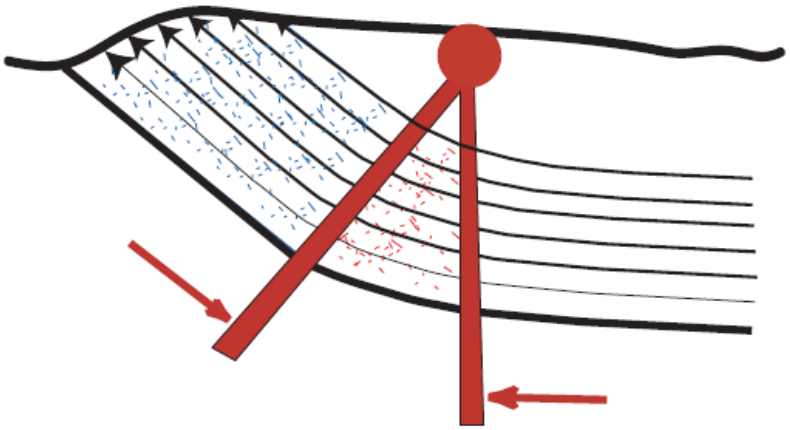

Figure 47: Conceptual illustration of the hanging wall at a subduction zone. While the rock layers move to the left, significant cracking occurs when the layers are bended (between the two red lines). The rate of fracturing is proportional to the depth of the layer. This results in the exhumation of more fractured rock closer to the main fault (Molnar et al., 2007, p. 3).

4.2.4 Landslide volume model

4.2.4.a Overall model performance

A robust LV model (Figure 24), which reduced some of uncertainty of the M-V relation (Figure 20), could be established. Moreover it is a fairly simple model to apply as it only requires information on the magnitude and the topography. Since the model is calibrated based on data distributed over most of the seismic active regions in the world (section 4.2.2.a), it can be used as a global tool to assess the LV generated by a certain earthquake event at a specific location (Objective 2).

To come back to the earlier discussion on the different subsets (directly reported landslide volumes, reported total landslide number, and reported total landslide number range) in section 4.2.3.a, it can be observed in Figure 24 that the slight deviations between the different subsets apparent in Figure 20, are further reduced. The remaining bias is largest for large magnitudes, but falls clearly within the uncertainty level of an order of magnitude. Moreover, the data scarcity for such large magnitudes makes that the three subsets heavily depend on only a few input data points. Additionally, it also seems reasonable that earthquake events triggering large LV or large LN attract more attention leading to more in detail investigations (i.e. LV assessments), possibly explaining why the largest LV data points were based on directly reported LV. Next to this, directly reported LV incline to overestimations when calculated based on a LA-LV relationship (section 4.1).

Even though, it is demonstrated that all available data should be used. We also tested the model for other input datasets. The explanatory power of the model is not significantly affected by subsequently leaving out data based on LN ranges and based on LN. Despite the smaller datasets, R^2 for these reduced models are in the range of 0.73-0.77 (compared to 0.75 for our model (equation 17)).

4.2.4.b Deviation from the trend for the Zhaotong and Luhuo earthquake

As mentioned in section 3.2.4, two events show larger deviations between the modeled and predicted LV, i.e. the Zhaotong earthquake (China, 1974, M_w 7.1) for which the predicted volume was 30 times higher than the reported LV and the Luhuo earthquake (China, 1973, M_w 7.6) which was overestimated by a factor 60. Both events had a large magnitude and were situated in a mountainous regions. Therefore, the reported number of landslides is surprisingly low, especially, compared to other events in the same region. E.g. Maowen (China, 1933, M_w 7.5) and Wenchuan (China, 2008, M_w 7.9). Two events with a similar or slightly higher magnitude, but inducing 50 to 4500 times larger LV according to the reports (USGS, 2010b; Parker et al., 2011; Chen et al., 2012).

Personal communication with the authors (Chen et al., 2012), suggests three possible explanations. First, it is a relatively detailed inventory, but only based on field

investigations in remote regions, which makes the omission of some of the landslides unavoidable. This suggest that the inventory of the Luhuo earthquake was only carried out in more accessible terrain, i.e the flatter area close to the fault along the river. This could explain why only landslides were reported in this relatively flat area and not even one landslide in the very mountainous areas at both sides of the alluvial plane. Secondly, the geological setting would contribute to the low LN. With all landslides occurring in Quaternary gravel layers, which are only found close to the river (Chen et al., 2012). However, also for the Wenchuan earthquake in the same region main lithologies were granitic, schist and limestone rock, which were on the other hand largely affected by landsliding after the event. Thirdly, it is suggested that smaller slope failures were not considered as being actual landslides. This last remark is also fundamental; if smaller slope failures are just omitted because of their size, this may distort the LN record. However, no information is available on which threshold would have been applied.

Even though these explanations strongly suggest an incomplete inventory, there is no objective ground (e.g. threshold size, or an explicit statement that only a limited area was investigated) to state that this investigation would be inferior to other studies, where it is also likely that smaller landslides are missing (section 4.1). It is observed that a model without event 85 and 86 has an R^2 of 0.78 (compared to 0.75 for our model), the regression is not largely affected as it concerns two data points in the center of the LV range.

4.3 The spatial distribution of earthquake-induced landslides

4.3.1 Reliability of the earthquake-induced landslide inventories

After georeferencing, most landslide inventories were assessed sufficiently accurate to develop a LD model, with assessed errors (column 7, Table 6) usually far below the model resolution of 500m. Moreover, there are several reasons, why the *assessed error is likely to be an overestimation of the real error*. First, reference points are often roads or rivers. These are digitized line features on the map entraining generalization errors. On the contrary, such a generalization error does not apply for landslides which are point elements. Secondly, validation of known reported landslide locations showed much smaller errors than the used georeferencing points. Thirdly, georeferencing points are often land-sea borders, located more in the periphery of the images. It is found that errors are sometimes larger in these peripheries because of the lack of georeferenced points. However the area of interest with landslides is mostly central in the map.

Some additional *problems with data accuracy were apparent*. As discussed in section 2.2, *epicenter locations* are often imprecisely reported. Likewise, reported epicenter coordinates sometimes did not match with the epicenter displayed on the published maps. Of course this location is highly important, as it indirectly influences all other factors in our

model. In order to be as consistent as possible, we always used the mapped epicenters, assuming that reported coordinates might be rounded sometimes. Indeed, many reported epicenters were rounded to a tenth of a degree, which can result in errors up to more than six kilometers

A second problem concerns the *landslides displayed* on the maps (column 5 in Table 6). Accurate digitalization was sometimes impeded by the fact that symbols indicating mapped landslides overlapped. This resulted in inconsistencies between the reported LN and the digitized LN of sometimes several dozens of landslides for smaller events (e.g. Lorca (Spain, 2011, M_w 5.1)) and several hundreds of landslides for larger events (e.g. Loma Prieta (United States, 1989, M_w 7.0)). This is not necessarily a problem; the largest fraction of landslides is displayed, which will already give a good representation of the spatial distribution.

4.3.2 Evaluation of the potential predictor variables based on individual landslide inventories

4.3.2.a Significance of the considered variables

As indicated in section 2.4.3, the considered landslide inventories need to be large enough to allow for reliable statistical testing. The fact that the Wald test statistic (W) and the likelihood ratio (lr) are in such a good agreement indicates that this is indeed the case (section 3.3.2). Hence, the more convenient statistic of W could be used to assess the variables' significance (Kleinbaum & Klein, 2002).

Based on the results of lr, W, the variable coefficients and R^2_{McF} in Figure 26, Figure 27 and Figure 28 it was found that *D, SMA, SME and ER* are the most appropriate parameters for assessing landslide probabilities. These results are in agreement with earlier research (section 1.2.5). However, the variables: SME, SMA and ER should not be taken into account together, as they all represent the topographic susceptibility of a pixel to landsliding. Analysis of the variance inflation factor (VIF, section 2.4.3) pointed out that multicollinearity exists for these variables, which is not the case for any of the other variable combinations. Moreover, it was found that each time only one of these variables significantly contributed to the logistic regression models (Figure 28).

On the other hand, the analysis also demonstrates that *for individual events other factors can be very important*. For instance, DR seems to be a crucial factor for events 85 and 86. For event 85 (Luhuo: China, 1973, M_w 7.6) this directly explains the inverse trend for the slope coefficients in Figure 27; all landslides are located, very close to the river, which is at lower elevation close to the alluvial plain. Another control on the absence of landslides in the relief rich surroundings might be the geological setting, with an important fault structure along the river or a substrate more prone to landsliding (Chen et al., 2012).

Also the other exception: event 239 (Rotoehu: New Zealand, 2004, M_w 5.4) with low lr and W for the topographic variables, was foreseen. The strongest control for this event seem to be 'roads' (see next section), with also 'topography' as a causative factor because of steep road cuts. This means that both events 85 and 239 can be clearly explained and probably modeled accurately individually, because of specific circumstances. However, exactly because of these specific conditions that cannot be taken into account in the combined model, both events might be wrongly represented by the variables taken into account based on their general significance. This is the *limitation and in the same time the strength of the model*, since it confirms its simplicity and global applicability not precisely meant for susceptibility hazard mapping for individual events, but rather to depict important landslide areas on a regional or continental scale (objective 3). This also indicates that a small fraction of landsliding might occur in relatively flat terrain, because of other influencing factors such as lithology, geological structure or roads.

Altogether this means that only D and one measure representing relief should be taken into account in the combined model. SMA and SME are found to be the best of these three relief measures based on analysis step one and two and consequently need to be tested for the combined model (see section 4.3.3). These findings are in line with Parker's (2013) suggestions to come to a global applicable model where distance to the seismic source and slope are the most important variables.

Finally, it is interesting to *compare our results* with those of Parker (2013) for events 8 (the Buller earthquake; New Zealand, 1929, M_w 7.7) and 9 (the Inangahua earthquake; New Zealand, 1968, M_w 7.1). For our models as well as for Parker's models two main important factors: D and a slope measure are found. R^2_{McF} for these events are in agreement between both investigations (Buller: 0.22 and 0.18 Inanaghua: 0.32 and 0.25 , both for respectively our model and Parker's model). These R^2_{McF} indicate that our model scores at least as good unlike the original data used by Parker (2013). However, the important difference is that Parker's model performs on a resolution of 30m whereas our model resolution is 500m.

4.3.2.b Potential relevance of other unconsidered variables

Because of data limitations two other potentially relevant factors could not be taken into account in the model: *distance to faults* (DF) and distance to roads. Especially DF is suggested to be an important factor. Parker (2013) states that the distance to the epicenter (D) gives a poor characterization for earthquake events with M_w larger than seven. This is confirmed by Figure 29, which shows that it is preferable to use DF instead of D, especially for larger events. Largest improvement in model performance were found for events 8, 85 and 92, with respectively M_w of 7.7, 7.3 and 7.6, being the three largest M_w of the nine

analyzed events. The better performance of DF asks for a global fault dataset to improve the current LD model.

Concerning *distance to roads*, different authors have stated its importance for landsliding because of a tremendous steepening of the slopes at roadcuts (e.g. Hancox et al., 2004; Ayalew & Yamagishi, 2005; Mahdavifar et al., 2006). It is certain that for some of the events, this factor is very important (e.g. Avaj: Iran, 2002, M_w 6.5 and Rotoehu: New Zealand, 2004, M_w 5.4). The difficulty however, is that many of the earthquake events occurred a couple of decennia ago, and no data on all these road networks at different times is available. On the other hand landslide inventories might be biased, with only landslides mapped along roads as these are more accessible. For most events however, the impact of roads might be limited as these are often absent or only marginal in the affected areas

4.3.3 Construction of a spatially distributed landslide model based on integrated landslide inventories

Figure 30 displays the results of the three different subset selection procedures (section 2.4.5) for different variable combinations of LD prediction. S*imilar model performances can be noted for the calibration validation dataset*s. This indicates that the calibrated model coefficients are representative for other pixel datasets and that our model is robust and not over fitted. Secondly, it can be observed that the *subset selection procedure (SSP)* has *important implications* for the modelling results. The 'fixed' SSP gives equal weights to each event, which seams a fair approach. However, this means that for the smaller events, almost the entire dataset is selected, whereas for larger datasets only a minor fraction (sometimes less than 1%) is selected. Moreover, the total amount of pixels taken into account for calibration is only about 4% of the total dataset. The 'fraction' SSP avoids this problem, by taking an equal fraction for each dataset into account, consequently resulting in a sub dataset that includes about 20% of the total number of pixels. However, this way the smaller events are almost neglected as they contribute less than 0.5% to the subset, while the largest event (ID 123) contributes about 30% to the sub dataset (Figure 25). The 'root' SSP therefore seems an attractive compromise. Datasets of smaller events still contribute significantly to the sub dataset, while large events still receive relatively more weight. The latter is clearly justifiable, since it is these events that generate the largest landslide volumes and consequently have the highest potential impact on the sediment discharge. Therefore, even though it is found that the 'fraction' approach gives highest R^2_{McF}, the '*root' SSP was preferred.* Testing for the influence of individual events (Figure 28), supports this choice, with on average larger deviations from the mean trend for the 'fraction' approach compared to the 'root' approach,

Together with a selection of the SSP, also the *best variable combination* should be selected. Standardized distance is a better variable than distance, which can be understood because of the large range in moment magnitude for the different events taken into account. Also M_w should be taken into account: larger earthquakes have a stronger impact at a certain place and a larger affected area (section 1.2.5.a). Finally the slightly better results for maximum slope compared to mean slope can be simply understood. Imagine a situation with one landslide pixel (500x500m) containing 3 pixels (100x100m) with very steep slopes and 22 pixels (100x100m) with rather gentle slopes. This means that the pixel is very prone to landsliding, which is correctly represented by a high maximum slope, but incorrectly represented by a rather small mean slope.

Taking previous considerations into account this means that the modeling results of the *'root' SSP for the variable combination 'M_w + DS + SMA'* should be used to construct a final LD model.

4.3.4 Application and validation of the landslide distribution model

Application of the LD model to the 25 events for which landslide patterns were known (Table 2), gives *in general good results*, (Figure 33, Figure 34 and Appendix 2). Only event 85 gives very poor results, with a ROC value below 0.5, which means that it is better to invert the model so that mapped landslides correspond to further distances from the epicenter and to lower slopes. Besides, only event 91, 92, 114 and 182, score less well, but ROC values are still clearly above 0.5, ranging between 0.62 and 0.74, indicating that the model can at least partially explain for the observed distribution.

For event 91 and 92, (respectively Wenchuan earthquake: China, 2008, M_w 7.9 and Chi-Chi earthquake: Taiwan, 1999, M_w 7.6) *faults* were mapped. These suggest that distance to the epicenter (D) gives a poor characterization with respect to landslide location. Indeed this is what can be expected for very large events as discussed in section 4.3.2.b. Concerning event 114 (Avaj earthquake: Iran, 2002, M_w 6.5), roads are an important factor, which is not taken into account by the model. Finally, event 182 (Coalinga: United States, 1982), shows a quite good agreement, but has some mapped landslides in the north west of the affected area, where probabilities are predicted low, and has a lack of landslides in the central east, with high probabilities. More in detail analysis of the region learns that the central east region is a relatively flat area, but with the epicenter located there, resulting in higher probabilities. In the north western area lower probabilities are found, because it is far from the epicenter. However, this area is clearly identified as a badland landscape, with quite high relief and absence of vegetation, explaining for the observed landslides. Nevertheless, it seems that the relief is expressed on such a small scale (gully erosion on meter to decameter scale) that 100 m resolution slope maps, cannot entirely capture the topography, resulting in an underestimation of the relief.

Events 8, 9, 91, 92 and 118 (for ID's see Table 5), were also investigated by Parker (2013). This allows for a direct *comparison* between his probability maps and our results (given in Appendix 2). As discussed in section 4.3.2.a, R^2_{McF} values are comparable for both studies. It is observed that also the generated probability patterns are comparable, especially for events 8 and 9. The other three events show larger differences, with higher probabilities predicted by the model of Parker along the fault structures for events 91 and 92 and with clearly lower probabilities close to the epicenter for event 118. For this last event however, the observed landslide pattern, seems to better correspond with the predictions by our model, demonstrating that for events of lower magnitude standardized distance to the epicenter can be a valuable predictor variable for landslide occurrence.

All these observations lead to the conclusion that the our *model overall performs well.* For 24 of the 25 considered events it results in clearly better predictions compared to a random model. Nevertheless better data on main faults, roads, vegetation and higher resolution topographic data are welcome to improve predictions.

4.4 The integrated spatially distributed landslide volume model

4.4.1 Predicting landslide numbers based on the distribution model

The resulting LN model (Figure 35) can be compared with the LV model (Figure 24). It is clear that the R^2 is significantly lower for the LN model. However, the range in LV values is about 2 orders of magnitudes larger, which is favorable for the R^2 (Figueiredo Filho et al., 2011). Moreover, the LV relation is determined by a few events for very high LV, which might also affect the R^2. Besides, it makes the relation less robust, which is not so much the case for the LN model with a better representation of events over the entire LN range. When we consider the deviation from the least square fit, the LN relation in fact shows a more consistent picture, with only few observations deviating more than an one order of magnitude. All in all both relations are useful, but for the integrated model the LN model was chosen. First because it gives more conservative estimates and second because the landslide number and not the total landslide volume is required as the basis input for the integrated model (section 2.5.2).

4.4.2 Model application and comparison with available inventories

Figure 36 compared the landslide number and volume predicted by the model (LN_m and LV_m, equation 19) with the simulated landslide number and volume (LN_s, LV_s). It shows the correctness of the integrated simulation model: the median LN_s and LV_s correspond to LN_m and LV_m, while the mean values are larger. The explanation for larger mean values is the fact that the randomization of LN_m in the first place and the random factor for Vl

assignment in the second place (section 2.5.2), causes larger positive absolute deviations than negative absolute deviations. The same is true for the assignment of volumes. However, the observed larger relative deviation between mean LV_s and LV_m than the deviation between mean LN_s and LN_m, has to do with the double increase in mean values for the final LV_s, i.e. first by the LN randomization and second by the volume randomization (inverse gamma distribution, equation 3). *It is important to realize that the inherent* larger *absolute positive LV_s deviations imply that the model uncertainty for earthquake-induced landslide volumes is in absolute terms larger towards the positive end.*

The results in Figure 37 reveal the probability pattern, presented in Figure 33 and a correspondence with the mapped landslides plotted on top. More scatter for the volume map results from the extra randomization step, whereby it is possible that a peripheral pixel gets only one landslide assigned, but with a volume larger than the summed volume of for instance 20 landslides in a central pixel with higher probability. In this respect future improvement for the spatial distribution of volumes can be expected from a better understanding of the relation between the size of landslides and the landslide susceptibility. As an hypothesis, it can be put forward that larger landslides are triggered closer to the epicenter (i.e. on locations with higher susceptibility). This was observed for one of the landslide inventories (ID 130, Table 5). Fry et al. (2010) namely gave an indication of the landslide size for the mapped landslides resulting from the Dusky Sound earthquake (New Zealand, 2009, M_w 7.6).

Based on 100 iterations, a better insight in the likely generated landslide numbers and landslide volumes could be obtained (Figure 37). In this respect the range between minimum and maximum LN_s and LV_s might raise questions about the usefulness of the model. It is true that the range is very large and it is true that this is correct with respect to the normally distributed uncertainty term included in the model. Still, it has to be kept in mind that the obtained minimum and maximum simulated values are highly unlikely. Since it concerns values in the tail of the normal distribution with more than 3.5 and 2.5 standard deviations from the mean value for respectively the maximum and minimum obtained LN_s. On the other hand the range between Q25 and Q75, spans only about an order of magnitude and by definition contains 50% of the iterations.

In practice this means that generated volumes by real world earthquakes have a significant chance (i.e. 50%) of deviating less than 5 times from the median volumes predicted by our model, but are unlikely (i.e. chance of 0.1%) to deviate more than 100 times from the median model volume.

Referring to the objectives it was not the intention to predict exact locations of individual landslides, but rather simulate the patterns of sediment mobilization by EIL. In this respect

the earlier validation by means of ROC values provides a good indication of the model performance. Nonetheless, given the rather coarse model resolution of 500m it is still useful to assess the pixel to pixel accuracy of the model. In this respect the K_I values in Figure 38 clearly show the model's ability to perform better than random in predicting landslide locations. This also confirms that the model is able to simulate more general patterns of sediment mobilization by EIL (objective 2). Only events 85 and 114 score very poor. Earlier discussion on these events explains for these shortcomings (section 4.2.4.b and 4.3.2.b). Secondly, the error budget (section 2.5.3) in Figure 39, learns that most of the improvement for correctly simulating landslide and non-landslide pixels, can be expected from a better quantification of the landslide number. This has an important implication: Even if the allocation procedure would be optimized (i.e. $K_I = 1$), still the largest fraction of currently wrongly classified pixels will remain. *Therefore, it is recommended to concentrate efforts on a better landslide number and volume prediction.*

4.5 Model application and comparison with sediment yield

Correlation analysis in Figure 41 demonstrates the *potential importance of earthquake-induced landslides for observed higher average sediment yields*. Not surprisingly these landslide masses (LM) are strongly correlated with areas of high expected peak ground acceleration and decrease with distance from the regions of highest seismicity (Dc, section 1.2.5.a and 1.2.5.b). Somewhat surprising might be the (negative) insignificant, trend of LV with average catchment slope. Two reasons might explain this. First, the range in average slope is fairly limited (5-18°). Secondly, the decrease in relief of the Siret basin from north to south (Vanmaercke et al., 2014b), is opposite to the increase in seismic activity along this transect (Figure 11). This demonstrates that earthquakes and associated landsliding are not always reflected in the topography and that distance to epicenter is more important than topography in terms of landsliding. Therefore, tectonic activity should be considered to explain for the spatial variation in SY as also stated by Vanmaercke et al. (2014b).

Figure 40 and Figure 43, allow for a comparison between the 1977 event and all events together. It is noteworthy that the largest earthquake during this period only contributed about 2.1% to the total LM, with however a large uncertainty on the Q5-Q95 interval (0.1-40.2%). Figure 40 and Figure 43 indicated that the contribution of the 1977 is location dependent. For some catchments with larger Dc the 1977 earthquake contributes significantly to the total volume (up to 50%), but for other catchments with lower Dc this share is indeed very limited. This observation demonstrates that *many smaller earthquake events can contribute significantly to the total generated landslide volume*.

A comparison between the upper left graph in Figure 41 and Figure 42 illustrates the importance of earthquake induced landslides in terms of *denudation and SY*. It is shown that earthquakes generate more sediment than what is transported by the river for

catchments in the region of highest seismicity. This implies that at least part of the generated sediment does not reach the river channel. Especially for the 1977 event, generated landslide masses surpass the annual average SY for catchments in the region of highest seismicity. Nevertheless, no clear pulse in the SD was observed after this event. Only the Nereju catchment (ID 38) showed a significant increase after the earthquake (Vanmaercke et al., 2014b), despite the low contribution to the total LM of the 1977 event in this catchment (Figure 43). A possible explanation is the large difference between the relatively low SY (533.4 t/km²/y) and the large LM (3494 t/km²) generated by the 1977 earthquake in this catchment. Also the relatively small size of this catchment might play a role. On the other hand, explanations for the absence of a clear increase in SD for most of the catchments are: (1) the saturation of rivers with sediment induced by previous earthquakes, (2) the importance of connectivity (landslides not necessarily reach the river channel), (3) the higher location on hillslopes for EIL compared to rainfall triggered landslides and (4) the fact that only suspended sediment concentration is considered, whereas landslides might significantly contribute to the bedload of the river (Vanmaercke et al., 2014b).

Finally, Figure 41 and Figure 42 also give an indication of the actual landscape denudation. Median annual LM for some catchments are as high as 10000 t/km²/y. Assuming a denudation of 1 mm for 15 t/ha, annual denudation due to earthquake induced landslides equals 6.7 mm/y in these catchments. A similar calculation for the 1977 event demonstrates a denudation of 2-3 mm in many of the catchments. These denudation rates are in the same order of magnitude as other important erosion processes such as gully erosion (Poesen et al., 2003). Once more, this confirms the *importance of considering earthquake induced landslides in terms of erosion and in terms of sediment yield of a river*.

5 Conclusions and scope for further research

5.3 Conclusions

The aim of this thesis was to construct a model that predicts landslide volumes associated with a given earthquake in a spatially explicit way, so that it can be used to explore the impact of earthquake induced-landslides on catchment sediment yields.

As a first step a dataset that contains information on 239 earthquakes and associated landslide parameters was compiled (objective 1). A substantial amount of data is available, but a bias exists towards data that induced many landslides. These data cover most of the seismic active regions in the world, with major data gaps on the African continent and the Indonesian Archipelago.

The constructed model (objective 2) only requires moment magnitude and slope as input variables. It was calibrated based on 77 globally distributed earthquake events and can consequently be used as a global tool (resolution 500m) to trace the impact of earthquake induced landslides on the sediment yield of a catchment. The model is far from perfect, but the applied Monte Carlo simulation approach, accounts for the existing uncertainty. Model validation based on 23 earthquake inventories, showed that landslide allocation performs better than random for 22 of the 23 inventories.

We applied our model to the Siret basin (Romania) in order to estimate the likely landslide volumes induced by earthquakes in the period 1965-2014, including a Mw 7.4 earthquake in 1977. These volumes were confronted with measured sediment yield data from 38 subcatchments (objective 3). It is found that simulated earthquake induced landslide masses (range of median values: 200-13000 t/km²/y) are mostly higher than the sediment yield (250-1800 t/km²/y) for catchments in the most seismically active region and are mostly lower (range of median values: 0-100 t/km²/y) than the sediment yield (55-400 t/km²/y) for catchments outside this region. The 1977 event contributed largely (20-50%) to the total generated landslide masses for this period in some of the catchments outside the region of highest seismicity, but little (0.4-10%) to most of the catchments in this region.

This application to the Siret basin demonstrates the practical relevance of our model that can also be applied to other regions in the world.

Referring to the research question and the different hypotheses (section 1.5), our research showed the following:

1) The main factors determining the total landslide volume and the landslide distribution induced by an earthquake are: the moment magnitude and related to this factor distance to the epicenter. The topography and the fraction of land in the

affected area should also be considered, but are less important. Other factors such as: lithology, treecover and precipitation were found to be insignificant, under reservation of data uncertainties.

2) Environmental characteristics and properties of an earthquake can be used to construct robust landslide volume and landslide distribution models, be it with an uncertainty in the order of a factor 10 for the volume predictions.
3) Such models can be integrated and can be applied to provide estimates of generated landslide volumes on the catchment scale as a result of a certain earthquake or a series of earthquakes at any location in the world.
4) A strong positive relation exists between the earthquake-induced landslide volume and the sediment yield in a catchment. This suggests the importance of these landslides for the overall higher average sediment yields in seismically active regions (section 4.5).
5) Pulses of sediment discharge after an earthquake are not always pronounced. The proportion between the earthquake-induced landslide volume and the sediment yield and size of a catchment might play an important role.

5.4 Scope for further reserach

Uncertainties exist on the constructed relationships that were taken into account by the integrated model simulations. Further model improvement can mainly be expected from better predictions of the total number and volume of landslides associated with an earthquake event, rather than a better spatial allocation of these landslides (section 4.4.2). Therefore we recommend future researchers to mainly focus on a better assessment and prediction of the total earthquake-induced landslide number and volume.

Further recommendations for future research are:

- Information on earthquake-induced landslide volumes and landslide numbers, should be reported more accurately. More detailed data is often available, but it is mostly difficult to assess the reliability of these data due to incomplete or undetailed reporting on the investigated area, on the applied techniques and on the general uncertainties.
- Since all earthquake events with information on the landslide volume, number and distribution were (partially) used to calibrate the constructed models in this thesis, further calibration and especially validation is recommended, when new data becomes available.
- Additional model improvement can also be expected from better data on the predictor variables. Especially, data on the main faults, data on the actual peak ground acceleration and higher resolution topographical and lithological data on a global scale can be expected to contribute to better predictions.

- Focusing on the research need for better total volume predictions, it should be investigated to what extent landslide number, area and volume are under-or overestimated as e result of the applied mapping techniques. Next to this there is also a need for more detailed landslide inventories of smaller earthquakes (M_W 4-5). These events occur most frequently, but are clearly underrepresented in current research.
- The somewhat strange role of topography trough ‘the standard deviation of local relief’ should be further investigated. Is it coincidence, or is there a physical mechanism behind (section 4.2.3.d)?
- A further refinement of the relation between spatially distributed landslide susceptibility and the size of landslides might be required. Are large landslides more likely to occur on locations with higher susceptibility?
- Finally, the model should be applied to other regions to investigate when pulses in sediment yield occur. Can we relate this to catchment characteristics?

6 References

6.3 References in text

Airinei, S. (1977) Microplăci litosferice pe teritoriul României, *SC GGG, seria Geologie*, 15.

Alfaro, P., Delgado, J., Garia-Tortosa, E.J., Giner, J.J., Lenti, I., Lopez-Casado, C., Martino, S. (2012) Widespread landslides induced by the Mw 5.1 earthquake of 11 May 2011 in Lorca, SE Spain, *Engineering Geology*, 137-138, 40-52.

Allison, P. (February 13, 2013) *What's the best R-squared for logistic regression*, online available on: http://www.statisticalhorizons.com/r2logistic.

Ammon, C.J. (2014) *Earthquake Magnitude*, online available on: http://eqseis.geosc. psu.edu/~cammon/HTML/Classes/IntroQuakes/Notes/earthquake_size.html.

Ayalew, L., Yamagishi, H. (2005) The application of GIS-based logistic regression for landslide susceptibility mapping in the Kakuda-Yahiko Mountains, Central Japan, *Geomorphology*, 65, 15-31.

Barnard, P.L., Owen, L.A., Sharma, M.C., Finkel, R.C. (2001) Natural and human-induced landsliding in the Garhwal Himalaya of northern India, *Geomorphology*, 40, 21-35.

Baumgart, F. (2000) Stiffness – an unknown world of mechanical science?, *injury-international journal of the care of the injured*, 31, S-B14-S-B23.

Beirlant, J., Dierckx, G., Hubert, M. (2005) *Statistiek en Wetenschap*, Acco, Leuven, Belgium, 337pp.

Binder, K. (2005) Monte-Carlo methods. In: Trigg, G.L. (ed.) *Mathematical Tools for Physicists*, WILEY-VCH Verlag GmbH & Co. KGaA, Weinheim, Germany.

Bommer, J.J., Martinez-Pereira, A. (1999) The effective duration of earthquake strong motion, *Journal of Earthquake Engineering*, 3, 127-172.

Brunetti, M.T., Guzzetti, F., Rossi, M. (2009) Probability distributions of landslide volumes, *Nonlinear Processes in Geophysics*, 16, 179-188.

Burbank, D.W., Leland, J., Fielding, E., Anderson, R.S., Brozovic, N., Reid, M.R., Duncan, C. (1996) Bedrock incision, rock uplift and threshold hillslopes in the northwestern Himalayas, *Nature*, 379, 505-510.

Campbell, K.W. (1997) Empirical near-source attenuation relationships for horizontal and vertical components of peak ground acceleration, peak ground velocity, and pseudo-absolute acceleration response spectra, *Seismological Research Letters*, 68, 154-179.

CGIAR-CSI (2004) *SRTM database*, online available on: http://srtm.csi.cgiar.org/ SELECTION /inputCoord.asp.

Chen, X.L., Zhou, Q., Ran, H., Dong, R. (2012) Earthquake-triggered landslides in southwest China, *Natural Hazards and Earth System Sciences*, 12, 351-363.

Chen, X., Ender, P., Mitchell, M., Wells, C. (2014) *Logistic regression with Stata*, online available on: http://www.ats.ucla.edu/stat/stata/webbooks/logistic/.

Chuang, S.C., Chen, H., Lin, G.W., Lin, C.W., Chang, C.P. (2009) Increase in basin sediment yield from landslides in storms following major seismic disturbance, *Engineering Geology*, 103, 59-65.

Clarklabs (2013) *IDRISI Selva*, online available on: http://clarklabs.org/.

Cruden, D.M. (1991) A simple definition of a landslide, *Bulletin of the International Association of Engineering Geology*, 43, 27-29.

Cox, R., Zentner, D.B., Rakotondrazafy, A.F.M, Rasoazanamparany, C.F. (2010) Shakedown in Madagascar: Occurrence of lavakas (erosional gullies) associated with seismic activity, Geology, 38, 179-182.

Dahal, R.K., Bhandary, N.P., Timilsina, M., Yatabe, R., Hasegawa, S. (2013) Earthquake-induced landslides in the roadside slopes of East Nepal after recent September 18, 2011 earthquake. In: Ugai, K., Yagi, H., Wakai, A. (Eds.) *Earthquake-Induced Landslides*, Springer-Verlag Berlin Heidelberg, Heidelberg, 996 pp.

Dai, F.C. Lee, C.F. (2003) A spatiotemporal probabilistic modelling of storm-induced shallow landsliding using aerial photographs and logistic regression, *Earth Surface Processes and Landforms*, 28, 527-545.

De Ferranti, J., Hormann, C. (2013) *Digital Elevation Data*, online available on: http://www.viewfinderpanoramas.org/dem3.html#altsrc

Defries, R.S., Hansen, M.C., Townshend, J.R.G., Janetos, A.C. (2000) A new global 1-km dataset of percentage tree cover derived from remote sensing, *Global Change Biology*, 6, 247-254.

de Vente, J., Poesen, J., Verstraeten, G., Govers, G., Vanmaercke, M., Van Rompaey, A., Arabkhedri, M., Boix-Fayos, C. (2013) Predicting soil erosion and sediment yield at regional scales: Where do we stand?, *Earth Science Reviews*, 127, 16-29.

Dürr, H.H., Meybeck, M., Dürr, S.H. (2005) Lithologic composition of the Earth's continental surfaces derived from a new digital map emphasizing riverine material transfer, *Global Biogeochemical Cycles*, 19, doi:10.1029/2005GB002515.

Earth Explorer (2009) *Motheplanet*, online available on: http://www.motherplanet.com/.

ESRI (2013) *Products*, online available on: http://www.esri.com/products.

Figueiredo Filho, D.B., Silva, J.A., Rocha, E. (2011) What is R^2 all about?, *Cadernos de Pesquisa Politica*, 3, 60-68.

Fry, B., Bannister, S., Beavan, J., Bland, L., Bradley, B., Cox, S., Cousins, J., Gale, N., Hancox, G., Holden, C., Jongens, R., Power, W., Prasetya, G., Reyners, M., Ristau, J., Robinson, R., Samsonov, S., Wilson, K., Geonet team (2010) The Mw 7.6 Dusky Sound earthquake of 2009: preliminary report, *Bulletin of the New Zealand Society for Earthquake Engineering*, 43, 24-40.

Giardini, D., Grünthal, G., Shedlock, K.M., Zhang, P. (1999) The GSHAP Global Seismic Hazard Map, *Annali di Geofisica*, 42, 1225-1228.

Google™ Earth (2013) *Google Earth*, online available on: http://www.google.com/earth/index.html.

Gutenberg, B., Richter, C.F. (2010) Magnitude and energy of earthquakes, *Annals of Geophysics*, 53, 7-12.

Guzzetti, F., Reichenbach, P., Ardizzone, F., Cardinali M., Galli, M. (2006) Estimating the quality of landslide susceptibility models. *Geomorphology*, 81, 166-184.

Guzzetti, F., Ardizzone, F., Cardinali, M., Rossi, M., Valigi, D. (2009a) Landslide volumes and landslide mobilization rates in Umbria, central Italy, *Earth and Planetary Science Letters*, 279, 222-229.

Guzzetti, F., Esposito, E., Balducci, V., Porfido, S., Cardinali, M., Violante, C., Fiorucci, F., Sacchi, M., Ardizzone, F., Mondini, A., Reichenbach, P., Rossi, M. (2009b) Central Italy seismic sequences-induced landsliding: 1997-1998 Umbria-Marche and 2008-2009 L'Aquila cases. In: *The next generation of research on earthquake-induced landslides: an international conference in commemoration of 10th anniversary of the Chi-Chi earthquake*, National Central University, Jhongli City, Taiwan, 21-26 September.

Hanks, T.C., Kanamori, H. (1979) A moment magnitude scale, *journal of geophysical research*, 84, 6229-6235.

Hansen, M.C., Defries, R.S., Townshend, J.R.G., Sohlberg, R. (2000) Global land cover classification at 1 km spatial resolution using a classification tree approach, *International Journal of Remote Sensing*, 21, 1331-1364.

Harp, E.L., Keefer, D.K. (1990) Landslides triggered by the earthquake, In: Rymer, M.J., Ellsworth, W.L. (Eds.) *The Coalinga, California, earthquake of May 2, 1983*, U.S. Geologial Survey Professional Paper 1487, United States Government Printing Office, Washington, 417 pp.

Harp, E.L., Jibson, R.W. (1995) Inventory of landslides triggered by the 1994 Northridge, California earthquake, *U.S. Gological Survey Open-File Report 95-213*.

Harp, E.L., Jibson, R.W. (1996) Landslides triggered by the 1994 Northridge, California, earthquake, *Bulletin of the Seismological Society of America*, 86, S319-S332.

Harp, E.L., Keefer, D.K., Sato, H.P., Yagi, H. (2011) Landslide inventories: The essential part of seismic landslide hazard analyses, *Engineering Geology*, 122, 9-21.

Hartmann, J., Moosdorf, N. (2012) Global lithological map database v1.0 (gridded to 0.5° spatial resolution), doi:10.1594/PANGAEA.788537, *Supplement to:* Hartmann, J., Moosdorf, N. (2012) The new global lithological map database GLiM: A representation of rock properties at the Earth surface, *Geochemistry,* Geophysics*, Geosystems*, 13, doi: 10.1029/2012GC004370.

Hovius, N., Meunier, P., Lin, C.W., Chen, H., Chen, Y.G., Dadson S., Hongey, M.J., Lines, M. (2011) Prolonged seismically induced erosion and the mass balance of a large earthquake, *Earth and Planetary Science Letters*, 304, 347-355.

Huang, M.Y.F., Montgomery, D.R. (2012) Fluvial response to rapid episodic erosion by earthquake and typhoons, Tachia River, central Taiwan, *Geomorphology*, 175-176, 126-138.

Hubbard, J., Shaw, J.H. (2009) Uplift of the Longmen Shan and Tibetan plateau, and the 2008 Wenchuan (M=7.9) earthquake, *Nature*, 458, 194-197.

IPCC (May 4, 2014) *Climate Change 2013: The Physical Science Basis*, online available on: http://www.ipcc.ch/report/ar5/.

Jibson, R.W. (2007) Regression models for estimating coseismic landslide displacement, *Engineering Geology*, 91, 209-218.

Jibson, R.W., Harp, E.L., Schulz, W., Keefer, D.K. (2006) Large rock avalanches triggered by the M 7.9 Denali fault, Alaska, earthquake of 3 November 2002, *Engineering Geology*, 83, 144-160.

Jibson, R.W., Harp, E.L. (2012) Extraordinary distance limits of landslides triggered by the 2011 Mineral, Virginia, earthquake, *Bulletin of the Seismological Society of America*, 102, 2368-2377.

Kanamori, H. (1977) The energy release in great earthquakes, *Journal of Geophysical Research*, 82, 2981-2987.

Keefer, D.K. (1984) Landslides caused by earthquakes, *Geological Society of America Bulletin*, 95, 406-421.

Keefer, D.K. (1994) The importance of earthquake-induced landslides to long-term slope erosion and slope-failure hazards in seismically active regions, *Geomorphology*, 10, 265-284.

Keefer, D.K. (2000) Statistical analysis of an earthquake-induced landslide distribution - the 1989 Loma Prieta, California event, *Engineering Geology*, 58, 231-249.

Keefer, D.K (2002) Investigating landslides caused by earthquakes- a historical review, *Surveys in geophysics*, 23, 473-510.

Kleinbaum, D. G., Klein, M. (2002) *Logistic regression: a self-learning text*, Springer-Verlag, New York, 517pp.

Koi, T., Hotta, N., Ishigaki, I., Matuzaki, N., Uchiyama, Y., Suzuki, M. (2008) Prolonged impact of earthquake induced landslides on sediment yield in a mountain watershed: The Tanzawa region, Japan, *Geomorphology*, 101, 692-702.

Korup, O. (2012) Earth's portfolio of extreme sediment transport events, *Earth Science Reviews*, 112, 115-125.

Lee, S., Evangelista, D.G. (2006) Earthquake-induced landslide-susceptibility mapping using an artificial neural network, *Natural Hazards and Earth System Sciences*, 6, 687-695.

Lungu, D., Arion, C., Aldea, A., Vacareanu, R. (2004) Representation of seismic action in the new Romanian code for design of earthquake resistant buildings P100-2003, *13th World Conference on Earthquake Engineering Vancouver*, B.C., Canada August 1-6, 2004 Paper No. 1796.

Mahdavifar, M.R., Solaymani, S., Jafari, M.K. (2006) Landslides triggered by the Avaj, Iran earthquake of June 22, 2002, *Engineering Geology*, 86, 166-182.

Malamud, B.D., Turcotte, D.L., Guzetti, F., Reichenbach, P. (2004a) Landslides, earthquakes, and erosion, *Earth and Planetary Science Letters*, 229, 45-59.

Malamud, B.D., Turcotte, D.L., Guzzetti, F., Reichenbach, P. (2004b) Landslide inventories and their statistical properties, *Earth Surface Processes and Landforms*, 29, 687-711.

MATLAB (2013), *MATLAB the language of technical computing,* online available on: http://www.mathworks.se/products/matlab/.

Meunier, P., Uchida, T., Hovius, N. (2013) Landslide patterns reveal the sources of large earthquakes, *Earth and Planetary Science Letters*, 363, 27-33.

Meunier, P., Hovius, N., Haines, J.A. (2008) Topographic site effects and the location of earthquake induced landslides, *Earth and Planetary Science Letters*, 275, 221-232.

Meybeck, M. (2003) Global analysis of river systems: from Earth system controls to Anthropocene syndromes, *Philosophical Transactions of the Royal Society B*, 358, 1935-1955.

Miles, S.B., Keefer, D.K. (2009) Evaluation of CAMEL – comprehensive areal model of earthquake-induced landslides, *Engineering Geology*, 104, 1-15.

Miyagi, T., Yamashina, S., Esaka, F., Abe, S. (2011) Massive landslide triggered by 2008 Iwate-Miyagi inland earthquake in the Aratozawa Dam area, Tohoku, Japan, *Landslides*, 8, 99-108.

Molnar, P., Anderson, R.S., Anderson, S.P. (2007) Tectonics, fracturing of rock, and erosion, *Journal of Geophysical research*, 112, F03014.

Montgomery, D.R., Brandon, M.T. (2002) Topographic controls on erosion rates in tectonically active mountain ranges, *Earth and Planetary Science Letters*, 201, 481-489.

National Research Council (2010) *Landscapes on the edge: new horizons for research on earth's surface*, The National Academies Press, Washington D.C., 180 pp.

NCECD (2013) *Northern California Earthquake Datacenter*, online available on: http://www.ncedc.org/.

New, M., Lister, D., Hulme, M., Makin, I. (2002) A high-resolution data set of surface climate over global land areas, *Climate Research*, 21, 1-25.

Owen, L.A., Kamp, U., Khattak, G.A., Harp, E.L., Keefer, D.K., Bauer, M.A. (2008) Landslides triggered by the 8 October 2005 Kashmir earthquake, *Geomorphology*, 94, 1-9.

Pan, K.L., Lee, C.T., Chang, C.W., Lin, Y.H., Lin, S.Y., Lee, J.F., Wei, C.Y., Liao, C.W. (2004) Inventory of event-induced landslides by using space imagery, *Proceedings of International Symposium on Landslide and Debris Flow Hazard Assessment*, Taiwan, 7-8 October.

Parker, R.N., Densmore, A.L., Rosser, N.J., Mechele, M.d., Li, Y., Hunag, R., Whadcoat, S., Petley, D.N. (2011) Mass wasting triggered by the 2008 Wenchuan earthquake is greater than orogenic growth, *Nature Geoscience*, 4, 449-452.

Parker, R.N. (2013) *Hillslope memory and spatial and temporal distributions of earthquake-induced landslides*, Durham theses, Durham University, Available at Durham E-Theses Online: http://etheses.dur.ac.uk/7761/.

PennState (2014) *Stat 501 – regression methods*, online available on: https://online courses.science.psu.edu/stat501/.

Poesen, J., Nachtergaele, J., Verstraeten, G., Valentin, C. (2003) Gully erosion and environmental change: importance and reserach needs, *Catena*, 50, 91-133.

Pontius, R.G. (2000) Quantification error versus location error in comparison of categorical maps, *Photogrammetric Engineering & Remote Sensing*, 66, 1011-1016.

Pontius, R.G., Schneider, L.C. (2001) Land-cover change model validation by an ROC method for the Ipswich watershed, Massachusetts, USA, *Agriculture, Ecosystems and Environment*, 85, 239-248.

Pontius, R.G., Huffaker, D., Denman, K. (2004) Useful techniques of validation for spatially explicit land-change models, *Ecological modelling*, 179, 445-461.

Porterfield, G. (1972) *Computation of fluvial-sediment discharge*, United States Government Printing Office, Washinton D.C., 66 pp.

Richter, C.F. (1935) An instrumental earthquake magnitude scale, *Bulletin of the Seismological Society of America*, 25, 1-32.

Rodriguez, C.E., Bommer, J.J., Chandler, R.J. (1999) Earthquake-induced landslides: 1980–1997, *Soil Dynamics and Earthquake Engineering*, 18, 325-346.

Săndulescu, M. (1984) *Geotectonica României*, Ed. Tehnică, Bucureşti.

Scholz, C.H. (1968) The frequency-magnitude relation of microfracturing in rock and its relation to earthquakes, *Bulletin of the Seismological Society of America*, 58, 399-415.

Schumm, S.A. (2005) *River variability and complexity*, Cambridge University Press, Cambridge, 234 pp.

Shedlock, K.M., Giardini, D., Grünthal, G., Zhang, P. (2000) The GSHAP Global Seismic Hazard Map, *Seismological Research Letters*, 71, 679-686.

Stokes, A., Atger, C., Bengough, A.G., Fourcaud, T., Sidle, R.C. (2009) Desirable plant root traits for protecting natural and engineered slopes against landslides, *Plant Soil*, 324, 1-30.

Syvitski, J.P.M., Milliman, J.D. (2007) Geology, Geography, and Humans Battle for Dominance over the Delivery of Fluvial Sediment to the Coastal Ocean, *The Journal of Geology*, 115, 1-19.

TRIGS (2009) Triggering instabilities in materials and geosystems, Sixth Framework Programme (FP6), New and Emerging Science and Technology Pathfinder, January 1, 2007 – June 30, 2009.

USGS (September, 6, 2010a) *HydroSHEDS*, online available on: http://hydrosheds. cr.usgs.gov/index.php

USGS (December 6, 2010b) *Overview of Large Landslides of the 20th and 21st Centuries*, online available on: http://landslides.usgs.gov/learning/majorls.php.

USGS (July 24, 2012) *Earthquake Glossary*, online available on: http://earthquake.usgs.gov/learn/glossary/.

USGS (October 23, 2013a) *Earthquake Archive Search & URL Builder*, online available on: http://earthquake.usgs.gov/earthquakes/search/.

USGS (November 5, 2013b) *Shakemap*, online available on: http://earthquake.usgs.gov/research/shakemap/..

USGS-EROS (April 16, 2013) *Earth Resources and Observation Science (EROS) Center*, online available on: http://eros.usgs.gov/#/Find_Data/Products_and_Data_Available/gtopo30_info.

Vanacker, V., Vanderschaeghe, M., Govers, G., Willems, E., Poesen, J., Deckers, J., De Bievre, B. (2003) Linking hydrological, infinite slope stability and land-use change models through GIS for assessing the impact of deforestation on slope stability in high Andean watersheds. *Geomorphology*, 52, 299-315.

Van Den Eeckhaut, M., Vanwalleghem, T., Poesen, J., Govers, G., Verstraeten, G., Vandekerckhove, L. (2006) Prediction of landslide susceptibility using rare events logistic regression: A case-study in the Flemish Ardennes (Belgium), *Geomorphology*, 76, 392-410.

Van Dessel, W., Van Rompaey, A., Poelmans, L., Szilassi, P. (2008) Predicting land cover changes and their impact on the sediment influx in the Lake Balaton catchment, *Landscape Ecology*, 23, 645-656.

Vanmaercke, M., Poesen, J., Maetens, W., de Vente, J., Verstraeten, G. (2011a) Sediment yield as a desertification risk indicator, *Science of the Total Environment*, 409, 1715-1725.

Vanmaercke, M., Poesen, J., Verstraeten, G., de Vente, J., Ocakoglu, F. (2011b) Sediment yield in Europe: spatial patterns and scale dependency, *Geomorphology*, 130, 142-161.

Vanmaercke, M. (2012) *Scale effects and human impact on sediment yield from European catchments*, PhD thesis, KU Leuven, Belgium.

Vanmaercke, M., Kettner, A.J., Van Den Eeckhaut, M., Poesen, J., Mamaliga, A., Verstraeten, G., Radoane, M., Obreja, F., Upton, P., Syvitski, J.P.M., Govers, G. (2014a) Moderate seismic activity affects contemporary sediment yields, *Progress in Physical Geography*, 30, doi: 10.1177/0309133313516160.

Vanmaercke, M., Obreja, F., Poesen, J. (2014b) Seismic controls on contemporary sediment export in the Siret river catchment, Romania, *Geomorphology*.

Van Rompaey, A.J.J., Gover, G., Puttemans, C. (2002) Modelling land use changes and their impact on soil erosion and sediment supply to rivers, *Earth Surface Processes and Landforms*, 27, 481-194.

6.4 References in Appendix 1 and Table 5

Adams, J. (1980) Contemporary uplift and erosion of the Southern Alps, New Zealand, *Geological Society of America Bulletin*, 91, 1-114.

ADRC (August 16, 2013) Country report 2003 Tajikistan, online available on: http://www.adrc.asia/countryreport/TJK/2003/page6.html.

Alfaro, P., Delgado, J., Garia-Tortosa, E.J., Giner, J.J., Lenti, I., Lopez-Casado, C., Martino, S. (2012b) Widespread landslides induced by the Mw 5.1 earthquake of 11 May 2011 in Lorca, SE Spain, *Engineering Geology*, 137-138, 40-52.

Ahmad, R. (1995) Earthquake-induced landslides in the Jamaican Neogene plate boundary zone, *3rd Geological Conference of The Geological Society of Trinadad & Tobago*, Port of Spain, Trinidad, 16-21 July.

Alfaro, P., Delgado, J., Garia-Tortosa, E.J., Giner, J.J., Lenti, I., Lopez-Casado, C., Martino, S. (2012) Widespread landslides induced by the Mw 5.1 earthquake of 11 May 2011 in Lorca, SE Spain, *Engineering Geology*, 137-138, 40-52.

Alomax (March, 2006), *Location of the Focal Region and Hypocenter of the California Earthquake of April 18, 1906*, online available on: http://alomax.free.fr/posters/1906-focus/.

Anderson, H., Beanland, S., Buck, G., Darby, D., Downes, G., Haines, J., Jackson, J., Robinson, R., Webb, T. (1994) The 1968 May 23 Inangahua, New Zealand, earthquake: an integrated geological, geodetic, and seismological source model, *New Zealand Journal of Geology and Geophysics*, 37, 59-86.

Antonini, G., Ardizzone, F., Cardinali, M., Galli, M., Guzzetti, F., Reichenbach, P. (2002) Surface deposits and landslide inventory map of the area affected by the 1997 Umbria-Marche earthquakes, *Bollettino della Società Geologica Italiana e del Servizio Geologico d'Italia*, Volume special n. 1, 843-853.

Barnard, P.L., Owen, L.A., Sharma, M.C., Finkel, R.C. (2001) Natural and human-induced landsliding in the Garhwal Himalaya of northern India, *Geomorphology*, 40, 21-35.

Bhandari, R.K. (2010) Importance of earthquake induced landslides in landslide hazard mapping. In: *SAARC workshop on landslide risk management in South Asia*, Thimpu, 11-12 May.

Blumetti, A.M., Comerci, V., Di Manna, P., Guerrieri, L., Vittori, E. (2009) Geological effects induced by the L'aquila earthquake (6 April 2009, Ml = 5.8) on the natural environment, preliminary report, *Dipartimento Difesa del Suolo Servizio Geologica d'Italia*, Roma, 38pp.

Bommer, J.J., Benito, M.B., Ciudad-Real, M., Lemoine, A., Lopez-Menjivar, M.A., Madariaga, R., Mankelow, J., Mendez de Hasbun, P., Murphy, W., Nieto-Lovo, M., Rodriguez-Pineda, C.E., Rosa, H. (2002) The El Salvador earthquakes of January and February 2001: context, characteristics and implications for seismic risk, *Soil Dynamics and Earthquake Engineering*, 22, 389-418.

Bommer, J.J., Rodriguez, C.E. (2002) Earthquake induced landslides in Central America, *Engineering Geology*, 63, 189-220.

Bouhadad, Y., Nour, A., Slimani, A., Laouami, N., Belhai, D. (2004) The Boumerdes (Algeria) earthquake of May 21, 2003 (Mw = 6.8): Ground deformation and intensity, *Journal of SeismologyI*, 8, 497-506.

Cheng, T.C.T. (2009) Estimation of earthquake-induced landslide. In: *The next generation of research on earthquake-induced landslides: an international conference in commemoration of 10th anniversary of the Chi-Chi earthquake*, National Central University, Jhongli City, Taiwan, 21-26 September.

Chen, X.L., Zhou, Q., Ran, H., Dong, R. (2012) Earthquake-triggered landslides in southwest China, *Natural Hazards and Earth System Sciences*, 12, 351-363.

Chigira, M., Yagi, H. (2006) Geological and geomorphological characteristics of landslides triggered by the 2004 Mid Niigta prefecture earthquake in Japan, *Engineering Geology*, 82, 202-221.

Chigira, M., Wu, Xiyong, Inokuchi, T., Wang, G., (2010) Landslides induced by the 2008 Wenchuan earthquake, Sichuan, China, *Geomorphology*, 118, 225-238.

Chigira, M., Nakasuji, A., Fujiwara, S., Sakagami, M. (2013) Catastrophic landslides of pyroclastics induced by the 2011 off the Pacific Coast of Tohoku earthquake. In: Ugai, K., Yagi, H., Wakai, A. (Eds.) *Earthquake-Induced Landslides*, Springer-Verlag Berlin Heidelberg, Heidelberg, 996 pp.

cnki (2006) Earthquake Research in China, online available on: http://www.cnki.com.cn/.

Cole, W.F., Marcum, D.R., Shires, P.O., Cotton, Shires and Associates (1998) Analysis of earthquake-reactivated landslides in the epicentral region, central Santa Cruz mountains, California. In: Keefer, D.K. (Ed.) The *Loma Prieta, California, earthquake of October 17, 1989-Landslides*, United States Government Printing Office, Washington, 185pp.

Collins, B.D., Kayen, R., Tanaka, Y. (2012) Spatial distribution of landslides triggered from the 2007 Niigata Chuetsu-Oki Japan earthquake, *Engineering Geology*, 127, 14-26.

Dadson, S.J., Hovius, N., Chen, H., Dade, W.B., Lin, J.C., Hsu, M.L., Lin, C.W., Horng, M.J., Chen, T.C., Milliman, J., Stark, C.P. (2004) Earthquake-triggered increase in sediment delivery from an active mountain belt, *Geology*, 32, 733-736.

Dahal, R.K., Bhandary, N.P., Timilsina, M., Yatabe, R., Hasegawa, S. (2013) Earthquake-induced landslides in the roadside slopes of East Nepal after recent September 18, 2011 earthquake. In: Ugai, K., Yagi, H., Wakai, A. (Eds.) *Earthquake-Induced Landslides*, Springer-Verlag Berlin Heidelberg, Heidelberg, 996 pp.

Dai, F.C., Xu, C., Yao, X., Xu, L., Tu, X.B., Gong, Q.M. (2011) Spatial distribution of landslides triggered by the 2008 Ms 8.0 Wenchuan earthquake, China, *Journal of Asian Earth Sciences*, 40, 883-895.

Delgado, J., Garrido, J., Lopez-Casado, C., Martino, S., Pelaez, J.A. (2011a) On far field occurrence of seismically induced landslides, *Engineering Geology*, 123, 204-213.

Delgado, J., Pelaez, J.A., Tomas, R., Garcia-Tortosa, F.J., Alfaro, P., Lopez Casado, C. (2011b) Seismically-induced landslides in the Betic Cordillera (S Spain), *Soil Dynamics and Earthquake Engineering*, 31, 1203-1211.

Delvaux, D., Abdrakhmatov, K.E., Lenzin, I.N., Strom, A.L. (2001) Landslides and surface breaks of the 1911 Ms 8.2 Kemin earthquake (Kyrgyzstan), *Russian Geology and Geophysics*, 42, 1583-1592.

Dunning, S.A., Mitchell, W.A., Rosser, N.J., Petley, D.N. (2007) The Hattian Bala rock avalanche and associated landslides triggered by the Kashmir Earthquake of 8 October 2005, *Engineering Geology*, 93, 130-144.

Esposito, E., Porfido, S., Simonelli, A.L., Mastrolorenzo, G., Iaccarino, G. (2000) Landslides and other surface effects induced by the 1997 Umbria-Marche seismic sequence, *Engineering Geology*, 58, 353-376.

Esposito, E., Porfido, S., Livio, F., Martin, S., Michetti, A.M., Chunga, K., Fanetti, D., Gambillara, R., Sileo, G., Vittori, E. (2005) Ground effects of the MI 5.2, November 24, 2004 earthquake, Northern Italy: a case study for the use of the INQUA scale, *International Symposium on Active Faulting*, Hokudan, 17-24 January.

Evans, S.G., Roberts, N.J., Ischuk, A., Delaney, K.B., Morozova, G.S., Tutubalina, O. (2009) Landslides triggered by the 1949 Khait earthquake, Tajikistan, and associated loss of life, *Engineering Geology*, 109, 195-212.

FindTheData (September 24, 2013) *Compare Earthquakes,* online available on: http://earthquakes.findthedata.org/.

Fry, B., Bannister, S., Beavan, J., Bland, L., Bradley, B., Cox, S., Cousins, J., Gale, N., Hancox, G., Holden, C., Jongens, R., Power, W., Prasetya, G., Reyners, M., Ristau, J., Robinson, R., Samsonov, S., Wilson, K., Geonet team (2010) The Mw 7.6 Dusky Sound earthquake of 2009: preliminary report, *Bulletin of the New Zealand Society for Earthquake Engineering*, 43, 24-40.

Furumura, T., Takemura, S., Noguchi, S., Takemoto, T., Maeda, T., Iwai, K., Padhy, S. (2011) Strong ground motions from the 2011 off-the Pacific-Coast-of-Tohoku, Japan (Mw=9.0) earthquake obtained from a dense nationwide seismic network, *Landslides*, 8, 333-338.

Gerolymos, N. (2010) Earthquake-triggered violent landslides. In: Schmitter, E.D., Mastorakis, N. (Eds.) *Water and Geoscience*, University of Cambridge, UK, 23-25 February.

Godt, J., Sener, B., Verdin, K., Wald, D., Earle, P., Harp, E., Jibson, R. (2008) Rapid assessment of earthquake-induced landsliding. In: *Proceedings of the First World Landslide Forum*, United Nations University, Tokyo, 18-21 November.

Gorum, T., Fan, X., van Westen, C.J., Huang, R.Q., Xu, Q., Tang, C., Wang, G. (2011) Distribution pattern of earthquake-induced landslides triggered by the 12 May 2008 Wenchuan earthquake, *Geomorphology*, 133, 152-167.

Gorum, T., van Westen, C.J., Korup, O., van der Meijde, M., Fan, X., van der Meer, F.D. (2013) Complex rupture mechanism and topography control symmetry of mass-wasting pattern, 2010 Haiti earthquake, *Geomorphology*, 184, 127-138.

Gosar, A. (2012) Application of environmental seismic intensity scale (ESI 2007) to Krn Mountains 1998 Mw = 5.6 earthquake (NW Slovenia) with emphasis on rockfalls, *Natural Hazards and Earth System Sciences*, 12, 1659-1670.

Guzzetti, F., Esposito, E., Balducci, V., Porfido, S., Cardinali, M., Violante, C., Fiorucci, F., Sacchi, M., Ardizzone, F., Mondini, A., Reichenbach, P., Rossi, M. (2009) Central Italy seismic sequences-induced landsliding: 1997-1998 Umbria-Marche and 2008-2009 L'Aquila cases. In: *The next generation of research on earthquake-induced landslides: an international conference in commemoration of 10th anniversary of the Chi-Chi earthquake*, National Central University, Jhongli City, Taiwan, 21-26 September.

Hancox, G.T., Cox, S.C., Turnbull, I.M., Crozier, M.J. (2003) Reconnaissance studies of landslides and other ground damage caused by the Mw 7.2 Fiorland earthquake of 22 August 2003, *institute of Geological & Nuclear Sciences science report*, 32pp.

Hancox, G.T., Dellow, G., Mc Saveney, M., Scott, B., Villamor, P. (2004) Reconnaissance studies of landslides caused by the ML 5.4 Lake Rotoehu earthquake and swarm of July 2003, *institute of Geological & Nuclear Sciences science report*, 26pp.

Harp, E.L., Wilson, R.C., Wieczorek, G.F. (1981) Landslides from the Febrary 4, 1976, Guatemala earthquake, U.S. Geological Survey Professional Paper 1204-A, United States Government Printing Office, Washington, 34 pp.

Harp, E.L., Tanaka, K., Sarmiento, J.S., Keefer, D.K. (1984) Landslides from the May 25-27, 1980, Mammoth Lakes, California, earthquake sequence, U.S. Geological Survey Professional Paper 1204-A, United States Government Printing Office, Washington, 35pp.

Harp, E.L., Jibson, R.W. (1995) Inventory of landslides triggered by the 1994 Northridge, California earthquake, U.S. Gological Survey Open-File Report 95-213.

Harp, E.L., Jibson, R.W. (1996) Landslides triggered by the 1994 Northridge, California, earthquake, *Bulletin of the Seismological Society of America*, 86, S319-S332.

Has, B., Ogawa, K., Onoda, S., Noro, T., Maruyama, K., Nakamura, A. (2013) Characteristics of earthquake-induced landslides in heavy snowy area: the case of the Northern Nagano Prefecture earthquake, March 12, 2011, Japan. In: Ugai, K., Yagi, H., Wakai, A. (Eds.) *Earthquake-Induced Landslides*, Springer-Verlag Berlin Heidelberg, Heidelberg, 996 pp.

Havenith, H.B., Bourdeau, C. (2010) Earthquake-induced landslide hazards in mountain regions: a review of case histories from Central Asia, *Geologica Beligica*, 13, 135-150.

Hovius, N., Meunier, P., Lin, C.W., Chen, H., Chen, Y.G., Dadson S., Hongey, M.J., Lines, M. (2011) Prolonged seismically induced erosion and the mass balance of a large earthquake, *Earth and Planetary Science Letters*, 304, 347-355.

INGV (September 24, 2013) *Datasets*, online available on: http://istituto.ingv.it/the-institute/datasets/view?set_language=en.

IRIS (May 14, 2012) *SeismoArchives*, online available on: http://www.iris.edu/seismo/quakes/.

Jain, S.K., Murty, C.V.R., Arlekar, J.N., Rajendran, C.P., Rajendran, K., Sinha, R. (1999) Chamoli (Himalaya, India) earthquake of 29 March 1999, *EERI Special Earthquake Report, EERI, Newsletter*, 33, No.7.

Jibson, R.W., Prentice, C.S., Borissoff, B.A., Rogozhin, E.A., Langer, C.J. (1994) Some observations of landslides triggered by the 29 April 1991 Racha earthquake, Republic of Georgia, *Bulletin of the Seismological Society of America*, 84, 963-973.

Jibson, R.W., Harp, E.L., Schulz, W., Keefer, D.K. (2004) Landslides triggered by the 2002 Denali fault, Alaska, earthquake and the inferred nature of the strong shaking, *Earthquake Spectra*, 20, 669-691.

Jibson, R.W., Harp, E.L., Schulz, W., Keefer, D.K. (2006) Large rock avalanches triggered by the M 7.9 Denali fault, Alaska, earthquake of 3 November 2002, *Engineering Geology*, 83, 144-160.

Jibson, R.W., Harp, E.L. (2011) Field reconnaissance report of landslides triggered by the January 12, 2010, Haiti earthquake, *U.S. Geological Survey Open-File Report*, 19pp.

Jibson, R.W., Harp, E.L. (2012) Extraordinary distance limits of landslides triggered by the 2011 Mineral, Virginia, earthquake, *Bulletin of the Seismological Society of America*, 102, 2368-2377.

Kamp, U., Growley, B., Khattak, G.A., Owen, L.A. (2008) GIS-based landslide susceptibility mapping for the 2005 Kashmir earthquake region, *Geomorphology*, 101, 631-642.

Kanamori, H. (1977) The energy release in great earthquakes, Journal of Geophysical Research, 82, 2981-2987.

Keefer, D.K. (1984) Landslides caused by earthquakes, *Geological Society of America Bulletin*, 95, 406-421.

Keefer, D.K. (1994) The importance of earthquake-induced landslides to long-term slope erosion and slope-failure hazards in seismically active regions, *Geomorphology*, 10, 265-284.

Keefer, D.K. (1998) The Loma Prieta, California, Earthquake of October 17, 1989 - Landslides, U.S. Geological Survey Professional Paper 1551-C, United States Government Printing Office, Washington, 185pp.

Keefer, D.K. (2000) Statistical analysis of an earthquake-induced landslide distribution - the 1989 Loma Prieta, California event, *Engineering Geology*, 58, 231-249.

Keefer, D.K (2002) Investigating landslides caused by earthquakes- a historical review, *Surveys in geophysics*, 23, 473-510.

King, J., Loveday, I., Schuster, R.L. (1989) The 1985 Bairaman landslide dam and resulting debris flow, Papua New Guinea, *Quarterly Journal of Engineering Geology*, 22, 257-270.

Koukouvelas, I., Mpresiakas, A., Sokos, E., Doutsos, T. (1996) The tectonic setting and earthquake ground hazards of the 1993 Pyrgos earthquake, Peloponnese, Greece, *Journal of the Geological Society*, 153, 39-49.

Kuchai, O.A., Muraliev, A.M., Abdrakhmatov, K.E., Delvaux, D., Duchkov, A.D. (2002) The 1992 Suusamyr earthquake and the aftershock strain field, *Russian Geology and Geophysics*, 43, 1038-1048.

Lacroix, P., Zavala, B., Berthier, E., Audin, L. (2013) Supervised method of landslide inventory using panchromatic SPOT5 images and application to the earthquake-triggered landslides of Pisco (Peru, 2007, Mw 8.0), *Remote Sensing*, 5, 2590-2616.

Lei, C.I. (2012) Earthquake-triggered landslides, *Civil and Environmental engineering Student Conference*, London, 25-26 June.

Mahdavifar, M.R., Solaymani, S., Jafari, M.K. (2006) Landslides triggered by the Avaj, Iran earthquake of June 22, 2002, *Engineering Geology*, 86, 166-182.

Mahdavifar, M.R., Memarian, P. (2013) Assessment of earthquake-induced landslides triggered by Roudbar-Manjil earthquake in Rostamabad (Iran) quadrangle using knowledge-based hazard analysis approach. In: Ugai, K., Yagi, H., Wakai, A. (Eds.) *Earthquake-Induced Landslides*, Springer-Verlag Berlin Heidelberg, Heidelberg, 996 pp.

Malamud, B.D., Turcotte, D.L., Guzetti, F., Reichenbach, P. (2004) Landslides, earthquakes, and erosion, Earth and Planetary Science Letters, 229, 45-59.

Meunier, P., Hovius, N., Haines, J. (2007) Regional patterns of earthquake-triggerd landslides and their relation to ground motion, *Geophysical research letters*, 34, doi:10.1029/2007GL031337.

Mikos, M., Fazarinc, R. (2000) Earthquake-induced erosion processes in two alpine valleys in Slovenia, *internationals Symposion Interpraevent*, Villach/Austria, Tagungspubliation, 143-154.

Mikos, M., Fazarinc, R., Ribicic, M. (2006) Sediment production and delivery from recent large landslides and earthquake-induced rock falls in the Upper Soca River Valley, Slovenia, *Engineering Geology*, 86, 198-210.

Mousavi, S.M., Omidvar, B., Ghazban, F., Feyzi, R. (2011) Quantitative risk analysis for earthquake-induced landslides- Emamzadeh Ali, Iran, *Engineering Geology*, 122, 191-203.

Murphy, W. (1995) The geomorphological controls on seismically triggered landslides during the 1908 Straits of Messina earthquake, Southern Italy, *Quarterly Journal of Engineering Geology*, 28, 61-74.

NOAA (September 24, 2013) *Natural Hazards,* online available on: http://www.noaa.gov/.

Okada, Y., Ochiai, H., Kurokawa, U., Ogawa, Y., Asano, S. (2008) A channelised long run-out debris slide triggered by the Noto Hanto earthquake in 2007, Japan, *Landslides*, 5, 235-239.

Oldham, R.D. (1923) The Pamir earthquake of 18th February, 1911, *Quarterly Journal of the Geological Society*, 79, 237-245.

Owen, L.A., Kamp, U., Khattak, G.A., Harp, E.L., Keefer, D.K., Bauer, M.A. (2008) Landslides triggered by the 8 October 2005 Kashmir earthquake, *Geomorphology*, 94, 1-9.

Papathanassiou, G., PaVlides, S., Ganas, A. (2005) The 2003 Lefkada earthquake: Field observations and preliminary microzonation map based on liquefaction potential index for the town of Lefkada, *Engineering Geology*, 82, 12-31.

Parise, M., Wasowski, J. (2002) Slope movements triggered by the 1980 Irpinia earthquake. In: Comerci, V. (Ed.), *Seismically induced ground ruptures and large schael mass movements*, Italian Agency for Environment Protection and Technical Services, Roma, 111 pp.

Parker, R.N., Densmore, A.L., Rosser, N.J., Mechele, M.d., Li, Y., Hunag, R., Whadcoat, S., Petley, D.N. (2011) Mass wasting triggered by the 2008 Wenchuan earthquake is greater than orogenic growth, *Nature Geoscience*, 4, 449-452.

Parker, R.N. (2013) *Hillslope memory and spatial and temporal distributions of earthquake-induced landslides*, Durham theses, Durham University, Available at Durham E-Theses Online: http://etheses.dur.ac.uk/7761/.

Paterson, B.R., Berrill, J.B. (1995) Damage to State Highway 73 from the 29 May 1995, Arthur's Pass earthquake, *Bulletin of the New Zealand National Society for Earthquake Engineering*, 28, 300-310.

Pearce, A.J., O'Loughlin, C.L. (1985) Landsliding during a M 7.7 earthquake: influence of geology and topography, *Geology*, 13, 855-858.

Plafker, G. (1969) *Tectonics of the March 27, 1964 Alaska Earthquake*, U.S. Governement Printing Office, Washington D.C., 174 pp.

Plafker, G., Ericksen, G.E., Concha, J.F. (1971) Geological aspects of the May 31, 1970, Peru earthquake, *Bulletin of the Seismological society of America*, 61, 543-578.

Porfido, S., Esposito, E., Vittori, E., Tranfaglia, G., Michetti, A.M., Blumetti, M., Ferreli, L., Guerrieri, L., Serva, L. (2002) Areal distribution of ground effects induced by strong erathquakes in the Southern Apennines (Italy), *Surveys in Geophysics*, 23, 529-562.

Qi, S., Xu, Q., Lan, H., Zhang, B., Liu, J. (2010) Spatial distribution analysis of landslides triggered by 2008.5. 12 Wenchuan earthquake, China, *Engineering Geology*, 116, 96-108.

Ravindran, K.V., Philip, G. (1999) 29 March 1999 Chamoli earthquake A preliminary report on earthquake-induced landslides using IRS-1C1D data, *Current Science*, 77, 21-25.

Rodriguez, C.E., Bommer, J.J., Chandler, R.J. (1999) Earthquake-induced landslides: 1980–1997, *Soil Dynamics and Earthquake Engineering*, 18, 325-346.

Rodriguez, C.E. (2006) Earthquake-induced landslides in Colombia, *Proceedings Geohazards, Engineering Conference International*.

Rogozhin, E.A., Ovsychenko, A.N., Marakhanov, A.V., Novikov, S.S. (2009) Tectonic position and geological manifestations of the 2006 olyutor earthquake in Koryakia, *Geotectonics*, 43, 443-461.

Rymer, M.J., Ellsworht, W.L. (1990) *The Coalinga, California, earthquake of May 2, 1983*, U.S. Geological Survey Professional Paper 1487, United States Government Printing Office, Washington, 417 pp.

Saraf, A.K. (2000) IRS-1C-PAN depicts Chamoli earthquake induced landslides in Garhwal Himalayas, India, *International Journal of Remote Sensing*, 21, 2345-2352.

Sato, H.P., Hasegawa, H., Fujiwara, S., Tobita, M., Koarai, M., Une, H., Iwahashi, J. (2007) Interpretation of landslide distribution triggered by the 2005 Northern Pakistan earthquake using SPOT 5 imagery, *Landslides*, 4, 113-122.

Sato, G., Hayashi, K., Yagi, H., Higaki, D. (2013) Distribution of landslides induced in Iwaki City, Japan, by two large-scale earthquakes in 2011. In: Ugai, K., Yagi, H., Wakai, A. (Eds.) *Earthquake-Induced Landslides*, Springer-Verlag Berlin Heidelberg, Heidelberg, 996 pp.

Schuster, R.L., Nieto, A.S., O'Rourke, T.D., Crespo, E., Plaza-Nieto, G. (1995) Mass wasting triggerd by the 5 March 1987 Ecuador earthquakes, *Engineering Geology*, 42, 1-23.

Sepulveda, S.A., Serey, A., Lara, M., Pavez, A., Rebolledo, S. (2010) Landslides induced by the April 2007 Aysén Fjord earthquake, Chilean Patagonia, *Landslides*, 7, 483-492.

Tang, C., Zhu, J., Qi, X., Ding, J. (2011) Landslides induced by the Wenchuan earthquake and the subsequent strong rainfall event: A case study in the Beichuan area of China, *Engineering Geology*, 122, 22-33.

Tibaldi, A., Farrari, L., Pasquarè, G. (1995) Landslides triggered by earthquakes and their relations with faults and mountain slope geometry: an example from Ecuador, *Geomorphology*, 11, 215-226.

TRIGS (2009) Triggering instabilities in materials and geosystems, Sixth Framework Programme (FP6), New and Emerging Science and Technology Pathfinder, January 1, 2007 – June 30, 2009.

USGS & NOAA (1971) The San Fernando, California, earthquake of February 9, 1971, U.S. Geological Survey Professional paper 733, United States Government Printing Office, Washington, 254pp.

USGS (December 6, 2010) Overview of Large Landslides of the 20th and 21st Centuries, online available on: http://landslides.usgs.gov/learning/majorls.php.

USGS (September 12, 2011) *Earthquake Hazards Program*, online available on: http://earthquake.usgs.gov/earthquakes/pager/events/us/2010rja6/index.html16/08/2013.

USGS (November 1, 2012a) *HISTORIC EARTHQUAKES*, online available on: http://earthquake.usgs.gov/earthquakes/world/events/1950_08_15.php.

USGS (November 30, 2012b) *Largest earthquakes in the world since 1900*, online available on: http://earthquake.usgs.gov/earthquakes/world/10_largest_world.

USGS (October 23, 2013) *Earthquake Archive Search & URL Builder*, online available on: http://earthquake.usgs.gov/earthquakes/search/.

Vidrih, R., Ribicic, M. (2004) The earthquake of 12 July 2004 in Upper Soca territory (NW Slovenia)-preliminary geological and seismological characterstics, *Geologija*, 47, 199-220.

Wang, W.N., Wu, H.L., Nakamura, H., Wu, S.C., Ouyang, S., Yu, M.F. (2003) Mass movements caused by recent tectonic activity: the 1999 Chi-chi earthquake in central Taiwan, *The Island Arc*, 12, 325-334.

Wartman, J., Dunham, L., Tiwari, B., Pradel, D. (2013) Landslides in eastern Honshu induced by the 2011 off the Pacific Coast of Tohoku earthquake, *Bulletin of Seismological Society of America*, 103, 1503-1521.

Wick, E., Baumann, V., Jaboyedoff, M. (2010) Report on the impact of the 27 February 2010 earthquake (Chile, Mw 8.8) on rockfalls in the Las Cuevas valley, Argentina, *Natural Hazards and Earth System Sciences*, 10, 1989-1993.

Wiggins-Grandison, M.D. () The earthquake of January 13, 1993, and implications for earthquake hazard in eastern Jamaica. In: Ambeh, W.B. (ed.) *Proceedings of the Caribbean Conference on Natural Hazards: Volcanoes, Windstorms, Floods*, Trinidad, Seismic Research Unit, UWI - St. Augustine, October 11-15, 65-67.

Xu, C., Xu, X.W. (2012) Spatial prediction models for seismic landslides based on support vector machine and varied kernel functions: a case study of the 14 April 2010 Yushu earthquake in China, *Chinese Journal of Geophysics*, 55, 666-679.

Xu, C., Xu, X.W. (2013) Quantitative study on landslide volume, gravitational potential energy reduction, and resulting in regional centroid change triggered by 2010 Yushu earthquake, 科技导报, 31:2.

Yagi, H., Sato, G., Higaki, D., Yamamoto, M., Yamasaki, T. (2009) Distribution and characteristics of landslides induced by the Iwate-Miyagi Nairiku earthquake in 2008 in Tohou District, northeast Japan, *Landslides*, 6, 335-344.

Yin, Y. (2009) features of landslides triggered by the Wenchuan earthquake, *Journal of Engineering Geology*, 17, 29-38.

Yu, S.B., Kuo, L.C., Hsu, Y.J., Su, H.H., Liu, C.C., Hou, C.S., Lee, J.F., Lai, T.C., Liu, C.C., Liu, C.L., Tseng, T.F., Tsai, C.S., Shin, T.C. (2001) Preseismic deformation

and coseismic displacement associated with the 1999 Chi-Chi, Taiwan, earthquake, Bulletin of the Seismological Society of America, 91, 995-1012.

Zavala, B., Hermanns, R., Valderrama, P., Costa, C., Rosado, M. (2009) Procesos Geologicos e intensidad macrosismica inqua del sismo de pisco del 15/08/2007, Peru, *Revista de la Asociacion Geologica Argentina*, 65, 760-779.

Zupancic, P., Cecic, I., Gosar, A., Placer, L., Poljak, M., Zvcic, M. (2001) The earthquake of 12 April 1998 in the Krn Mountains (Upper Soca valley, Slovenia) and its seismotectonic characteristics, *Geologija*, 44, 169-192.

7 Appendix

Appendix 1

Overview of all earthquake events (n = 239) included in the earthquake landslide (E-L) dataset, ordered according to country, year of occurrence and magnitude. For each event the identifier (ID), date (year, month, day), epicenter location and magnitude (M) are indicated. It is also mentioned which events were used in the landslide volume (LV) model, moment magnitude – maximum landslide distance to epicenter (M-D) model and landslide distribution (LD) model (landslide inventory) with respectively 'v','d','i' (own processing).

ID	Country	Date			epicenter (°)		M (a)	models (b)	sources
		Year	Month	Day	latitude	longitude			
201	Afghanistan	1976	Mar	19	36.610	67.790	5.5	v	Keefer, 1984; NOAA, 2013; USGS, 2013
113	Algeria	2003	May	21	36.964	3.634	6.8	d	Delgado et al., 2011a; Bouhadad et al., 2004; NOAA, 2013
205	Argentina	1977	Nov	23	-31.030	-67.770	7,4*		Keefer, 1984; NOAA, 2013
222	Armenia	1988	Dec	7	40.987	44.185	6.7		Rodriguez et al., 1999; NOAA, 2013
190	Canada	1946	Jun	23	49.87	-124.92	7.6	v	Keefer, 1984; NOAA, 2013; USGS, 2013
221	Canada	1988	Nov	25	48.117	-71.183	5.8		Rodriguez et al., 1999; NOAA, 2013
185	Chile	1960	May	22	-38.29	-73.05	9.5	v	Keefer, 1984; USGS, 2012b; USGS, 2010
213	Chile	1985	Mar	3	-33.132	-71.708	8.1		Rodriguez et al., 1999; NOAA, 2013
122	Chile	2007	Apr	21	-45.240	-72.670	6.2	v,d	Delgado et al., 2011a; Sepulveda et al., 2010; USGS, 2013
126	Chile	2010	Feb	27	-35.9	-72.7	8.8	d	Wick et al., 2010; Delgado et al., 2011a
127	Chile	2010	Mar	11	-34.3	-71.9	6.9	d	Wick et al., 2010; Delgado et al., 2011a
128	Chile	2010	Mar	11	-34.3	-71.8	6.7	d	Wick et al., 2010; Delgado et al., 2011a
68	China	1515	Jun	27	26.7	100.7	7.75		Chen et al., 2012
69	China	1588	Aug	9	24	102.8	7		Chen et al., 2012
70	China	1652	Jul	13	25.2	100.6	7		Chen et al., 2012
71	China	1733	Aug	2	26.3	103.1	7.75		Chen et al., 2012
72	China	1789	Jun	7	24.2	102.9	7		Chen et al., 2012
73	China	1799	Aug	27	23.8	102.4	7		Chen et al., 2012
74	China	1833	Sep	6	25	103	8		Chen et al., 2012
75	China	1850	Sep	12	27.7	102.4	7.5		Chen et al., 2012

76	China	1887	Dec	16	23.7	102.5	7		Chen et al., 2012
77	China	1913	Dec	21	24.15	102.45	7		Chen et al., 2012
138	China	1920	Dec	16	36.601	105.317	7.8	v	Havenith & Bourdeau, 2010; USGS, 2013
78	China	1923	Mar	24	31.3	100.8	7.3		Chen et al., 2012
79	China	1925	Mar	16	25.7	100.2	7		Chen et al., 2012
80	China	1933	Aug	25	32	103.7	7.5	v	Chen et al., 2012; USGS, 2010; USGS, 2013
81	China	1941	May	16	23.7	99.4	7		Chen et al., 2012
82	China	1948	May	25	29.5	100.5	7.3		Chen et al., 2012
83	China	1955	Apr	14	30	101.9	7.5		Chen et al., 2012
84	China	1970	Jan	5	24	102.7	7.8		Chen et al., 2012
85	China	1973	Feb	6	31.48	100.53	7.6	v,i	Chen et al., 2012
86	China	1974	May	11	28.181	103.994	7.1	v,i	Chen et al., 2012; USGS, 2013
203	China	1976	Jul	27	39.570	117.980	7.5		Keefer, 1984; Kanamori, 1977; NOAA, 2013
87	China	1976	May	29	24.45	98.87	7.4		Chen et al., 2012
88	China	1976	Aug	16	32.61	104.13	7.2		Chen et al., 2012
215	China	1987	Jan	7	34.22	103.30	5.3		Rodriguez et al., 1999; cnki, 2006
89	China	1988	Nov	6	23.37	99.5	7.2		Chen et al., 2012
90	China	1996	Feb	3	27.083	100.267	7		Chen et al., 2012
91	China	2008	May	12	31.214	103.618	7.9	v,i	Chen et al., 2012; Dai et al., 2011; Parker et al., 2011; Chigira et al., 2010; Gorum et al., 2011; Qi et al., 2010; Tang et al., 2011; Yin, 2009; Parker, 2013; USGS, 2013
176	China	2010	Apr	14	33.165	96.548	6.9	v	Xu & Xu, 2012; Xu & Xu, 2013; NOAA, 2013; USGS, 2013
157	Colombia	1644	Mar	16	7.6	-73	6,0*		Rodriguez, 2006; FindTheData, 2013
158	Colombia	1785	Jul	12	4.6	-74	6,5*		Rodriguez, 2006; NOAA, 2013
159	Colombia	1834	Jan	20	1.2	-77	7,0*		Rodriguez, 2006; FindTheData, 2013
160	Colombia	1875	May	18	7.9	-72.5	7,5*		Rodriguez, 2006; NOAA, 2013
161	Colombia	1883	Mar	8	7	-76	6,0*		Rodriguez, 2006; NOAA, 2013
162	Colombia	1903	Dec	1	-	-	5,0*		Rodriguez, 2006
164	Colombia	1936	Jan	9	1.1	-77.6	7,0*		Rodriguez, 2006; NOAA, 2013
165	Colombia	1947	Jul	14	1.2	-77.2	5,5*		Rodriguez, 2006; NOAA, 2013
166	Colombia	1950	Jul	9	7.8	-72.5	7.0	d	Rodriguez, 2006; USGS, 2013; NOAA, 2013

167	Colombia	1962	Jul	30	5.2	-76.4	6.7		Rodriguez, 2006; USGS, 2013; NOAA, 2013
168	Colombia	1967	Feb	9	2.9	-74.9	7.2	d	Rodriguez, 2006; USGS, 2013; NOAA, 2013
169	Colombia	1970	Sep	26	6.2	-77.6	6.6	d	Rodriguez, 2006; USGS, 2013; NOAA, 2013
170	Colombia	1973	Apr	3	-	-	6.1	d	Rodriguez, 2006; USGS, 2013
172	Colombia	1979	Dec	12	1.598	-79.358	8.1	d	Rodriguez, 2006; USGS, 2013; NOAA, 2013
171	Colombia	1979	Nov	23	4.805	-76.217	7.2	d	Rodriguez, 2006; USGS, 2013; NOAA, 2013
173	Colombia	1983	Mar	31	2.461	-76.686	5.5	d	Rodriguez, 2006; USGS, 2013; NOAA, 2013
228	Colombia	1992	Oct	17	6.845	-76.806	6.7	d	Rodriguez et al., 1999; Rodriguez, 2006; NOAA, 2013
233	Colombia	1994	Jun	6	2.917	-76.057	6.8	d	Rodriguez et al., 1999; Rodriguez, 2006
235	Colombia	1995	Jan	19	5.050	-72.916	6.5	d	Rodriguez et al., 1999; Rodriguez, 2006; NOAA, 2013
174	Colombia	1999	Jan	25	4.461	-75.724	6.1	d	Rodriguez, 2006; USGS, 2013; NOAA, 2013
21	Costa Rica	1911	Oct	10	10.61	-84.89	6,5*		Bommer & Rodriguez, 2002
20	Costa Rica	1911	Aug	29	10.22	-84.30	5,8*		Bommer & Rodriguez, 2002
22	Costa Rica	1912	Jun	6	10.25	-84.30	5,1*		Bommer & Rodriguez, 2002
26	Costa Rica	1916	Feb	27	11.0	-86.0	7.3	d	Bommer & Rodriguez, 2002; USGS, 2013
30	Costa Rica	1924	Mar	4	9.8	-84.7	7.0	d	Bommer & Rodriguez, 2002; USGS, 2013
39	Costa Rica	1950	Oct	5	10.0	-85.7	7.8	d	Bommer & Rodriguez, 2002; USGS, 2013
41	Costa Rica	1952	Dec	30	10.05	-83.92	5,9*		Bommer & Rodriguez, 2002
42	Costa Rica	1955	Sep	1	10.25	-84.25	5,9*		Bommer & Rodriguez, 2002
48	Costa Rica	1973	Apr	14	10.47	-84.97	6.5	d	Bommer & Rodriguez, 2002; USGS, 2013
56	Costa Rica	1983	Apr	3	8.80	-83.11	7.5	d	Bommer & Rodriguez, 2002; USGS, 2013
57	Costa Rica	1983	Jul	3	9.40	-83.65	6.1	d	Bommer & Rodriguez, 2002; USGS, 2013
60	Costa Rica	1990	Jun	3	9.86	-84.38	5,1*		Bommer & Rodriguez, 2002
59	Costa Rica	1990	Mar	25	9.81	-84.83	7.1	d	Bommer & Rodriguez, 2002; USGS, 2013
61	Costa Rica	1991	Apr	22	9.69	-83.07	7.6	d	Bommer & Rodriguez, 2002; USGS, 2013
225	Costa Rica	1991	Apr	22	9.685	-83.073	7.5		Rodriguez et al., 1999; NOAA, 2013
62	Costa Rica	1993	Jul	10	9.80	-83.60	5.6	d	Bommer & Rodriguez, 2002; USGS, 2013
175	Ecuador	1987	Mar	5	0.083	-77.785	7.2	v	Schuster et al., 1995; Tibaldi et al., 1995; Keefer, 1994; Rodriguez et al., 1999; NOAA, 2013
163	Ecuador/Colombia	1906	Jan	31	1.0	-81.5	8.6	d	Rodriguez, 2006; USGS, 2013
25	El Salvador	1915	Sep	7	13.9	-89.6	7.4	d	Bommer & Rodriguez, 2002; USGS, 2013
29	El Salvador	1919	Apr	28	13.69	-89.19	5,9*		Bommer & Rodriguez, 2002

34	El Salvador	1936	Dec	20	13.72	-88.93	6,1*		Bommer & Rodriguez, 2002
40	El Salvador	1951	May	6	13.50	-88.36	5,9*		Bommer & Rodriguez, 2002
44	El Salvador	1965	May	3	13.70	-89.17	6,0*		Bommer & Rodriguez, 2002
55	El Salvador	1982	Jun	19	13.29	-89.39	7.3	d	Bommer & Rodriguez, 2002; USGS, 2013
58	El Salvador	1986	Oct	10	13.67	-89.18	5.4	v,d	Bommer & Rodriguez, 2002; Keefer, 1994; Keefer, 2002; Rodriguez et al., 1999
65	El Salvador	2001	Jan	13	13.049	-88.660	7.7		Bommer & Rodriguez, 2002; Bommer et al., 2002; Jibson et al., 2004
66	El Salvador	2001	Feb	13	13.671	-88.938	6.5	v	Bommer et al., 2002; Jibson et al., 2004
142	Georgia	1991	Apr	29	42.453	43.673	7.1	v	Jibson et al., 1994
214	Greece	1986	Sep	13	37.014	22.176	6.0		Rodriguez et al., 1999; NOAA, 2013
220	Greece	1988	Oct	16	37.938	20.932	5.9		Rodriguez et al., 1999; NOAA, 2013
145	Greece	1993	Mar	26	37.7	21.5	5.4	v	Koukouvelas et al., 1996; USGS, 2013
120	Greece	2003	Aug	14	38.79	20.56	6.2	d	Delgado et al., 2011a; Papathanassiou et al., 2005
18	Guatemala	1902	Apr	19	14.9	-91.5	7.5	d	Bommer & Rodriguez, 2002; USGS, 2013
28	Guatemala	1917	Dec	26	14.53	-90.53	5,6*		Bommer & Rodriguez, 2002
36	Guatemala	1942	Aug	6	14.8	-91.3	7.7	d	Bommer & Rodriguez, 2002; USGS, 2013
37	Guatemala	1945	Aug	10	15.25	-89.13	5,7*		Bommer & Rodriguez, 2002
51	Guatemala	1976	Feb	4	15.28	-89.19	7.6	v,d	Bommer & Rodriguez, 2002: Keefer, 2002; Godt et al., 2008; Keefer, 1984; Keefer, 1994; USGS, 2012a
140	Haiti	2010	Jan	12	18.443	-72.571	7	v,d,i	USGS, 2011, Jibson & Harp, 2011; Gorum et al., 2013; USGS, 2013
198	Hawaii	1973	Apr	26	19.936	-155.098	6,1*		Keefer, 1984; NOAA, 2013
200	Hawaii	1975	Nov	29	19.334	-155.024	7.5	v	Keefer, 1984; NOAA, 2013; USGS, 2013
16	India	1991	Oct	19	30.780	78.774	7,0*	v	Bhandari, 2010; NOAA, 2013
17	India	1999	Mar	29	30.49	79.28	6.8	v	Bhandari, 2010; Jain et al., 1999; Ravindran & Philip, 1999; Saraf, 2000
13	India	1999	Mar	28	30.49	79.29	6.5		Barnard et al., 2001; USGS, 2013
204	Iran	1977	Mar	21	27.610	56.390	6.7	v	Keefer, 1984; NOAA, 2013; USGS, 2013
148	Iran	1990	June	21	36.820	49.410	7.3	v	Mahdavifar & Memarian, 2013; Mousavi et al., 2011; Rodriguez et al., 1999; USGS, 2013
114	Iran	2002	Jun	22	35.67	48.93	6.5	v,d,i	Delgado et al., 2011a; Mahdavifar et al., 2006
154	Italy	1805	Jul	26	41.5	14.47	6.8		Porfido et al., 2002; INGV, 2013

155	Italy	1857	Dec	16	40.35	15.85	6.9	d	Porfido et al., 2002; INGV, 2013
152	Italy	1908	Dec	28	38.15	15.68	7.0	v,d	Murphy, 1995; INGV, 2013; USGS, 2013
11	Italy	1930	Jul	23	41.050	15.370	6.7	d,i	Esposito et al., 2009; Delgado et al., 2011a
202	Italy	1976	May	6	46.241	13.119	6.5	v	Keefer, 1984; INGV, 2013; USGS, 2013
12	Italy	1980	Nov	23	41.083	15.617	6.9	v,d	Esposito et al., 2000; Parise & Wasowski, 2002; Esposito et al., 1980; Rodriguez et al., 1999; Porfido et al., 2002
10	Italy	1997	Sep	26	42.970	12.840	6	v,d,i	Antonini et al., 2002; Esposito et al., 2000, Rodriguez et al., 1999; Guzzetti et al., 2009
238	Italy	1997	Oct	14	42.930	12.875	5.6	v,i	Guzzetti et al., 2009; USGS, 2013
115	Italy	2002	Sep	6	38.081	13.422	5.89	d	Delgado et al., 2011a; INGV, 2013
116	Italy	2002	Oct	31	41.694	14.925	5.78	d	Delgado et al., 2011a; INGV, 2013
156	Italy	2004	Nov	24	45.6	10.5	5		Esposito et al., 2005
125	Italy	2009	Apr	6	42.334	13.334	6.3	v,d,i	Blumetti et al., 2009; Guzzetti et al., 2009; NOAA, 2013
237	Jamaica	1993	Jan	13	18.060	-76.766	5.4		Ahmad, 1995; Wiggins-Grandison, 1993
191	Japan	1948	Jun	28	36.142	136.144	7.0	v	Keefer, 1984; USGS, 2013
195	Japan	1964	Jun	16	38.65	139.19	7,3*		Keefer, 1984; FindTheData, 2013
206	Japan	1978	Jan	14	34.809	139.259	6.7	v	Keefer, 1984; NOAA, 2013; USGS, 2013
212	Japan	1984	Sep	14	35.789	137.488	6.2		Rodriguez et al., 1999; USGS, 2013
229	Japan	1993	Jul	12	42.851	139.197	7.8		Rodriguez et al., 1999; NOAA, 2013
184	Japan	1995	Jan	17	34.583	135.018	6.9	v	Keefer, 2002; Rodriguez, 1999; Malamud et al, 2004a; Gerolymos, 2010; NOAA, 2013
93	Japan	2004	Oct	23	37.226	138.779	6.6	v,d	Chigira & Yagi, 2006; NOAA, 2013
95	Japan	2007	Jul	16	37.493	138.603	6.6	v,d,i	Collins et al., 2012; Lei, 2012; USGS, 2013
153	Japan	2007	Mar	25	37.340	136.540	6.6	v	Okada et al., 2008; USGS, 2013
124	Japan	2008	Jun	14	39.02	140.88	7.2	v	Yagi et al., 2009
94	Japan	2011	Mar	11	38.10	142.86	9.0	v,d	Chigira et al., 2013; Wartman et al., 2013; Furumura et al., 2011; Lei, 2012; Sato et al., 2013
133	Japan	2011	Mar	12	37.0	138.6	6.7	v,d,i	Has et al., 2013
207	Japan	1978	Jun	12	38.190	142.028	7,4*		Keefer, 1984; NOAA, 2013
134	Kazakhstan	1911	Jan	3	43.5	77.5	7.8		Havenith & Bourdeau, 2010; Delvaux et al., 2001; USGS, 2013

137	Kyrgyzstan	1992	Aug	19	42.110	73.607	7	v	Havenith & Bourdeau, 2010; Kuchai et al., 2002; Rodriguez et al., 1999; USGS, 2013
31	Mexico	1931	Jan	15	16.10	-96.64	7.8	d	Bommer & Rodriguez, 2002; USGS, 2013
43	Mexico	1959	Aug	26	18.45	-94.27	6.7	d	Bommer & Rodriguez, 2002; USGS, 2013
47	Mexico	1973	Jan	30	18.53	-102.93	7.6	d	Bommer & Rodriguez, 2002; USGS, 2013
53	Mexico	1978	Nov	29	15.76	-96.78	7.8	d	Bommer & Rodriguez, 2002; USGS, 2013
54	Mexico	1979	Mar	14	17.76	-101.29	7.5	d	Bommer & Rodriguez, 2002; USGS, 2013
63	Mexico	1995	Oct	9	19.06	-104.21	8.0	d	Bommer & Rodriguez, 2002; USGS, 2013
64	Mexico	1999	Jun	15	18.41	-97.34	7.0	d	Bommer & Rodriguez, 2002; USGS, 2013
119	Mexico	2003	Jan	21	18.770	-104.104	7.6	v,d	Keefer et al., 2006; Delgado et al., 2011a; NOAA, 2013
188	Nepal	1934	Jan	15	26.773	86.762	8.1	v	Keefer, 1984; NOAA, 2013
219	Nepal	1988	Aug	21	26.755	86.616	6.8		Rodriguez et al., 1999; NOAA, 2013
146	Nepal	2011	Sep	18	27.73	88.08	6.9		Dahal et al., 2013; USGS, 2013
5	New Zealand	1820	-	-	-41.6	171.8	7.4		Adams, 1980
6	New Zealand	1855	Jan	-	-41.0	175.4	8		Adams, 1980
7	New Zealand	1929	Mar	9	-42.8	171.85	6.9	v	Adams, 1980; Keefer, 1994; Rodriguez et al., 1999
8	New Zealand	1929	Jun	17	-41.7	172.2	7.7	v,i	Adams, 1980; Keefer, 1994; Anderson et al., 1994; Pearce & Loughlin, 1985; Parker, 2013; USGS, 2013
9	New Zealand	1968	May	23	-41.83	171.97	7.1	v,i	Adams, 1980; Keefer, 1984; Keefer, 1994; Parker, 2013
216	New Zealand	1987	Mar	2	-37.965	176.765	6.5		Rodriguez et al., 1999; NOAA, 2013
231	New Zealand	1993	Aug	10	-45.219	167.007	6.8		Rodriguez et al., 1999
230	New Zealand	1993	Aug	10	-38.495	177.795	6.2		Rodriguez et al., 1999
234	New Zealand	1994	Jun	18	-42.963	171.658	6.8		Rodriguez et al., 1999; NOAA, 2013
236	New Zealand	1995	May	29	-40.90	171.40	6,5*		Rodriguez et al., 1999; Paterson & Berrill, 1995
132	New Zealand	2003	Aug	22	-45.13	166.93	7.2	v,d	Hancox et al., 2003
240	New Zealand	2003	Aug	21	-45.200	167.140	7	i	Trigs, 2009; USGS, 2013
239	New Zealand	2004	Jul	18	-38.00	176.53	5.4	v,i	Hancox et al., 2004; USGS, 2013
130	New Zealand	2009	Jul	15	-45.762	166.562	7.6	v,d,i	Fry et al., 2010; NOAA, 2013
147	New Zealand	2011	Feb	22	-43.583	172.680	6.3		Lei, 2012; USGS, 2013
32	Nicaragua	1931	Mar	31	12.15	-86.28	6,2*		Bommer & Rodriguez, 2002
38	Nicaragua	1947	Jan	26	12.2	-86.3	7.0	d	Bommer & Rodriguez, 2002; USGS, 2013

45	Nicaragua	1968	Jan	4	11.76	-86.61	4,6"		Bommer & Rodriguez, 2002
46	Nicaragua	1972	Dec	23	12.15	-86.28	6.2	d	Bommer & Rodriguez, 2002; USGS, 2013
49	Nicaragua	1974	Mar	6	12.33	-86.42	5.7	d	Bommer & Rodriguez, 2002; USGS, 2013
199	Pakistan	1974	Dec	28	35.025	72.901	6.2	v	Keefer, 1984; USGS, 2013
67	Pakistan	2005	Oct	8	34.493	73.629	7.6	v	Dunning et al., 2007; Kamp et al., 2008; Owen et al., 2008; Lei, 2012; Sato et al., 2007
19	Panama	1904	Dec	20	7.0	-82.0	7.2	d	Bommer & Rodriguez, 2002; USGS, 2013
23	Panama	1913	Oct	2	7.1	-80.6	6,7*		Bommer & Rodriguez, 2002
24	Panama	1914	May	28	8.0	-80.0	6.9	d	Bommer & Rodriguez, 2002; USGS, 2013
27	Panama	1916	Apr	26	9.2	-83.1	7.1	d	Bommer & Rodriguez, 2002; USGS, 2013
33	Panama	1934	Jul	18	8.1	-82.6	7.6	d	Bommer & Rodriguez, 2002; USGS, 2013
35	Panama	1941	Dec	5	8.7	-83.2	7.3	d	Bommer & Rodriguez, 2002; USGS, 2013
50	Panama	1974	Jul	13	7.76	-77.57	7.2	d	Bommer & Rodriguez, 2002; USGS, 2013
52	Panama	1976	Jul	11	7.48	-78.28	7.0	v,d	Bommer & Rodriguez, 2002; Keefer, 1984; Keefer, 1994
178	Papua New Guinea	1935	Sep	20	-3.920	141.330	7.9	v	Keefer, 1994; USGS, 2013
180	Papua New Guinea	1970	Oct	31	-4.907	145.469	7.1	v	Keefer, 1984; Keefer, 1994; USGS, 2013
144	Papua New Guinea	1985	May	11	-5.579	151.081	7.2	d	King et al., 1989; USGS, 2013
149	Papua New Guinea	1993	Oct	13	-5.889	146.020	6.9	v	Meunier et al., 2007; NOAA, 2013
139	Peru	1970	May	31	-9.248	-78.842	7.9	v	Havenith & Bourdeau, 2010; Plafker et al., 1971; Keefer, 1984; Keefer, 1994; USGS, 2010; USGS, 2013
123	Peru	2007	Aug	15	-13.66	-76.75	7.9	v,d,i	Zavala et al., 2009; Delgado et al., 2011a; Lacroix et al., 2013
224	Philippines	1990	Jul	16	15.679	121.172	7.7		Rodriguez et al., 1999; NOAA, 2013
121	Russia	2006	Apr	20	60.949	167.089	7.6		Rogozhin et al., 2009; Delgado et al., 2011a; NOAA, 2013
131	Slovenia	1998	Apr	12	46.309	13.632	5.6	v,i	Mikos & Fazarinc, 2000; Zupancic et al., 2001; Gosar, 2012
150	Slovenia	2004	Jul	12	46.32	13.63	5.2	v,i	Mikos et al., 2006; Vidrih & Ribicic, 2004; USGS, 2013
96	Spain	1504	Apr	5	37.383	-5.467	6.9	d	Delgado et al., 2011b
97	Spain	1518	Nov	9	37.233	-1.867	6.1	d	Delgado et al., 2011b
98	Spain	1620	Dec	2	38.700	-0.467	5.5	d	Delgado et al., 2011b
99	Spain	1680	Oct	9	36.800	-4.600	6.8	d	Delgado et al., 2011b

100	Spain	1748	Mar	23	39.033	-0.633	6.2	d	Delgado et al., 2011b
101	Spain	1755	Nov	1	36.500	-10.000	8.7	d	Delgado et al., 2011b
102	Spain	1804	Aug	25	36.767	-2.833	6.4	d	Delgado et al., 2011b
103	Spain	1829	Mar	21	38.083	-0.683	6.6	d	Delgado et al., 2011b
104	Spain	1863	Jun	10	37.367	-1.933	4.2	d	Delgado et al., 2011b
105	Spain	1884	Dec	25	37.000	-3.983	6.5	d	Delgado et al., 2011b
106	Spain	1945	Jul	1	38.800	-0.583	4.8	d	Delgado et al., 2011b
107	Spain	1956	Apr	19	37.192	-3.683	5	d	Delgado et al., 2011b
108	Spain	1964	Jun	9	37.737	-2.567	4.8	d	Delgado et al., 2011b
109	Spain	1984	Jun	24	36.838	-3.738	5	d	Delgado et al., 2011b
2	Spain	1999	Feb	2	38.11	-1.49	4.7	v	Alfaro et al., 2012
110	Spain	1999	Feb	2	38.096	-1.501	4.7	d	Delgado et al., 2011b
3	Spain	2002	Aug	6	37.88	-1.83	5.0	v	Alfaro et al., 2012
111	Spain	2002	Aug	6	37.883	-1.830	5	d	Delgado et al., 2011b
4	Spain	2005	Jan	29	37.93	-1.76	4.8	v	Alfaro et al., 2012
112	Spain	2005	Jan	29	37.854	-1.756	4.8	d	Delgado et al., 2011b
1	Spain	2011	May	11	37.69	-1.68	5.1	v,d,i	Alfaro et al., 2012
92	Taiwan	1999	Sep	21	23.85	120.82	7.6	v,d,i	Yu et al., 2001; Wang et al., 2003; Keefer, 2002, Hovius et al., 2011; Cheng, 2009 ; Delgado et al., 2011a; Hung, 2010; Dadson et al., 2004
135	Tajikistan	1911	Feb	18	39	71.5	7,6*		Havenith & Bourdeau, 2010; ADRC, 2013; Oldham, 1923
129	Tajikistan	1949	Jul	10	39.180	70.708	7.4	v	Evans et al., 2009; USGS, 2013
223	Tajikistan	1989	Jan	23	38.465	68.694	5.5		Rodriguez et al., 1999; NOAA, 2013; USGS, 2013
15	Tibet	1950	Aug	15	28.290	96.657	8.6	v	Bhandari, 2010; USGS, 2012a; Keefer, 1994; Keefer, 1984; USGS, 2013
226	Turkey	1992	Mar	13	39.710	39.605	6.7		Rodriguez et al., 1999; NOAA, 2013
177	United States	1812	Feb	7	-	-	7,8*		Keefer, 1984
186	United States	1886	Sep	1	32.9	-80.0	6,8*		Keefer, 1984; USGS, 2013
187	United States	1906	Apr	18	37.75	-122.55	7.9		Keefer, 1984; Kanamori, 1977; Alomax, 2006
189	United States	1940	May	19	32.733	-115.5	7.1	v	Keefer, 1984; NOAA, 2013; USGS, 2013
192	United States	1949	Apr	13	47.167	-122.617	6.5	v	Keefer, 1984; NOAA, 2013; USGS, 2013
179	United States	1957	Mar	22	37.67	-122.48	5.3	v	Keefer, 1984; Keefer, 1994; Keefer, 2002; IRIS, 2012

193	United States	1958	Jul	10	58.34	-136.52	7.7		Keefer, 1984; Kanamori, 1977; NOAA, 2013
194	United States	1959	Aug	18	44.712	-111.215	7,1*		Keefer, 1984; NOAA, 2013
14	United States	1964	Mar	27	61.06	-147.44	9.2	d	Barnhardt&Kayen, 2000; Plafker, 1969; Jibson et al., 2006; Keefer, 1984; USGS, 2010
196	United States	1965	Apr	29	47.400	-122.300	6.5	v	Keefer, 1984; NOAA, 2013; USGS, 2013
197	United States	1966	Jun	28	35.87	-120.48	5.6	v	Keefer, 1984; IRIS, 2012
151	United States	1971	Feb	9	34.412	-118.4	6.5	v	U.S. Geological Survey, 1971; Keefer, 1984; USGS, 2013; NOAA, 2013
208	United States	1978	Aug	13	34.350	-119.700	5,6*		Keefer, 1984; NOAA, 2013
209	United States	1979	Mar	15	34.317	-116.450	5.6	v	Keefer, 1984; USGS, 2013
210	United States	1979	Aug	6	37.070	-121.598	5.5	v	Keefer, 1984; USGS, 2013
181	United States	1980	May	25	37.600	-118.840	6.2	v,i	Keefer, 1984; Keefer, 1994; Keefer, 2002; NOAA, 2013
183	United States	1980	Jan	24	37.855	-121.816	5.6	v	Keefer, 1984; Keefer, 2002; NOAA, 2013; USGS, 2013
211	United States	1983	Oct	28	43.974	-113.916	6.9		Rodriguez et al., 1999; NOAA, 2013
182	United States	1983	May	2	36.219	-120.317	6.5	v,i	Keefer, 1994; Keefer, 2002; Rodriguez et al., 1999; NOAA, 2013
218	United States	1987	Nov	24	33.082	-115.775	6.2		Rodriguez et al., 1999; NOAA, 2013
217	United States	1987	Oct	1	34.061	-118.078	6.1		Rodriguez et al., 1999; NOAA, 2013
143	United States	1989	Oct	17	37.036	-121.883	7.0	v,i	Cole et al., 1998; Keefer, 1994; Keefer, 2002; Keefer, 2000; Rodriguez et al., 1999; NOAA, 2013
227	United States	1992	Apr	25	40.368	-124.316	7.0		Rodriguez et al., 1999; NOAA, 2013
232	United States	1993	Sep	21	42.314	-122.012	5.9		Rodriguez et al., 1999; NOAA, 2013
118	United States	1994	Jan	17	34.213	-118.537	6.7	v,i	Jibson et al., 2006; Keefer, 2002; Godt et al., 2008; Harp & Jibson 1996; Rodriguez et al., 1999; Malamud et al., 2004a; NOAA, 2013; Parker, 2013
117	United States	2002	Nov	3	63.517	-147.444	7.9	v,d	Delgado et al., 2011a; Jibson et al., 2006; NOAA, 2013
141	United States	2011	Aug	23	37.936	-77.933	5.8	d	Jibson & Harp, 2012; USGS, 2013

(a) Magnitudes are expressed in moment magnitude (M_w) be it conditionally as some might not be real moment magnitudes according to the USGS (2013a). Next to this, surface-wave magnitudes (M_s) are indicated by an asterisk (*) and body-wave magnitudes (M_b) are indicated by a quotation mark (“).

Appendix 2

Landslide probability maps for all events in Table 5, except from events 85 and 181 displayed in Figure 33, with mapped landslides indicated by the black dots or by a separate plot at the left for events 8, 9, 91, 92 (for ID's see Table 5), coordinates are in the UTM projection (Table 5, own processing).

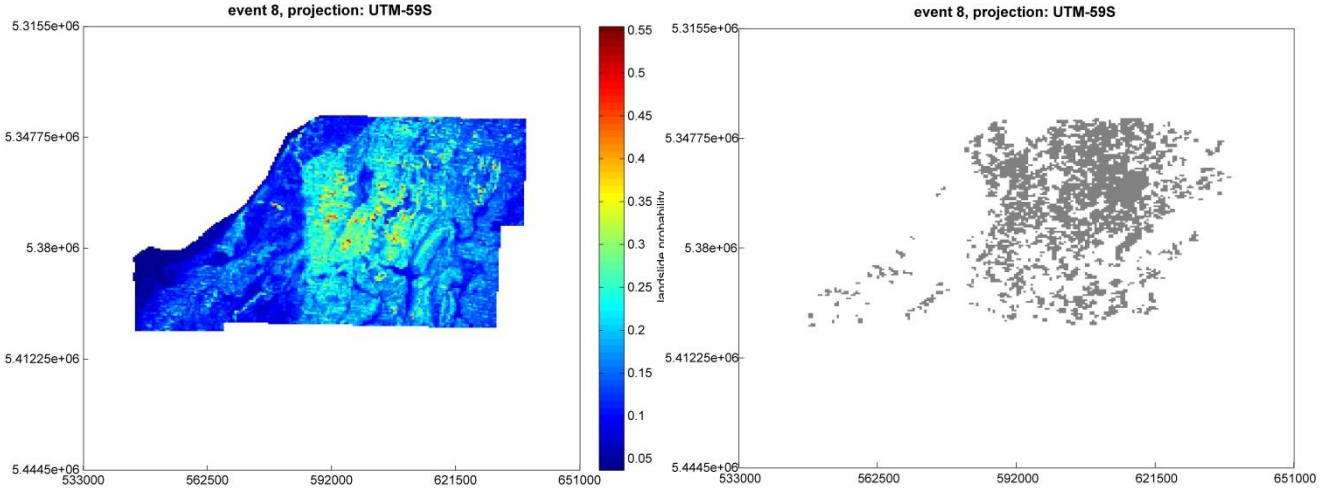

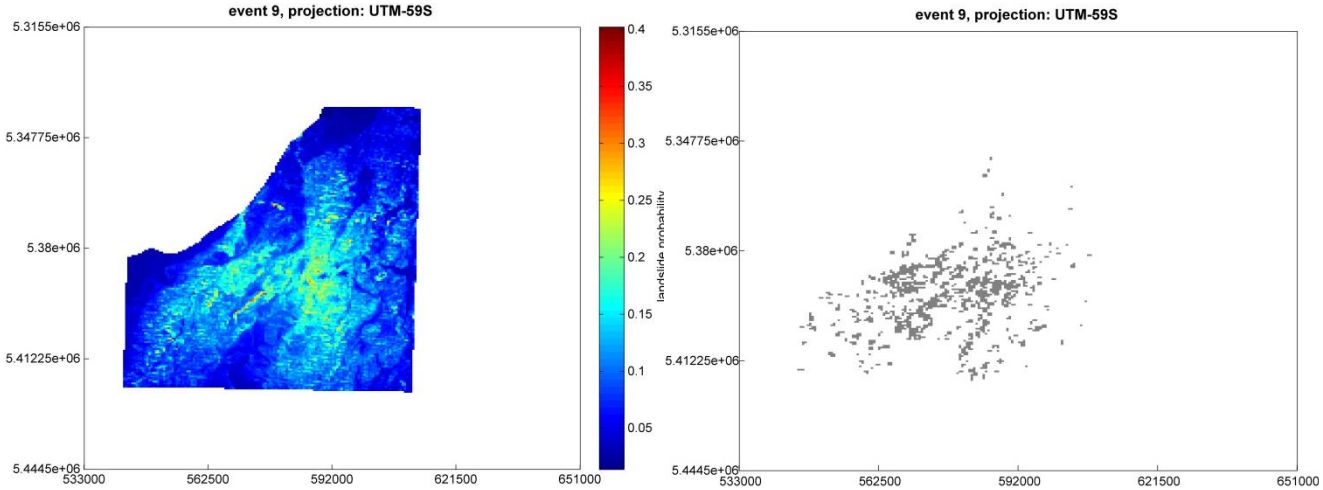

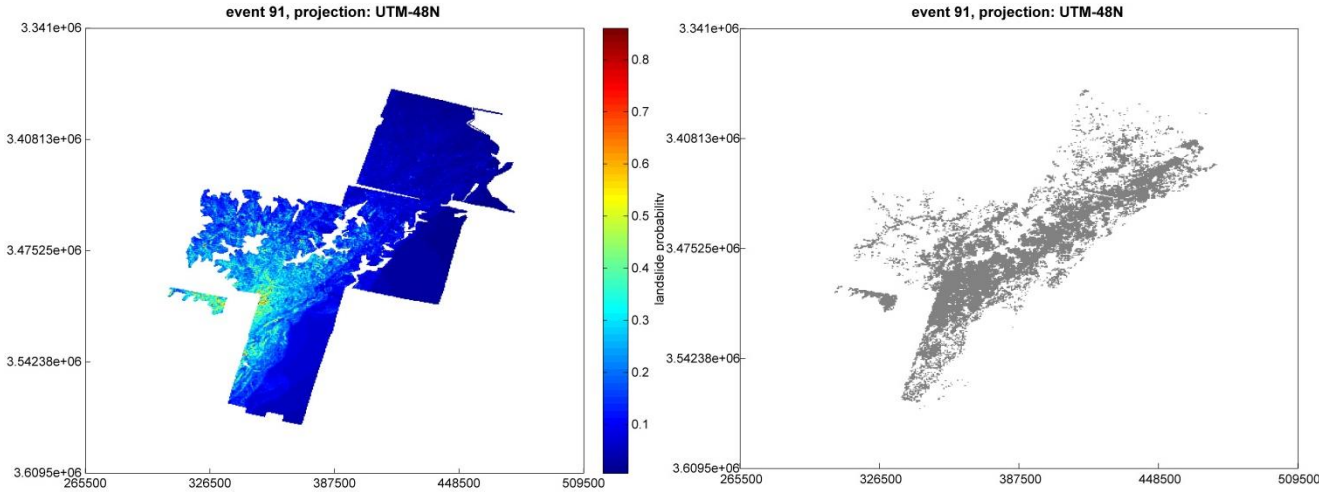

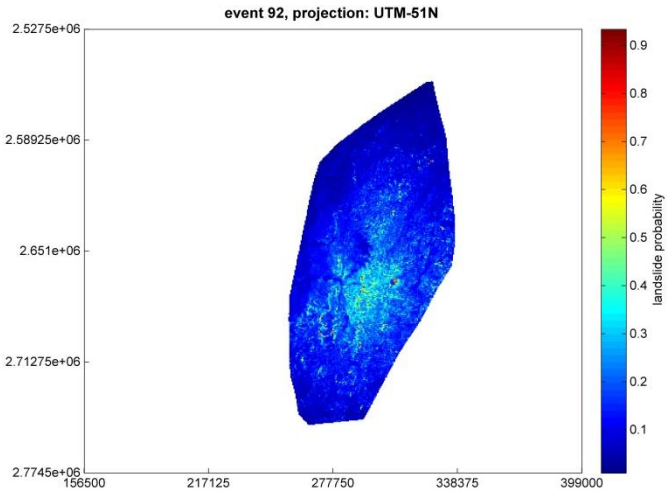
event 92, projection: UTM-51N
2.5275e+06
2.58925e+06
2.651e+06
2.71275e+06
2.7745e+06
156500
217125
277750
338375
399000
landslide probability
0.9
0.8
0.7
0.6
0.5
0.4
0.3
0.2
0.1

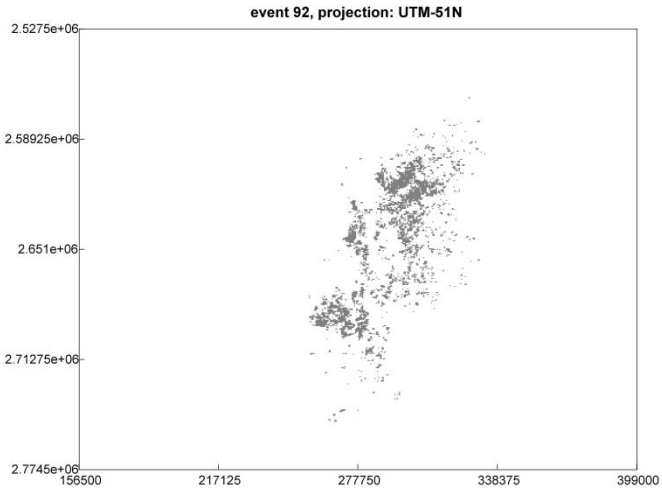
event 92, projection: UTM-51N
2.5275e+06
2.58925e+06
2.651e+06
2.71275e+06
2.7745e+06
156500
217125
277750
338375
399000

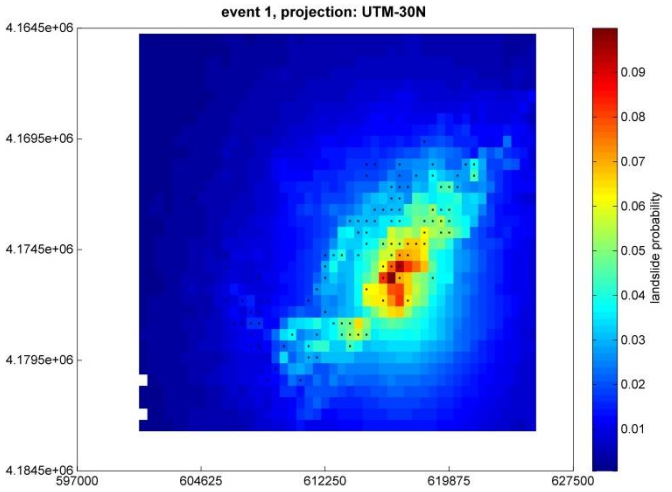
event 1, projection: UTM-30N
4.1645e+06
4.1695e+06
4.1745e+06
4.1795e+06
4.1845e+06
597000
604625
612250
619875
627500
landslide probability
0.09
0.08
0.07
0.06
0.05
0.04
0.03
0.02
0.01

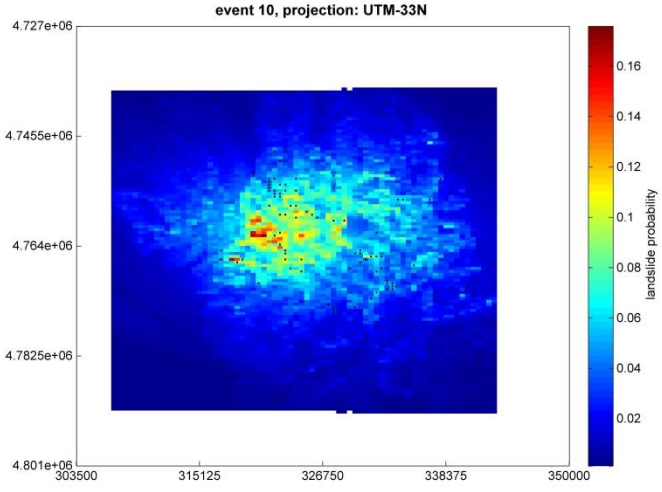
event 10, projection: UTM-33N
4.727e+06
4.7455e+06
4.764e+06
4.7825e+06
4.801e+06
303500
315125
326750
338375
350000
landslide probability
0.16
0.14
0.12
0.1
0.08
0.06
0.04
0.02

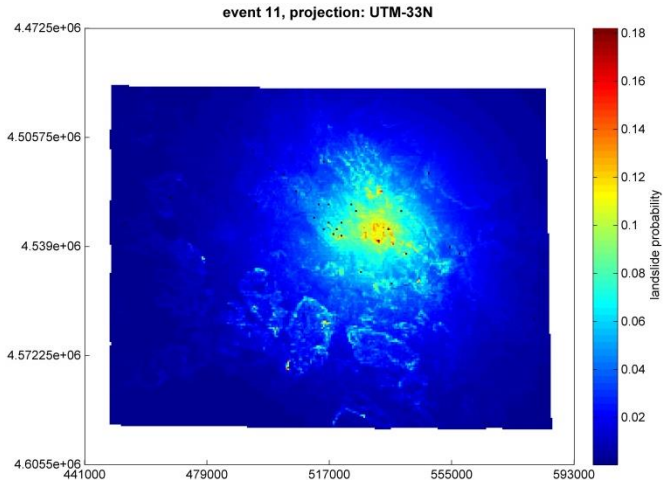
event 11, projection: UTM-33N
4.4725e+06
4.50575e+06
4.539e+06
4.57225e+06
4.6055e+06
441000
479000
517000
555000
593000
landslide probability
0.18
0.16
0.14
0.12
0.1
0.08
0.06
0.04
0.02

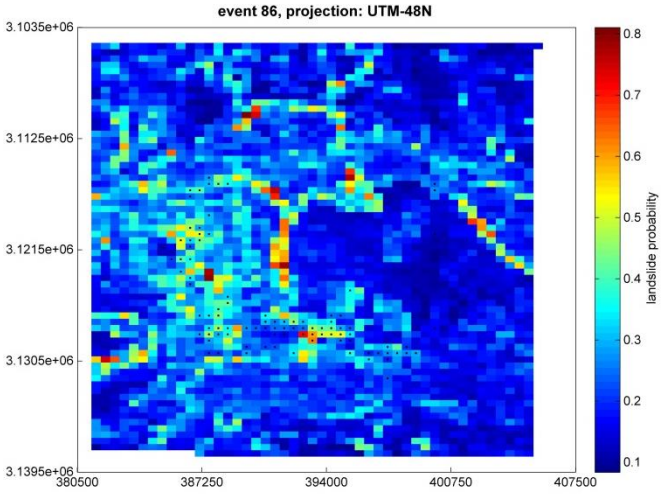
event 86, projection: UTM-48N
3.1035e+06
3.1125e+06
3.1215e+06
3.1305e+06
3.1395e+06
380500
387250
394000
400750
407500
landslide probability
0.8
0.7
0.6
0.5
0.4
0.3
0.2
0.1

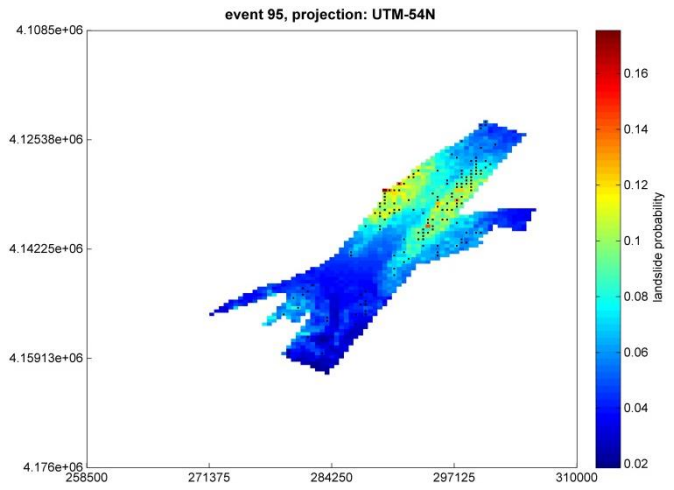
event 95, projection: UTM-54N
4.1085e+06
4.12538e+06
4.14225e+06
4.15913e+06
4.176e+06
258500
271375
284250
297125
310000
0.16
0.14
0.12
0.1
0.08
0.06
0.04
0.02
landslide probability

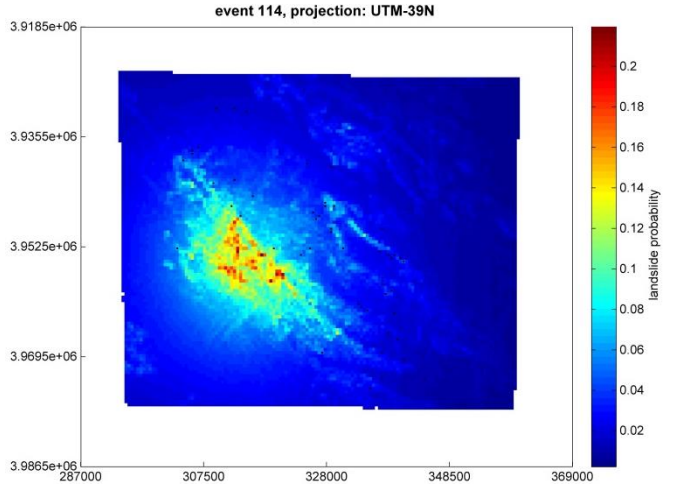
event 114, projection: UTM-39N
3.9185e+06
3.9355e+06
3.9525e+06
3.9695e+06
3.9865e+06
287000
307500
328000
348500
369000
0.2
0.18
0.16
0.14
0.12
0.1
0.08
0.06
0.04
0.02
landslide probability

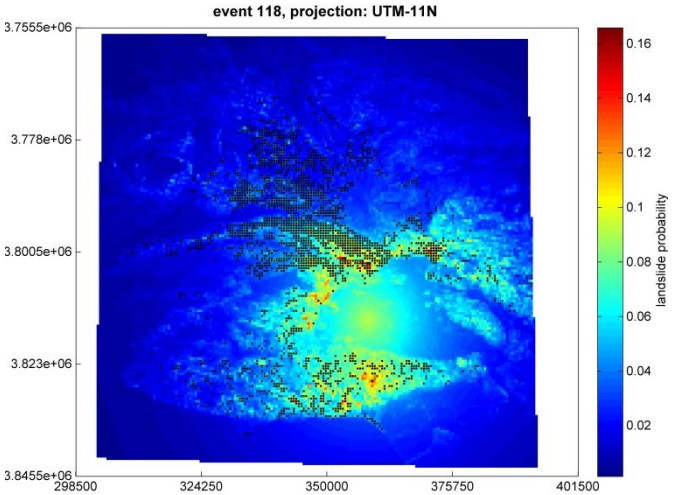
event 118, projection: UTM-11N
3.7555e+06
3.778e+06
3.8005e+06
3.823e+06
3.8455e+06
298500
324250
350000
375750
401500
0.16
0.14
0.12
0.1
0.08
0.06
0.04
0.02
landslide probability

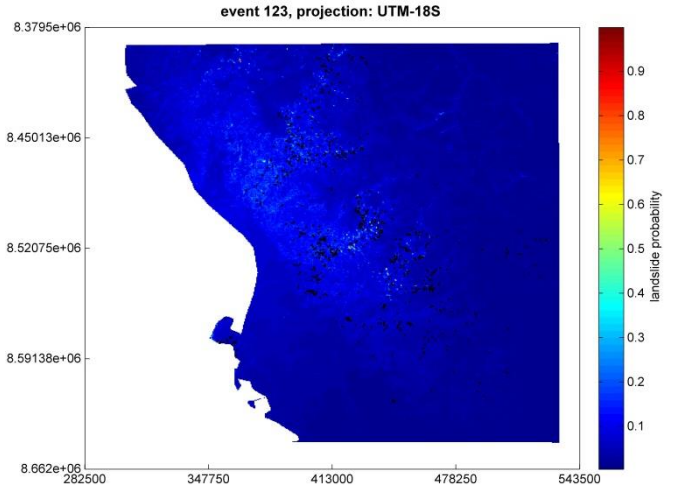
event 123, projection: UTM-18S
8.3795e+06
8.45013e+06
8.52075e+06
8.59138e+06
8.662e+06
282500
347750
413000
478250
543500
0.9
0.8
0.7
0.6
0.5
0.4
0.3
0.2
0.1
landslide probability

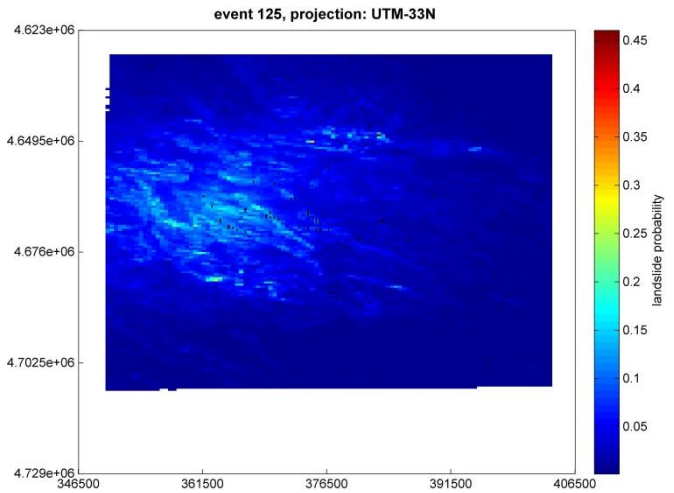
event 125, projection: UTM-33N
4.623e+06
4.6495e+06
4.676e+06
4.7025e+06
4.729e+06
346500
361500
376500
391500
406500
0.45
0.4
0.35
0.3
0.25
0.2
0.15
0.1
0.05
landslide probability

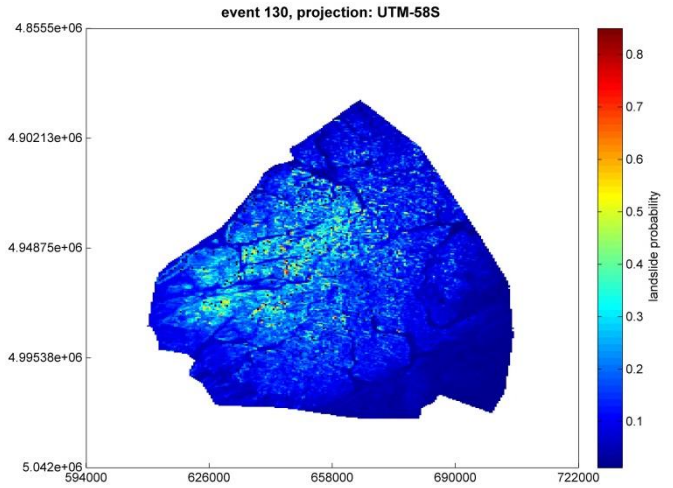
event 130, projection: UTM-58S
4.8555e+06
4.90213e+06
4.94875e+06
4.99538e+06
5.042e+06
594000
626000
658000
690000
722000
0.8
0.7
0.6
0.5
0.4
0.3
0.2
0.1
landslide probability

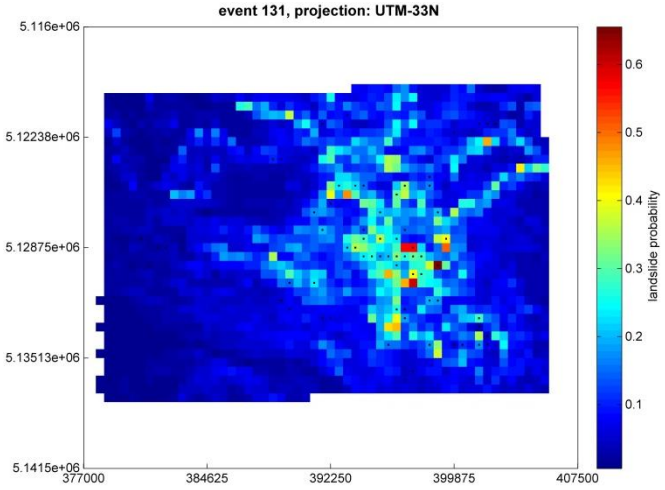
event 131, projection: UTM-33N
5.116e+06
5.12238e+06
5.12875e+06
5.13513e+06
5.1415e+06
377000
384625
392250
399875
407500
0.6
0.5
0.4
0.3
0.2
0.1
landslide probability

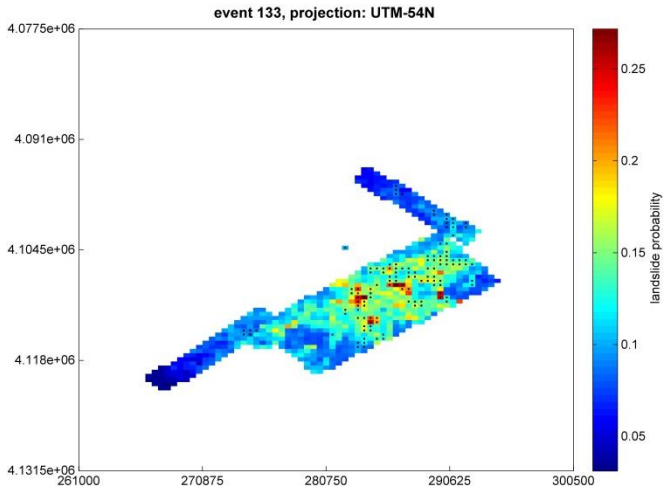
event 133, projection: UTM-54N
4.0775e+06
4.091e+06
4.1045e+06
4.118e+06
4.1315e+06
261000
270875
280750
290625
300500
0.25
0.2
0.15
0.1
0.05
landslide probability

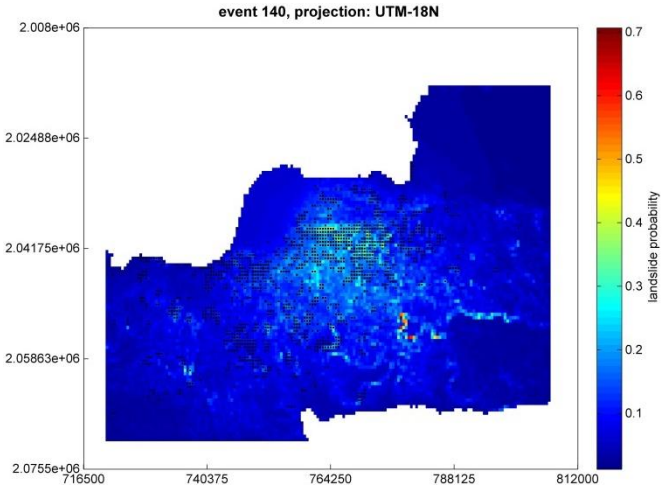
event 140, projection: UTM-18N
2.008e+06
2.02488e+06
2.04175e+06
2.05863e+06
2.0755e+06
716500
740375
764250
788125
812000
0.7
0.6
0.5
0.4
0.3
0.2
0.1
landslide probability

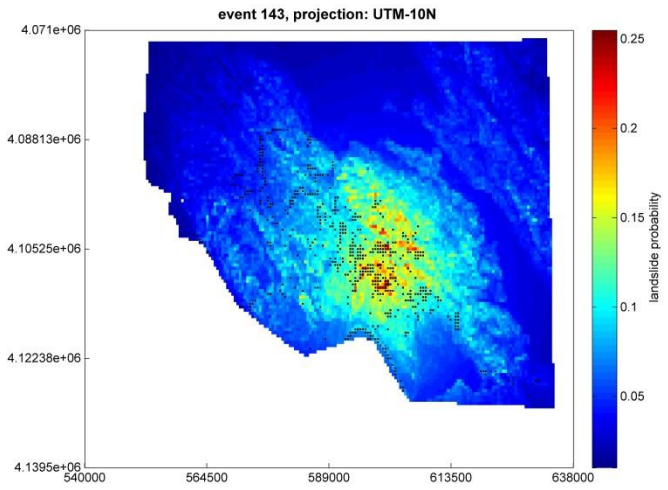
event 143, projection: UTM-10N
4.071e+06
4.08813e+06
4.10525e+06
4.12238e+06
4.1395e+06
540000
564500
589000
613500
638000
0.25
0.2
0.15
0.1
0.05
landslide probability

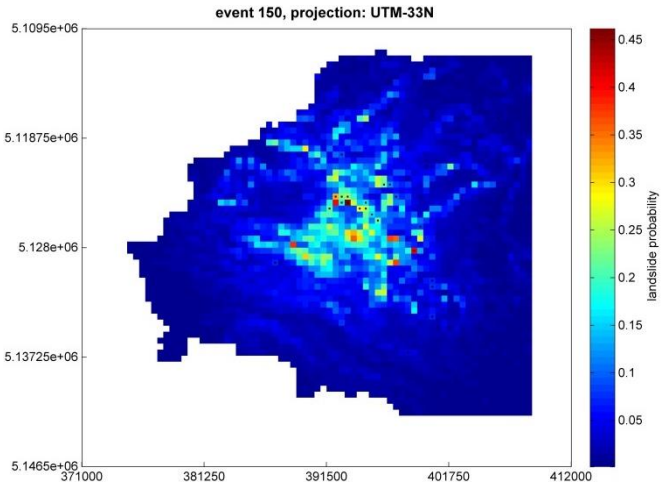
event 150, projection: UTM-33N
5.1095e+06
5.11875e+06
5.128e+06
5.13725e+06
5.1465e+06
371000
381250
391500
401750
412000
0.45
0.4
0.35
0.3
0.25
0.2
0.15
0.1
0.05
landslide probability

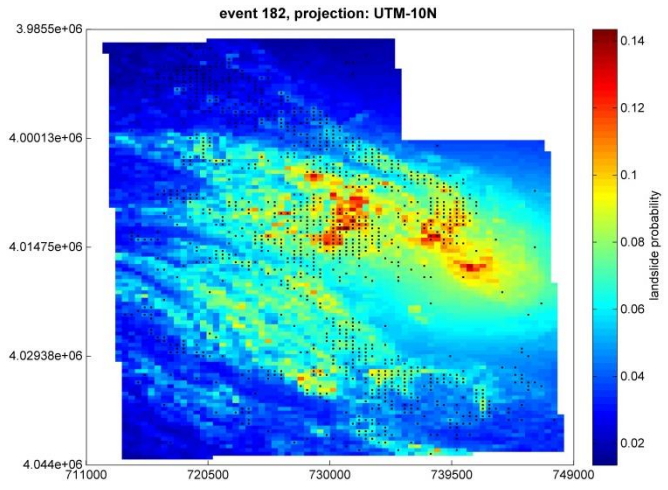
event 182, projection: UTM-10N
3.9855e+06
4.00013e+06
4.01475e+06
4.02938e+06
4.044e+06
711000
720500
730000
739500
749000
0.14
0.12
0.1
0.08
0.06
0.04
0.02
landslide probability

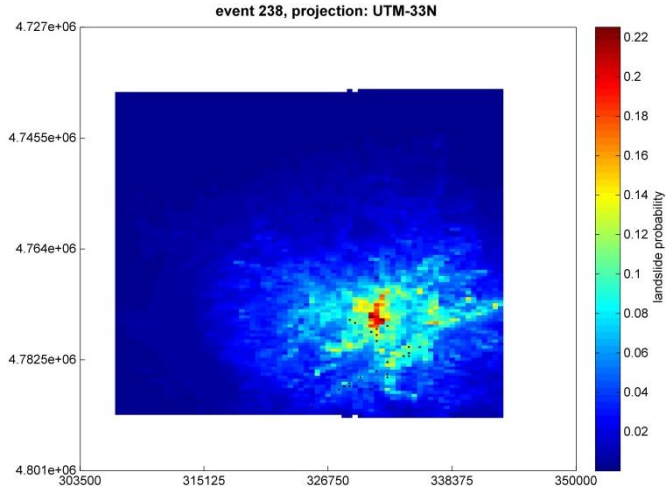
event 238, projection: UTM-33N
4.727e+06
4.7455e+06
4.764e+06
4.7825e+06
4.801e+06
303500
315125
326750
338375
350000
0.22
0.2
0.18
0.16
0.14
0.12
0.1
0.08
0.06
0.04
0.02
landslide probability

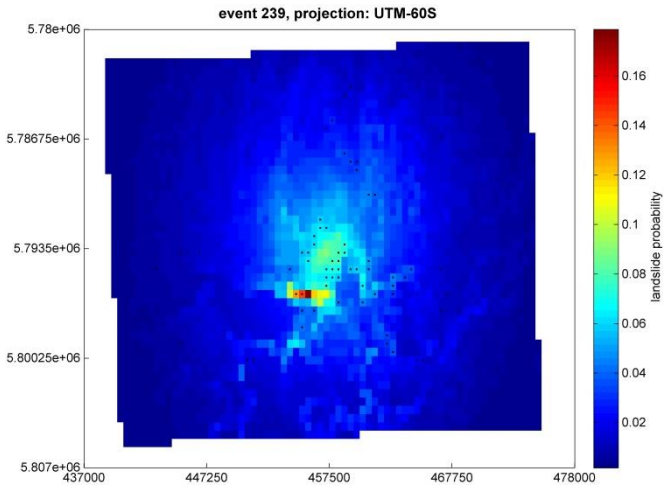
event 239, projection: UTM-60S
5.78e+06
5.78675e+06
5.7935e+06
5.80025e+06
5.807e+06
437000
447250
457500
467750
478000
0.16
0.14
0.12
0.1
0.08
0.06
0.04
0.02
landslide probability

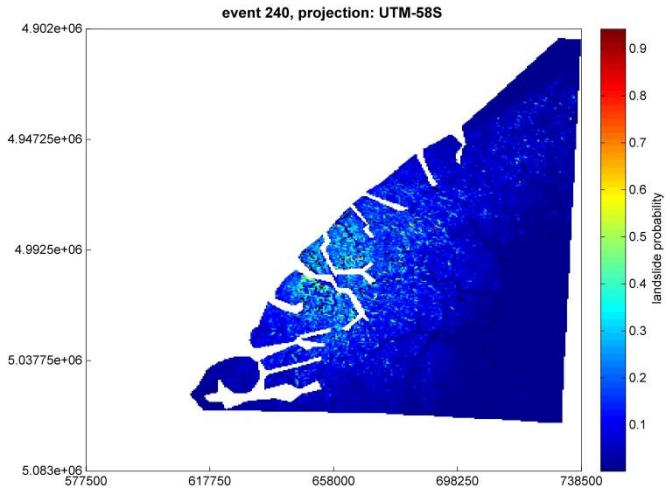
event 240, projection: UTM-58S
4.902e+06
4.94725e+06
4.9925e+06
5.03775e+06
5.083e+06
577500
617750
658000
698250
738500
0.9
0.8
0.7
0.6
0.5
0.4
0.3
0.2
0.1
landslide probability

GEOGRAFIE
Celestijnenlaan 200E bus 2411
B- 3001 LEUVEN-HEVERLEE, BELGIË
tel. + 32 16 32 14 50
fax + 32 16 32 29 80
www.kuleuven.be